博士論文

Direct Synthesis of Methane and Methanol from Carbon Dioxide and Steam in Intermediate-temperature Electrolysis Cells

（中温作動型電解セルにおける二酸化炭素と水蒸気からのメタン・メタノール直接合成）

藤原　直也

Doctoral Dissertation

Direct Synthesis of Methane and Methanol from Carbon Dioxide and Steam in Intermediate-temperature Electrolysis Cells

中温作動型電解セルにおける
二酸化炭素と水蒸気からのメタン・メタノール直接合成

Naoya Fujiwara

Department of Chemical System Engineering
School of Engineering
The University of Tokyo

Table of Contents

Chapter 1

Introduction

1.1. General Background

Our society has flourished by relying heavily on fossil resources such as coal and oil. The extensive use of fossil resources has increased the concentration of carbon dioxide (CO_2) in the atmosphere, which is considered as a cause of global warming. Depletion of the fossil resources is also an upcoming problem. The use of renewable energy can help realize a sustainable society and has been encouraged worldwide. According to World Energy Outlook 2020 by the International Energy Agency[1], the fraction of renewable energy sources to satisfy the world's total primary energy demand was *ca.* 10% in 2019. This should be increased to *ca.* 22% in 2030 to achieve internationally-agreed objectives on climate change, air quality and universal access to modern energy. One of the major drawbacks of renewable energy is its intermittency. In most cases, renewable energy (*e.g.* solar or wind energy) is converted into electricity. The resultant electric power naturally fluctuates and can cause problems in electric power supply networks (*e.g.* supply and demand gap, frequency fluctuation, a fault of the system voltage by inverse power flow[2]).

To mitigate the problems about energy sources, various energy systems and technologies have been proposed and investigated. In this dissertation, I focus on electrolysis technologies. Figure 1-1 shows the general scheme of the targeted energy system. Conventionally, fuels and chemicals are derived from fossil resources, and by using them, CO_2 and water are generated. On the contrary, in the proposed sustainable energy system, valuable compounds will be synthesized from CO_2 and water. Electrolysis is considered the key technology in this synthesis process. Required energy will be supplied by renewable power and waste heat.

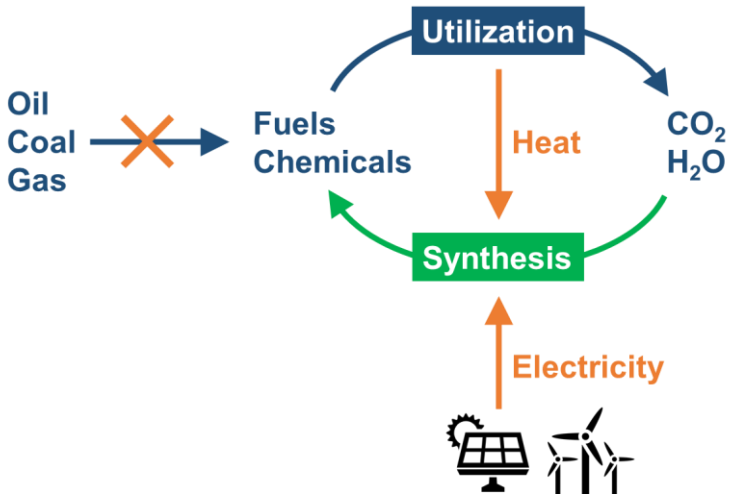

Figure 1-1. Sustainable energy system discussed in this dissertation.

The proposed system (Figure 1-1) will contribute to establish the anthropogenic carbon cycle[3]. CO_2 can be used to synthesize fuels and valuable chemicals, so the consumption of fossil resources will be suppressed and CO_2 emission to the environment will be suppressed at the same time. In addition, the utilization of electrolysis is beneficial because intermittent renewable power can be converted into stable chemical energy of the products, which is suitable for large-scale and long-term storage[2].

Process chains for the conversion of electricity into various products or applications are called "power-to-X"[4]. X represents the output product of the process concerned. For example, power-to-gas indicates the production of gaseous compounds such as hydrogen, syngas (mixture of hydrogen and carbon monoxide), and methane. Power-to-liquid or power-to-fuel includes the formation of alcohols and liquid hydrocarbons. Figure 1-2 shows the major reactions relating to power-to-X technologies. Orange arrows indicate electrochemical reactions, while blue ones indicate thermocatalytic reactions. Names of the reactions (or their abbreviations) are also shown where available. H_2, CO, and syngas can be produced from H_2O and CO_2 by electrochemical reactions. Those gases can be further converted by thermocatalytic reactions (Figure 1-2a). Electrochemical synthesis of alcohols and hydrocarbons is also investigated (Figure 1-2b).

The power-to-X processes with CO_2 as a reactant can be classified into two categories based on how CO_2 is converted: First ones utilize the hydrogen production by water electrolysis, and the CO_2 conversion is

done separately by catalytic reactors. Second ones directly convert CO_2 in electrochemical cells. Accordingly, in the following part, detailed reviews of water electrolysis technologies (Section 1.2) and CO_2 electrolysis technologies (Section 1.3) are presented.

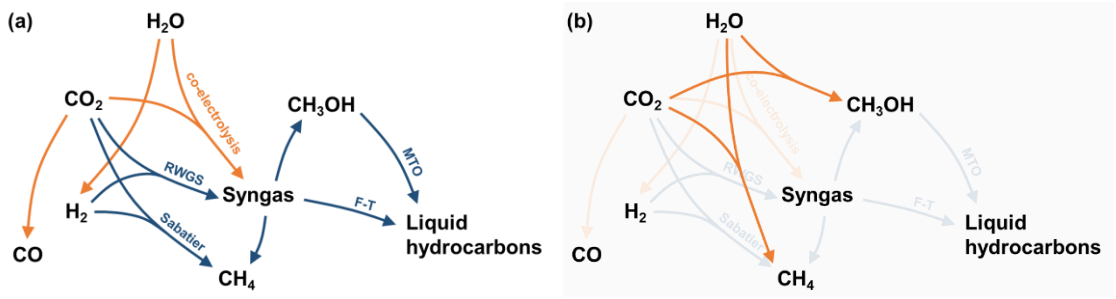

Figure 1-2. Major reactions constituting power-to-X. Orange arrows indicate electrochemical reactions, while blue ones indicate thermocatalytic reactions. (a) Electrochemical production of H_2, CO, or syngas and subsequent catalytic synthesis of various products. (b) Electrochemical synthesis of CH_4 and CH_3OH.

1.2. Water Electrolysis Technologies

Water electrolysis is one of the most basic electrolysis reactions. Hydrogen and oxygen are synthesized by splitting water:

$$H_2O \rightarrow H_2 + 0.5O_2 \quad (1\text{-}1)$$

According to thermodynamics, enthalpy change of a reaction can be written as $\Delta H = \Delta G + T\Delta S$, where H, G, S, and T are enthalpy, Gibbs free energy, entropy, and temperature, respectively. This tells us that the total energy demand for water electrolysis (ΔH) can be satisfied by electrical energy (ΔG) and heat ($T\Delta S$). Figure 1-3 shows the standard enthalpy and standard Gibbs free energy of the steam electrolysis reaction (Eq. 1-1). For details of the calculation, refer to Appendix A. As shown in the graph, ΔG decreases with the temperature while ΔH slightly increases. This means that the electric power required for the electrolysis becomes smaller at higher temperatures.

In the following part, several types of water electrolysis technologies are reviewed. The technologies are classified based on the electrolyte materials.

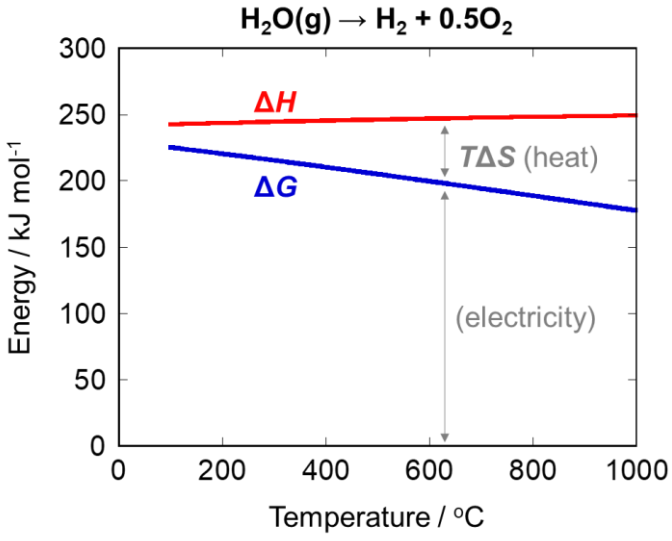

Figure 1-3. Standard enthalpy and standard Gibbs free energy of the steam electrolysis reaction (Eq. 1-1).

1.2.1. Alkaline electrolysis

Alkaline electrolysis utilizes aqueous alkaline electrolytes (*e.g.* KOH solution) and is generally operated below 100°C[5]. This is the most widely studied type of water electrolysis since the discovery of the electrolysis phenomenon by Paets van Troostwijk and Deiman in 1789[6,7]. The technology is well established, and megawatt-scale plants are already commercialized[8]. The cathode reaction is

$$2H_2O(l) + 2e^- \rightarrow H_2 + 2OH^- \quad (1\text{-}2)$$

while the anode reaction is

$$2OH^- \rightarrow 0.5O_2 + 2e^- + H_2O(l) \quad (1\text{-}3)$$

The main drawbacks of the alkaline electrolysis are the gas crossover between two chambers and the low maximum achievable current density due to the high ohmic loss across the electrolyte and diaphragm[9]. Operation of alkaline electrolysis cells at high temperatures (> 150°C) is examined under elevated pressure[10]. Such conditions are beneficial because the conductivity of electrolyte increases and the overpotentials for electrode reactions decrease.

1.2.2. Proton exchange membrane electrolysis

Proton exchange membrane (PEM) electrolysis is often performed with solid polymer electrolytes made of proton-conducting perfluorosulfonated acid, represented by Nafion. Typical operation temperature is below 100°C[9]. The anode reaction is

$$H_2O(l) \rightarrow 0.5O_2 + 2H^+ + 2e^- \quad (1\text{-}4)$$

And the cathode reaction is

$$2H^+ + 2e^- \rightarrow H_2 \quad (1\text{-}5)$$

The solid polymer electrolytes allow compact module design, and achievable current densities become higher than those in alkaline electrolysis[8]. The technology is mature for small scale commercialization. Electron-conducting noble metal oxides such as IrO_2 and RuO_2 are typically used as anode catalysts while Pt/C (platinum nanoparticles supported on carbon) is often used as a cathode catalyst[9].

It is also known that phosphoric acid-doped polymer membranes (especially polybenzimidazole) act as

proton-conducting electrolytes at temperatures higher than 100°C[11]. Such membranes are utilized for fuel cells, which are called high-temperature PEM fuel cells (HT-PEMFCs) operating at 120-200°C[12,13]. The HT-PEM technology is applied for water electrolysis[14,15]. In this case, water is supplied to the anode in the form of steam. Elevated operation temperature leads to high ionic conductivity of the electrolyte and enhanced electrode kinetics, which result in small overpotentials.

1.2.3. Anion exchange membrane electrolysis

Anion exchange membrane (AEM) electrolysis utilizes solid polymer membranes made of quaternary ammonia polysulfones, which conduct hydroxide ions[16]. Being similar to PEM electrolysis, typical operation temperature is below 100°C. Electrode reactions are the same as those of alkaline electrolysis. Usually, aqueous solution is introduced only to the anode side[17]. Water migrates through the membrane to the cathode side and the hydrogen evolution reaction (Eq. 1-5) occurs. The amount of water content in the produced hydrogen is expressed by the dewpoint of the gas.

1.2.4. Molten carbonate electrolysis

Molten carbonate electrolysis is usually performed at temperatures higher than 600°C utilizing molten alkali carbonates (*e.g.* Li_2CO_3, Na_2CO_3, K_2CO_3, and their mixtures)[18,19]. CO_2 gas is needed to produce carbonate ions, the charge carrier in the molten carbonate electrolyte. The electrode reactions are the following. The cathode reaction is

$$H_2O(g) + CO_2 + 2e^- \rightarrow H_2 + CO_3^{2-} \quad (1\text{-}6)$$

Ni is often used for the cathode. The anode reaction is

$$CO_3^{2-} \rightarrow 0.5O_2 + CO_2 + 2e^- \quad (1\text{-}7)$$

NiO is the typical anode material. It should be noted that the CO_2 reduction reaction can occur at the cathode:

$$2CO_2 + 2e^- \rightarrow CO + CO_3^{2-} \quad (1\text{-}8)$$

However, the reaction (Eq. 1-8) is slow enough compared to the water electrolysis reaction (Eq. 1-6), so

the main electrochemical reaction at the cathode is Eq. 1-6. The produced H_2 can react with CO_2 and form CO (reverse water gas shift reaction):

$$CO_2 + H_2 \rightarrow CO + H_2O \quad (1\text{-}9)$$

The products of the molten carbonate electrolysis are obtained as gas mixtures. Thus, separation processes are necessary to produce pure hydrogen or oxygen.

1.2.5. Solid oxide electrolysis

Solid oxide electrolysis is conducted at > 600°C using oxide ion-conducting solid oxide electrolytes[10]. The electrochemical cells are called solid oxide electrolysis cells (SOECs). The electrode reactions are as follows. The cathode reaction is

$$H_2O(g) + 2e^- \rightarrow H_2 + O^{2-} \quad (1\text{-}10)$$

And the anode reaction is

$$O^{2-} \rightarrow 0.5O_2 + 2e^- \quad (1\text{-}11)$$

Typical electrolyte materials are ceramics based on zirconia and ceria. Yttria-stabilized zirconia (YSZ, $(ZrO_2)_{1-x}(Y_2O_3)_x$) and scandia-stabilized zirconia (ScSZ, $(ZrO_2)_{1-x}(Sc_2O_3)_x$) are the most widely used ones. Doping of yttria or scandia (5~10mol%) leads to the formation of oxygen vacancies, which are responsible for the oxide ion conduction[20]. Samarium-doped ceria (SDC, $Ce_{1-x}Sm_xO_{2-\delta}$) and gadolinium-doped ceria (GDC, $Ce_{1-x}Gd_xO_{2-\delta}$) are also widely studied. The conductivity of these doped ceria materials is higher than that of stabilized zirconia[21,22]. Doping of Sm or Gd results in the formation of oxygen vacancies in the lattice. Electron conduction also arises under reducing atmosphere due to the reduction of Ce^{4+} to Ce^{3+}[21]. Perovskite-type oxides are studied as electrolyte materials. For example, $La_{1-x}Sr_xGa_{1-y}Mg_yO_{3-\delta}$ (LSGM), which is based on $LaGaO_3$, is considered promising. It has high oxide ion conductivity and negligible electron conductivity in a wide range of oxygen partial pressure ($1\text{-}10^{-20}$ atm)[23,24].

For the cathode, Ni-based cermets (= ceramic + metal) are often utilized. NiO powder and oxide ion-conducting ceramic powder are mixed and sintered to form the cermets. NiO is reduced to metallic Ni by

hydrogen before usage and provides electron conduction pathways, while ceramics provide oxide ion conduction pathways. The cermets should be porous to facilitate gas diffusion to the reaction sites (triple phase boundary of Ni, ceramic, and the gas phase).

For the anode, mixed electronic and ionic conductors are utilized. Famous materials include perovskite-type oxides such as $La_{1-x}Sr_xMnO_{3-\delta}$ (LSM)[25], $La_{1-x}Sr_xCo_{1-y}Fe_yO_{3-\delta}$ (LSCF)[26], and $Sm_{1-x}Sr_xCoO_{3-\delta}$ (SSC)[27]. These materials are used alone or mixed with powders of electrolyte materials[28,29].

Based on the thermodynamic consideration, solid oxide electrolysis can provide the highest conversion efficiency from electricity to hydrogen if appropriate heat sources are available. However, the high temperature leads to fast degradation of the cells and is not suitable for quick start-up and shutdown. Thus, solid oxide electrolysis at relatively low temperatures is also examined. For example, utilization of proton-conducting solid oxide electrolytes may lower the operation temperature to 400-600°C[10,30]. Typical materials are perovskite-type oxides based on barium zirconate ($BaZrO_3$) and barium cerate ($BaCeO_3$)[30]. When proton-conducting electrolytes are utilized, steam is supplied to the anode side. the anode reaction becomes

$$H_2O(g) \rightarrow 0.5O_2 + 2H^+ + 2e^- \quad (1\text{-}12)$$

And the cathode reaction is the same as that of PEM electrolysis cells (hydrogen evolution reaction, Eq. 1-5).

1.2.6. Solid acid electrolysis

The abovementioned status of the electrolysis research indicates the need for electrolysis technologies feasible in the intermediate temperature range (100-600°C). The intermediate temperature range has potential for both the small cell overpotentials and the flexible operability suitable for the utilization of renewable energy resources. One of the promising technologies in the intermediate temperature range is solid acid electrolysis. Solid acid electrolysis is performed at around 200°C by employing proton-conducting solid acids as electrolytes. The electrode reactions are the same as those of proton-conducting SOECs (Eqs. 1-12 and 1-5).

1.2.6.1. Development of solid acid electrolytes and their application for fuel cells

Several solid oxoacids are known as proton conductors working at around 200°C. Examples are expressed by a generic formula of $M_xH_y(AO_4)_z$, where M = Li, K, Rb, Cs, NH_4 and A = S, Se, P, As[31].

One of the most studied materials is cesium dihydrogen phosphate, CsH_2PO_4. CsH_2PO_4 shows a conductivity jump at around 230°C[32]. The conductivity increases almost five times when the temperature becomes higher than the threshold. This is due to the phase transition from monoclinic structure to cubic structure[33]. The latter phase is called superprotonic phase. Proton conduction in CsH_2PO_4 occur *via* Grotthuss mechanism[34–36]: rotation of PO_4 tetrahedra allows the hopping of H atom bonded to O atoms. It is noted that CsH_2PO_4 is dehydrated under dry conditions to form pyrophosphates or phosphites such as $Cs_2H_2P_2O_7$ or $CsPO_3$, leading to the decrease of the proton conductivity[37–39]. To prevent the dehydration, electrochemical cells should be operated under humidified atmosphere. Cesium pentahydrogen diphosphate, $CsH_5(PO_4)_2$, is another example of the proton conducting oxoacids. $CsH_5(PO_4)_2$ has a melting point (~155°C[40,41]) much lower than that of CsH_2PO_4 (~345°C[42]). Molten $CsH_5(PO_4)_2$ shows higher proton conductivity (> 10^{-1} S cm^{-1} under 30%H_2O/Ar) than the superprotonic CsH_2PO_4 (10^{-2}-10^{-1} S cm^{-1})[43]. Note that $CsH_5(PO_4)_2$ is classified as a "solid acid" in this dissertation, even though the material is in its molten state under operation conditions. The term solid indicates the phase at room temperature.

A group of pyrophosphates are also reported as proton conductors. Nagao *et al.* tested $M^{IV}P_2O_7$ (M = Sn, Ti, Si, Ge, Ce, Zr)[44]. Among them, SnP_2O_7 exhibited the highest ionic conductivity. The conductivity was further increased by doping In^{3+} to the Sn^{4+} site. Shen *et al.* tested $A^{III}_{0.5}B^{V}_{0.5}P_2O_7$ type pyrophosphates (A = Al, Fe, Ga, Y, In, Sb, Bi, La, Nd, Sm, B = Sb, Nb, Ta)[45]. Among them, $In_{0.5}Sb_{0.5}P_2O_7$, $Fe_{0.5}Nb_{0.5}P_2O_7$, and $Fe_{0.5}Ta_{0.5}P_2O_7$ was found to be promising. The authors further examined the conductivity of the pyrophosphates with non-stoichiometric compositions and found that $Fe_{0.4}Ta_{0.5}P_2O_7$ showed the highest conductivity (> 0.4 S cm^{-1} under 20%H_2O/air at 300°C).

The solid acids are used alone or as mixtures with matrices[31]. Oxides and pyrophosphates such as SiO_2, SiP_2O_7, and TiP_2O_7 are often utilized as matrices[40]. Utilization of quartz fiber[46], glass[47], and porous

alumina membranes[48,49] were also reported. It is promising to utilize polymers such as Nafion[50], epoxy resin[51], polyvinylidene fluoride (PVDF)[52], polyvinyl butyral (PVB)[53], polyvinylpyrrolidone (PVP)[54], polybenzimidazole (PBI)[55], SiO_2/PBI composite[56], and sulfonated polystyrene-*b*-poly(ethylene/butylene)-*b*-polystyrene (sSEBS)[57].

It is known that properties of the solid acids are affected by the matrices. Otomo *et al.*[33] reported that the conductivity of CsH_2PO_4 under the superprotonic phase transition temperature was increased by making composite with hydrophilic silica. The possible explanation of the phenomenon is as follows. Proton vacancies are formed in CsH_2PO_4 near the CsH_2PO_4/SiO_2 interface due to the proton stabilization by the hydroxy groups on the SiO_2 surface. The proton vacancies induce the phase transition of CsH_2PO_4, *i.e.*, the superprotonic phase can be formed near the CsH_2PO_4/SiO_2 interface even at temperatures below the threshold.

The melting point of $CsH_5(PO_4)_2$ is decreased by matrices (*e.g.* SiO_2, SiP_2O_7) due to the surface interaction[40,41]. In addition, it is recognized that highly conductive phase can be formed at the interface of $CsH_5(PO_4)_2$ and pyrophosphate matrices[40,58]. Formation of such interfacial phases is facilitated by high crystallinity, large acid amount, and high wettability of the matrix.

These solid acids have been widely investigated as electrolytes of fuel cells[31,46,47,59,60]. For example, Uda and Haile[61] reported a peak power density of 415 mW cm^{-2} at 240°C using a 25 μm-thick CsH_2PO_4 electrolyte. Pt was typically used as electrode catalysts[46,47,61,62], while carbon nanotubes[63] and boron-doped graphene[64] were also utilized as electrode catalysts.

Stability problem hinders the widespread application of solid acid fuel cells. Recently, Wagner *et al.*[65] reported that the morphological change of CsH_2PO_4 near the cathode caused performance degradation of the cell. Large local current densities close to the cathode current collector led to the formation of hotspots, and the heat induced the melting of CsH_2PO_4 or the increase in the plasticity of CsH_2PO_4. The heated CsH_2PO_4 crept through the cathode catalyst and degrade its activity.

1.2.6.2. Application for electrolysis

Application of the proton-conducting solid acid electrolytes to electrolysis cells is considered promising[31]. Such cells are called solid acid electrolysis cells (SAECs) hereafter. The heat required for the electrolysis should be abundant because most of the global waste heat is of temperatures below 300°C[66,67]. Nevertheless, the number of experimental demonstrations of steam electrolysis with SAECs is scarce. Prag[68] and Navarrete *et al.*[69] reported hydrogen production by steam electrolysis with solid acid electrolytes, while Berg *et al.*[70] and Nikiforov *et al.*[71] performed electrolysis using molten phosphate electrolytes. Quantification of hydrogen is essential to the evaluation of SAECs but is barely reported. To the best of the author's knowledge, ref. [69] is the only example reporting the Faraday efficiency (proportion of current which contribute to the formation of a certain product) for the hydrogen production. The stability of SAECs is another issue which has not been focused so far. Elucidating the potential causes of cell degradation is necessary to develop practical SAECs.

1.3. CO_2 Electrolysis Technologies

As mentioned in Section 1.1, CO_2 conversion in power-to-X systems has two types. One type is the thermocatalytic reactions of CO_2 and hydrogen. Hydrogen is obtained from water electrolysis (Section 1.2). In this case, the water electrolysis and the CO_2 conversion are performed separately. The other type is the CO_2 conversion inside electrochemical cells. This type has potential to integrate the hydrogen production step and the following catalytic step, leading to a compact system which will be suitable for distributed power sources.

In this section, the latter type is focused on, and CO_2 electrolysis techniques in different temperature ranges are reviewed. The research area has been attracting attention, as reflected in the increase numbers of papers published[72].

1.3.1. CO_2 electrolysis at low temperatures

1.3.1.1. Overview

In this section, CO_2 electrolysis at low temperatures (< 150°C, typically at room temperature) is reviewed. One of the first reports was made by Royer in 1870, where formation of formic acid was suggested[73]. Several reports were also published in the early 19th century[74–76]. Intensive research efforts over the past several decades were triggered by a report by Hori *et al.* in 1985[77], where the authors used various metals as electrodes and summarized product selectivity. As discussed later in derail, some different cell configurations have been proposed, but generally the cells consist of two chambers separated by ion-conducting membranes, where the anode and the cathode are located. The basic technology is shared with alkaline electrolysis, PEM electrolysis and AEM electrolysis (Sections 1.2.1, 1.2.2, and 1.2.3). For the CO_2 electrolysis, aqueous solutions of $KHCO_3$, KOH, and KCl are typically used as the catholyte and the anolyte[78]. CO_2 is bubbled to the catholyte, and reactions occur at the surface of the electrodes. At the anode, oxygen is generated (Eq. 1-4). At the cathode, various products are formed depending on the used materials and operation conditions. Major products are carbon monoxide (CO), formate (or formic acid),

formaldehyde, methanol, methane, and ethylene[78]. Corresponding reaction formulae are:

$$CO_2 + 2H^+ + 2e^- \rightarrow CO + H_2O \quad (1\text{-}13)$$

$$CO_2 + H^+ + 2e^- \rightarrow HCOO^- \quad (1\text{-}14)$$

$$CO_2 + 4H^+ + 4e^- \rightarrow HCHO + H_2O \quad (1\text{-}15)$$

$$CO_2 + 6H^+ + 6e^- \rightarrow CH_3OH + H_2O \quad (1\text{-}16)$$

$$CO_2 + 8H^+ + 8e^- \rightarrow CH_4 + 2H_2O \quad (1\text{-}17)$$

$$2CO_2 + 12H^+ + 12e^- \rightarrow C_2H_4 + 4H_2O \quad (1\text{-}18)$$

1.3.1.2. Electrode catalysts and product selectivity

According to Lu and Jiao[79], heterogeneous cathode catalysts used in the low-temperature CO_2 electrolysis are classified into metallic catalysts and non-metallic catalysts.

Among monometallic catalysts, Au, Ag, and Zn prefer CO formation. Sn, In, and Pb are used to produce formate. Fe, Ni, and Pt are not suitable for CO_2 conversion, *i.e.*, hydrogen is the main product at the cathode. Cu cathodes have an exceptional feature: hydrocarbons and alcohols can be produced. For example, formation of methane[77,80–82], methanol[83], ethylene[84–88], and ethanol[84,85,87] were reported. The product selectivity on Cu cathodes are regulated by the factors such as surface structure of Cu[89,90], particle size of Cu[91], applied potential[90], cations in the electrolyte solution[92,93], and so on.

Alloys are also widely used as catalysts[94]. For example, nanoporous Cu-Ag alloys were used for production of ethylene and ethanol[95]. Bi-Sn bimetallic electrocatalysts[96] and Pd alloys[97] were utilized for formate production.

Non-metallic catalysts include carbon nanofibers, N-doped carbon, N- or B-doped diamond, and MoS_2[79]. Reported products are CO[98,99], formic acid[99], methane[100], methanol[101], ethanol[102], acetone[102], and so on.

1.3.1.3. Configurations of the electrolysis cells

Several types of electrochemical reactors have been proposed for the low-temperature CO_2

electrolysis[78,103]. The early studies used one-chamber reactor where CO_2 was bubbled in an aqueous electrolyte and two metal plates immersed in the electrolyte were functioned as electrodes. Recent studies often utilize two-chamber reactors, where the anolyte and the catholyte are separated by ion exchange membranes. There are three types of ion exchange membranes: cation exchange membranes (CEMs, conducting H^+ or K^+), anion exchange membranes (AEMs, conducting OH^- or HCO^{3-}), and bipolar membranes. The last one consists of a CEM and an AEM laminated together, and catalyst at the interface of the two layers to facilitate water dissociation ($H_2O \leftrightarrow H^+ + OH^-$)[104,105]. It was reported that, when using CEMs, the pH at reaction sites becomes low and hydrogen evolution reaction proceeds at a high rate, suppressing the CO_2 reduction reactions[106]. Such a problem can be mitigated by introducing AEMs. Bipolar membranes are considered effective to inhibit undesirable product crossover[105].

Utilization of gas diffusion electrodes (GDEs) is attracting attention because high reaction rates are expected by feeding CO_2 directly to reaction sites in gas phase[78,107–109]. In cases where CO_2 is bubbled in aqueous catholytes, the diffusion of CO_2 to the reaction sites may become the rate-limiting step[79]. Because the molecular diffusion of gaseous CO_2 is much faster than that of CO_2 dissolved in water, the reaction rate can become higher if GDEs are utilized. According to literature[107], the diffusion coefficient of CO_2 in aqueous solutions under the standard condition is 0.0016 $mm^2\ s^{-1}$, while that of humidified CO_2 in a gas phase is 16 $mm^2\ s^{-1}$.

Application of the HT-PEM technology to CO_2 electrolysis is also investigated. Gao *et al.*[110] utilized a phosphoric acid-doped PBI membrane and synthesized CO and methane at 170°C with PtMo/C cathode catalysts. Gutiérrez-Guerra *et al.*[111] used a similar membrane and performed CO_2 electrolysis at 110°C using a Cu-CNF catalyst (Cu supported on carbon nanofibers). Main products were acetaldehyde, methanol, methyl formate, and CO. Selectivity for the products changed depending on the applied current density.

1.3.2. CO_2 electrolysis at high temperatures

1.3.2.1. Molten carbonate electrolysis cells

As explained in Section 1.2.4, CO_2 is incorporated into the chemistry of molten carbonate electrolysis cells. Reduction of CO_2 takes place in the cathode catalytically and/or electrochemically. Formation of CO and solid carbon (*e.g.* carbon nanotubes) are reported[112–114].

1.3.2.2. Solid oxide electrolysis cells

SOECs allow the electrolysis of CO_2:

$$CO_2 + 2e^- \rightarrow CO + O^{2-} \quad (1\text{-}19)$$

This reaction is endothermic. Considering the anodic reaction Eq. 1-11, the overall reaction can be written as

$$CO_2 \rightarrow CO + 0.5O_2 \quad (1\text{-}20)$$

Figure 1-4 shows the standard enthalpy and standard Gibbs free energy of Eq. 1-20. ΔG decreases with the temperature while ΔH is almost constant. The trends are similar to those of the water electrolysis.

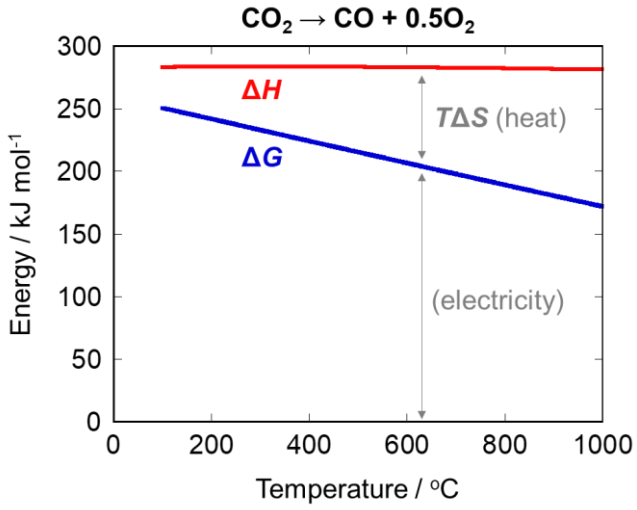

Figure 1-4. Standard enthalpy and standard Gibbs free energy of the CO_2 electrolysis reaction (Eq. 1-20).

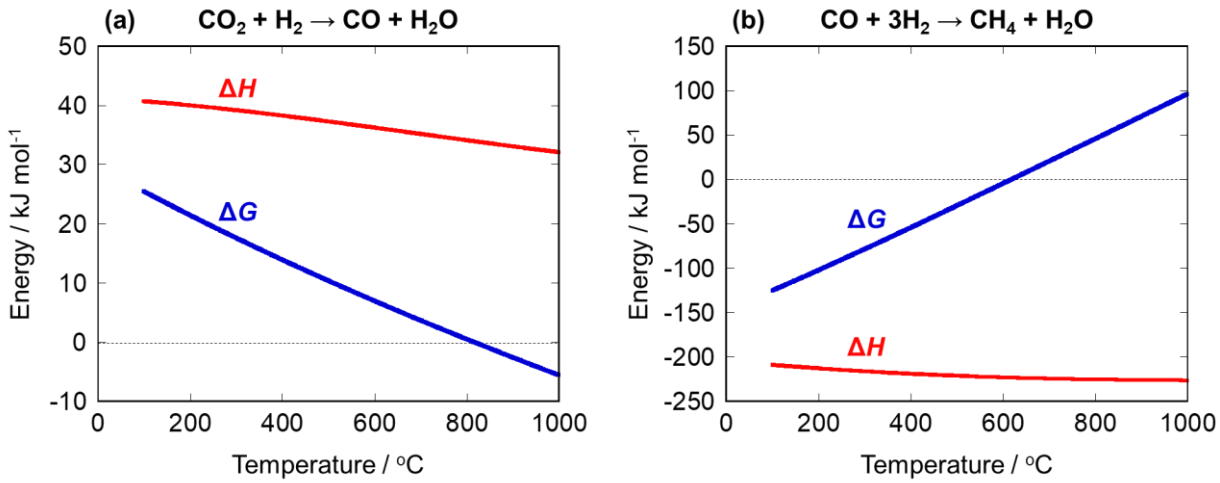

Figure 1-5. Standard enthalpy and standard Gibbs free energy of (a) the reverse water gas shift reaction (Eq. 1-9) and (b) the CO methanation reaction (Eq. 1-21).

If CO_2 and steam are mixed and supplied to the SOEC cathode, syngas can be obtained through electrolysis reactions (Eqs. 1-10 and 1-19) and the reverse water gas shift reaction (Eq. 1-9). This process is called co-electrolysis. Obtained syngas can be converted into various chemicals by catalytic reactions. The reverse water gas shift reaction is an endothermic reaction. Figure 1-5a shows the temperature dependence of ΔH and ΔG of the reaction.

As mentioned earlier, syngas can be converted into various chemicals (Figure 1-2). Here, formation of methane is focused. Methane is a promising energy carrier candidate because it can utilize the existing infrastructure for natural gas[115–117]. When methane is synthesized from electrochemically-obtained syngas, the whole process is regarded as a power-to-gas process. Note that the term power-to-gas includes the production of hydrogen, syngas, and methane[4,115,118]. To avoid misunderstanding, methane-producing processes with SOECs are denoted as power-to-methane (PtM) hereunder. Methane can be catalytically synthesized from syngas as follows:

$$CO + 3H_2 \rightarrow CH_4 + H_2O \quad (1\text{-}21)$$

The CO methanation reaction (Eq. 1-21) is an exothermic reaction. Figure 1-5b shows the standard enthalpy and standard Gibbs free energy of the reaction at 100-1000°C. Figure 1-6a illustrates the two-step PtM process utilizing co-electrolysis in a SOEC. Synthesized methane is introduced to the gas

network and dealt with the existing infrastructure for natural gas. By connecting the power grid and the gas grid, flexible energy management can be achieved. Figure 1-7a shows the details of the two-step process. Here, the reaction heat of methanation ($\dot{Q}_{\mathrm{M}}$) in the external catalytic reactors cannot be directly utilized for heating the SOEC stack because SOEC operating temperature is usually around 800°C while that of the catalytic methanation is much lower (around 300°C). If $\dot{Q}_{\mathrm{M}}$ can be utilized for endothermic co-electrolysis reactions, the energy required in the SOEC (P_{SOEC}) can be suppressed and the overall system efficiency will become higher.

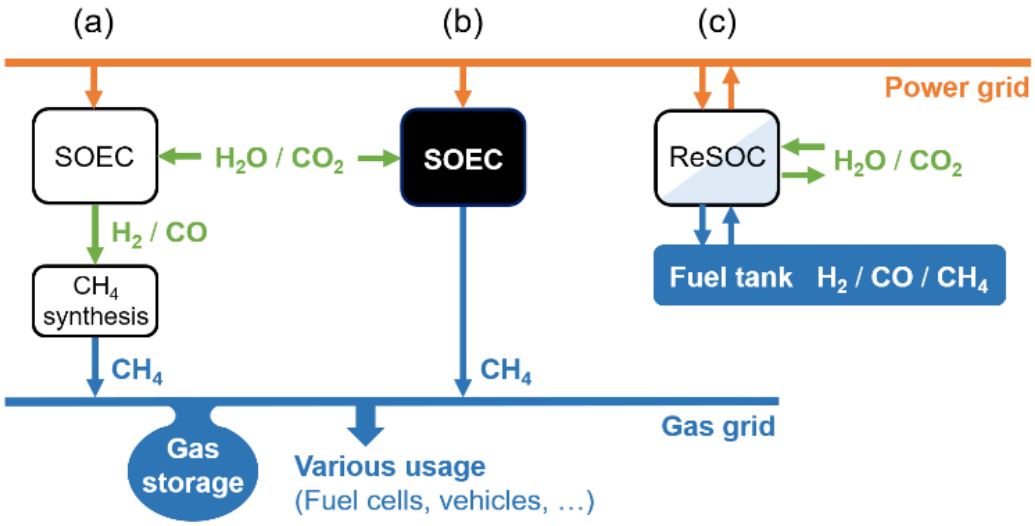

Figure 1-6. General scheme of power-to-methane processes with solid oxide cells.

Recently, some researchers have proposed the concept of one-step PtM, where the electrolysis step and the methanation step are integrated into a single SOEC reactor (Figure 1-6b). Such a novel reactor can be economically advantageous due to the unnecessity of the external catalytic reactors. Initial investment and maintenance costs of the system could be lowered. A space-saving feature of the direct process also matches the concept to utilize the distributed renewable energy resources.

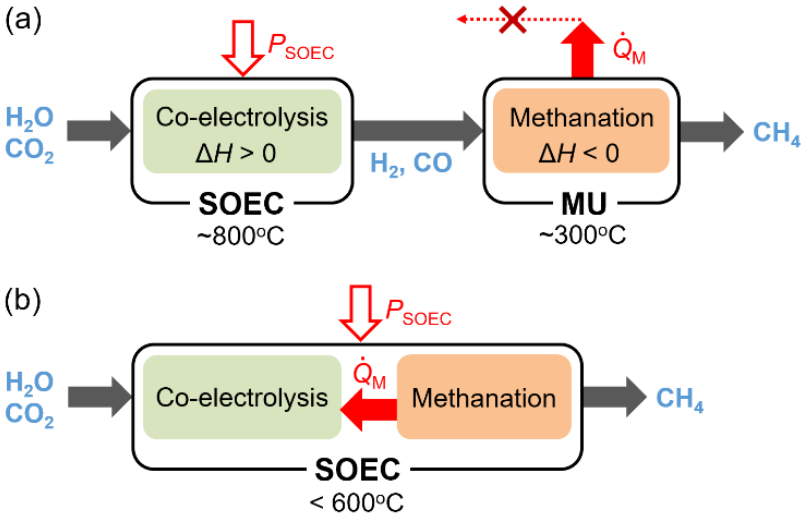

Figure 1-7. Details of the two power-to-methane systems. (a) Two-step process: CO_2/H_2O co-electrolysis in a high-temperature SOEC coupled with catalytic CO methanation in a methanation unit (MU). (b) Direct process: Direct methane synthesis in an intermediate-temperature SOEC. Only desired reactants and products are shown for simplicity.

The proposed one-step reactors can be classified into two types. One is a reactor with temperature gradients, which is first reported by Chen *et al.*[119] They prepared a tubular SOEC and made the cathode support layer and the electrolyte layer longer than the anode layer. The excess part of the cathode layer, which is located in the cooled downstream region, functions as a methanation catalyst. SOEC cathode materials can catalyse the methanation reaction because components of the cathodes are similar to those of heterogeneous CO_x methanation catalysts[120]. In ref. [119], a reaction test was performed for 24 h with a cathode inlet gas composition of $H_2O/CO_2/H_2$ = 20/11.4/68.6. The SOEC part of the reactor was kept at 800°C while the downstream region was placed under a temperature gradient of 800-250°C. The reactor showed a stable performance: Average current density, CO_2 conversion, and CH_4 yield were 0.42 A cm^{-2}, 64.1%, and 39.7%, respectively. In the reactor, the places for the electrolysis reactions and the methanation reaction were spatially separated, and the temperatures were also different. Therefore, heat exchange mechanism should be carefully designed to realize the heat utilization. It is suggested that a counter flow condition is preferred to a parallel flow condition to create the desirable temperature distributions[121,122]. In the counter flow condition, the reaction heat of methanation in the cathode

downstream region can be efficiently used to heat up the anode inlet gas flow. Luo *et al.*[122] established a two-dimensional model and investigated the effects of operating conditions and cell materials on the methane production. They found that a cell composed of LSGM-based materials could achieve an electricity-to-gas efficiency of 94.5% at 29 bar. Based on the same concept, Lei *et al.*[123] fabricated a micro-tubular SOEC reactor and tested it experimentally. A methane yield of 21.1% and a CO_2 conversion of 87.7% were achieved with a feed gas composition of $CO_2/H_2/H_2O$ = 10.7/69.3/20.

The other type of the one-step PtM reactors is the isothermal ones. According to thermodynamics, methane can be directly formed in SOEC cathodes when the co-electrolysis is performed at low temperature and high pressure[120,124]. It is supposed that hydrogen and CO produced by the co-electrolysis further react to form methane on the surface of the cathode material. Such a PtM process utilizing the isothermal one-step reactor is called direct PtM process hereafter. Figure 1-7b shows the direct process, where methane is directly synthesized in a SOEC unit. The SOEC in the direct process is assumed to work at intermediate temperatures under 600°C, and the methanation reaction takes place inside the cell. Therefore, the reaction heat of methanation ($\dot{Q}_{\mathrm{M}}$) can be directly utilized for the endothermic electrolysis reactions. The simplified thermal management has potential to decrease the energy required for the SOEC unit (P_{SOEC}).

However, there are some challenges to make the direct PtM process practical. First, attention should be paid to the system outlet gas compositions. Equipment designed for natural gas requires high methane concentration and low hydrogen concentration because hydrogen can deteriorate the durability of such equipment. Note that limits of the acceptable hydrogen fraction differ depending on the equipment, and there is no common agreement about the exact values[118]. Here are some examples of reported upper limits: 2vol% for gas storage tanks[118], 15vol% for natural gas pipeline network[125], and 30vol% for internal combustion engines of natural gas-fueled vehicles[126]. Most of the previous researches featuring the internal methanation in SOECs are based on the concept of reversible solid oxide cells (ReSOCs) coupled with isolated gas storage tanks (Figure 1-6c)[120,124,127–130]. In those cases, the fuel gas is not introduced to the natural gas grid, so the limitations of gas compositions were not severe. However, if the

utilization of natural gas infrastructure is aimed (Figure 1-6b), those limitations have to be taken into account. Luo *et al.* simulated the direct PtM process in ref. [125]. According to their model, the product gas of the isothermal SOEC reactor operated at 550°C and 25 bar contains 54vol% of hydrogen, which exceeds the upper limit of acceptable hydrogen fraction in the existing natural gas infrastructure. Therefore, hydrogen removal from the product gas is needed, resulting in a system exergy efficiency lower than that of the two-step process or the temperature-gradient SOEC reactor. Reznicek and Braun[131] modelled a reversible direct PtM system connected to a natural gas pipeline and a CO_2 pipeline. When the reversible cell was operated in a SOEC mode at 600°C, 20 bar, the system outlet gas contained 60% of methane and 33% of hydrogen. It should be noted that the hydrogen amount of 33% could be unacceptable for natural gas pipelines[125]. A system lower heating value efficiency of 68.1% was reported in ref. [131] while the comparison with the two-step PtM systems was not performed.

Materials development is also a problem. Methanation is a highly exothermic reaction, so it is thermodynamically advantageous to lower the SOEC operating temperature to obtain a significant amount of methane. However, today's typical SOECs are not suitable for operation below 600°C due to the large overpotentials caused by low ionic conductivity in the electrolytes and slow reaction rates at the electrodes. Even though the idea of the PtM process utilizing internal methanation in SOECs was already recognized in literature in 2011[132], only a few experiments have been reported on this topic until now[133–135]. Li *et al.*[133] conducted experiments of methane synthesis using a planar button-type SOEC in a temperature range of 550-650°C. Methane compositions of less than 1% in the outlet gas (dry basis) were reported under ambient pressure. Corresponding current values ranged from 0 A to 1.095 A. Yamaguchi *et al.*[134] conducted experiments using tubular type SOECs at 400°C, 1 atm. They compared an yttria-stabilized zirconia (YSZ) electrolyte and a gadolinium-doped ceria (GDC) electrolyte and stated that the GDC electrolyte is more suitable at 400°C. In the GDC case, methane concentrations around 30-40% were reported for a current range of 19-312 mA.

Performance improvement of the isothermal SOEC reactors could be achieved by applying the technologies of low- or intermediate-temperature solid oxide cells. For example, oxide ion-conducting

materials such as doped bismuth oxides[136,137] or lanthanum silicates[138,139] have been investigated as electrolytes for lower temperatures. The performance of such electrolyte materials can be enhanced or stabilized by forming multilayered structures[140,141]. Proton-conducting perovskites are also widely studied as low- or intermediate-temperature electrolyte materials[30,142]. Application of those ceramics to CO_2 reduction has been reported[143–145] while stability issues caused by the reaction between the perovskites and CO_2 should be settled[146].

The discussions above are based on the consideration that methane is synthesized catalytically from syngas in SOECs (Eq. 1-21). In other words, electrochemical syngas production and thermocatalytic methanation occur sequentially in the SOEC cathode. However, it may also be possible that methane formation is incorporated into charge-transfer reactions, that is, electrochemically-generated surface species react directly to form methane:

$$2H_2O(g) + CO_2 + 8e^- \rightarrow CH_4 + 4O^{2-} \quad (1\text{-}22)$$

$$2H_2O(g) + CO + 6e^- \rightarrow CH_4 + 3O^{2-} \quad (1\text{-}23)$$

$$2H_2 + CO_2 + 4e^- \rightarrow CH_4 + 2O^{2-} \quad (1\text{-}24)$$

$$2H_2 + CO + 2e^- \rightarrow CH_4 + O^{2-} \quad (1\text{-}25)$$

If such reaction pathways exist, the methane formation will not be limited by the thermodynamics of Eq. 1-21. Nevertheless, it is quite difficult to distinguish between thermocatalytic reactions and electrocatalytic reactions. Development of novel techniques for characterization of the electrode surface (*e.g. operando* spectroscopy) are required to elucidate the complex reaction mechanism in SOEC cathodes.

1.3.3. CO_2 electrolysis at intermediate temperatures with SAECs

As reviewed in Section 1.2.6, solid acid electrolysis cells (SAECs) can be operated at around 200°C, so the application of SAECs to the intermediate-temperature CO_2 conversion seems promising. However, there had been no papers published on the topic until Christensen *et al.*[147] reported the formation of methane in 2020. They utilized a composite electrolyte composed of CsH_2PO_4, SiC, and a small amount

of H_3PO_4. Ni was used as the cathode, and a mixture of IrO_2 and polybenzimidazole was used as the anode. The cell was operated at 300°C, 8 atm. Steam was electrolyzed in the anode to form protons, and the protons reacted with CO_2 in the cathode to produce methane. Methane was produced with Faraday efficiencies of 70-100%, and hydrogen was also formed as a by-product. This is a prominent demonstration of the intermediate-temperature CO_2 electrolysis, while further researches about cell materials, stability, and reaction mechanisms are required to improve the technology. The working temperature of solid acid electrolytes (*ca.* 150-300°C) is near the lower limit of the operation temperature of industrial methanation reactors (*ca.* 250-700°C[116]). The operation temperature of 300°C is suitable for methane production from the catalysis viewpoint. The nominal cathode reaction is Eq. 1-17. This reaction may be interpreted as a combination of the hydrogen evolution reaction (Eq. 1-5) and the catalytic CO_2 methanation (Sabatier reaction, Eq. 1-26 below), although the detailed reaction mechanism has not been clarified so far.

$$CO_2 + 4H_2 \rightarrow CH_4 + 2H_2O \quad (1\text{-}26)$$

As shown in Figure 1-8a, the CO_2 methanation (Eq. 1-26) is an exothermic reaction. Methane formation is favored at low temperatures and high pressures.

Methanol is another desirable product which may be synthesized in SAECs. Catalytic methanol production from CO_2 and H_2 is typically performed at 200-300°C, 10-100 bar[148]. The working temperature of SAECs is considered suitable for the methanol formation. The cathode reaction is expected to be the same as Eq. 1-16. This reaction can proceed electrochemically, *i.e.*, protons and CO_2 may directly react to form methanol. On the other hand, it is also likely that protons are once converted to hydrogen (Eq. 1-5). The hydrogen reacts catalytically with CO_2 to form methanol (Eq. 1-27):

$$CO_2 + 3H_2 \rightarrow CH_3OH + H_2O \quad (1\text{-}27)$$

The CO_2-to-methanol reaction is exothermic (Figure 1-8b), and methanol formation is favored at low temperatures and high pressures.

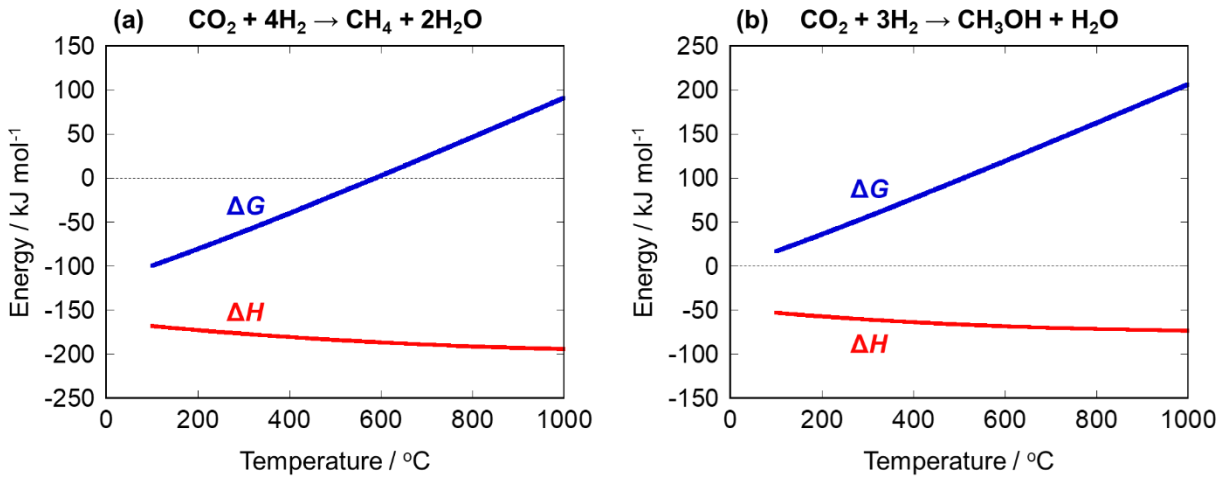

Figure 1-8. Standard enthalpy and standard Gibbs free energy of (a) CO_2 methanation reaction (Sabatier reaction, Eq. 1-26) and (b) the CO_2-to-methanol reaction (Eq. 1-27).

1.4. NEMCA Effect

It is known that the activity of heterogeneous catalysts can be modified by applying voltage. Such effects are called NEMCA effect (non-Faradaic electrochemical modification of catalytic activity) or EPOC (electrochemical promotion of catalysis)[149–152]. A Greek research group has extensively investigated the NEMCA effect for the CO_2 hydrogenation using a single-chamber reactor fed with CO_2 and H_2[153–157]. As discussed in Sections 1.3.2 and 1.3.3, catalytic CO_x hydrogenation reactions can proceed at cathodes in high-temperature and intermediate-temperature CO_2 electrolysis, and the NEMCA effect may emerge in those cases. The author examined the NEMCA effect in a two-camber SOEC reactor and found that the methane formation in the cathode was accelerated by the polarization (see Appendix E).

1.5. Research Objectives and Outline of the Dissertation

For the realization of the sustainable energy system depicted in Figure 1-1, electrochemical reduction of CO_2 and water will play an important role. Figure 1-9 summarizes the CO_2 electrolysis technologies reviewed in Section 1.3. CO_2 electrolysis at low temperature has potential for production of various chemicals. A major drawback is the low current density, which is not desirable for commercialization. On the other hand, high-temperature CO_2 electrolysis allows large current density (~1 A cm^{-2})[132,158]. It is also advantageous that theoretical energy conversion efficiency from electricity to chemical energy is high (Figure 1-3 and Figure 1-4). However, it is difficult to obtain products other than CO, due to the thermodynamic limitations. Accordingly, CO_2 electrolysis at intermediate temperatures (100-600°C) is attracting attention as a potential technology for the production of hydrocarbons and oxygenates (*e.g.* alcohols, ethers, carboxylic acids). It is expected that high reaction rates and high selectivity to the desired products are achieved simultaneously.

The objective of the present study is **to develop energy-efficient intermediate-temperature electrolysis cells with which hydrocarbons and oxygenates can be directly synthesized from CO_2 and water**. To achieve the goal, the following steps were set:

- **Simulations to figure out the promising candidate technology** → [Chapter 2]

  Although there are some candidate electrolysis technologies, their characteristics have not been fully understood. I performed numerical simulations to offer prospect of the impacts of the technologies and to provide insight into the direction of research and development.

- **Experimental work for the development of desired cells** → [Chapter 3]

  After the simulations, target technology was determined. I performed experiments to clarify and solve the problems.

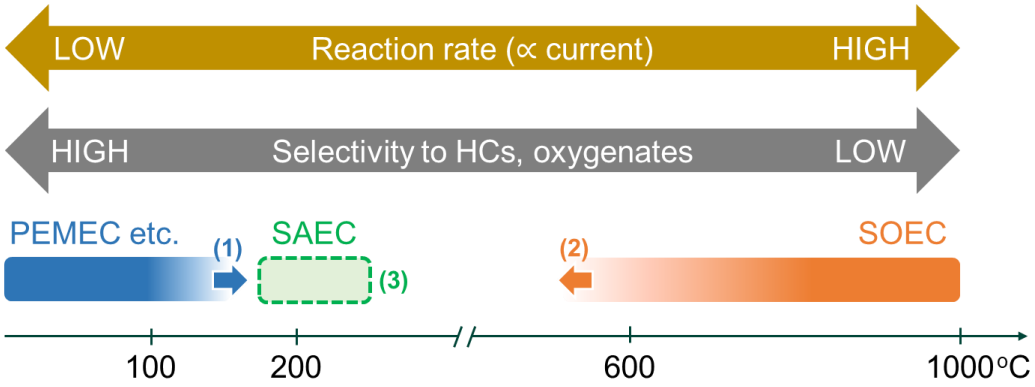

Figure 1-9. CO_2 electrolysis technologies at different operation temperatures. General trend of the reaction rates and the selectivity to hydrocarbons and oxygenates are shown. Three possible approaches to the intermediate-temperature CO_2 electrolysis are indicated by (1)-(3).

There are three possible approaches to the intermediate-temperature CO_2 electrolysis: (1) to increase the operation temperature of the low-temperature cells, (2) to decrease the operation temperature of the high-temperature cells, and (3) to develop novel intermediate-temperature electrolysis cells. For all the approaches, only small numbers of studies have been reported so far. Potential advantages and drawbacks of each approach are not clear. Therefore, it is worthwhile to investigate the characteristics of possible electrolysis technologies quantitatively. **Chapter 2** addresses the simulations of the intermediate-temperature CO_2 electrolysis processes. The approaches (2) and (3) are focused on. In **Section 2.1**, direct methane production in solid oxide electrolysis cells (SOECs) is studied, representing the approach (2). The direct process is compared with the conventional two-step process, which consists of the syngas production in SOECs and the successive methanation in catalytic reactors. In **Section 2.2**, CO_2 electrolysis in solid acid electrolysis cells (SAECs) is simulated as a promising candidate technology of the approach (3). The production of methane and methanol are targeted, and the thermodynamic properties and current-voltage characteristics are examined by changing parameters.

According to the simulation results, experimental investigations were made to develop SAECs for the CO_2 conversion. **Chapter 3** addresses the topic. First, steam electrolysis in SAECs was investigated (**Section 3.1**). SAEC research is in the initial stage, and even the basic experimental setup for stable measurements has not been established so far. Thus, I examined the factors affecting the cell stability in

detail. Based on the findings in the steam electrolysis study, CO_2 electrolysis in SAECs was performed (**Section 3.2**). Different cathode materials and structures were examined, and the desirable directions of the cell development are discussed.

Chapter 4 summarizes the studies. Future perspective of the intermediate-temperature CO_2 electrolysis technologies is also given.

Chapter 2

Simulations of Electrolysis Cells for Direct CO_2 Conversion

In this chapter, the applicability of solid oxide electrolysis cells (SOECs) and solid acid electrolysis cells (SAECs) to the direct CO_2 conversion is discussed based on the results of numerical modeling. For both SOECs and SAECs, methane production was targeted. In the case of SAECs, the possibility of methanol production was also examined.

2.1. SOECs for Methane Production

2.1.1. Objective

As discussed in Section 1.3.2.2, the direct power-to-methane (PtM) processes with isothermal one-step SOEC reactors have potential for highly efficient energy conversion because the reaction heat of methanation can be directly utilized for the endothermic electrolysis reactions. However, such processes have never been discussed intensively, possibly due to the difficulty to overcome the limitations: the necessity of high methane concentration and low hydrogen concentration in the system outlet, and the absence of cell materials feasible for the operation below 600°C. As a result, the characteristics of the processes are not yet fully understood. To obtain a comprehensive view of the concept, the significance of advantages and drawbacks of the direct process should be revealed quantitatively in comparison to the two-step process. It is worthwhile to investigate the system operating conditions and SOEC properties required to make the most of the possible advantage, and to clarify how significant the impact will be.

Accordingly, in Section 2.1, I focus on the isothermal conditions for the direct PtM. A process model was established with which both the direct process and the two-step process can be simulated. First, the performance of the direct PtM process was simulated with changing the operating temperature, assuming

the cell properties of conventional high-temperature SOECs. For a low-temperature region, properties at higher temperatures were extrapolated. The results were compared with that of the two-step process. After that, highly pressurized operations of the direct process were simulated in expectation of improved performance. Finally, improved current-voltage characteristics were postulated for the direct-methanation SOEC at 400°C and 500°C. Detailed discussions about the energy conversion properties were made to reveal the problems and the potential advantages of the proposed systems. The present work is intended to offer insights into the direction of future investigations of the direct PtM processes with SOECs.

2.1.2. Theory and models

Use of process simulators in SOEC modeling makes it easier to discuss energy efficiencies in the whole system. Barelli *et al.*[126] used *Aspen Plus* platform to model a system for production of CH_4/H_2 mixture which consisted of a SOEC unit and a catalytic methanation unit. However, the SOEC unit was only used for co-electrolysis and the direct methanation in cathode was not considered in their work. In the present study, a SOEC-based energy system was modeled so that both the direct and the two-step power-to-gas processes can be simulated in a single model. A process simulator *Aspen Plus V8.8* (Aspen Technology, Inc.) was utilized. Major features of the model are the following: (1) The CO methanation in SOEC cathode is considered. (2) Each component of the cell overpotentials can be separately calculated. The present model is basically zero-dimensional, so the distributions of temperature and gas concentrations inside the SOEC are not taken into consideration. Zero-dimensional models are widely used to simulate SOEC systems[126,128,159,160]. In some of the zero-dimensional models, current-voltage characteristics of the cells are modeled by considering area specific resistances (ASR) as functions of temperature and pressure[126,159]. While the ASR simplifies the calculation, such an approach limits detailed discussions of the overpotentials. In the present model, three components of the overpotential (ohmic, activation and concentration overpotentials) were calculated separately. This allows us to simulate how cell geometry parameters and electrochemical parameters affect the SOEC performance. It is necessary to consider the gas concentration gradients in electrode layers for the calculation of the concentration overpotentials.

Accordingly, even though the overall model is zero-dimensional, one-dimensional gas concentration profiles in the electrode thickness direction were postulated[128,160].

Figure 2-1 shows the outline of the simulation. Once the current density is set, the corresponding reacting moles are obtained. Then, using the *Aspen Plus* model, system outlet gas compositions and heat duties of each module are calculated. Using the resultant gas compositions, cell operation voltage is calculated for the designated current density. Based on the current density, the cell potential, and the heat duties, energy conversion efficiencies of the system are determined. Table 2-1 shows the general settings of *Aspen Plus V8.8*. The property method of IDEAL utilizes the ideal gas equation of state for the vapor phase.

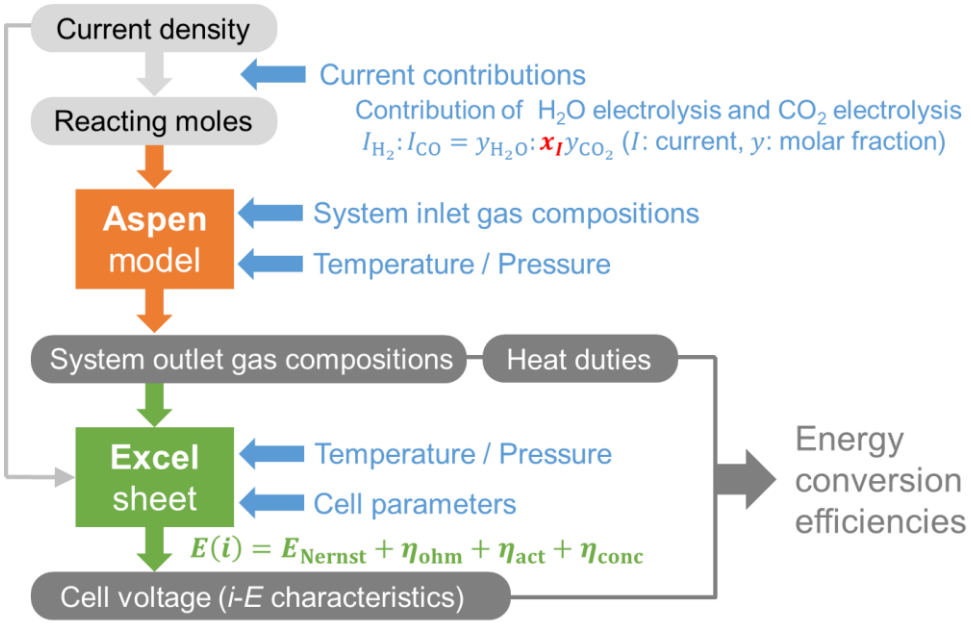

Figure 2-1. Outline of the simulation.

Table 2-1. General settings of *Aspen Plus V8.8*.

Property method	IDEAL
Input mode	Steady-State
Stream class	CONVEN
Substream	MIXED

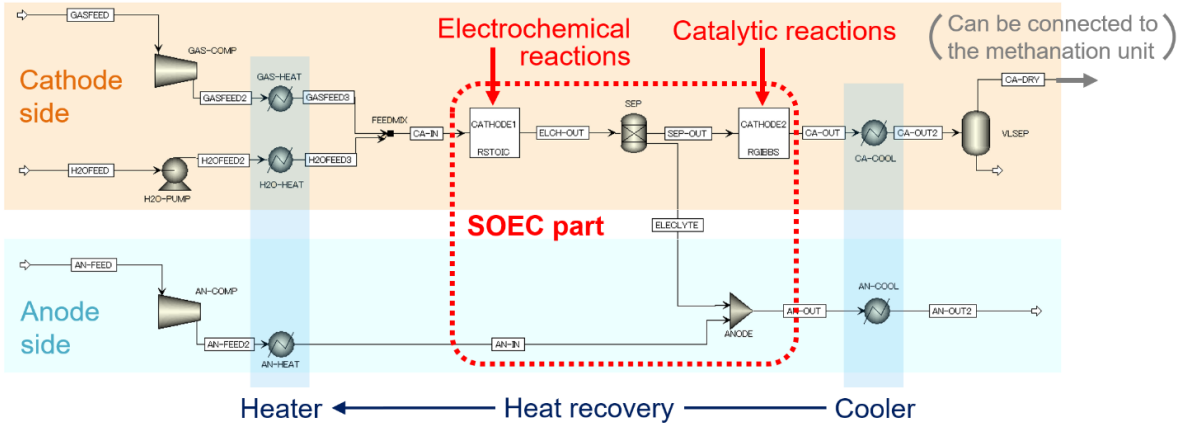

Figure 2-2. Model of the SOEC unit.

Table 2-2. Detailed settings of each module in the SOEC unit model.

Module	Type	Regulation
CATHODE1	RStioc	Molar extent of the reactions (Eqs. 2-3 and 2-4): $I_{H_2}/2F$ and $I_{CO}/2F$
		Temperature: (SOEC temp.) / Pressure: (SOEC press.)
CATHODE2	RGibbs	Calculate phase equilibrium and chemical equilibrium
		Temperature: (SOEC temp.)
GAS-COMP	Compr	Model: Compressor / Type: Isentropic
		Discharge pressure: (SOEC press.)
AN-COMP	Compr	(same as above)
H2O-PUMP	Pump	Model: Pump
		Discharge pressure: (SOEC press.)
GAS-HEAT	Heater	Temperature: (SOEC temp.) / Pressure: (SOEC press.)
H2O-HEAT	Heater	(same as above)
AN-HEAT	Heater	(same as above)
CA-COOL	Heater	Temperature: 25℃ / Pressure: (SOEC press.)
AN-COOL	Heater	(same as above)
FEEDMIX	Mixer	-
ANODE	Mixer	-
SEP	Sep	Outlet stream: ELECLYTE
		Split fraction: 1 for O_2, 0 for the others
VLSEP	Flash2	Vapor-liquid separation at 25℃
		Pressure: (SOEC press.)

2.1.2.1. SOEC unit

The SOEC unit was modeled using *Aspen Plus V8.8*. Figure 2-2 shows an overview of the model. The detailed settings of each module in the model are listed in Table 2-2.

In this model, SOEC cathode reactions were simulated by two virtual reactors CATHODE1 and CATHODE2. CATHODE1 is a stoichiometric reactor which is correspondent to electrochemical reactions. Here electrochemical half reactions Eqs. 2-1 and 2-2 were modeled by full reactions Eqs. 2-3 and 2-4, respectively.

$$H_2O + 2e^- \rightarrow H_2 + O^{2-} \quad (2\text{-}1)$$

$$CO_2 + 2e^- \rightarrow CO + O^{2-} \quad (2\text{-}2)$$

$$H_2O \rightarrow H_2 + 0.5O_2 \quad (2\text{-}3)$$

$$CO_2 \rightarrow CO + 0.5O_2 \quad (2\text{-}4)$$

The rate of each reaction was determined by considering the contributions of steam electrolysis and CO_2 electrolysis to the total current. The following relationship was assumed:

$$\frac{I_{H_2}}{I_{CO}} = \frac{1}{x_I}\frac{y_{H_2O}}{y_{CO_2}} \quad (2\text{-}5)$$

I_{H_2} and I_{CO} are current values correspond to the steam electrolysis and the CO_2 electrolysis, respectively. The sum of I_{H_2} and I_{CO} is defined as I_{total} ($I_{total} = I_{H_2} + I_{CO}$). y_{H_2O} and y_{CO_2} are the molar fractions of each species in the cathode inlet stream (CA-IN). Parameter x_I was introduced to adjust the ratio of current contributions. x_I indicates the possibility of a CO_2 molecule to be electrolyzed while that of a water molecule is set to unity. This parameter x_I is considered to reflect physicochemical factors such as gas adsorption properties and activation barriers of charge-transfer reactions. The value can depend on the experimental conditions, but it is reasonable to use values of $x_I \leq 1$ because the steam electrolysis is known to be more possible than the CO_2 electrolysis[161]. O_2 species generated in CATHODE1 is separated (SEP) and sent to the anode side (ELECLYTE). Then the O_2 species is mixed with sweep air (AN-IN) to form O_2-rich anode outlet gas (AN-OUT). This part simulates the anodic oxygen evolution reaction:

$$O^{2-} \rightarrow 0.5O_2 + 2e^- \quad (2\text{-}6)$$

Cathode gas species except O_2 are introduced to the second virtual reactor, CATHODE2. This reactor calculates the Gibbs free energy minimum, which corresponds to a situation that all possible reactions go to the equilibrium. In this case, the major two reactions are the following:

$$H_2O + CO \rightleftarrows H_2 + CO_2 \quad (2\text{-}7)$$

$$H_2O + CH_4 \rightleftarrows 3H_2 + CO \quad (2\text{-}8)$$

The forward reaction of the first equilibrium (Eq. 2-7) is called water gas shift, and the reverse reaction is called reverse water gas shift. For the second equilibrium (Eq. 2-8), the forward reaction is steam reforming of methane, and the reverse reaction is CO methanation. The assumption that the cathode gas reaches the equilibrium is reasonable for cathode-supported SOECs. There are two reasons for that: first, the gas space velocity in cathodes of cathode-supported SOECs is comparable to that of thermocatalytic CO_2 methanation systems. For example, Li *et al.*[133] used a cell with a Ni-YSZ cathode support layer (680 μm-thick, ϕ26) and a Ni-ScSZ cathode active layer (15 μm-thick, ϕ26). The cathode gas flow rate was 175 mL min^{-1}. In this case, the space velocity was *ca.* 2.8×10^4 h^{-1}. According to a review paper[162], the gas space velocity in thermocatalytic CO_2 methanation studies ranged as 7640-60000 h^{-1} and 3600-75000 mL h^{-1} g_{cat}^{-1}. The value in the ref. [133] (*ca.* 2.8×10^4 h^{-1}) was in the range. Second, the cathode cermet materials have sufficient catalytic activity for CO_2 methanation. Bierschenk *et al.*[120] tested the catalytic activity of a Ni-YSZ cermet disk (Ni 44wt%) at 500-800°C. They fed a gas mixture composed of 79.4% H_2, 14.4% CO, and 6.2% CO_2. With a space velocity of *ca.* 2.7×10^3 mL h^{-1} $g_{Ni\text{-}YSZ}^{-1}$, outlet gas compositions near the equilibrium were observed. This suggests that the tested Ni-YSZ cermet disk had significant catalytic activity. In the present simulation, the cathode-supported SOEC configuration was considered so that the assumption in CATHODE2 was valid (see Section 2.1.4). The Feedstock conversion in the cathode was calculated by the following equation;

$$U = \frac{\left(\dot{n}_{H_2O}^{in} + \dot{n}_{CO_2}^{in}\right) - \left(\dot{n}_{H_2O}^{out} + \dot{n}_{CO_2}^{out}\right)}{\dot{n}_{H_2O}^{in} + \dot{n}_{CO_2}^{in}} \quad (2\text{-}9)$$

where $\dot{n}_i^{in}$ and $\dot{n}_i^{out}$ are the molar flow rate of species i in the cathode inlet (CA-IN) and the cathode

outlet (CA-OUT), respectively. The cathode outlet gas (CA-OUT) contains a certain amount of water vapor, which is not desirable for methanation reaction. Therefore, the gas is cooled to 25°C (CA-COOL) and resultant liquid phase is separated at VLSEP (vapor-liquid separator) before introduced into a methanation unit. Heat recovery is also considered in the present model. Cell outlet gas flows were cooled to 25°C (CA-COOL and AN-COOL) and it was assumed that 50% of the removed heat can be recycled to heat up the cell inlet flows (GAS-HEAT, H2O-HEAT and AN-HEAT). In actual systems, this kind of heat management can be achieved by using heating media such as high-temperature steam, or by the direct heat exchange between cell outlet and inlet flows.

Based on the above process model, information about gas compositions in each flow and energy duties in each component (heater, compressor, reactor, etc.) can be obtained. In the next section, the calculation methods for electrochemical characteristics will be described.

2.1.2.2. Current-voltage characteristics

The cell voltage during operation, E, is calculated as

$$E = E_{\mathrm{Nernst}} + \eta_{\mathrm{ohm}} + \eta_{\mathrm{act}} + \eta_{\mathrm{conc}} \quad (2\text{-}10)$$

E_{Nernst} is the Nernst potential, and η_{ohm}, η_{act}, and η_{conc} are the ohmic overpotential, the activation overpotential, and the concentration overpotential, respectively.

2.1.2.2.1. Nernst potential

For the cathodic water electrolysis reaction Eq. 2-1, it holds that

$$\Delta_{\mathrm{f}}G^0_{\mathrm{H_2O}}(T) - 2FE^0(T) = \Delta_{\mathrm{f}}G^0_{\mathrm{H_2}} + \Delta_{\mathrm{f}}G^0_{\mathrm{O^{2-}}}(T) \quad (2\text{-}11)$$

Here, $\Delta_{\mathrm{f}}G^0_i$ is the standard Gibbs free energy of formation of species *i*. $\Delta_{\mathrm{f}}G^0_{\mathrm{H_2}}$ is defined as zero regardless of the temperature. Thus,

$$E^0(T) = \frac{\Delta_{\mathrm{f}}G^0_{\mathrm{H_2O}}(T) - \Delta_{\mathrm{f}}G^0_{\mathrm{O^{2-}}}(T)}{2F} \quad (2\text{-}12)$$

Under non-standard conditions, the cathodic Nernst potential becomes that

$$E^{c}_{\mathrm{Nernst,H_2O}} = E^{0}(T) + \frac{RT}{2F}\ln\frac{p^{c}_{\mathrm{H_2O}}}{\left(p^{c}_{\mathrm{H_2}}\right)\left(a^{c}_{\mathrm{O^{2-}}}\right)} \quad (2\text{-}13)$$

where $a^{c}_{\mathrm{O^{2-}}}$ is the activity of O^{2-} at the cathode.

For the cathodic CO_2 electrolysis reaction Eq. 2-2, it holds that

$$\Delta_f G^{0}_{\mathrm{CO_2}}(T) - 2FE^{0}(T) = \Delta_f G^{0}_{\mathrm{CO}}(T) + \Delta_f G^{0}_{\mathrm{O^{2-}}}(T) \quad (2\text{-}14)$$

Therefore

$$E^{0}(T) = \frac{\Delta_f G^{0}_{\mathrm{CO_2}}(T) - \Delta_f G^{0}_{\mathrm{CO}}(T) - \Delta_f G^{0}_{\mathrm{O^{2-}}}(T)}{2F} \quad (2\text{-}15)$$

Under non-standard conditions, the cathodic Nernst potential becomes that

$$E^{c}_{\mathrm{Nernst,CO_2}} = E^{0}(T) + \frac{RT}{2F}\ln\frac{p^{c}_{\mathrm{CO_2}}}{\left(p^{c}_{\mathrm{CO}}\right)\left(a^{c}_{\mathrm{O^{2-}}}\right)} \quad (2\text{-}16)$$

For the anodic oxygen evolution reaction Eq. 2-6, it holds that

$$2\Delta_f G^{0}_{\mathrm{O^{2-}}}(T) = \Delta_f G^{0}_{\mathrm{O_2}} - 4FE^{0}(T) \quad (2\text{-}17)$$

Because $\Delta_f G^{0}_{\mathrm{O_2}}$ is zero regardless of the temperature, it becomes that

$$E^{0}(T) = -\frac{\Delta_f G^{0}_{\mathrm{O^{2-}}}(T)}{2F} \quad (2\text{-}18)$$

Under non-standard conditions, the anodic Nernst potential becomes that

$$E^{a}_{\mathrm{Nernst}} = E^{0}(T) + \frac{RT}{4F}\ln\frac{p^{a}_{\mathrm{O_2}}}{\left(a^{a}_{\mathrm{O^{2-}}}\right)^{2}} \quad (2\text{-}19)$$

where $a^{a}_{\mathrm{O^{2-}}}$ is the activity of O^{2-} at the anode.

Assuming that $a^{c}_{\mathrm{O^{2-}}} = a^{a}_{\mathrm{O^{2-}}}$, the cell voltage for water electrolysis can be obtained from Eqs. 2-12, 2-13, 2-18, and 2-19:

$$E_{\mathrm{Nernst,H_2O}} = E^{a}_{\mathrm{Nernst}} - E^{c}_{\mathrm{Nernst,H_2O}}$$

$$= -\frac{\Delta_f G^{0}_{\mathrm{O^{2-}}}(T)}{2F} + \frac{RT}{4F}\ln\frac{p^{a}_{\mathrm{O_2}}}{\left(a^{a}_{\mathrm{O^{2-}}}\right)^{2}} - \frac{\Delta_f G^{0}_{\mathrm{H_2O}}(T) - \Delta_f G^{0}_{\mathrm{O^{2-}}}(T)}{2F} - \frac{RT}{2F}\ln\frac{p^{c}_{\mathrm{H_2O}}}{\left(p^{c}_{\mathrm{H_2}}\right)\left(a^{c}_{\mathrm{O^{2-}}}\right)}$$

$$= -\frac{\Delta_f G^{0}_{\mathrm{H_2O}}(T)}{2F} - \frac{RT}{2F}\ln\frac{p^{c}_{\mathrm{H_2O}}}{\left(p^{c}_{\mathrm{H_2}}\right)\left(p^{a}_{\mathrm{O_2}}\right)^{0.5}} \quad (2\text{-}20)$$

In the same manner, the cell voltage for CO_2 electrolysis can be obtained from Eqs. 2-15, 2-16, 2-18, and 2-19:

$$E_{\mathrm{Nernst,CO_2}} = E^{a}_{\mathrm{Nernst}} - E^{c}_{\mathrm{Nernst,CO_2}}$$

$$= -\frac{\Delta_f G^0_{O^{2-}}(T)}{2F} + \frac{RT}{4F}\ln\frac{p^a_{O_2}}{\left(a^a_{O^{2-}}\right)^2} - \frac{\Delta_f G^0_{CO_2}(T) - \Delta_f G^0_{CO}(T) - \Delta_f G^0_{O^{2-}}(T)}{2F} - \frac{RT}{2F}\ln\frac{p^c_{CO_2}}{\left(p^c_{CO}\right)\left(a^c_{O^{2-}}\right)}$$

$$= -\frac{\Delta_f G^0_{CO_2}(T) - \Delta_f G^0_{CO}(T)}{2F} - \frac{RT}{2F}\ln\frac{p^c_{CO_2}}{\left(p^c_{CO}\right)\left(p^a_{O_2}\right)^{0.5}} \quad (2\text{-}21)$$

In actual co-electrolysis conditions, both water electrolysis and CO_2 electrolysis occur. Therefore, the Nernst potential was estimated by taking a weighted average[163,164]:

$$E_{\text{Nernst}} = \frac{1}{y_{H_2O} + y_{CO_2}}\left(y_{H_2O}E_{\text{Nernst},H_2O} + y_{CO_2}E_{\text{Nernst},CO_2}\right) \quad (2\text{-}22)$$

where y_i is the molar fraction of gas species *i*.

$\Delta_f G^0_{H_2O}(T)$, $\Delta_f G^0_{CO_2}(T)$, and $\Delta_f G^0_{CO}(T)$ in Eqs. 2-20 and 2-21 were calculated as

$$\Delta_f G^0_i(T) = \Delta_f H^0_i - T\Delta_f S^0_i \quad (2\text{-}23)$$

where $\Delta_f H^0_i$ and $\Delta_f S^0_i$ are the standard enthalpy and entropy of formation of species *i*. Temperature dependence of $\Delta_f H^0_i$ and $\Delta_f S^0_i$ was not considered here, *i.e.* values at 25°C (taken from ref. [165]) were used.

2.1.2.2.2. Ohmic overpotential

Ohmic overpotential, η_{ohm}, was obtained by

$$\eta_{\text{ohm}} = \frac{\delta_e}{\sigma} i \quad (2\text{-}24)$$

where δ_e is the thickness of the electrolyte. For the YSZ electrolyte, electrical conductivity, σ, in S m^{-1} can be calculated by the following equation[166]:

$$\sigma = 1.63 \times 10^4 \exp\left(-\frac{0.79 \times 1.602 \times 10^{-19}}{k_B T}\right) \quad (2\text{-}25)$$

k_B is the Boltzmann constant in J K^{-1}. Contributions of electrodes were ignored because the conductivity values of the electrodes are considered to be several orders of magnitude higher than that of the electrolyte.

2.1.2.2.3. Activation overpotential

Activation overpotential, η_{act}, is generally expressed by the Butler-Volmer equation;

$$i = i_0 \left[\exp\left(\frac{\alpha n F \eta_{\mathrm{act}}}{RT}\right) - \exp\left(-\frac{(1-\alpha) n F \eta_{\mathrm{act}}}{RT}\right)\right] \quad (2\text{-}26)$$

where α is the symmetry factor, and i_0 is the exchange current density. In the present model, cathode activation overpotential was divided into $\eta^{\mathrm{c}}_{\mathrm{act,H_2}}$ and $\eta^{\mathrm{c}}_{\mathrm{act,CO}}$. They were determined to satisfy the following equations:

$$i_{\mathrm{H_2}} = i^{\mathrm{c}}_{0,\mathrm{H_2}} \left[\exp\left(\frac{\alpha_{\mathrm{H_2}} 2F\eta^{\mathrm{c}}_{\mathrm{act,H_2}}}{RT}\right) - \exp\left(-\frac{(1-\alpha_{\mathrm{H_2}}) 2F\eta^{\mathrm{c}}_{\mathrm{act,H_2}}}{RT}\right)\right] \quad (2\text{-}27)$$

$$i_{\mathrm{CO}} = i^{\mathrm{c}}_{0,\mathrm{CO}} \left[\exp\left(\frac{\alpha_{\mathrm{CO}} 2F\eta^{\mathrm{c}}_{\mathrm{act,CO}}}{RT}\right) - \exp\left(-\frac{(1-\alpha_{\mathrm{CO}}) 2F\eta^{\mathrm{c}}_{\mathrm{act,CO}}}{RT}\right)\right] \quad (2\text{-}28)$$

$i_{\mathrm{H_2}}$ and i_{CO} are the current densities corresponding to the water electrolysis and the CO_2 electrolysis, respectively, and obtained as follows:

$$i_{\mathrm{H_2}} = \frac{I_{\mathrm{H_2}}}{I_{\mathrm{total}}} i = \frac{I_{\mathrm{H_2}}}{S_{\mathrm{SOEC}}} \quad (2\text{-}29)$$

$$i_{\mathrm{CO}} = \frac{I_{\mathrm{CO}}}{I_{\mathrm{total}}} i = \frac{I_{\mathrm{CO}}}{S_{\mathrm{SOEC}}} \quad (2\text{-}30)$$

S_{SOEC} is the total electrode area of the SOEC. For the anode side, the symmetry factor α was assumed to be 0.5 and the Butler-Volmer equation was rearranged as

$$\eta^{\mathrm{a}}_{\mathrm{act}} = \frac{RT}{F} \sinh^{-1}\left(\frac{i}{2i^{\mathrm{a}}_0}\right) \quad (2\text{-}31)$$

To obtain overpotentials from the equations above, values of exchange current densities were needed. According to literature, the exchange current density of the steam electrolysis in cathode ($i^{\mathrm{c}}_{0,\mathrm{H_2}}$) and that of the oxygen evolution reaction in anode (i^{a}_0) can be determined by the following equations[167]:

$$i^{\mathrm{c}}_{0,\mathrm{H_2}} = 3.9 \times 10^8 \exp\left(-\frac{1.0\times10^5}{RT}\right) \quad (2\text{-}32)$$

$$i^{\mathrm{a}}_0 = 1.4 \times 10^9 \exp\left(-\frac{1.2\times10^5}{RT}\right) \quad (2\text{-}33)$$

In Eqs. 2-32 and 2-33, the unit for $i^{\mathrm{c}}_{0,\mathrm{H_2}}$ and i^{a}_0 is A m^{-2}, and that for R is J K^{-1} mol^{-1}. Note that the pressure dependences of the exchange current densities are not included in Eqs. 2-32 and 2-33. Here the pressure dependence is considered as follows. In general, exchange current densities of the steam electrolysis and the oxygen evolution is expressed as

$$i_{0,\mathrm{H_2}} = \gamma_{\mathrm{H_2}} \left(\frac{p_{\mathrm{H_2}}}{p_{\mathrm{std}}}\right)^{\mathrm{A}} \left(\frac{p_{\mathrm{H_2O}}}{p_{\mathrm{std}}}\right)^{\mathrm{B}} \exp\left(-\frac{E_{\mathrm{a,H_2}}}{RT}\right) \tag{2-34}$$

$$i_{0,\mathrm{O_2}} = \gamma_{\mathrm{O_2}} \left(\frac{p_{\mathrm{O_2}}}{p_{\mathrm{std}}}\right)^{\mathrm{E}} \exp\left(-\frac{E_{\mathrm{a,O_2}}}{RT}\right) \tag{2-35}$$

where $\gamma_{\mathrm{H_2}}$ and $\gamma_{\mathrm{O_2}}$ are constants. Partial pressures of hydrogen, steam and oxygen are related to the total pressure as

$$p_{\mathrm{H_2}} = p_{\mathrm{total}} y_{\mathrm{H_2}} \tag{2-36}$$

$$p_{\mathrm{H_2O}} = p_{\mathrm{total}} y_{\mathrm{H_2O}} \tag{2-37}$$

$$p_{\mathrm{O_2}} = p_{\mathrm{total}} y_{\mathrm{O_2}} \tag{2-38}$$

$y_{\mathrm{H_2}}$, $y_{\mathrm{H_2O}}$ and $y_{\mathrm{O_2}}$ are molar fractions of each gas. When the total pressure increases from $p^{\mathrm{I}}_{\mathrm{total}}$ to $p^{\mathrm{II}}_{\mathrm{total}}$ and the molar fractions are unchanged, the ratios of exchange current densities become

$$\frac{i^{\mathrm{II}}_{0,\mathrm{H_2}}}{i^{\mathrm{I}}_{0,\mathrm{H_2}}} = \left(\frac{p^{\mathrm{II}}_{\mathrm{total}} y_{\mathrm{H_2}}}{p^{\mathrm{I}}_{\mathrm{total}} y_{\mathrm{H_2}}}\right)^{\mathrm{A}} \left(\frac{p^{\mathrm{II}}_{\mathrm{total}} y_{\mathrm{H_2O}}}{p^{\mathrm{I}}_{\mathrm{total}} y_{\mathrm{H_2O}}}\right)^{\mathrm{B}} = \left(\frac{p^{\mathrm{II}}_{\mathrm{total}}}{p^{\mathrm{I}}_{\mathrm{total}}}\right)^{\mathrm{A+B}} \tag{2-39}$$

$$\frac{i^{\mathrm{II}}_{0,\mathrm{O_2}}}{i^{\mathrm{I}}_{0,\mathrm{O_2}}} = \left(\frac{p^{\mathrm{II}}_{\mathrm{total}} y_{\mathrm{O_2}}}{p^{\mathrm{I}}_{\mathrm{total}} y_{\mathrm{O_2}}}\right)^{\mathrm{E}} = \left(\frac{p^{\mathrm{II}}_{\mathrm{total}}}{p^{\mathrm{I}}_{\mathrm{total}}}\right)^{\mathrm{E}} \tag{2-40}$$

Based on Eqs. 2-39 and 2-40, Eqs. 2-32 and 2-33 are modified as follows:

$$i^{\mathrm{c}}_{0,\mathrm{H_2}} = 3.9 \times 10^{8} \exp\left(-\frac{1.0\times10^{5}}{RT}\right) \left(\frac{p_{\mathrm{total}}}{p_{\mathrm{std}}}\right)^{\mathrm{A+B}} \tag{2-41}$$

$$i^{\mathrm{a}}_{0} = 1.4 \times 10^{9} \exp\left(-\frac{1.2\times10^{5}}{RT}\right) \left(\frac{p_{\mathrm{total}}}{p_{\mathrm{std}}}\right)^{\mathrm{E}} \tag{2-42}$$

For i^{a}_{0}, E = 0.25 is used in this study as is often assumed in literature[168]. On the contrary, reported values of exponents A and B differ significantly among studies (see Appendix B). Consequently, A+B values range from 0.23 to 3. This time, I examined two cases, A+B = 0.25 and 2, to see how the SOEC performance is affected by this factor.

The exchange current density of the CO_2 electrolysis in cathode ($i^{\mathrm{c}}_{0,\mathrm{CO}}$) was calculated from $i^{\mathrm{c}}_{0,\mathrm{H_2}}$ by assuming the ratio of $i^{\mathrm{c}}_{0,\mathrm{CO}}/i^{\mathrm{c}}_{0,\mathrm{H_2}}$. Because the value of $i^{\mathrm{c}}_{0,\mathrm{CO}}/i^{\mathrm{c}}_{0,\mathrm{H_2}}$ changes depending on experimental conditions and materials of the cathode[169], $i^{\mathrm{c}}_{0,\mathrm{CO}}/i^{\mathrm{c}}_{0,\mathrm{H_2}}$ was used as a fitting parameter in this study. The value was determined by fitting the literature data of co-electrolysis conducted at ambient pressure (see Section 2.1.3). The same $i^{\mathrm{c}}_{0,\mathrm{CO}}/i^{\mathrm{c}}_{0,\mathrm{H_2}}$ value was used to simulate pressurized operations.

2.1.2.2.4. Concentration overpotential

Concentration overpotential is originated from gas concentration gradients in electrode layers. Such gradients can be explained by considering mass balances in the electrodes, which includes molecular diffusion and gas conversion by electrochemical and catalytic reactions. In *Aspen Plus*, the electrode processes are described by the zero-dimensional model, which does not care about the gas concentration profiles. Hence, the additional model is needed to calculate the concentration overpotentials. Here, simplification was made and linear concentration gradients from the electrode surface to the electrode/electrolyte interface were considered.

For the cathode side, the following formulae were used[170]:

$$\eta^{\mathrm{c}}_{\mathrm{conc,H_2}} = \frac{RT}{2F}\left(1+\frac{1}{\alpha_{\mathrm{H_2}}}\right)\ln\frac{i_{\mathrm{L,H_2}}}{i_{\mathrm{L,H_2}}-i} \tag{2-43}$$

$$\eta^{\mathrm{c}}_{\mathrm{conc,CO}} = \frac{RT}{2F}\left(1+\frac{1}{\alpha_{\mathrm{CO}}}\right)\ln\frac{i_{\mathrm{L,CO}}}{i_{\mathrm{L,CO}}-i} \tag{2-44}$$

$\alpha_{\mathrm{H_2}}$ and α_{CO} are the symmetry factors in Butler-Volmer equations (Eqs. 2-27 and 2-28). $i_{\mathrm{L,H_2}}$ and $i_{\mathrm{L,CO}}$ are limiting current densities for the steam electrolysis and the CO_2 electrolysis, respectively. For the steam electrolysis, a linear concentration profile of steam in the cathode layer was assumed. At the outer surface of the cathode ($z = 0$), the steam concentration was the same as that in the bulk gas flow, $C^0_{\mathrm{H_2O}}$. The concentration decreased linearly along the z axis. The limiting current density, $i_{\mathrm{L,H_2}}$, is the current density which corresponds to the depletion of reactant steam at the cathode-electrolyte interface ($z = \delta_{\mathrm{c}}$):

$$i_{\mathrm{L,H_2}} = 2FD^{\mathrm{eff}}_{\mathrm{H_2O}}\frac{C^0_{\mathrm{H_2O}}}{\delta_{\mathrm{c}}} \tag{2-45}$$

In the case of co-electrolysis, the CO_2 electrolysis was also taken into consideration. The limiting current density for the CO_2 electrolysis was calculated in the same manner:

$$i_{\mathrm{L,CO}} = 2FD^{\mathrm{eff}}_{\mathrm{CO_2}}\frac{C^0_{\mathrm{CO_2}}}{\delta_{\mathrm{c}}} \tag{2-46}$$

Reactant concentrations in the bulk flow, C^0_i, were obtained from the averaged gas composition of cathode inlet and outlet flows. In the above calculations of limiting current densities, effective

diffusion coefficients, D_i^{eff}, were needed. They were defined as

$$D_i^{\mathrm{eff}} = \frac{\varepsilon}{\xi} D_i \tag{2-47}$$

where ε and ξ are the porosity and tortuosity of the electrode, respectively. Gas diffusion in electrode pores includes two mechanisms, Knudsen diffusion and molecular diffusion. Therefore, the following relationship was used to know the diffusion coefficient D_i.

$$\frac{1}{D_i} = \frac{1}{D_i^{\mathrm{K}}} + \frac{1}{D_i^{\mathrm{M}}} \tag{2-48}$$

The Knudsen diffusion coefficient of species i, D_i^{K}, can be obtained as

$$D_i^{\mathrm{K}} = \frac{d_{\mathrm{p}}}{3}\sqrt{\frac{8RT}{\pi M_i}} \tag{2-49}$$

where d_{p} is the electrode pore diameter, M_i is the molecular weight of species i in kg mol^{-1}. For molecular diffusion coefficients, D_i^{M}, there are no established calculation methods for multi-component systems. In this study, a weighted average of interdiffusion coefficients $D_{i,j}^{\mathrm{M}}$ was used as an approximated value:

$$D_{\mathrm{H_2O}}^{\mathrm{M}} = \sum_{j\neq \mathrm{H_2O}}(y_j D_{\mathrm{H_2O},j}^{\mathrm{M}}) \,/\, \sum_{j\neq \mathrm{H_2O}}(y_j) \tag{2-50}$$

$$D_{\mathrm{CO_2}}^{\mathrm{M}} = \sum_{j\neq \mathrm{CO_2}}(y_j D_{\mathrm{CO_2},j}^{\mathrm{M}}) \,/\, \sum_{j\neq \mathrm{CO_2}}(y_j) \tag{2-51}$$

Molar fraction y_j is based on the averaged composition of cathode inlet and outlet. $D_{i,j}^{\mathrm{M}}$ values were obtained by the Chapman-Enskog theory assuming Lennard-Jones potential[171] (see Appendix C).

For the anode side, there are no reactants and only the formation of oxygen molecules occurs. In this case, a formulation using limiting current densities cannot be applied. Ni *et al.*[172] proposed the following equation by considering the oxygen permeation inside the anode layer driven by a partial pressure gradient:

$$\eta_{\mathrm{conc}}^{\mathrm{a}} = \frac{RT}{4F}\frac{\sqrt{\frac{iRT\mu\delta_{\mathrm{a}}}{2FB_{\mathrm{g}}} + p_{\mathrm{O_2}}^{0\ 2}}}{p_{\mathrm{O_2}}^{0}} \tag{2-52}$$

δ_{a} is the anode thickness, and $p_{\mathrm{O_2}}^{0}$ is the oxygen partial pressure at the anode outer surface. The average value of anode inlet and outlet flows were used for $p_{\mathrm{O_2}}^{0}$. μ is the kinetic viscosity of

oxygen gas, which can be calculated easily by using a six-order approximate formula provided by Todd and Young[173]. B_g is the oxygen permeability derived from the Kozeny-Carman relationship[174]:

$$B_g = \frac{\varepsilon^3}{72\xi(1-\varepsilon)^2} d_p^2 \quad (2\text{-}53)$$

2.1.2.3. Methanation reactors unit

In this study, we used a model of a catalytic methanation unit where three adiabatic reactors were connected in series (Figure 2-3)[126]. The detailed settings of each module in the model are listed in Table 2-3. When a large amount of methane is synthesized in a reactor *via* the highly exothermic methanation reaction, the reactor temperature will dramatically increase. To avoid an undesirably high reactor temperature which can cause catalyst deactivation, inlet gas temperature of each reactor was adjusted to 250°C. Also, 75% of the outlet gas of the first reactor was recycled to limit the temperature rising in the reactor. The operating pressure of the three reactors was set to the same pressure as that of the SOEC unit. This methanation unit (MU) was used only in the simulations of the two-step power-to-gas process. As explained earlier, the SOEC cathode outlet gas was dried and then introduced to the MU. In the simulations of the direct methane synthesis in SOEC cathode, this MU was not included.

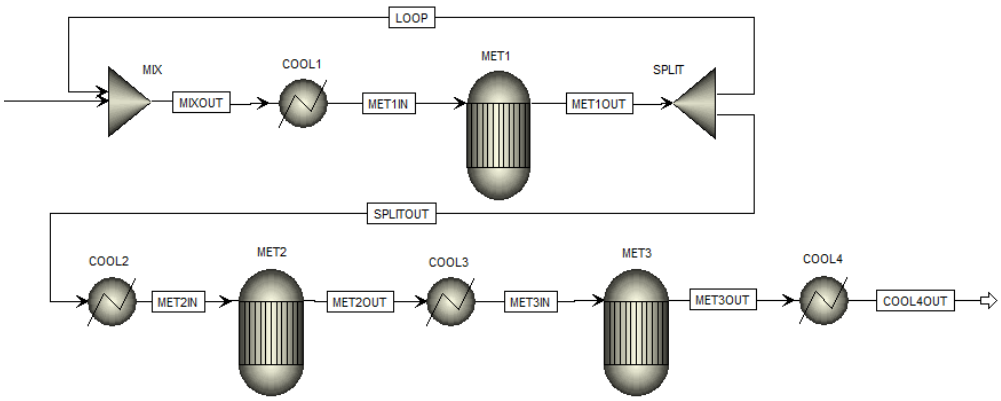

Figure 2-3. Model of the methanation reactors unit.

Table 2-3. Detailed settings of each module in the methanation reactors unit model.

Module	Type	Regulation
MET1	RGibbs	Calculate phase equilibrium and chemical equilibrium Heat duty: 0 W (adiabatic) / Pressure: (SOEC press.)
MET2	RGibbs	(same as above)
MET3	RGibbs	(same as above)
COOL1	Heater	Temperature: 250℃ / Pressure: (SOEC press.)
COOL2	Heater	(same as above)
COOL3	Heater	(same as above)
COOL4	Heater	Temperature: 25℃ / Pressure: (SOEC press.)
MIX	Mixer	-
SPLIT	FSplit	Split fraction: 0.75 for stream LOOP

2.1.3. Model validation

To check the validity of the model, experimental data presented by Li *et al.*[133] were employed. They used cathode-supported planar button cells which consisted of Ni-YSZ cathode support layer (thickness: 680 μm), Ni-ScSZ cathode active layer (15 μm), ScSZ electrolyte (20 μm) and LSM-ScSZ anode (15 μm). ScSZ and LSM are scandia-stabilized zirconia and lanthanum strontium manganate, respectively. The diameter of their electrodes was 1.3 cm. For the calculation, the ionic conductivity of ScSZ electrolyte was determined by referring to the literature[175], instead of using Eq. 2-25. The exchange current densities of the Ni-ScSZ cathode and the LSM-ScSZ anode were approximated by those of Ni-YSZ and LSM-YSZ, respectively (Eqs. 2-41 and 2-42).

First, the parameters in the model were fitted to reproduce three current-voltage curves corresponding to H_2O electrolysis, CO_2 electrolysis, and co-electrolysis operations at 750°C, 1 atm. The cathode inlet gas compositions for each operation were $H_2O/H_2/Ar$ = 28.6/14.3/57.1, $CO_2/CO/Ar$ = 28.6/14.3/57.1, and $H_2O/CO_2/H_2/Ar$ = 28.6/28.6/14.3/28.5, respectively. In all electrolysis modes, the cathode total gas flow rate was 350 mL min^{-1}. The anode gas was fixed to air (350 mL min^{-1}). Figure 2-4 shows the fitting results. Simulated current-voltage curves are in good agreement with the reported experimental data, and differences between the three operation types are successfully described by the proposed model. The determined values for each parameter are listed in Table 2-4. The feedstock conversions in each operation

were 6.1% at 600 mA cm^{-2} for the H_2O electrolysis, 3.0% at 300 mA cm^{-2} for the CO_2 electrolysis and 2.3% at 450 mA cm^{-2} for the co-electrolysis.

Next, using the fitted parameters, co-electrolysis operation at 650°C, 1 atm was simulated. The cathode inlet gas composition was $H_2O/CO_2/Ar$ = 28.6/14.3/57.1, and the total flow rate was 175 mL min^{-1}. The anode inlet gas was 175 mL min^{-1} air. The current for the simulation was set to the same value as the reported one in the literature, then the operating voltage and the cathode outlet gas composition were calculated. Table 2-5 shows the comparison between the reported experimental data and the simulation results. Note that argon and steam are excluded from the list of cathode outlet gas compositions for simplicity. For both the operating voltages and the gas compositions, trends of the experimental data are successfully traced by the simulation. Calculated feedstock conversions are also shown in Table 2-5. The conversion is almost proportional to the current and reached 11.1% when 1.095 A was applied. Under the present co-electrolysis condition, the thermoneutral voltage of the SOEC, at which the electrical power input becomes equal to the overall enthalpy change in the cell, was calculated to be 1.32 V. This means that the cell is endothermic in the simulated cases corresponding to 0 A and 0.101 A, while exothermic in the cases of 0.676 A and 1.095 A.

Figure 2-5 visualizes the cathode outlet gas compositions corresponding to polarization condition at a current load of 1.095 A. General trend of the experimental data is replicated by the simulation, while there are some discrepancies in fractions of hydrogen and CO. The discrepancy in the gas composition could be ascribed to the technical problems in actual experiments. In the simulations, equilibrium (Gibbs free energy minimum) was assumed for the catalytic reactions. However, the equilibrium gas composition is not always achievable in actual experiments, due to a short gas contact time and an insufficient number of (electro-) catalytically active sites in the cathode of planar SOECs. In addition, there is a possibility that oxygen (air) leaks into the cathode chamber, resulting in re-oxidation of produced hydrogen, CO, and methane.

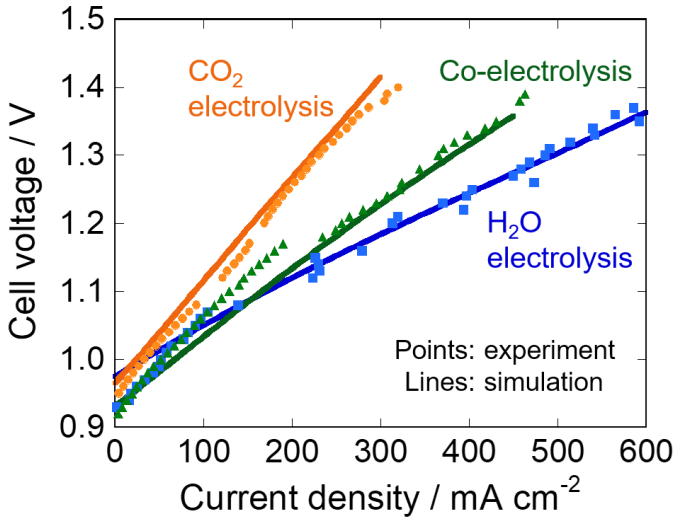

Figure 2-4. Current-voltage characteristics reported in ref. [133] and corresponding fitting results obtained by the present model. SOEC operating condition is 750°C, 1 atm.

Table 2-4. Fitted values for parameters in the model.

Parameter	Fitted value
x_{I}	0.8
$i^{\mathrm{c}}_{0,\mathrm{CO}}/i^{\mathrm{c}}_{0,\mathrm{H_2}}$	0.25
$\alpha_{\mathrm{H_2}}$	0.5
α_{CO}	0.35
ε	0.4
ξ	6
d_{p} [μm]	1

Table 2-5. Reported experimental data and simulation results for co-electrolysis operation at 650°C, 1 atm.

	Operating voltage / V	Average current / A	Cathode outlet gas composition / %				Feedstock conv. / %
			H_2	CO_2	CO	CH_4	
Experiment (Ref. [133])	0	0	0.289	99.640	0.071	0	-
	1	0.101	0.657	99.127	0.216	0	-
	1.5	0.676	7.653	89.533	2.814	0	-
	2	1.095	13.685	79.186	7.110	0.019	-
Simulation (This work)	0.32	0	8.2×10^{-6}	100.0	2.0×10^{-6}	2.4×10^{-24}	0.0
	1.03	0.101	2.4	97.0	0.59	3.3×10^{-8}	1.0
	1.76	0.676	14.1	82.4	3.6	6.3×10^{-5}	6.8
	2.28	1.095	20.9	73.7	5.4	0.00043	11.1

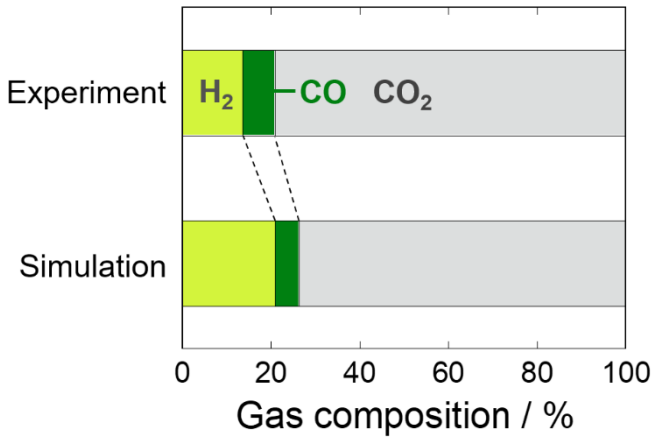

Figure 2-5. Comparison of the SOEC cathode outlet gas compositions which correspond to polarization condition at a current load of 1.095 A. SOEC operating condition is 650°C, 1 atm.

2.1.4. Condition for process simulations

2.1.4.1. SOEC operating conditions

I considered a SOEC stack made of cathode-supported cells with the composition of Ni-YSZ|YSZ|LSM-YSZ. The thickness of the Ni-YSZ cathode, YSZ electrolyte, and LSM-YSZ anode were assumed to be 500 μm, 20 μm, and 15 μm, respectively. The fitted values in Table 2-4 were used as parameters in the model. Cathode inlet gas composition was 50% H_2O, 25% CO_2 and 25% N_2. Steam to carbon ratio was set to S/C = 2, which follows the stoichiometry of the overall reaction formula of electrochemical methane formation (Eq. 2-54).

$$2H_2O + CO_2 \rightarrow CH_4 + 2O_2 \quad (2\text{-}54)$$

Anode inlet gas was air (21% O_2, 79% N_2). Total inlet gas flow rate at each electrode was set to 1.0 mol s^{-1}. Operation pressure of 5 atm was selected, and the cell current density was changed in the range of 0-1000 mA cm^{-2}. The total electrode area of SOEC stack, S_{SOEC}, was set to 10 m^2, which allows 100 kW-class operation. Based on the above conditions, the space velocity of the cathode feed gas is calculated to be 1.8×10^4 h^{-1}. Assuming that the density of the Ni-YSZ cermet (Ni 60wt%, porosity 0.4) is 3.83 g cm^{-3}, the space velocity can also be expressed as 4.6×10^3 mL h^{-1} $g_{Ni\text{-}YSZ}^{-1}$. These space velocities are comparable to those of thermocatalytic CO_2 methanation systems (see Section 2.1.2.1).

Figure 2-6 illustrates the simulated PtM processes. The direct PtM process and the two-step PtM process

were compared. In the cases of the direct process, SOEC cathode outlet gas (CA-OUT in Figure 2-2) was regarded as the system outlet gas. Operations at 800°C, 700°C, 600°C, 500°C and 400°C were simulated this time. On the other hand, the two-step process was modelled by combining the SOEC operated at 800°C and the following methanation unit (MU). In this case, the outlet gas flow of the MU (MET3OUT in Figure 2-3) was regarded as the system outlet.

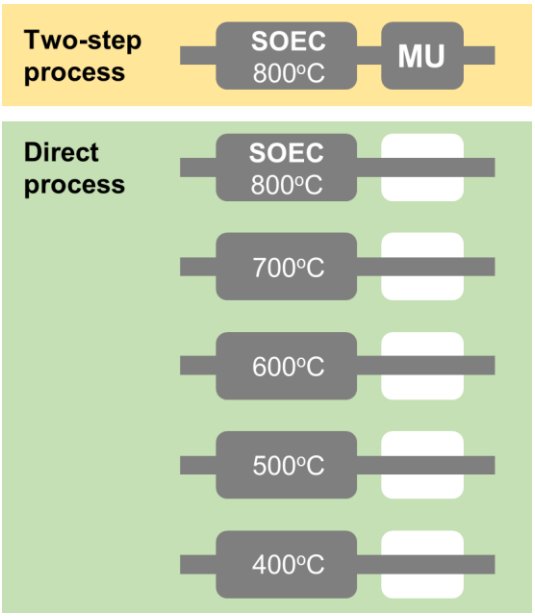

Figure 2-6. Different PtM processes simulated in this section.

2.1.4.2. Energy conversion efficiencies

I compared the proposed systems based on system energy efficiencies. Those were calculated using lower heating values (LHV) of product gas species. LHV is defined by the enthalpy change in the complete combustion reaction of a fuel gas into CO_2 and steam. The values are 802.7 kJ mol^{-1}, 241.8 kJ mol^{-1}, and 282.9 kJ mol^{-1} for methane, hydrogen, and CO, respectively. In this work, two types of system energy efficiencies were introduced. One is η_{CH_4}, which was calculated based on the LHV of produced methane:

$$\eta_{CH_4} = \frac{\dot{n}_{CH_4} LHV_{CH_4}}{P_{system}} \quad (2\text{-}55)$$

The other is η_{total}, defined as

$$\eta_{\text{total}} = \frac{\dot{n}_{\text{CH}_4}\text{LHV}_{\text{CH}_4} + \dot{n}_{\text{H}_2}\text{LHV}_{\text{H}_2} + \dot{n}_{\text{CO}}\text{LHV}_{\text{CO}}}{P_{\text{system}}} \quad (2\text{-}56)$$

where $\dot{n}_i$ is the molar production rate of species *i* in the system outlet gas flow (mol s^{-1}), LHV_i is the lower heating value of species *i* (J mol^{-1}), and P_{system} is the total power input of the whole system (kW). For η_{total}, not only LHV_{CH_4} but also LHV_{H_2} and LHV_{CO} were taken into account. Methane LHV ratio, x_{CH_4}, was calculated by the following equation:

$$x_{\text{CH}_4} = \frac{\dot{n}_{\text{CH}_4}\text{LHV}_{\text{CH}_4}}{\dot{n}_{\text{CH}_4}\text{LHV}_{\text{CH}_4} + \dot{n}_{\text{H}_2}\text{LHV}_{\text{H}_2} + \dot{n}_{\text{CO}}\text{LHV}_{\text{CO}}} = \frac{\eta_{\text{CH}_4}}{\eta_{\text{total}}} \quad (2\text{-}57)$$

The parameter x_{CH_4} is the ratio of η_{CH_4} to η_{total}, and reflects the product selectivity of the system. The system total power input in Eqs. 2-55 and 2-56, P_{system}, was calculated as the sum of the following factors (i)~(iii).

(i) Electrical and thermal power supplied to the SOEC.

The power supplied to the SOEC unit, P_{SOEC}, was calculated as

$$P_{\text{SOEC}} = \max\{\Delta\dot{H}_{\text{SOEC}}, I_{\text{total}} \times E\} \quad (2\text{-}58)$$

Here, E is the cell operating voltage which is calculated from Eq. 2-10. $\Delta\dot{H}_{\text{SOEC}}$ is the enthalpy difference per unit time between SOEC inlet flows and outlet flows:

$$\Delta\dot{H}_{\text{SOEC}} = \left(\dot{H}_{\text{CA-OUT}} + \dot{H}_{\text{AN-OUT}}\right) - \left(\dot{H}_{\text{CA-IN}} + \dot{H}_{\text{AN-IN}}\right) \quad (2\text{-}59)$$

The term $I_{\text{total}} \times E$ indicates the power supplied by electricity. When $\Delta\dot{H}_{\text{SOEC}} > I_{\text{total}} \times E$, the electrical power supply is not enough to carry out the desired (electro-) chemical reactions. Therefore, the deficit ($\Delta\dot{H}_{\text{SOEC}} - I_{\text{total}} \times E$) is compensated thermally. This type of a heat duty is denoted as "Cell heating" in the latter sessions. On the other hand, cooling of the cell is required when $\Delta\dot{H}_{\text{SOEC}} < I_{\text{total}} \times E$. In this case, the difference ($I_{\text{total}} \times E - \Delta\dot{H}_{\text{SOEC}}$) will become a thermal loss. This type of energy loss is denoted as "Loss (SOEC power)". If thermal insulation of the cell is perfect, no heating or cooling is needed when $\Delta\dot{H}_{\text{SOEC}} = I_{\text{total}} \times E$ (thermoneutral point).

(ii) Energy used for heating and compression of the inlet flows.

Energy requirements of GAS-COMP, H2O-PUMP and AN-COMP were taken from *Aspen Plus* results. Since the heat recovery with 50% efficiency is assumed, the duty for heating up the SOEC inlet flows

was calculated by the following formula:

$$Q_{\mathrm{HEAT}} = (Q_{\mathrm{GAS-HEAT}} + Q_{\mathrm{H2O-HEAT}} + Q_{\mathrm{AN-HEAT}}) - 0.5(Q_{\mathrm{CA-COOL}} + Q_{\mathrm{AN-COOL}}) \quad (2\text{-}60)$$

(iii) Heat duty in the methanation unit.

When simulating the two-step PtM process, the methanation unit (MU) was installed in the downstream of the SOEC unit. As described earlier, the inlet gas temperature of each reactor of the MU was maintained at 250°C. Generally, the reactor inlet flows are cooled to remove the excess reaction heat of the methanation. However, one has to care the case that the low current density in the SOEC produces only a small amount of hydrogen and CO which are introduced into the MU. In the case, the reaction heat in the first reactor is small and the inlet gas temperature of the reactor becomes lower than 250°C. Accordingly, some heat input was needed to fulfil the temperature requirement of 250°C.

2.1.5. Results and discussion

I simulated two cases for the pressure dependence of the cathodic exchange current density (Eq. 2-41): A + B = 0.25 and 2. In the following part, results are shown only for the case of A + B = 0.25. The results obtained by assuming A + B = 2 are omitted because the trends of the results are shared in the two cases, even though the individual values are different.

2.1.5.1. Electrochemical properties

Figure 2-7a shows the calculated current-voltage characteristics of the SOEC unit at 400-800°C. It is clear that lower temperature requires larger overpotential. Figure 2-7b, c, d, e, and f represent the breakdown of the overpotentials at each temperature. At high temperatures, the main contribution to the total overpotential is the activation overpotential. As the temperature decreases, the ohmic overpotential becomes greater. These characteristics are reflected in system energy efficiencies discussed hereunder.

2.1.5.2. Details of the energy conversion in the system

Figure 2-8 shows the details of energy input and output of the examined systems. Figure 2-8a, b, and c are the results of the direct PtM process operated at 800°C, 600°C and 400°C. SOEC current density was changed from 0 to 1000 mA cm^{-2}. For the energy input, it is obvious that the required electric power significantly increases with lowering the operation temperature, which corresponds to the current-voltage characteristics shown in Figure 2-7. As mentioned in the previous section, "Cell heating" in Figure 2-8a1 and b1 represents the required heat to compensate the imbalance between $\Delta\dot{H}_{\mathrm{SOEC}}$ and $I_{\mathrm{total}} \times E$. The value of "Cell heating" is zero in Figure 2-8c1, because the current density corresponding to the thermoneutral point at 400°C is less than 100 mA cm^{-2}. For the energy output, it is noteworthy that LHV values of produced hydrogen and CO are much larger than that of methane at 800°C (Figure 2-8a2), while LHV of methane is dominant at 400°C (Figure 2-8c2). The high selectivity of methane against hydrogen and CO is an advantage of the low-temperature operation. At the same time, the large electric power needed at 600°C and 400°C results in the large thermal losses in the energy output, which are denoted as

"Loss (SOEC power)" in Figure 2-8b2 and c2.

Figure 2-8d is the result of the two-step process. In the process, the SOEC operation temperature was set to 800°C while the inlet gas temperature of the methanation reactors was set to 250°C. Comparing Figure 2-8a1 and d1, total energy inputs are almost the same because the only difference is the small heat duty in the methanation unit (MU). However, energy output profiles differ significantly. One of the main features in Figure 2-8d2 is a large proportion of the methane LHV. Hydrogen and CO in the SOEC outlet gas flow are converted into methane by the MU, resulting in the quite low level of H2 LHV and CO LHV in the energy output of the two-step system. It should also be noted that the loss in the energy output increased in the two-step case because the reaction heat of the methanation cannot be recovered in the MU. The corresponding portions are denoted as "Loss (MU heat)" in Figure 2-8d2.

Based on the results in Figure 2-8, energy conversion efficiencies were calculated. Figure 2-9a summarizes the relation of η_{total} and $x_{\mathrm{CH_4}}$ in the direct process (400-800°C) and the two-step process. Ten points plotted for each process indicate the results corresponding to the SOEC current density of every 100 mA cm^{-2} from 100 to 1000 mA cm^{-2}. The arrows indicate the ascending order of current density: the first point is for 100 mA cm^{-2} and the last one is for 1000 mA cm^{-2}. As shown in the figure, there is a trade-off relationship between η_{total} and $x_{\mathrm{CH_4}}$ in the direct process. High η_{total} can be achieved at high temperatures because of the small SOEC power loss. However, methane formation is thermodynamically suppressed at those temperatures, leading to the low $x_{\mathrm{CH_4}}$. In the two-step process, $x_{\mathrm{CH_4}}$ values are near 100% because the fraction of methane in the system outlet gas can be dramatically increased by the methanation unit. At the same time, η_{total} values are smaller compared to those in the direct process operated at 800°C, due to the loss of reaction heat of the methanation. Figure 2-9b shows the $\eta_{\mathrm{CH_4}}$ as a function of methane production rate, $r_{\mathrm{CH_4}}$. Comparing at the same $r_{\mathrm{CH_4}}$, the two-step process produces methane at higher efficiencies than does the direct process.

Figure 2-10 compares system outlet gas compositions obtained in each of the simulated cases with the SOEC current density of 1000 mA cm^{-2}. Significant amounts of hydrogen and CO are included in the cases of the direct process, while almost all products are methane in the two-step process. In the present

model, equilibrium was assumed for the catalytic reactions in the cathode, and consequently the methane concentration in the outlet gas depends only on the operation temperature and pressure. When the direct process is operated at 400°C, molar fractions of the product gas species are 79.4%, 0.9%, and 19.7% for methane, CO, and hydrogen, respectively. Hydrogen fraction of 19.7% is a little higher than the allowable upper limit of the existing natural gas pipeline network[125] while it could be used for the automobiles[126]. To further decrease the hydrogen content, operation temperature lower than 400°C or operation pressure higher than 5 atm is needed unless additional hydrogen separation is applied.

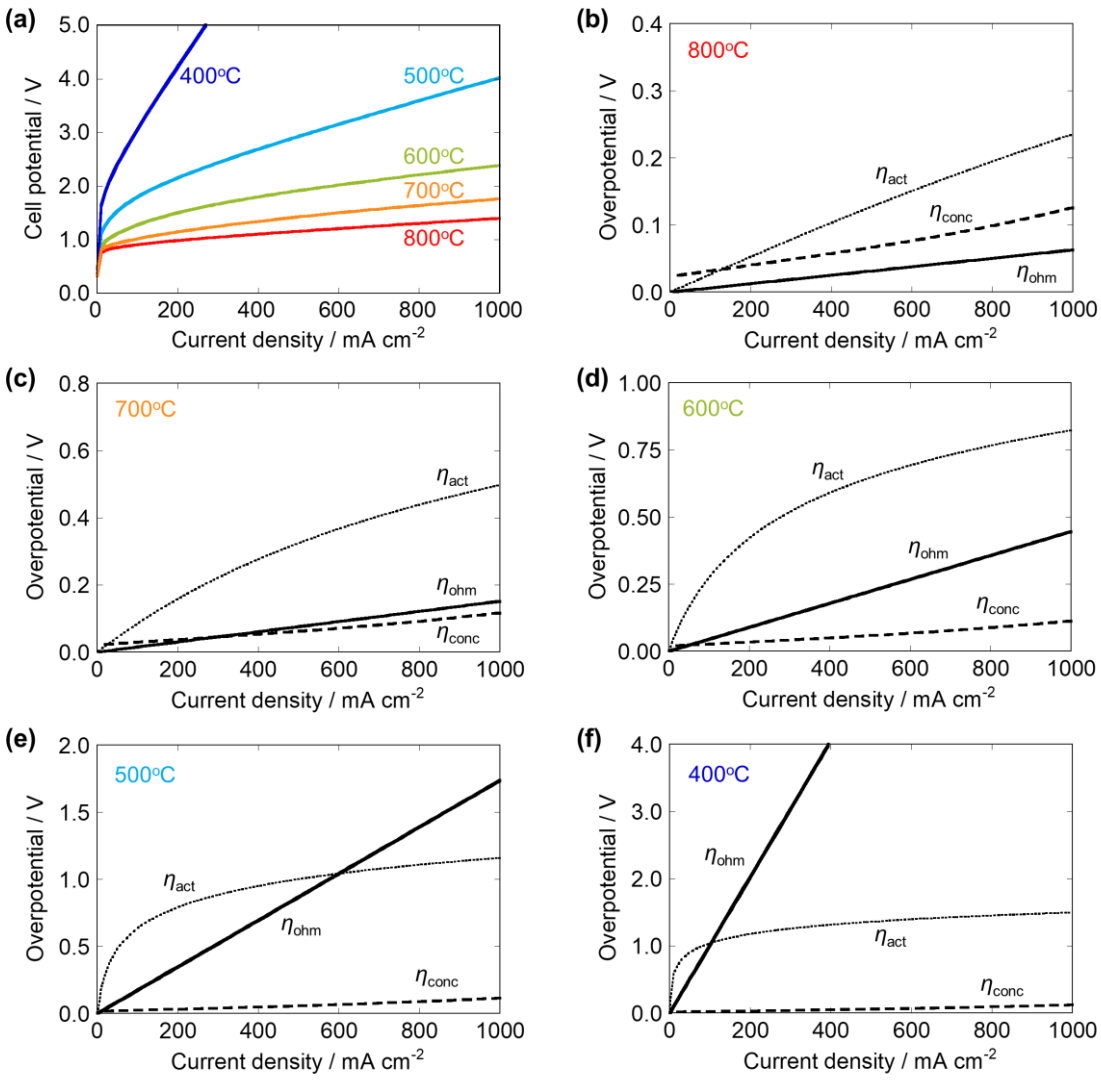

Figure 2-7. (a) Current-voltage characteristics of the SOEC unit at 400°C -800°C, 5 atm. (b)-(f) Breakdown of the overpotentials at each temperature.

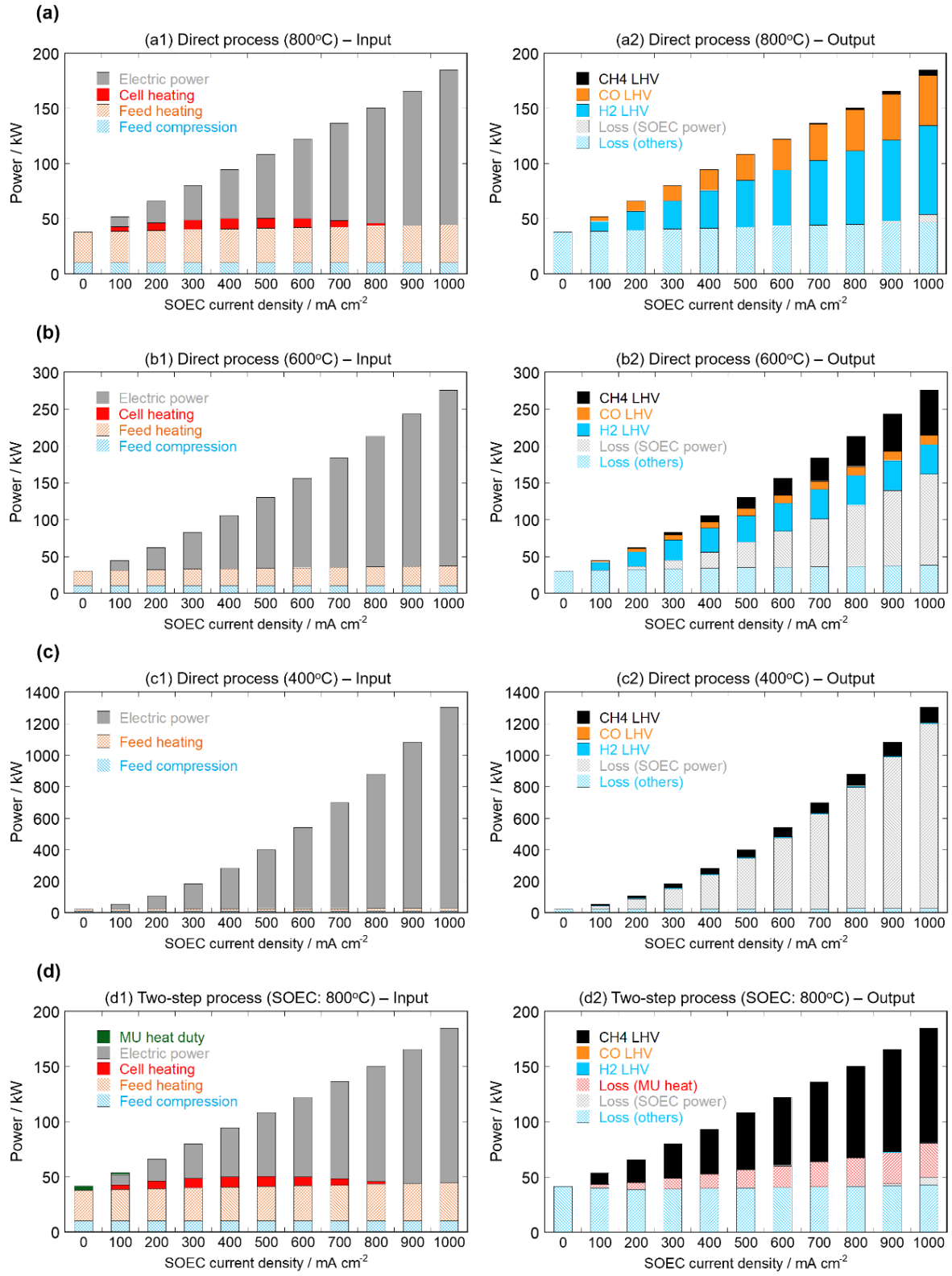

Figure 2-8. Details of the energy input and output of the examined power-to-methane systems. SOEC operation pressure is 5 atm.

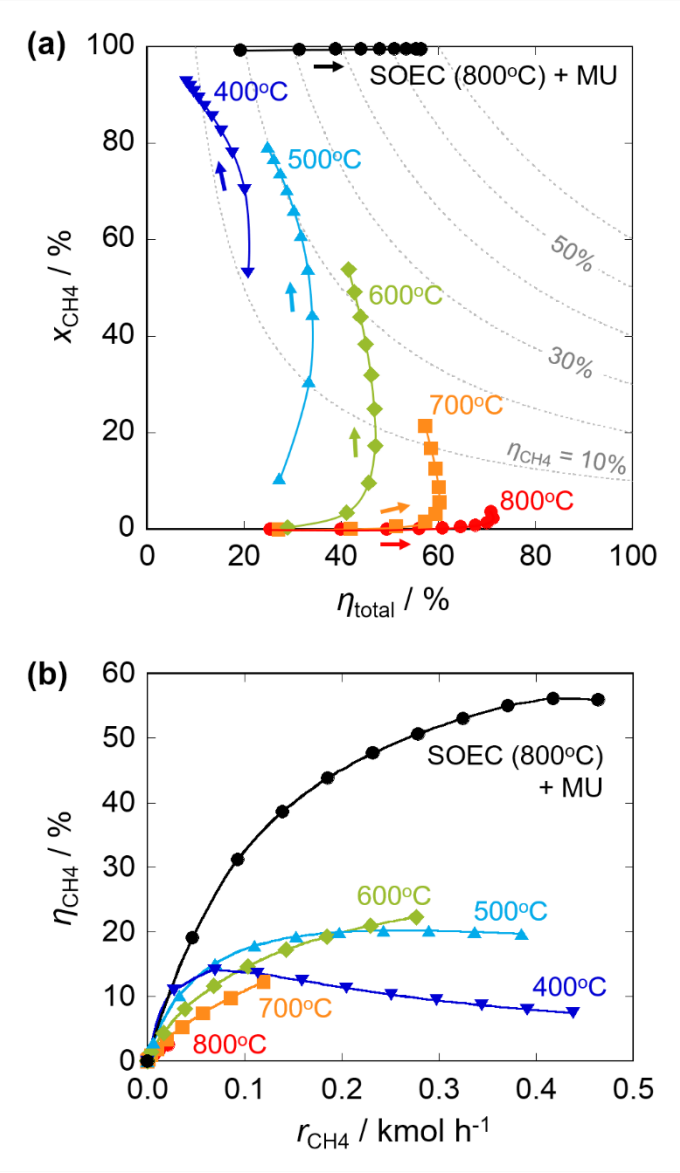

Figure 2-9. Energy conversion efficiencies of simulated systems. (a) x_{CH_4} *vs.* η_{total} plot, (b) η_{CH_4} *vs.* r_{CH_4} plot. Data corresponding to SOEC current density of 0-1000 mA cm^{-2} are shown. SOEC operation pressure is 5 atm.

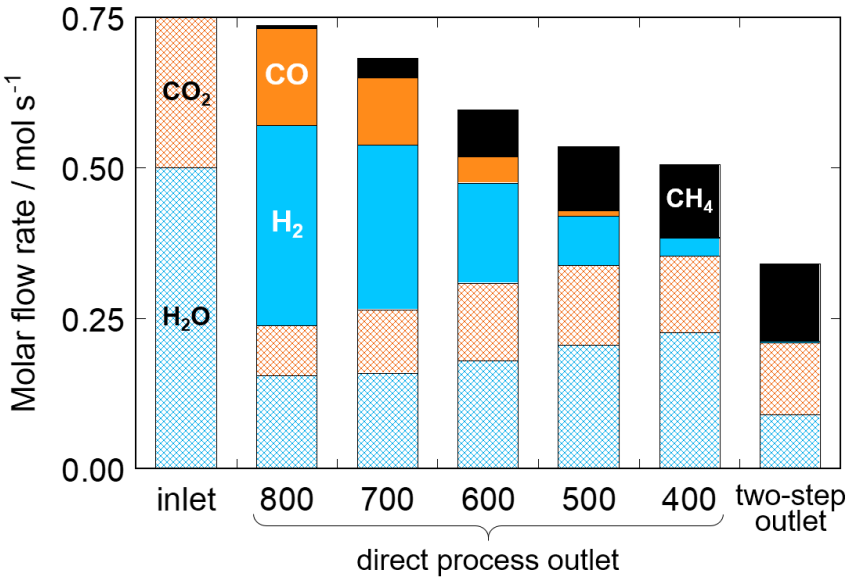

Figure 2-10. System inlet gas composition and system outlet gas compositions corresponding to 1000 mA cm^{-2}. The system outlet gas flow is CA-OUT in Figure 2-2 (for the direct processes) or MET3OUT in Figure 2-3 (for the two-step process). N_2 is excluded for simplicity. SOEC operation pressure is 5 atm.

2.1.6. Improved scenarios

2.1.6.1. Pressurization

As pointed out in the previous section, pressurization is one of the approaches to achieve a higher methane concentration in the product gas. Therefore, simulations of the direct process operated at a high pressure of 20 atm were performed. The pressure dependence of the cathodic exchange current density was calculated by Eq. 2-41 with A+B = 0.25. Figure 2-11 compares the system outlet gas compositions at 5 atm and 20 atm corresponding to SOEC current density of 1000 mA cm^{-2}. The methane production rate and its selectivity against hydrogen and CO are increased by the pressurization at both 400°C and 600°C. Simultaneously, the water content is increased due to the promotion of methanation reaction (Eq. 2-8, the reverse reaction). At 400°C and 20 atm, molar fractions of the product gas species are 88.6%, 0.5%, and 10.9% for methane, CO, and hydrogen, respectively. Because the hydrogen fraction is almost halved from 19.7% at 5 atm, the pressurization is effective to reduce the hydrogen content. Figure 2-12 shows the x_{CH_4} *vs.* η_{total} plot and the η_{CH_4} vs. r_{CH_4} plot. Changes in the product gas compositions result in the increase in x_{CH_4} and η_{CH_4}. However, η_{total} is almost unchanged by the pressurization, indicating that

the changes in cell overpotentials are not so significant in the simulated cases. The improved η_{CH_4} values are still far below those of the two-step process. The present results indicate that radical improvement of the current-voltage characteristics of the cell is necessary to make the direct process comparable or even superior to the two-step process.

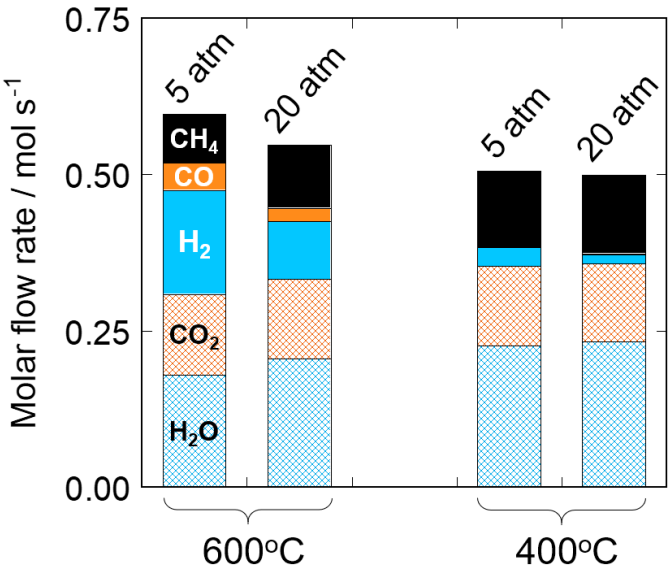

Figure 2-11. Outlet gas compositions of the direct power-to-methane process operated at 5 atm and 20 atm, corresponding to 1000 mA cm^{-2}. N_2 is excluded for simplicity.

2.1.6.2. Improvement in current-voltage characteristics

In this section, simulation results of the direct PtM process with improved SOEC current-voltage characteristics are presented and discussed. When the cell is operated at 5 atm, low temperature such as 400°C or 500°C is needed for the direct process to achieve a methane production rate comparable to that of the two-step process (Figure 2-9b). In improved scenarios, the ohmic and activation overpotentials (η_{ohm} and η_{act}) are decreased at 400°C or 500°C. The concentration overpotential (η_{conc}) was kept unchanged. Table 2-6 summarizes the examined cases. For the operation at 400°C, η_{ohm} and η_{act} values were set to be equivalent to those of 500°C, 600°C, 700°C and 800°C. For the operation at 500°C, the values equivalent to those of 600°C, 700°C and 800°C were considered.

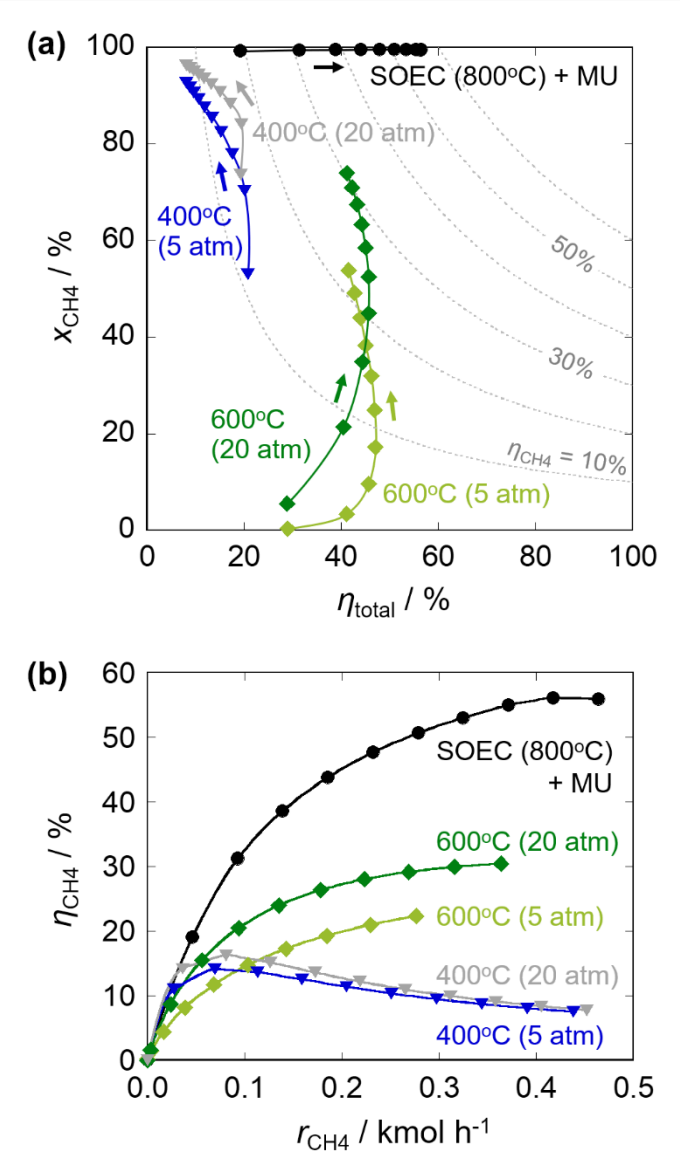

Figure 2-12. Effects of operation pressure of the direct process on energy conversion efficiencies: (a) x_{CH_4} vs. η_{total} plot, (b) η_{CH_4} vs. r_{CH_4} plot. Data corresponding to SOEC current density of 0-1000 mA cm^{-2} are shown.

Table 2-6. Summary of the simulated improved scenarios.

Case	Temperature	η_{ohm} and η_{act} equivalent to
4-5	400°C	500°C
4-6		600°C
4-7		700°C
4-8		800°C
5-6	500°C	600°C
5-7		700°C
5-8		800°C

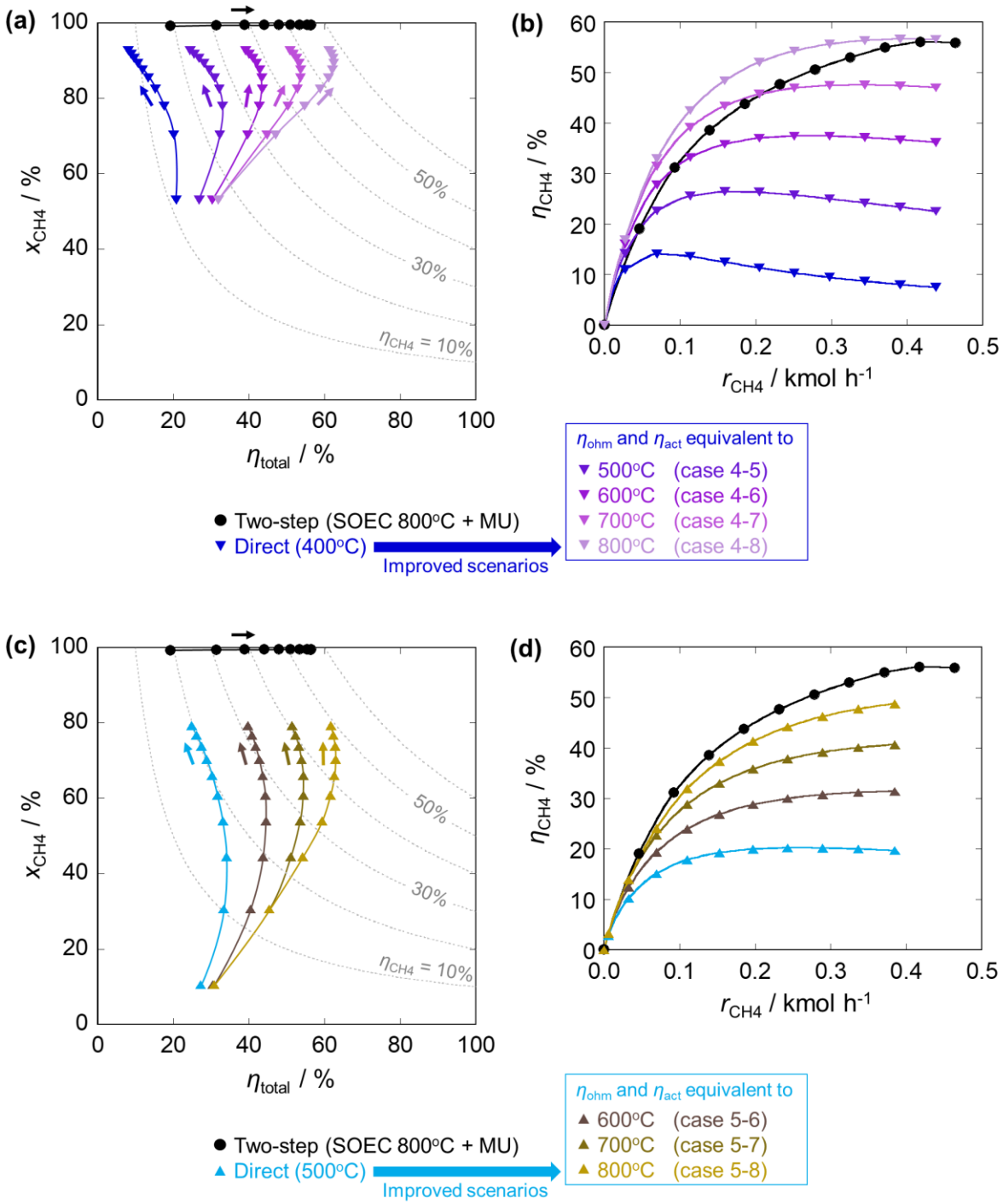

Figure 2-13. Summary of energy conversion efficiencies calculated by assuming improved cell performances. (a) (b) SOECs operated at 400°C with improved current-voltage characteristics. (c) (d) SOECs operated at 500°C with improved current-voltage characteristics. SOEC operation pressure is 5 atm.

The resultant energy conversion efficiencies are shown in Figure 2-13. As can be seen in Figure 2-13a and c, η_{total} increased with the improvement of polarization characteristics while $x_{\mathrm{CH_4}}$ remains

unchanged. Consequently, η_{CH_4} is also improved (Figure 2-13b and d). In the cases of 4-5,4-6 and 4-7, the value of η_{CH_4} exceeds that of the two-step process at low r_{CH_4} conditions. In the case 4-8, η_{CH_4} becomes larger than that of the two-step for the whole examined region. On the other hand, in the cases of 5-6, 5-7 and 5-8, the efficiency goes below that of the two-step.

The reason for the superior performance of the direct process in the improved case 4-8 was further examined by analyzing the energy conversion properties. Figure 2-14 shows the details of the energy input and output in the case 4-8. From Figure 2-14b and Figure 2-8d2, the SOEC power loss and the MU heat loss are specified as key factors because their behaviors to the SOEC current density are characteristic among other components of the losses. Figure 2-15a explains those two types of losses accruing in the two-step process. For the SOEC unit operated at 800°C, the magnitude relation of the SOEC electrical power input ($I_{\text{total}} \times E$) and the enthalpy change corresponding to the chemical reactions inside the SOEC ($\Delta\dot{H}_{\text{SOEC}}$) is important. When $I_{\text{total}} \times E < \Delta\dot{H}_{\text{SOEC}}$, the energy shortage is made up by additional heating. Conversely, when $I_{\text{total}} \times E > \Delta\dot{H}_{\text{SOEC}}$, the surplus will become an energy loss (Area 1). In addition to the SOEC power loss, the MU heat loss is also present in the two-step case because a certain amount of reaction heat in the methanation unit (MU) is not recovered. The amount of the MU heat loss is illustrated in Figure 2-15a as Area 2. For example, when 400 mA cm^{-2} is applied to the cell, $I_{\text{total}} \times E$ (44 kW) is insufficient to satisfy the SOEC heat duty $\Delta\dot{H}_{\text{SOEC}}$ (54 kW), so the additional heating of 10 kW is needed. Nevertheless, reaction heat of 13 kW was lost in the MU and this amount was even larger than the additional heat supplied to the cell unit. Figure 2-15b is for the direct process at 400°C. Under the default condition, the SOEC power loss corresponds to the area between the power curve (blue line) and the $\Delta\dot{H}_{\text{SOEC}}$ line, *i.e.*, Area 3+4. If the improved scenario is taken into account, the power curve will shift to the purple line. In this case, the SOEC power loss will correspond to Area 3 only. When 400 mA cm^{-2} is applied in the case 4-8, the SOEC power loss is 4 kW. This is much smaller than the MU heat loss in the two-step process (13 kW), resulting in the higher η_{CH_4} values (48%) than that of the two-step process (44%). In other words, the concept of the recuperative reaction heat utilization takes effect in the improved case 4-8.

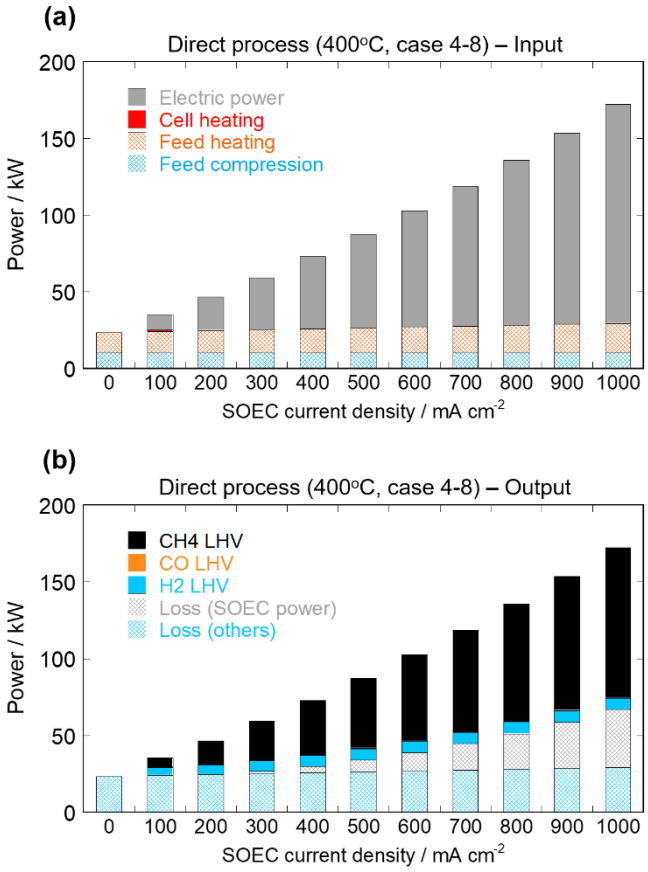

Figure 2-14. Details of the energy input and output of the direct process in the improved case 4-8. SOEC operation pressure is 5 atm.

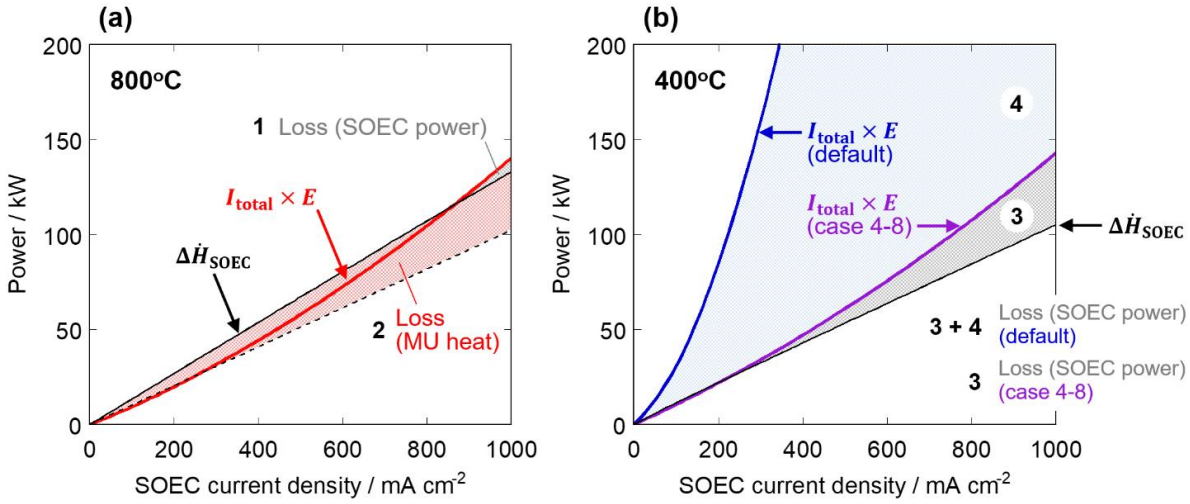

Figure 2-15. Illustrations of SOEC power loss and MU heat loss: (a) two-step process. (b) direct process at 400°C. SOEC operation pressure is 5 atm.

2.1.7. Summary

In Section 2.1, the power-to-methane (PtM) process featuring the direct internal methanation reaction in the SOEC cathode was modeled by using *Aspen Plus*. First, the performance of the direct PtM process was simulated and compared to that of the two-step process, which consists of a serial combination of the high-temperature SOEC unit and the methanation unit. As a result, energy conversion efficiencies of the direct process were lower than that of the two-step process, mainly due to the large overpotentials at low temperatures and the thermodynamic limitation of the methane formation. After that, the operation of the direct process at a high pressure of 20 atm was simulated. The high pressure in the SOEC unit was found to be effective to lower the hydrogen content in the product gas, but the methane LHV-based energy conversion efficiency was not improved significantly by the pressurization. Finally, improved current-voltage characteristics were postulated for the SOEC in the direct process. When the ohmic and activation overpotentials at 400°C were decreased, the methane LHV-based efficiency became higher than that of the two-step process especially at small methane production rates. The superior performance of the improved direct process was ascribed to the recuperative reaction heat utilization.

Figure 2-16 is a piece of artwork describing the study in Section 2.1. The two-step process ("SYNGAS") and the direct process ("DIRECT") are depicted. The missing pieces of the jigsaw puzzle indicate the difficulty of the realization of practical direct processes.

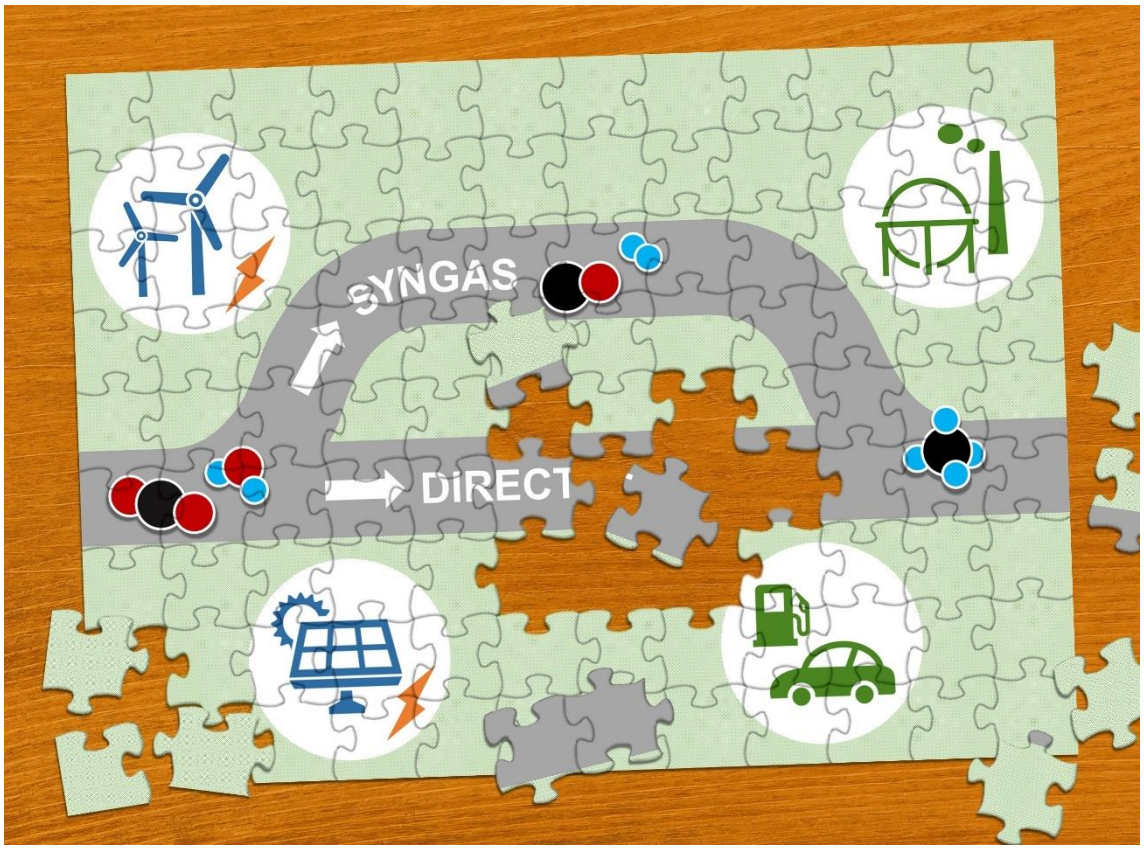

Figure 2-16. Artwork describing the study in Section 2.1.

2.2. SAECs for Production of Methane or Methanol

2.2.1. Objective

The simulations in the previous section revealed that the methane formation in SOECs is strongly limited by the operation temperature. Drastic improvement of the SOEC performance at around 400°C is required to make the process feasible. Such improvement might be accomplished by future development of game-changing materials but is hardly anticipated at the present stage. Consequently, in this section, I focus on solid acid electrolysis cells (SAECs) as a novel electrochemical reaction system. As already discussed in Section 1.3.3, the working temperature of solid acid electrolytes (*ca.* 150-300°C) is near the lower limit of the operation temperature of industrial methanation reactors (*ca.* 250-700°C[116]). Therefore, the application of SAECs to methane synthesis is promising. In addition, the working temperature of SAECs is considered suitable for the methanol formation because catalytic methanol production from CO_2 and H_2 is typically performed at 200-300°C, 10-100 bar[148]. The methanol synthesis in SAECs is also worth investigating. Methanol is one of the promising energy carriers[3,176]. It can be used as a liquid fuel, especially in the transportation sector. In addition, methanol is an important feedstock in the chemical industry. It can be used as a starting material of the production of various compounds including dimethyl ether, olefins, and polymers.

Here, simulations were performed to estimate the characteristics of SAECs for the production of methane and methanol. For the thermodynamic calculations, *Aspen Plus V8.8* (Aspen Technology, Inc.) was used. Current-voltage characteristics were computed according to the equations described below.

2.2.2. Theory and models

2.2.2.1. Reaction formulae

The possible reactions in SAECs for CO_2 electrolysis were discussed in Section 1.3.3. Here, the reaction formulae are reshown.

At the anode, steam is electrolyzed to form protons:

$$2H_2O \rightarrow O_2 + 4H^+ + 4e^- \quad (2\text{-}61)$$

At the cathode, the following reactions can occur to produce hydrogen, methane, and methanol:

$$2H^+ + 2e^- \rightarrow H_2 \quad (2\text{-}62)$$

$$CO_2 + 8H^+ + 8e^- \rightarrow CH_4 + 2H_2O \quad (2\text{-}63)$$

$$CO_2 + 6H^+ + 6e^- \rightarrow CH_3OH + H_2O \quad (2\text{-}64)$$

It is not clear whether electrochemical reactions Eqs. 2-63 and 2-64 actually take place or not. Production of methane and methanol may proceed by the following thermocatalytic reactions:

$$CO_2 + 4H_2 \rightarrow CH_4 + 2H_2O \quad (2\text{-}65)$$

$$CO_2 + 3H_2 \rightarrow CH_3OH + H_2O \quad (2\text{-}66)$$

The reverse water gas shift reaction (Eq. 2-67) can also be involved in the cathodic chemistry.

$$CO_2 + H_2 \rightarrow CO + H_2O \quad (2\text{-}67)$$

Methane and methanol can be formed from CO and hydrogen (Eqs. 2-68 and 2-69).

$$CO + 3H_2 \rightarrow CH_4 + H_2O \quad (2\text{-}68)$$

$$CO + 2H_2 \rightarrow CH_3OH \quad (2\text{-}69)$$

This time, the simulation was performed based on the assumption that the electrochemical reactions Eqs. 2-63 and 2-64 do not occur. Stream electrolysis (Eqs. 2-61 and 2-62) is the only electrochemical reaction under consideration.

2.2.2.2. Current-voltage characteristics

The cell voltage of a SAEC under operation is calculated by

$$E = E_{\mathrm{Nernst}} + \eta_{\mathrm{ohm}} + \eta_{\mathrm{act}} + \eta_{\mathrm{conc}} \quad (2\text{-}70)$$

where E_{Nernst}, η_{ohm}, η_{act}, and η_{conc} are the Nernst potential, the ohmic overpotential, the activation overpotential, and the concentration overpotential, respectively. To calculate the overpotentials, parameters in equations should be determined based on the morphologies and performance of actual SAECs. However, there are not enough experimental data available at the present stage. Therefore, this time, the parameters were determined by referring to the known values in PEMECs or SOECs.

2.2.2.2.1. Nernst potential

When the anodic reaction Eq. 2-61 is under equilibrium, it holds that

$$2\Delta_{\mathrm{f}}G^{0}_{\mathrm{H_2O}}(T) = 2\Delta_{\mathrm{f}}G^{0}_{\mathrm{O_2}} + 4\Delta_{\mathrm{f}}G^{0}_{\mathrm{H^+}} - 4FE^{0}(T) \quad (2\text{-}71)$$

$\Delta_{\mathrm{f}}G^{0}_{i}$ is the standard Gibbs free energy of formation of species *i*. $\Delta_{\mathrm{f}}G^{0}_{\mathrm{O_2}}$ and $\Delta_{\mathrm{f}}G^{0}_{\mathrm{H^+}}$ are defined as zero regardless of the temperature. Thus, the standard electrode potential, E^{0}, becomes

$$E^{0}(T) = -\frac{\Delta_{\mathrm{f}}G^{0}_{\mathrm{H_2O}}(T)}{2F} \quad (2\text{-}72)$$

For details of the temperature dependence of $\Delta_{\mathrm{f}}G^{0}_{i}(T)$, refer to Appendix A.

According to Nernst equation, the electrode potential under non-standard conditions becomes

$$E^{\mathrm{a}}_{\mathrm{Nernst}} = E^{0}(T) + \frac{RT}{4F}\ln\frac{\left(p^{\mathrm{a}}_{\mathrm{O_2}}\right)\left(a^{\mathrm{a}}_{\mathrm{H^+}}\right)^{4}}{\left(p^{\mathrm{a}}_{\mathrm{H_2O}}\right)^{2}} = E^{0}(T) + \frac{RT}{2F}\ln\frac{\left(p^{\mathrm{a}}_{\mathrm{O_2}}\right)^{0.5}}{p^{\mathrm{a}}_{\mathrm{H_2O}}} + \frac{RT}{F}\ln a^{\mathrm{a}}_{\mathrm{H^+}} \quad (2\text{-}73)$$

Here, $a^{\mathrm{a}}_{\mathrm{H^+}}$ is the activity of protons at the anode.

For the cathodic reaction Eq. 2-62, the standard electrode potential E^{0} is defined as zero regardless of the temperature. Therefore,

$$E^{\mathrm{c}}_{\mathrm{Nernst}} = \frac{RT}{2F}\ln\frac{\left(a^{\mathrm{c}}_{\mathrm{H^+}}\right)^{2}}{p^{\mathrm{c}}_{\mathrm{H_2}}} = \frac{RT}{2F}\ln\frac{1}{p^{\mathrm{c}}_{\mathrm{H_2}}} + \frac{RT}{F}\ln a^{\mathrm{c}}_{\mathrm{H^+}} \quad (2\text{-}74)$$

Assuming that $a^{\mathrm{a}}_{\mathrm{H^+}} = a^{\mathrm{c}}_{\mathrm{H^+}}$, the Nernst potential of the cell, E_{Nernst}, is obtained from Eqs. 2-73 and 2-74 as follows:

$$E_{\mathrm{Nernst}} = E^{\mathrm{a}}_{\mathrm{Nernst}} - E^{\mathrm{c}}_{\mathrm{Nernst}} = E^{0}(T) + \frac{RT}{2F}\ln\frac{\left(p^{\mathrm{c}}_{\mathrm{H_2}}\right)\left(p^{\mathrm{a}}_{\mathrm{O_2}}\right)^{0.5}}{p^{\mathrm{a}}_{\mathrm{H_2O}}} \quad (2\text{-}75)$$

The partial pressures of H_2, O_2, and H_2O in Eq. 2-75 were determined from the cell outlet gas compositions obtained from *Aspen Plus*.

2.2.2.2.2. Ohmic overpotential

The ohmic overpotential, η_{ohm}, was calculated as

$$\eta_{\mathrm{ohm}} = \frac{\delta_{\mathrm{e}}}{\sigma} i \quad (2\text{-}76)$$

In this study, a CsH_2PO_4/SiP_2O_7 composite electrolyte is supposed. The conductivity of CsH_2PO_4/SiP_2O_7 (molar ratio 1:2, under 30%H_2O/Ar atmosphere) is taken form the literature[177]. The conductivity at 140-

300°C shown in Fig. 4 of ref. [177] was approximated by a quartic equation:

$$y = -10.390x^4 + 91.897x^3 - 306.80x^2 + 455.81x - 254.76 \quad (2\text{-}77)$$

$$x = 1000/T \quad (2\text{-}78)$$

$$y = \log(\sigma / \mathrm{S\ cm^{-1}}) \quad (2\text{-}79)$$

The thickness of the electrolyte, δ_{e}, was set to 500 μm.

2.2.2.2.3. Activation overpotential

Activation overpotentials at each electrode were estimated as follows (see Appendix D for details):

$$\eta_{\mathrm{act}}^{\mathrm{a}} = \frac{RT}{2F}\sinh^{-1}\left(\frac{i}{2i_0^{\mathrm{a}}}\right) \quad (2\text{-}80)$$

$$\eta_{\mathrm{act}}^{\mathrm{c}} = \frac{2RT}{F}\sinh^{-1}\left(\frac{i}{2i_0^{\mathrm{c}}}\right) \quad (2\text{-}81)$$

i_0^{a} and i_0^{c} are the exchange current densities at the anode and the cathode, respectively. Exchange current densities of SAECs have not been reported so far. This time, values typically used for PEMFCs[9,178] were adopted: $i_0^{\mathrm{a}} = 1.0 \times 10^{-7}\mathrm{A\ cm^{-2}}$ and $i_0^{\mathrm{c}} = 1.0 \times 10^{-3}\mathrm{A\ cm^{-2}}$. Our preliminary SAEC experiments with a Pt mesh anode, a Pt/C cathode, and a Pt reference electrode (details are not shown here) suggested that the exchange current densities of SAECs are about the same as these values, supporting the approximation.

2.2.2.2.4. Concentration overpotential

The concentration overpotential of a SAEC for steam electrolysis can be written as follows (see Appendix D for details):

$$\eta_{\mathrm{conc}} = \frac{RT}{2F}\ln\left(\frac{p_{\mathrm{H_2O}}^{\mathrm{a}}}{p_{\mathrm{H_2O}}^{\mathrm{a*}}}\right) + \frac{RT}{4F}\ln\left(\frac{p_{\mathrm{O_2}}^{\mathrm{a*}}}{p_{\mathrm{O_2}}^{\mathrm{a}}}\right) + \frac{RT}{2F}\ln\left(\frac{p_{\mathrm{H_2}}^{\mathrm{c*}}}{p_{\mathrm{H_2}}^{\mathrm{c}}}\right) \quad (2\text{-}82)$$

$p_{\mathrm{H_2O}}^{\mathrm{a*}}$, $p_{\mathrm{O_2}}^{\mathrm{a*}}$, and $p_{\mathrm{H_2}}^{\mathrm{c*}}$ indicate the partial pressures at the reaction sites during the operation while $p_{\mathrm{H_2O}}^{\mathrm{a}}$, $p_{\mathrm{O_2}}^{\mathrm{a}}$, and $p_{\mathrm{H_2}}^{\mathrm{c}}$ indicate the bulk gas partial pressures. Superscripts a and c indicate anode and cathode, respectively. $p_{\mathrm{H_2O}}^{\mathrm{a*}}$, $p_{\mathrm{O_2}}^{\mathrm{a*}}$, and $p_{\mathrm{H_2}}^{\mathrm{c*}}$ can be estimated by using effective diffusion coefficients:

$$p_{\mathrm{H_2O}}^{\mathrm{a}*} = p_{\mathrm{H_2O}}^{\mathrm{a}} - \frac{RT}{2F}\frac{\delta_{\mathrm{a}} i}{D_{\mathrm{H_2O}}^{\mathrm{eff}}} \quad (2\text{-}83)$$

$$p_{\mathrm{O_2}}^{\mathrm{a}*} = p_{\mathrm{O_2}}^{\mathrm{a}} + \frac{RT}{4F}\frac{\delta_{\mathrm{a}} i}{D_{\mathrm{O_2}}^{\mathrm{eff}}} \quad (2\text{-}84)$$

$$p_{\mathrm{H_2}}^{\mathrm{c}*} = p_{\mathrm{H_2}}^{\mathrm{c}} + \frac{RT}{2F}\frac{\delta_{\mathrm{c}} i}{D_{\mathrm{H_2}}^{\mathrm{eff}}} \quad (2\text{-}85)$$

The thickness of the anode layer (δ_{a}) and the cathode layer (δ_{c}) were both estimated to be 100 μm. The effective gas diffusion coefficients, D_i^{eff}, were obtained in the same manner as the simulation of SOECs (see Section 2.1.2.2.4). Pore diameter, porosity, and tortuosity of the electrodes were estimated to be 1 μm, 0.5, and 5, respectively.

2.2.2.3. *Aspen Plus* model

Figure 2-17 shows the flowsheet of the *Aspen Plus* model used in this study. The temperature and the pressure of the feed gases were controlled before introduced to the cell. The cell was modeled by a combination of two virtual reactors. One is "ELECHEM", where the electrochemical reactions Eqs. 2-61 and 2-62 were modeled by the reaction of Eq. 2-3. Hydrogen produced in ELECHEM is separated and sent to the second reactor, "CATAL". In CATAL, equilibrium gas compositions were calculated by considering catalytic reactions. For the methane synthesis, the reverse water gas shift reaction (Eq. 2-67) and the CO methanation reaction (Eq. 2-68) were considered. For the methanol synthesis, the CO_2-to-methanol reaction (Eq. 2-66) and the methanol decomposition reaction (Eq. 2-86) were taken into account.

$$CH_3OH \rightarrow CO + 2H_2 \quad (2\text{-}86)$$

Note that, for the methanol synthesis, the combination of the CO_2-to-methanol reaction and the methanol decomposition reaction will give the same result as the combination of the reverse water gas shift reaction and the CO-to-methanol reaction (Eq. 2-69).

The present model is basically zero-dimensional. Detailed geometries of the electrochemical reactor (*e.g.* the shape of flow channels) cannot be incorporated into the model. The electrode area of 1 cm^2 was assumed. Therefore, properties simulated by the model will automatically be normalized by the electrode area. The values can be used to predict the performance of large-sized reactors by multiplying them by

the desired electrode area.

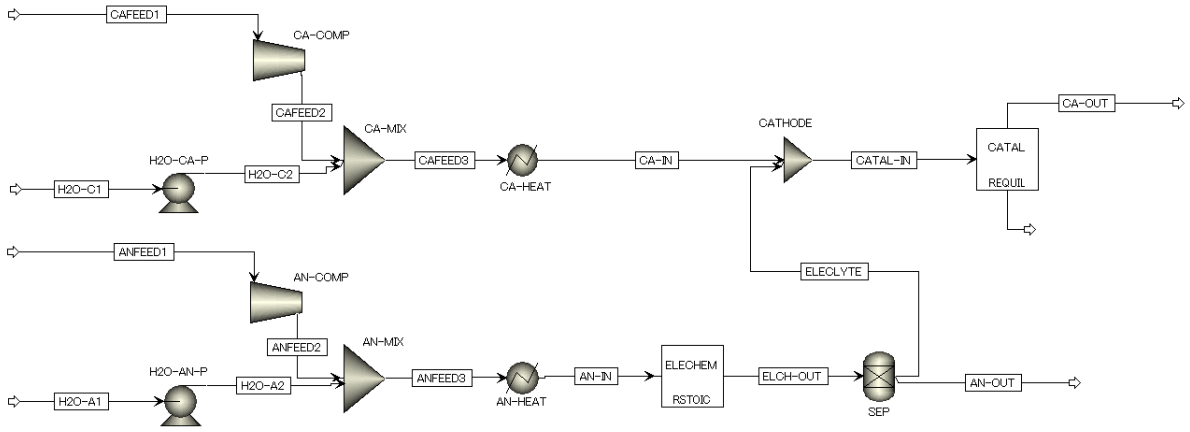

Figure 2-17. Process flowsheet of the *Aspen Plus* model to simulate SAECs.

2.2.3. Methane synthesis

2.2.3.1. Effects of CO_2/H^+ ratio

First, the effects of CO_2/H^+ ratio was examined. The operation temperature and pressure were set to 250°C and 1 atm, respectively. The anode inlet gas was 70%H_2O/30%N_2 (total 4 μmol s^{-1}). The current density was fixed at 100 mA cm^{-2}. Dry CO_2 was fed to the cathode side. The flow rate of CO_2 was varied so that the CO_2/H^+ ratio ranged from 0 to 20. The corresponding CO_2 molar flow rate was 0-20.7 μmol s^{-1}. Figure 2-18a shows the methane production rates at different CO_2/H^+ conditions. The production rate was around 0.13 μmol s^{-1} and slightly decreased with the CO_2/H^+ ratio. Figure 2-18b shows the CO_2 conversion calculated by Eq. 2-87.

$$(\mathrm{CO_2\ conversion}) = \left(F_{\mathrm{CO_2,in}} - F_{\mathrm{CO_2,out}}\right)/F_{\mathrm{CO_2,in}} \quad (2\text{-}87)$$

$F_{\mathrm{CO_2,in}}$ and $F_{\mathrm{CO_2,out}}$ are the molar flow rates of CO_2 in the cathode inlet and outlet, respectively. When CO_2/H^+ was smaller than the stoichiometric value of 0.125 (corresponding to Eq. 2-63 or Eq. 2-65), the conversion was nearly 100%. Then, the conversion decreased with the CO_2/H^+ ratio. Figure 2-18c shows the nominal Faraday efficiencies (FE) for the production of H_2, CO, and CH_4. The efficiencies were calculated as follows:

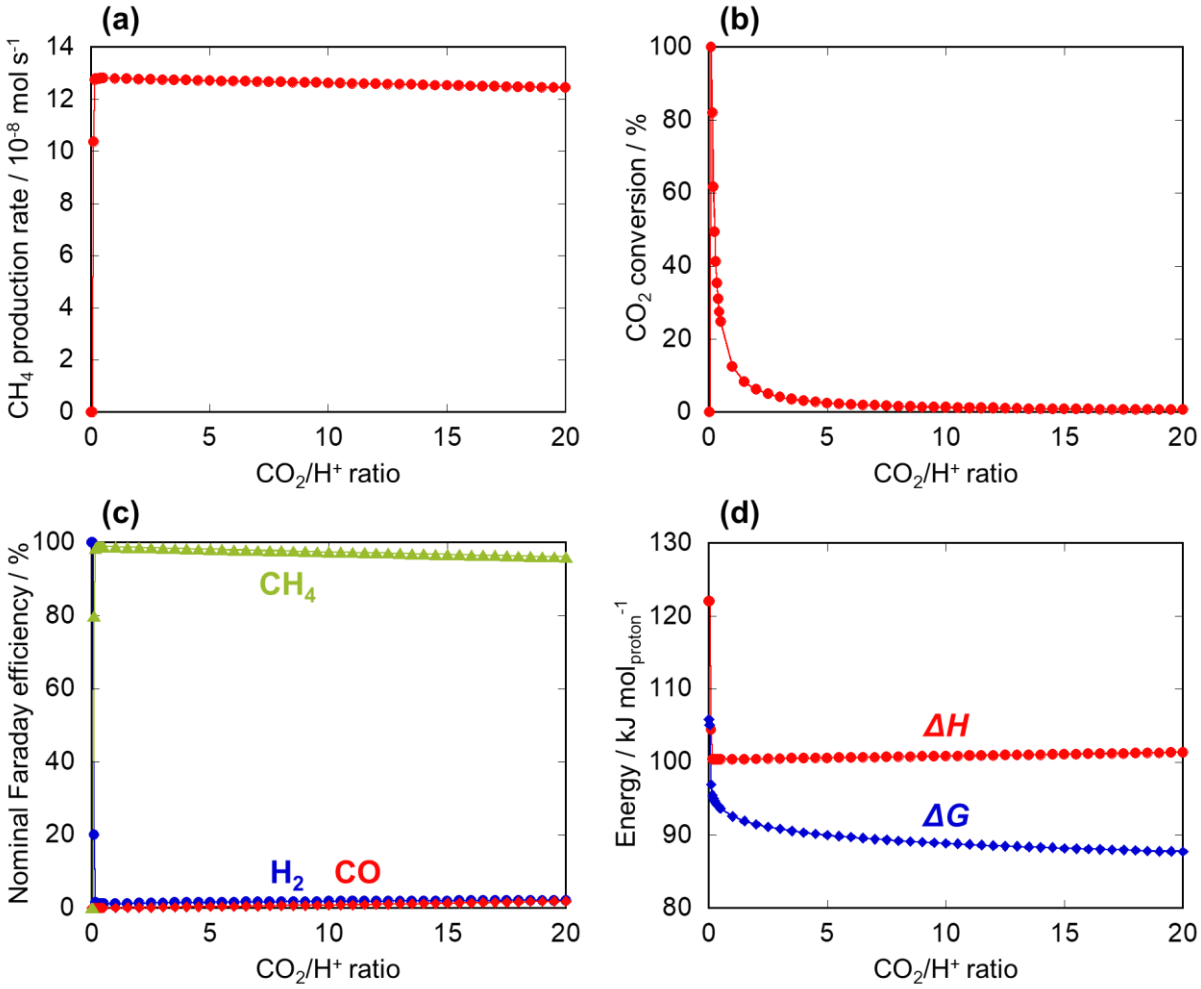

Figure 2-18. Effects of the CO_2/H^+ ratio on the SAEC performance for methane production. Cell operation temperature and pressure were set to 250°C and 1 atm. (a) Methane production rate. (b) CO_2 conversion. (c) Nominal Faraday efficiencies for the production of H_2, CO, and CH_4. (d) Changes of enthalpy and Gibbs free energy in the cell per 1 mol of protons transferred.

$$\mathrm{FE}_{\mathrm{H_2}} = 2F_{\mathrm{H_2,out}}/(2F_{\mathrm{H_2,out}} + 2F_{\mathrm{CO,out}} + 8F_{\mathrm{CH_4,out}}) \quad (2\text{-}88)$$

$$\mathrm{FE}_{\mathrm{CO}} = 2F_{\mathrm{CO,out}}/(2F_{\mathrm{H_2,out}} + 2F_{\mathrm{CO,out}} + 8F_{\mathrm{CH_4,out}}) \quad (2\text{-}89)$$

$$\mathrm{FE}_{\mathrm{CH_4}} = 8F_{\mathrm{CH_4,out}}/(2F_{\mathrm{H_2,out}} + 2F_{\mathrm{CO,out}} + 8F_{\mathrm{CH_4,out}}) \quad (2\text{-}90)$$

where the term $(2F_{\mathrm{H_2,out}} + 2F_{\mathrm{CO,out}} + 8F_{\mathrm{CH_4,out}})$ is equal to the total electrons transferred in the cell (100 mA). At $CO_2/H^+ = 0$, $\mathrm{FE}_{\mathrm{H_2}}$ was 100%. By introducing CO_2, $\mathrm{FE}_{\mathrm{H_2}}$ decreased steeply and $\mathrm{FE}_{\mathrm{CH_4}}$ increased drastically. $\mathrm{FE}_{\mathrm{CH_4}}$ reached its maximum of *ca.* 99% at around $CO_2/H^+ = 0.45$. After that, $\mathrm{FE}_{\mathrm{CH_4}}$ decreased gradually with the CO_2/H^+ ratio while $\mathrm{FE}_{\mathrm{H_2}}$ and $\mathrm{FE}_{\mathrm{CO}}$ increased slightly. Figure

2-18d shows the changes of enthalpy and Gibbs free energy in the cell, which are normalized by the mole of protons transferred. $CO_2/H^+ = 0$ corresponds to the hydrogen production. When CO_2 is present in the cathode, ΔH and ΔG became smaller than those in the hydrogen production case. This is due to the characteristics of the exothermic methanation reaction ($\Delta H < 0$ and $\Delta G < 0$ at 250°C, see Figure 1-8a).

2.2.3.2. Effects of temperature and pressure

Next, effects of operation temperature and pressure was examined under constant CO_2/H^+ ratio of 0.5. The current density was fixed to 100 mA cm^{-2}. The corresponding CO_2 flow rate in the cathode inlet was 0.518 µmol s^{-1}. Figure 2-19a shows the nominal Faraday efficiencies for H_2, CO, and CH_4 at different temperatures. The operation pressure was 1 atm. At all examined temperatures, FE_{CH_4} was close to 100% while FE_{H_2} and FE_{CO} were negligible. Figure 2-19b shows the dependence of the nominal Faraday efficiencies on the operation pressure at 250°C. Being similar to Figure 2-19a, methane production was dominant at all pressures. These results mean that, under the simulated conditions, the equilibrium shifts almost completely to the formation of methane. Thus, the methane formation in SAECs is quite advantageous from the thermodynamic viewpoint.

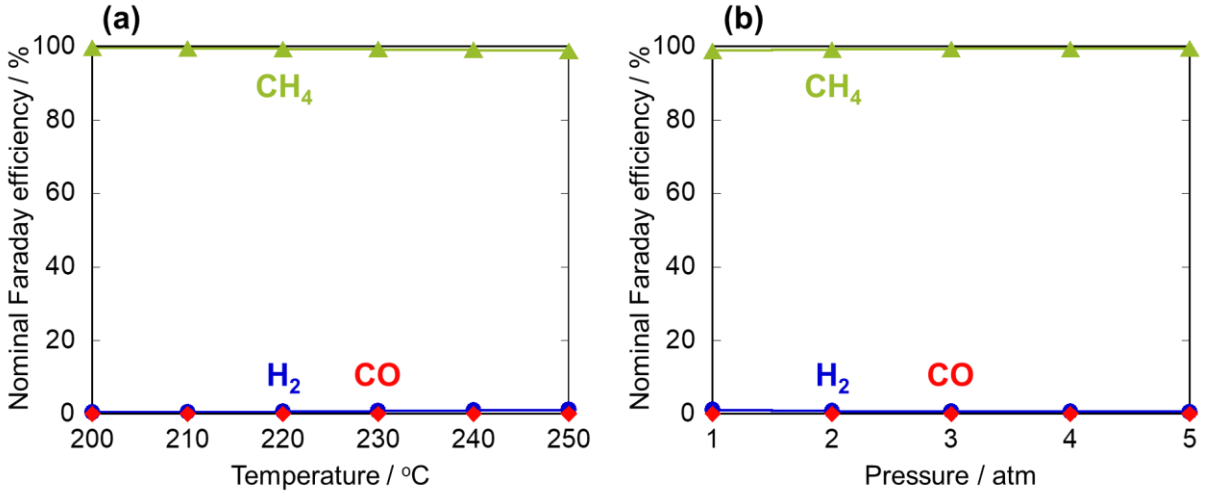

Figure 2-19. Effects of the operation temperature and pressure on the nominal Faraday efficiencies. (a) Efficiencies at different temperatures (pressure: 1 atm). (b) Efficiencies at different pressures (temperature: 250°C).

2.2.3.3. Cell voltage and energy balance

Current-voltage characteristics of the SAEC for methane synthesis was simulated under a constant cathode inlet CO_2 flow rate of 0.518 μmol s^{-1}. This flow rate corresponds to $CO_2/H^+ = 0.5$ (CO_2:H_2 = 1:1) at 100 mA cm^{-2}. In the simulations described above (Sections 2.2.3.1 and 2.2.3.2), the anode inlet gas was fixed (70% H_2O and 30% N_2, total 4 μmol s^{-1}). The current density was also fixed to 100 mA cm^{-2}, so the steam utilization was constant at 18.5%. The steam utilization of 18.5% is relatively low for the practical applications. For example, in a SOEC simulation study, steam utilization of 80% at 500 mA cm^{-2} was assumed[179]. In an experimental study of industrial scale SOECs, similar steam utilizations were reported (*e.g.* 70% at 520 mA cm^{-2})[180]. Note that in these SOEC studies a small amount of hydrogen was mixed in the steam feed, and that the steam feed was introduced to SOEC cathodes, where hydrogen was produced. Therefore, even under high steam utilizations, those hydrogen may suppress the oxidation of SOEC cathodes. In SAECs, steam is fed to the anode side and oxygen is formed. It is expected that SAEC anodes are more prone to be oxidized than SOEC cathodes. Accordingly, a constant steam utilization of 50% was assumed in the present simulation. The anodic gas composition was fixed to 70% H_2O and 30% N_2, and the flow rate was varied depending on the current density so that 50% of the supplied steam was electrolyzed at the anode.

Figure 2-20a shows the calculated cell voltage E and thermoneutral voltage E_{TN} of the SAEC for the methane production at 250°C, 1 atm. E and E_{TN} of a SAEC for the hydrogen production (cathode gas was changed to 0.518 μmol s^{-1} of nitrogen) are also shown for comparison. A thermoneutral voltage is the voltage at which the electrical power input becomes equal to the overall enthalpy change in the cell, and can be calculated as

$$E_{\mathrm{TN}} = \Delta H / I \tag{2-91}$$

In Eq. 2-91, ΔH is the overall enthalpy change in the cell and I is the total current flowing in the cell. The electric power corresponding to the difference between E and E_{TN} will not be converted into chemical energy of the products but will be emitted as waste heat. According to Figure 2-20a, E and E_{TN} under the methane production condition is smaller than those in the hydrogen production condition.

This is because the enthalpy change in the cell becomes smaller due to the exothermic nature of the methanation. Figure 2-20b compares the heat loss in the two operation modes (denoted as A and B), which was calculated as

$$(\text{heat loss}) = I(E - E_{\text{TN}}) \tag{2-92}$$

Because the difference between E and E_{TN} is smaller in the hydrogen production case, the heat loss is also smaller (A > B). However, the value does not include the methanation heat. If a catalytic methanation reactor is connected downstream of the H_2-producing SAEC, and the methanation heat is not recovered, the total energy loss will become larger. The methanation heat was estimated by comparing the H_2-producing SAEC and the CH_4-producing SAEC:

$$(\text{methanation heat}) = I\left(E_{\text{TN},H_2} - E_{\text{TN},CH_4}\right) = \Delta H_{H_2} - \Delta H_{CH_4} \tag{2-93}$$

The dotted line in Figure 2-20b (denoted as C) indicates the sum of the heat loss in the H_2-producing SAEC and the methanation heat. The value is larger than the heat loss in the CH_4-producing SAEC (C > A). The results here indicate that the direct methane synthesis in SAECs can serve as a more energy-efficient PtM system than the two-step PtM with a H_2-producing SAEC and a methanation unit.

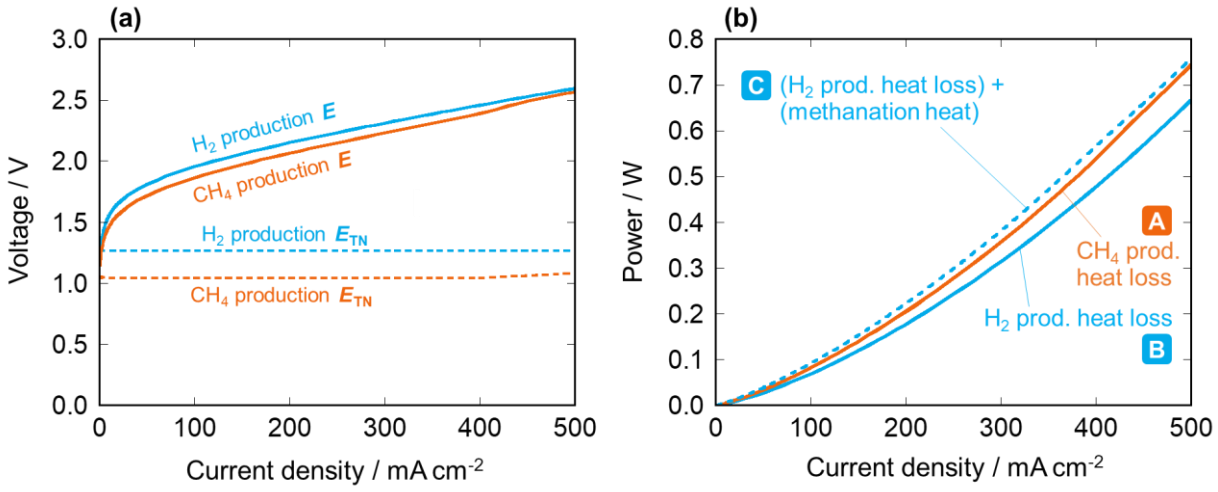

Figure 2-20. (a) Cell voltages and thermoneutral voltages of SAECs for the methane production and the hydrogen production at 250°C, 1 atm. (b) Comparison of system energy losses. [A] heat loss in the CH_4-producing SAEC. [B] heat loss in the H_2-producing SAEC. [C] Sum of the heat loss in the H_2-producing SAEC and the methanation heat.

Figure 2-21 shows a breakdown of the overpotential of a SAEC for the methane production (corresponding to Figure 2-20a). Contributions of each overpotential component are piled up. Among the components, activation overpotentials and ohmic overpotential account for large portions. It is desirable to decrease the activation overpotentials by improving the electrode kinetics. Development of thinner electrolyte membranes will lead to higher energy efficiency by suppressing the ohmic resistance.

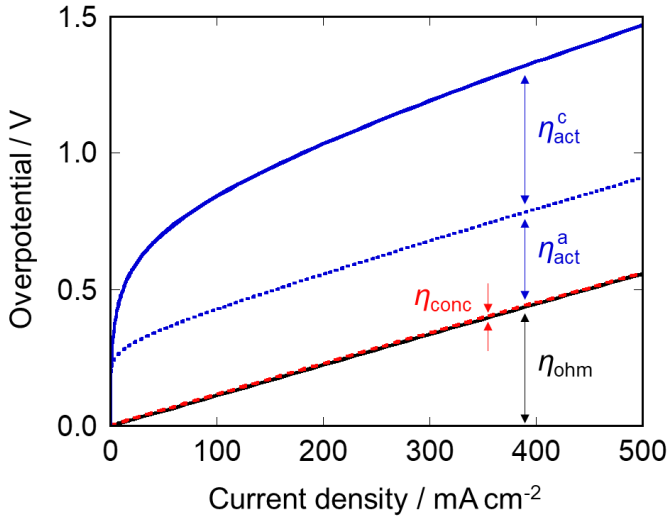

Figure 2-21. Components of the overpotential of a SAEC for the methane production.

2.2.4. Methanol synthesis

2.2.4.1. Effects of CO_2/H^+ ratio

The effects of the CO_2/H^+ ratio on the performance at 180°C and 10 atm were examined. A gas mixture of 70%H_2O/30%N_2 (total 4 μmol s^{-1}) was fed to the anode. The current density was fixed at 100 mA cm^{-2}. The flow rate of the dry CO_2 cathode feed was varied so that the CO_2/H^+ ratio ranged from 0 to 20. Figure 2-22a shows the methanol production rates. The production rate was reached its maximum of 2.2×10^{-8} mol s^{-1} at around $CO_2/H^+ = 0.3$. However, this rate is about an order of magnitude lower than that of the methane formation. Figure 2-22b shows the CO_2 conversion calculated by Eq. 2-87. Even under a H_2-rich condition of $CO_2/H^+ = 0.1$, the conversion was 22%. This is significantly lower than the CO_2 conversion

in the methane production (~100%). Figure 2-22c shows the nominal Faraday efficiencies (FE) for the production of H_2, CO, and CH_3OH. The efficiencies were calculated as follows:

$$\mathrm{FE}_{\mathrm{H_2}} = 2F_{\mathrm{H_2,out}}/(2F_{\mathrm{H_2,out}} + 2F_{\mathrm{CO,out}} + 6F_{\mathrm{CH_3OH,out}}) \quad (2\text{-}94)$$

$$\mathrm{FE}_{\mathrm{CO}} = 2F_{\mathrm{CO,out}}/(2F_{\mathrm{H_2,out}} + 2F_{\mathrm{CO,out}} + 6F_{\mathrm{CH_3OH,out}}) \quad (2\text{-}95)$$

$$\mathrm{FE}_{\mathrm{CH_3OH}} = 6F_{\mathrm{CH_3OH,out}}/(2F_{\mathrm{H_2,out}} + 2F_{\mathrm{CO,out}} + 6F_{\mathrm{CH_3OH,out}}) \quad (2\text{-}96)$$

where the term $(2F_{\mathrm{H_2,out}} + 2F_{\mathrm{CO,out}} + 6F_{\mathrm{CH_3OH,out}})$ is equal to the total electrons transferred in the cell (100 mA). The methanol production is not so thermodynamically advantageous as the methane production: the highest $\mathrm{FE}_{\mathrm{CH_3OH}}$ was *ca.* 13% at around $CO_2/H^+ = 0.3$. In the region of $CO_2/H^+ > 0.3$, $\mathrm{FE}_{\mathrm{CH_3OH}}$ decreases with the CO_2/H^+ ratio while $\mathrm{FE}_{\mathrm{CO}}$ increased. This means that the formation of CO is favored at high CO_2/H^+ ratios. Figure 2-22d shows the changes of enthalpy and Gibbs free energy in the cell per 1 mol of protons transferred. $CO_2/H^+ = 0$ corresponds to the hydrogen production. *ΔH* decreased slightly at low CO_2/H^+ ratios due to the exothermic CO_2-to-methanol reaction (Figure 1-8b). However, at larger CO_2/H^+ ratios, *ΔH* increased reflecting the endothermic nature of the reverse water gas shift reaction (Figure 1-5a). *ΔG* decreased monotonically with the CO_2/H^+ ratio.

2.2.4.2. Effects of temperature and pressure

Effects of operation temperature and pressure was examined under constant CO_2/H^+ ratio of 0.5. The current density was fixed to 100 mA cm^{-2}. Figure 2-23a shows the nominal Faraday efficiencies for H_2, CO, and CH_3OH at 1 atm and different temperatures. At all examined temperatures, $\mathrm{FE}_{\mathrm{CH_3OH}}$ was near 0%. $\mathrm{FE}_{\mathrm{CO}}$ was below 10% and increased gradually with the CO_2/H^+ ratio. Methanol production is hardly expected under ambient pressure from the thermodynamic viewpoint. Figure 2-23b and c show the dependence of the nominal Faraday efficiencies on the operation pressure at 250°C and 180°C, respectively. $\mathrm{FE}_{\mathrm{CH_3OH}}$ increased with the operation pressure while $\mathrm{FE}_{\mathrm{H_2}}$ and $\mathrm{FE}_{\mathrm{CO}}$ decreased. At 250°C, $\mathrm{FE}_{\mathrm{CH_3OH}}$ reached only 1.2% under 10 atm. At 180°C, $\mathrm{FE}_{\mathrm{CH_3OH}}$ under 10 atm was 12%, about ten times larger than the value at 250°C. Methanol formation is favored at low temperatures and high pressures. It should be noted that the thermodynamic equilibrium calculated in this model includes CO.

If methanol is directly formed from CO_2 and H_2, and CO is formed only *via* the decomposition of methanol, selectivity higher than the equilibrium value may be achieved by kinetically suppressing the methanol decomposition.

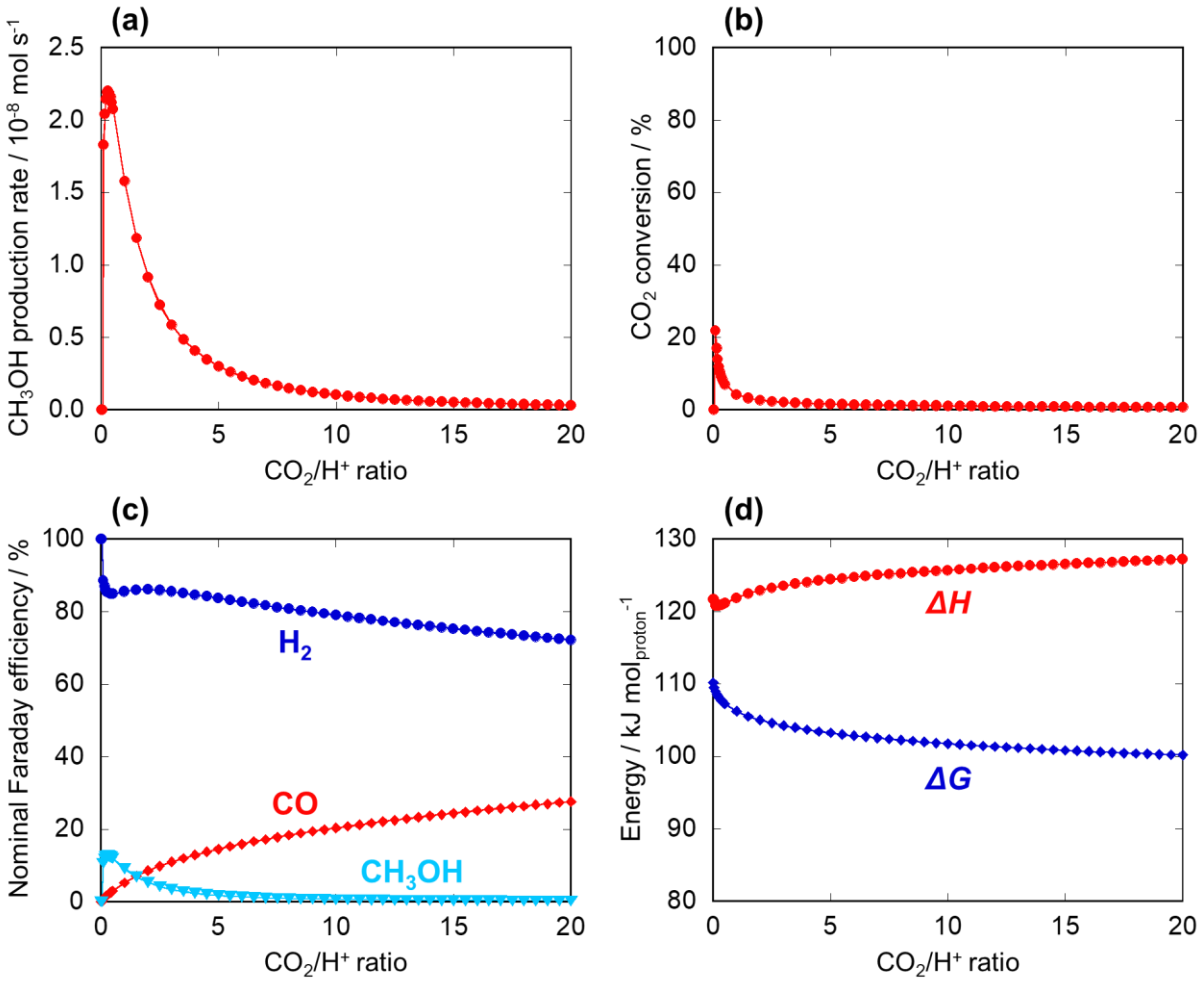

Figure 2-22. Effects of the CO_2/H^+ ratio on the SAEC performance for methanol production. Cell operation temperature and pressure were set to 180°C and 10 atm. (a) Methanol production rate. (b) CO_2 conversion. (c) Nominal Faraday efficiencies for the production of H_2, CO, and CH_3OH. (d) Changes of enthalpy and Gibbs free energy in the cell per 1 mol of protons transferred.

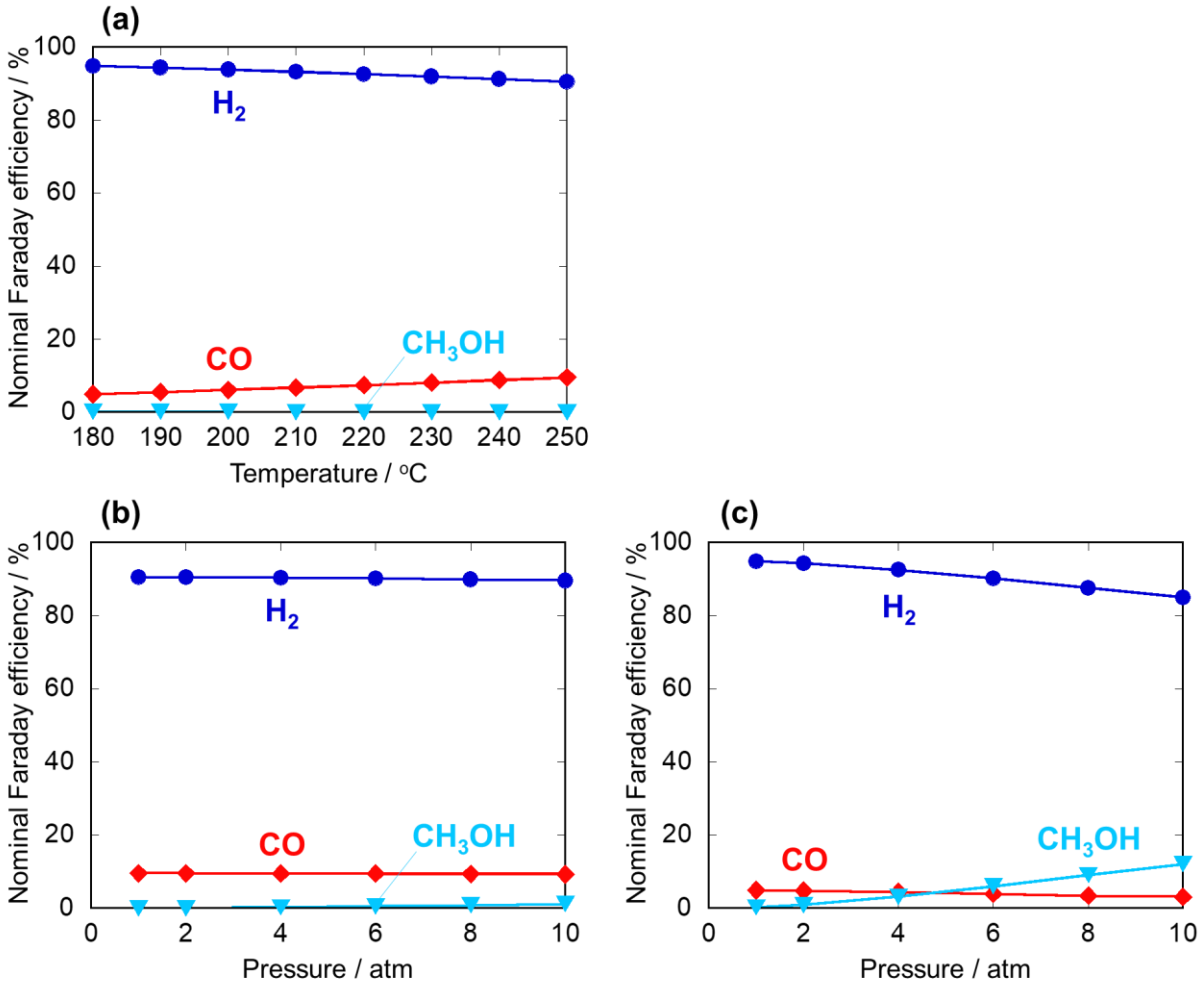

Figure 2-23. Effects of the operation temperature and pressure on the nominal Faraday efficiencies. (a) Efficiencies at different temperatures (pressure: 1 atm). (b) Efficiencies at different pressures (temperature: 250°C). (c) Efficiencies at different pressures (temperature: 180°C).

2.2.4.3. Cell voltage and energy balance

Current-voltage characteristics of the SAEC for methanol synthesis was simulated under a constant cathode inlet CO_2 flow rate of 0.518 μmol s^{-1}. This flow rate corresponds to $CO_2/H^+ = 0.5$ (CO_2:H_2 = 1:1) at 100 mA cm^{-2}. A constant steam utilization of 50% was assumed. The anodic gas composition was fixed to 70% H_2O and 30% N_2, and the flow rate was varied depending on the current density so that 50% of the supplied steam was electrolyzed at the anode.

Figure 2-24a shows the calculated cell voltage E and thermoneutral voltage E_{TN} of the SAEC for the methanol production at 180°C, 10 atm. E and E_{TN} of a SAEC for the hydrogen production (cathode

gas was changed to 0.518 μmol s^{-1} of nitrogen) are also shown for comparison. The thermoneutral voltage was calculated according to Eq. 2-91. E and E_{TN} in the CH_3OH-producing SAEC and the H_2-producing SAEC are almost the same. This means that the enthalpy change caused by the internal CO_2-to-methanol reaction was quite small. Figure 2-24b compares the system energy losses. heat loss in the two operation modes (denoted as A and B) were obtained according to Eq. 2-92. The case was simulated where a catalytic CO_2-to-methanol reactor is connected downstream of the H_2-producing SAEC. The CO_2-to-methanol reaction heat was estimated as

$$(CO_2\text{-to-methanol heat}) = I\left(E_{TN,H_2} - E_{TN,CH_3OH}\right) = \Delta H_{H_2} - \Delta H_{CH_3OH} \quad (2\text{-}97)$$

The dotted line in Figure 2-24b (denoted as C) indicates the sum of the heat loss in the H_2-producing SAEC and the CO_2-to-methanol heat. The three lines A, B, and C are almost identical. This means that, from the thermodynamic viewpoint, reduction of the energy loss is not expected in the CH_3OH-producing SAEC under the simulated conditions.

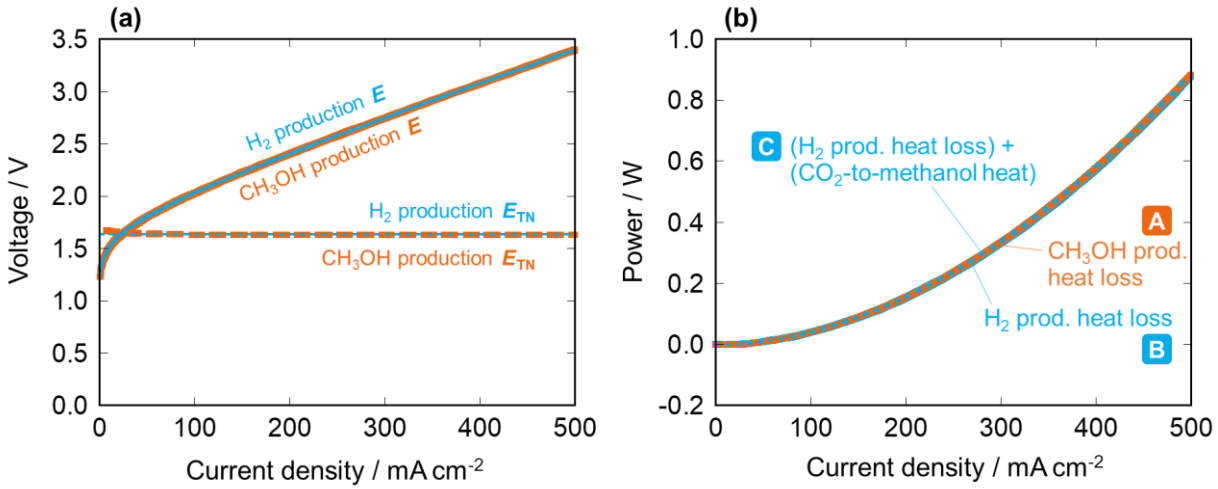

Figure 2-24. (a) Cell voltages and thermoneutral voltages of SAECs for the methanol production and the hydrogen production at 180°C, 10 atm. (b) Comparison of system energy losses. [A] heat loss in the CH_3OH-producing SAEC. [B] heat loss in the H_2-producing SAEC. [C] Sum of the heat loss in the H_2-producing SAEC and the CO_2-to-methanol reaction heat.

2.2.5. Summary

In Section 2.2, simulations were performed to examine the characteristics of SAECs for the production of methane and methanol. It was confirmed that the methane formation is highly favored from the thermodynamic viewpoint. Comparing the hydrogen production and the methane production, the cell voltage will become smaller in the latter case. The direct methane synthesis in SAECs can serve as a more energy-efficient PtM system than the two-step PtM which consists of a H_2-producing SAEC and a methanation unit. For the methanol synthesis, low temperatures and high pressures are desired. Suppression of the CO formation in the cathode will be a key to the development of SAECs for methanol synthesis. It should also be noted that electrochemical reaction pathways will not follow the present simulations based on the thermodynamic equilibrium. If CO_2 conversion proceeds with charge transfer (*i.e.* protons and electrons directly react with CO_2), methanol production rates higher than the maximum rate predicted by thermodynamics could be achieved.

Chapter 3

Development of Solid Acid Electrolysis Cells

CO_2 electrolysis at intermediate temperatures is expected as a potential technology for the production of hydrocarbons and oxygenates because high reaction rate and high selectivity to the desired products may be achieved simultaneously. The simulations in Section 2.2 showed that solid acid electrolysis cells (SAECs) are applicable to the direct synthesis of methane and methanol. However, experimental attempts for the realization of CO_2 conversion in SAECs have rarely been reported. This chapter addresses the development of SAECs for steam electrolysis and the application of the steam electrolysis technology to the CO_2 conversion.

3.1. Hydrogen Production by Steam Electrolysis

3.1.1. Objective

As mentioned in Section 1.2.6, the application of solid acid electrolytes to fuel cells are widely studied. On the other hand, the application to electrolysis cells has not been studied in detail so far. As the number of reports is limited, characteristics of solid acid electrolysis cells (SAECs) are not fully understood. Fundamental research is still required even for steam electrolysis, the most typical electrolysis reaction. Quantification of hydrogen is necessary to evaluate the current efficiency. Major stability issues should be specified and solved before trying to improve the current-voltage performance.

This time I developed SAECs for steam electrolysis and quantified the produced hydrogen by using an on-line gas chromatograph. A proton-conducting phosphate composite, CsH_2PO_4/SiP_2O_7, was used as an electrolyte. It is known that CsH_2PO_4 and SiP_2O_7 react at their interface to form $CsH_5(PO_4)_2$ under hydrothermal conditions (Eq. 3-1)[177,181].

$2CsH_2PO_4 + SiP_2O_7 + 3H_2O \rightarrow 2CsH_5(PO_4)_2 + SiO_2$ (3-1)

The formation of $CsH_5(PO_4)_2$ prevents a conductivity jump inherent in CsH_2PO_4 and provides high conductivity (*ca.* 10^{-2}-10^{-1} S cm^{-1}) in a wide temperature range from 150°C to 280°C. Pt/C (platinum nanoparticles supported on carbon) was used as electrocatalysts of both the anode and the cathode. Pt is a common electrode material of solid acid fuel cells[46,60,182] and is also used for SAEC electrodes[68,183,184]. The electron-conductive carbon support provides high dispersion of Pt, which allows us to decrease the amount of Pt. However, at the same time, carbon is subject to oxidation under polarized conditions and may cause performance degradation[185,186]. Thus, the performance of SAECs was examined paying attention to the stability of the electrodes, as well as the electrolyte.

In the present work, factors affecting the cell stability were investigated in detail for the first time. Based on the investigations of the Pt/C|CsH_2PO_4/SiP_2O_7|Pt/C cell, Pt mesh was also tested as an anode aiming at improved stability. This study addresses the primary aspects of the steam electrolysis using SAECs and enumerates the essential points which should be cared, providing insight into the future development of SAEC technology.

3.1.2. Experimental

3.1.2.1. Preparation of an electrolysis cell

Cesium dihydrogen phosphate (CsH_2PO_4) was prepared by dissolving stoichiometric amounts of Cs_2CO_3 (Wako Pure Chemical Industries) and H_3PO_4 (Sigma Aldrich, 85wt% in water) in distilled water and drying the solution (at 100°C for 24 h, at 120°C for 15 h). Silicon pyrophosphate (SiP_2O_7) was synthesized as follows. First, SiO_2 (Wako Pure Chemical Industries) and H_3PO_4 were mixed at a molar ratio of 1:2.5. The resultant sample was dried successively at 200°C for 3 h, at 100°C for 24 h and at 120°C for 24 h. Finally, the sample was calcined at 700°C for 3 h to obtain SiP_2O_7. The synthesized materials were mixed in a mortar for 15 min. The molar ratio was CsH_2PO_4:SiP_2O_7 = 1:2. To fabricate an electrolysis cell, 0.44 g of the obtained CsH_2PO_4/SiP_2O_7 composite and ϕ10 Pt/C sheets (Miclab, Pt loading 1.0 mg cm^{-2}) were co-pressed in a ϕ20 uniaxial die at 20 MPa for 10 min. The Pt/C electrode sheet consisted of a carbon

paper and a Pt/C catalyst layer fabricated on one side of the carbon paper. The sheets were placed so that the Pt/C catalyst layer was in contact with the CsH_2PO_4/SiP_2O_7 electrolyte. For the Pt/C|CsH_2PO_4/SiP_2O_7|Pt/C symmetrical cell, the electrolyte composite was sandwiched between two Pt/C sheets. For the Pt(mesh)|CsH_2PO_4/SiP_2O_7|Pt/C cell, only the Pt/C cathode was co-pressed. The Pt mesh anode was attached later in assembling the reactor.

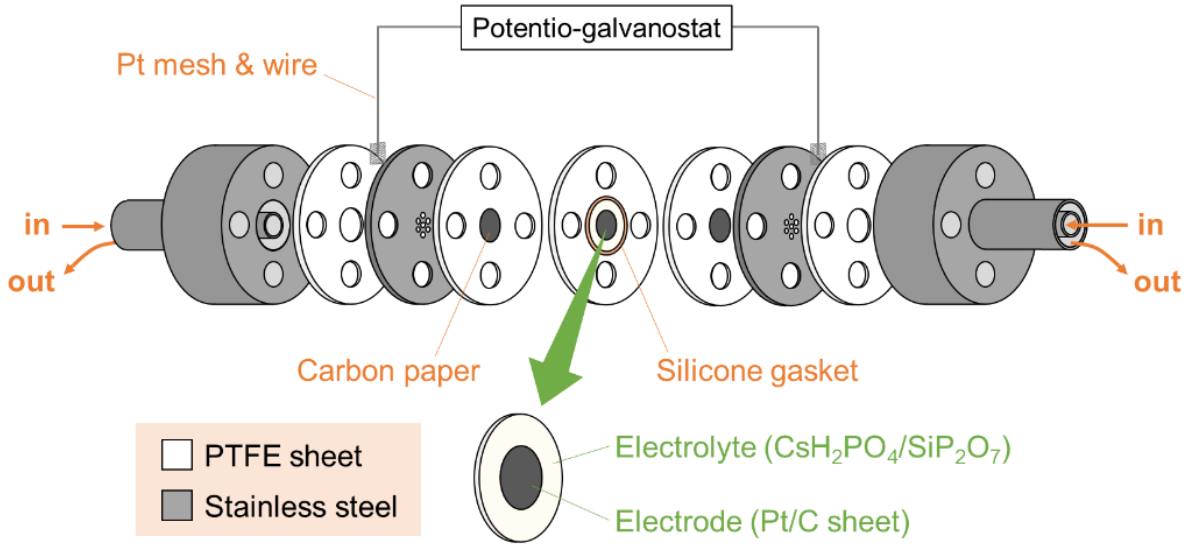

Figure 3-1. Schematic image of the reactor setup for the Pt/C|CsH_2PO_4/SiP_2O_7|Pt/C cell.

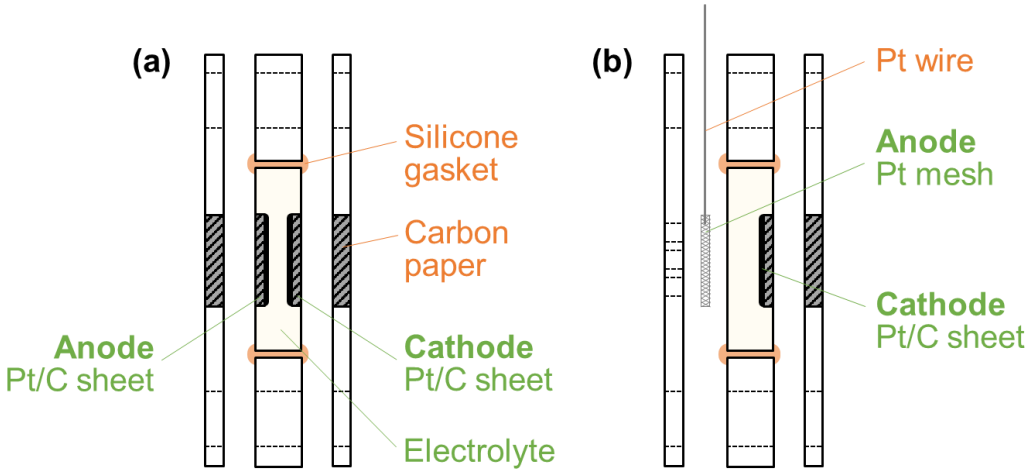

Figure 3-2. Cross-sectional schematic images around the SAECs. (a) Pt/C|CsH_2PO_4/SiP_2O_7|Pt/C symmetrical cell. (b) Pt(mesh)|CsH_2PO_4/SiP_2O_7|Pt/C cell.

3.1.2.2. Steam electrolysis tests

Figure 3-1 illustrates the reactor setup for the Pt/C|CsH_2PO_4/SiP_2O_7|Pt/C cell. A cross-sectional schematic image around the cell is shown in Figure 3-2a. The cell was fitted into a polytetrafluoroethylene (PTFE) sheet. Silicone gasket was used to fill the gaps between the cell and the PTFE sheet. Current was collected through carbon papers, stainless steel plates, Pt mesh, and Pt wires. The parts shown in Figure 3-1 were screwed up and mounted in a furnace. For the Pt(mesh)|CsH_2PO_4/SiP_2O_7|Pt/C cell, a ϕ10 Pt mesh (Nilaco, 100 mesh, 70 μm-thick) was attached to the cell (Figure 3-2b). In this case, current was directly collected from the Pt mesh anode by using Pt wire. Dry argon was introduced to both sides of the cell, and temperature was raised from the room temperature to 220°C at a rate of 200°C h^{-1}. Once the temperature reached 120°C, the electrode gas flows were humidified with distilled water using a liquid delivery pump (LC-20AD, Shimadzu) and a homemade vaporizer. Before conducting steam electrolysis at designated temperatures, both electrodes were reduced by a humidified hydrogen flow (H_2 35 mL min^{-1}, H_2O 7.5 mL min^{-1}) at 220°C for 1 h.

Steam electrolysis was performed at designated temperatures by introducing a 30%-humidified argon flow (Ar 17.5 mL min^{-1}, H_2O 7.5 mL min^{-1}) to both electrodes. Electrochemical measurements were conducted by two-terminal method using a potentio-galvanostat (SP-300, Bio-Logic). Current and cell voltage were monitored between the working electrode (WE) and the counter electrode (CE). The outlet gas from the WE was first dehumidified by a cold trap and then analyzed by an on-line gas chromatograph (CP-4900, Varian). As illustrated in Figure 3-3, two operation modes were used. One is a standard operation mode where the WE was cathodically polarized (Figure 3-3a). In this case, cathode outlet gas was analyzed. The other is an inverse operation mode where the WE was anodically polarized (Figure 3-3b). In this case, anode outlet gas was monitored.

Faraday efficiency for hydrogen production in the cathode was calculated based on gas compositions measured under an open circuit condition (before applying current) and a galvanostatic condition:

$$\eta_{H_2} = 2F\Delta\dot{n}_{H_2}/iS \quad (3\text{-}2)$$

F, *i*, and *S* are the Faraday constant, the current density, and the electrode area (0.785 cm^2), respectively.

$\Delta\dot{n}_{H_2}$ is an increment in the hydrogen molar flow rate caused by the polarization. In the anode, oxygen production was expected. However, as described in the following sections, a significant amount of CO_2 was detected in the anode outlet gas of the Pt/C|CsH_2PO_4/SiP_2O_7|Pt/C cell. A small amount of CO was also detected. Nominal Faraday efficiencies for the formation of CO_2 and CO in the anode were calculated as

$$\eta_{CO_2} = 4F\Delta\dot{n}_{CO_2}/iS \quad (3\text{-}3)$$

$$\eta_{CO} = 2F\Delta\dot{n}_{CO}/iS \quad (3\text{-}4)$$

where $\Delta\dot{n}_{CO_2}$ and $\Delta\dot{n}_{CO}$ are increments in the molar flow rates of CO_2 and CO, respectively.

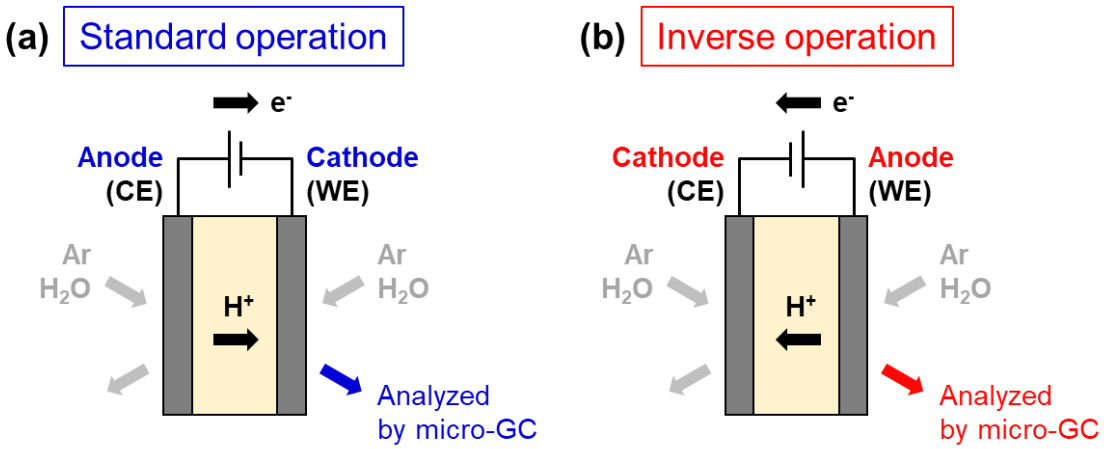

Figure 3-3. Two operation modes tested in this study. (a) Standard operation. (b) Inverse operation.

3.1.2.3. Characterization

Impedance measurements of the electrolysis cell were conducted at 220°C under open circuit conditions by two-terminal method. The frequency of alternate current (AC) was swept from 10^6 Hz to 0.05 Hz. The amplitude (root mean square value) of the AC signal was 10 mV.

X-ray diffraction (XRD) measurements were conducted for synthesized electrolyte materials (CsH_2PO_4 and SiP_2O_7) using a diffractometer (RINT 2400, Rigaku). The electrolyte after a long-term galvanostatic test at 220°C was also characterized with another diffractometer (SmartLab, Rigaku).

Cross sections of the cells before and after long-term galvanostatic tests were examined by a scanning

electron microscope (SEM, S-4700, Hitachi) equipped with an energy dispersive X-ray spectroscopy (EDX) detector (Super Xerophy, Horiba).

3.1.3. Results and discussion

3.1.3.1. Hydrogen production performance of the Pt/C|CsH_2PO_4/SiP_2O_7|Pt/C cell

To demonstrate the hydrogen production performance of the Pt/C|CsH_2PO_4/SiP_2O_7|Pt/C symmetrical cell, galvanostatic tests were conducted at 220°C by loading different current densities. Current density was changed in the following order: 10 → 25 → 50 → 75 → 100 → 10 mA cm^{-2}. These measurements were conducted in the standard operation mode (Figure 3-3a), and the cathode outlet gas was analyzed. Each current density was kept for about 30 min to achieve constant gas compositions. Figure 3-4a shows hydrogen production rates and corresponding Faraday efficiencies. The result of the repeated 10 mA cm^{-2} test is shown by open symbols. The hydrogen production rates increased almost linearly with the current density, and the Faraday efficiencies reached around 80%. Because hydrogen was the only detectable product in the cathode, it is unlikely that reactions other than the hydrogen evolution reaction (Eq. 3-5) occurred.

$$2H^+ + 2e^- \rightarrow H_2 \quad (3\text{-}5)$$

Accordingly, the Faraday efficiencies smaller than 100% may be ascribed to leakage of the produced hydrogen from the cathode chamber to the anode chamber or to the outside of the reactor. The hydrogen production rate recorded in the repeated 10 mA cm^{-2} operation was slightly higher than that of the initial operation, indicating that the gas tightness of the reactor was not significantly changed during the tests. Figure 3-4b shows the average cell voltage at each current density. Data obtained from 500 s to 1000 s in each measurement were averaged. Larger current densities resulted in lower cell potentials. In the repeated 10 mA cm^{-2} test, the average cell voltage decreased significantly compared to the initial voltage. This means that required overpotential was increased, suggesting the deterioration of the cell during the tests.

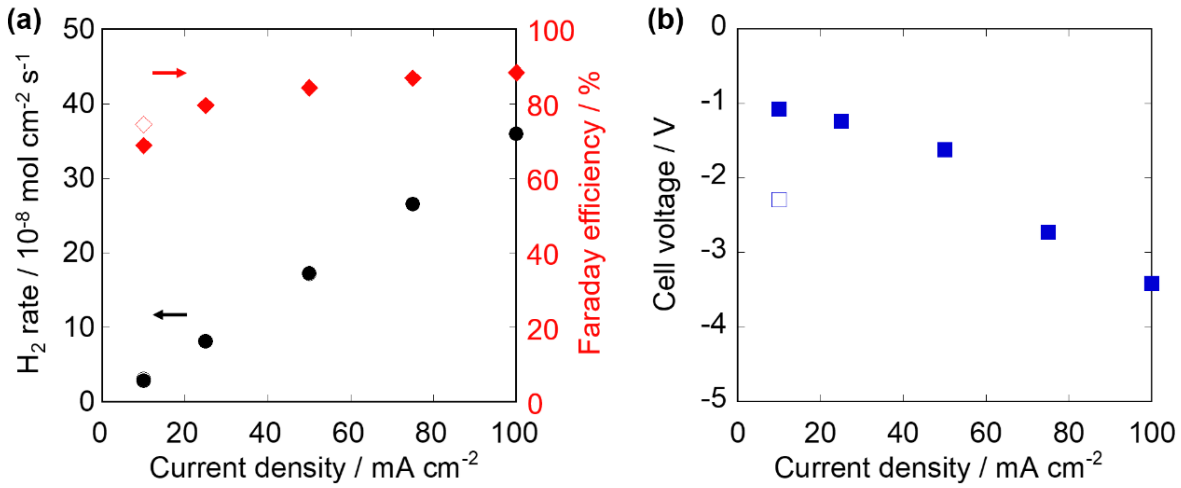

Figure 3-4. Galvanostatic tests at 220°C using the Pt/C|CsH_2PO_4/SiP_2O_7|Pt/C cell. (a) Hydrogen production rates and corresponding Faraday efficiencies at different current densities. (b) Average cell voltages at each current density. Current density was changed in the following order: 10 → 25 → 50 → 75 → 100 → 10 mA cm^{-2}. The result of the repeated 10 mA cm^{-2} test is shown by open symbols.

Long-term galvanostatic tests at different temperatures were conducted to examine the stability of the Pt/C|CsH_2PO_4/SiP_2O_7|Pt/C cell. The tests were done in the standard operation mode (Figure 3-3a). Current density was set to 10 mA cm^{-2}, and the cell voltage and the cathode outlet gas compositions were monitored. Figure 3-5a shows the cell voltage as functions of time, and Figure 3-5b shows the corresponding Faraday efficiencies for hydrogen production in the cathode. At 220°C and 180°C, the cell voltage decreased drastically at around 8.8 h and 5.1 h, respectively, and the galnvanostatic operation was no longer possible. At 160°C, the cell was continuously operated for 50 h. The fatal decrease in the cell voltage was not observed. The behavior of the cell voltage from 0 h to 4 h was almost the same at every temperature. It is suggested that the first voltage plateau is the region where the SAECs were operated properly. Cell voltage lower than -2 V indicates that the cell was deteriorated. Calculated Faraday efficiencies were near 80% regardless of the opetating temperature and the cell voltage. The nearly constant Faraday efficiencies demonstrate the potential of SAECs for continuous hydrogen production.

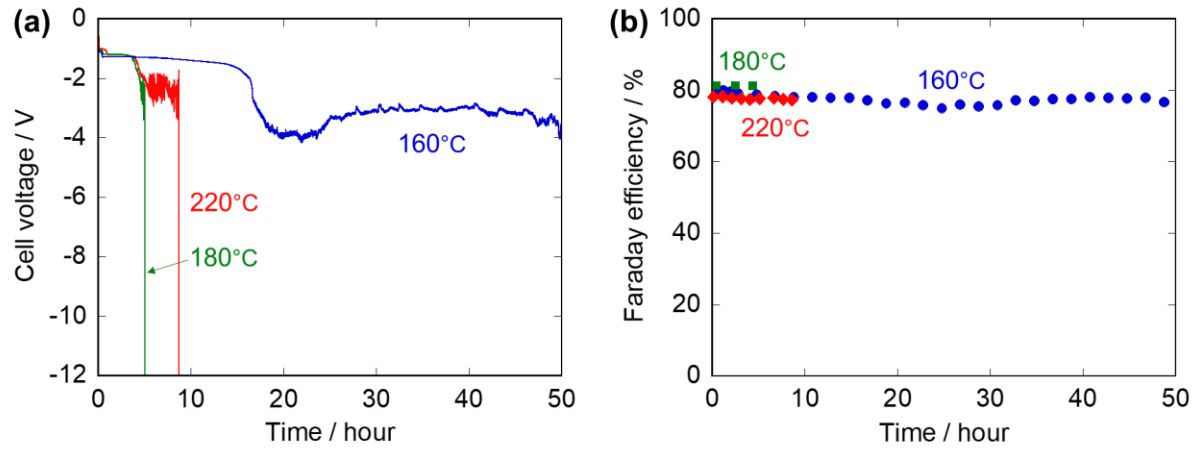

Figure 3-5. Stability tests at different temperatures using the Pt/C|CsH_2PO_4/SiP_2O_7|Pt/C cell. Current density was kept at 10 mA cm^{-2}. (a) Cell voltages as functions of time. (b) Corresponding Faraday efficiencies for the hydrogen production.

3.1.3.2. Investigations of the stability of the Pt/C|CsH_2PO_4/SiP_2O_7|Pt/C cell

For the realization of stable operation, it is essential to elucidate the causes of the cell degradation. The following part is devoted to discussions about the factors affecting the stability of the Pt/C|CsH_2PO_4/SiP_2O_7|Pt/C cell.

3.1.3.2.1. Impedance analysis

Figure 3-6 shows the impedance spectra recorded before and after the stability test at 220°C using the Pt/C|CsH_2PO_4/SiP_2O_7|Pt/C cell. The *x*-intercept in each spectrum corresponds to the ohmic resistance, which reflects the proton conductivity of the electrolyte and the electron conductivity of the electrodes. The size of the semiarcs represents the non-ohmic resistance originating from the physicochemical processes in both electrodes: charge transfer reactions and gas diffusion. The ohmic resistance was increased from *ca.* 2 Ω cm^2 to *ca.* 4 Ω cm^2, but the increase was less significant compared to the remarkable increase in the non-ohmic resistance. This result indicates that the electrode processes were mainly responsible for the cell degradation.

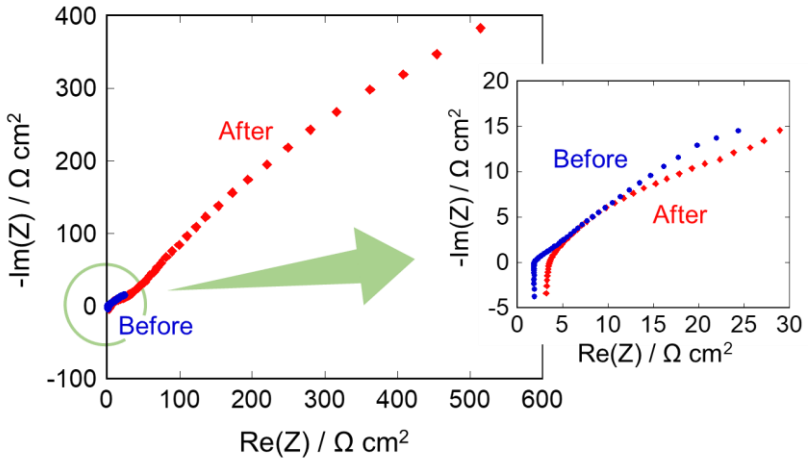

Figure 3-6. Impedance spectra measured before and after the stability test at 220°C using the Pt/C|CsH_2PO_4/SiP_2O_7|Pt/C cell. The impedance measurements were done under open circuit conditions.

To identify the frequency range where impedance was significantly increased, analysis with a $\Delta\dot{Z}'$ spectrum[187] was conducted. In this method, the change of the impedance is characterized by the following indicator:

$$\Delta\dot{Z}(\omega) = \frac{\partial Z(\omega)}{\partial \ln \omega}\Big|_{\mathrm{B}} - \frac{\partial Z(\omega)}{\partial \ln \omega}\Big|_{\mathrm{A}} \tag{3-6}$$

where Z is the impedance and ω is the angular frequency of the AC signal. Subscripts A and B represent the different cell conditions. In the present case, A and B correspond to the measurements before and after the stability test at 220°C, respectively. Practically, $\Delta\dot{Z}'(\omega_{\mathrm{n}})$ defined as Eq. 8 is used instead of $\Delta\dot{Z}(\omega)$.

$$\Delta\dot{Z}'(\omega_{\mathrm{n}}) = \frac{[Z'_{\mathrm{B}}(\omega_{\mathrm{n+1}}) - Z'_{\mathrm{B}}(\omega_{\mathrm{n-1}})] - [Z'_{\mathrm{A}}(\omega_{\mathrm{n+1}}) - Z'_{\mathrm{A}}(\omega_{\mathrm{n-1}})]}{\ln \omega_{\mathrm{n+1}} - \ln \omega_{\mathrm{n-1}}} \tag{3-7}$$

Here Z' indicates the real part of Z, and ω_{n} is the angular frequency of each data point. Units of Z and ω_{n} are Ω cm^2 and rad s^{-1}, respectively. The moving average of $\Delta\dot{Z}'(\omega_{\mathrm{n}})$ at $\omega_{\mathrm{n-1}}$, ω_{n}, and $\omega_{\mathrm{n+1}}$ is taken to reduce the effect of noise. Figure 3-7 is the obtained $\Delta\dot{Z}'$ spectrum where the averaged $\Delta\dot{Z}'(\omega_{\mathrm{n}})$ values are plotted against the frequency. It is clear that $\Delta\dot{Z}'(\omega_{\mathrm{n}})$ decreased notably at low frequencies (< 1 Hz). This means that the cell impedance of this frequency range increased significantly during the stability test. Impedance at low frequencies is often associated with the mass transfer processes[188]. Therefore, it is suggested that the performance deterioration of the SAECs was related to gas diffusion properties in the electrodes.

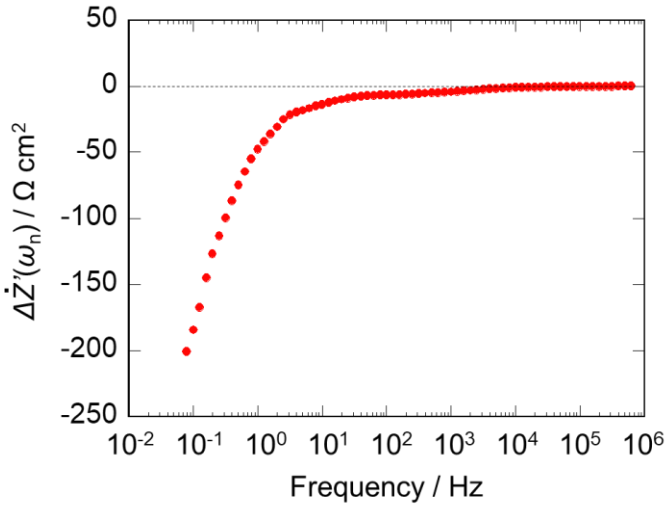

Figure 3-7. $\Delta\dot{Z}'$ spectrum obtained from the impedance of the Pt/C|CsH_2PO_4/SiP_2O_7|Pt/C cell before and after the stability test at 220°C.

3.1.3.2.2. XRD measurements

Figure 3-8 shows the XRD patterns of the electrolyte materials. Figure 3-8a is the pattern of as-prepared CsH_2PO_4. Almost all peaks were attributed to the monoclinic structure of CsH_2PO_4, indicating the successful preparation. Figure 3-8b is the pattern of as-prepared SiP_2O_7. Observed peaks indicate that the sample was a mixture of tetragonal, monoclinic, and hexagonal phases of SiP_2O_7. This result is consistent with our previous work[189]. Formation of impurity phases were not indicated. Figure 3-8c is the XRD pattern of the CsH_2PO_4/SiP_2O_7 electrolyte composite after the stability test at 220°C. Peaks in the pattern were assigned to $CsH_5(PO_4)_2$ and SiP_2O_7. Peaks corresponding to CsH_2PO_4 were not observed. The present result agrees well with the previous studies reporting the interfacial reaction of CsH_2PO_4 and SiP_2O_7 to form $CsH_5(PO_4)_2$[177,181]. It is recognized that one of the major problems of the solid phosphate electrolytes is the decrease in their proton conductivity caused by the dehydration of the phosphates. If CsH_2PO_4 is dehydrated, pyrophosphates or phosphites such as $Cs_2H_2P_2O_7$ or $CsPO_3$ will be formed[38,39]. However, no peaks were assigned to such dehydrated compounds in the present case, supporting the idea that the ohmic processes are not the main factor of the cell degradation.

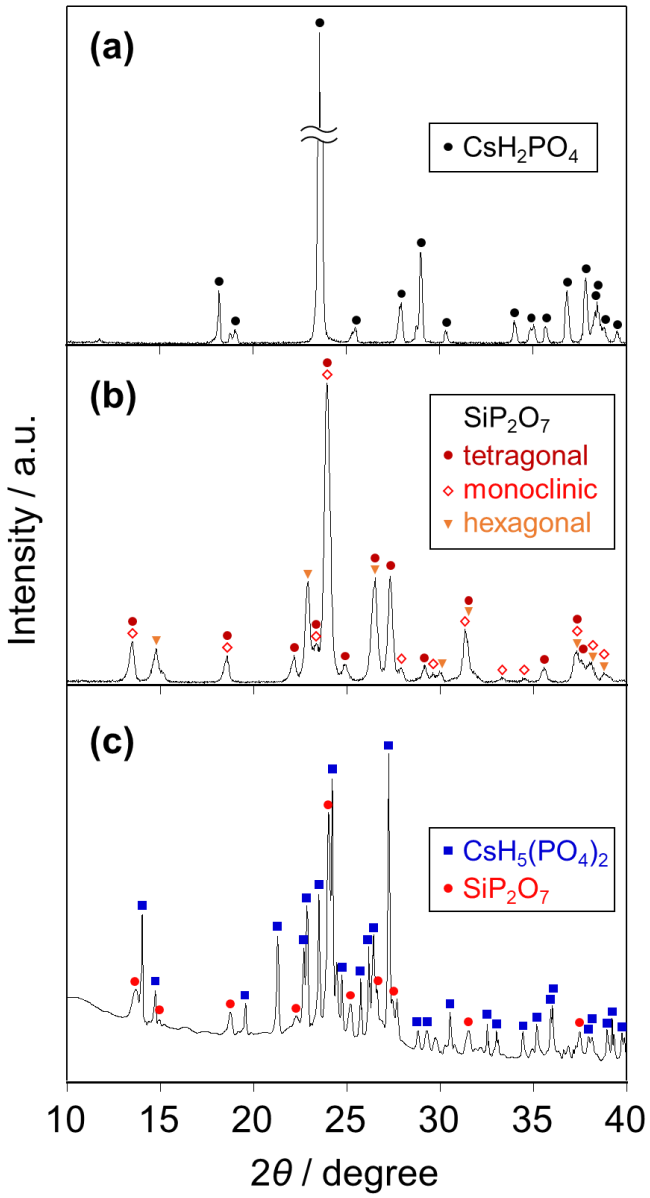

Figure 3-8. XRD patterns of (a) as prepared CsH_2PO_4, (b) as prepared SiP_2O_7, and (c) CsH_2PO_4/SiP_2O_7 electrolyte after the stability test at 220°C.

3.1.3.2.3. SEM-EDX measurements

Figure 3-9 shows the results of the cross-sectional SEM-EDX measurements of Pt/C electrodes. Before the stability test (Figure 3-9a), a porous electrode layer and a dense electrolyte layer were observed. Phosphorus, cerium, and oxygen were detected only from the electrolyte layer. The signal of carbon came from the carbon paper and the carbon support of the Pt/C catalyst, showing the position of the electrode layer. After the stability test at 220°C, phosphorus, cerium, and oxygen were detected not only from the

electrolyte but also from the anode layer (Figure 3-9b). Distribution of these elements were almost identical, suggesting the existence of the electrolyte material. In a magnified SEM image of the anode shown at the far right, particles with a size of 5-20 μm were observed in the porous structure of the carbon paper (marked with arrows). These particles were not found in the electrode before the test. Existence of the electrolyte material was not indicated in the cathode layer (Figure 3-9c). Correspondingly, no distinctive particles were found in a magnified image of the cathode after the test.

Based on these observations, it is considered that a part of the electrolyte was migrated exclusively to the anode layer during the test. Migration of phosphoric acid (PA) from the electrolyte layer to the anode layer is recognized in phosphoric acid fuel cells (PAFCs) and high-temperature PEM fuel cells (HT-PEMFCs)[190,191]. In PAFCs, PA electrolyte is retained matrices typically made of silicon carbide[192]. In HT-PEMFCs, PA is impregnated to polymer membranes and serves as a proton conductor. In the latter case some PA molecules are bound to the membrane but a majority of PA can move freely[191]. PA in these fuel cells can migrate to the anode by electrochemical pumping[190,191]. This is explained by a finite transport number of hydrogen phosphate anions. While the dominant charge carrier is protons, part of the current is carried by hydrogen phosphate anions. The charge of hydrogen phosphate anions should be balanced in the anode, leading to the migration of PA. The movement of PA reaches a steady state when the electrochemical pumping balances the back diffusion induced by the PA concentration gradient and/or hydraulic pressure. In the present case, $CsH_5(PO_4)_2$ was formed in the electrolyte. Pure $CsH_5(PO_4)_2$ has a melting point around 155°C, and the melting point can be lowered by the existence of the matrices[40,41,181]. Therefore, the $CsH_5(PO_4)_2$ phase formed during the electrolysis test at 220°C must have been in a viscous liquid form. Although most of the liquid $CsH_5(PO_4)_2$ was held in the SiP_2O_7 matrix, a certain part of the $CsH_5(PO_4)_2$ could have migrated into the porous structure of the anode. Moreover, it is reported that $CsH_5(PO_4)_2/SiP_2O_7$ composite can adsorb water under hydrothermal conditions[189]. If the liquid $CsH_5(PO_4)_2$ phase is mixed with the adsorbed water at 220°C and become a solution, its susceptibility to the migration will increase even more. It was also possible that PA, which can migrate, was formed from SiP_2O_7 and steam according to the following equilibrium:

$$SiP_2O_7 + 3H_2O \leftrightarrow SiO_2 + 2H_3PO_4 \quad (3\text{-}8)$$

The migrated electrolyte components were cooled and solidified to form the particles observed in Figure 3-9b. Figure 3-9d and e show the SEM-EDX results of the anode and the cathode after the stability test at 160°C, respectively. The trends are the same as the results after the stability test at 220°C (Figure 3-9b and c), indicating that the migration of the electrolyte to the anode took place at 160°C, too.

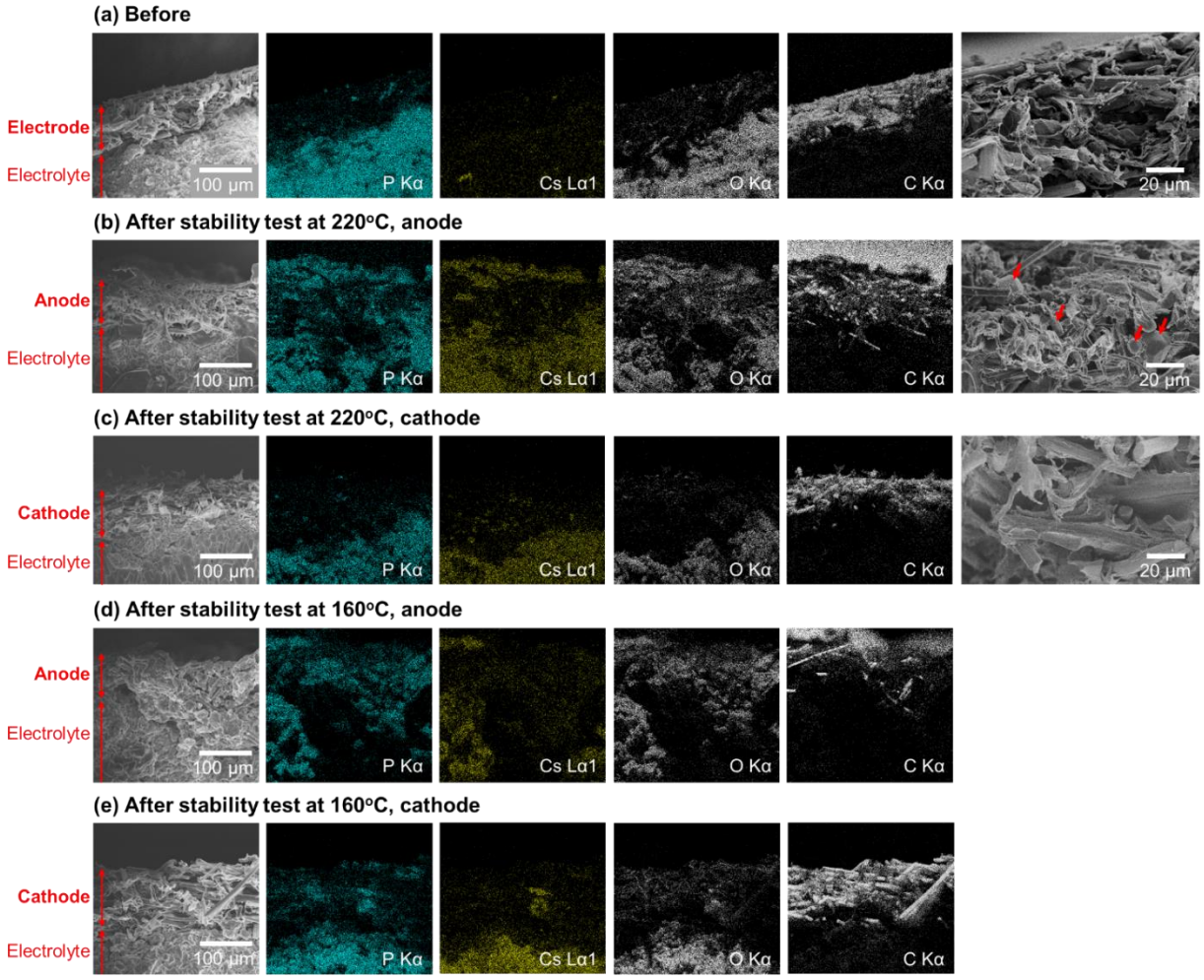

Figure 3-9. Cross-sectional SEM images and corresponding EDX elemental mappings of P, Cs, O, and C. (a) A Pt/C electrode just after the cell fabrication. (b) and (c) The Pt/C anode and the Pt/C cathode after the stability test at 220°C, respectively. (d) and (e) The Pt/C anode and the Pt/C cathode after the stability test at 160°C, respectively. For (a), (b), and (c), magnified SEM images of the electrode layer are also shown at the far right. Note that strong C Kα signal observed in uppermost parts of C-mappings in (b) and (d) can be ascribed to carbon paste and carbon tape used for fixing the samples to the holder.

3.1.3.2.4. Effects of the electrolyte migration

The migration of the electrolyte can facilitate the formation of electrochemical reaction sites (triple-phase boundaries of the electrolyte, the Pt/C catalyst, and the gas phase)[46,193]. However, excessive migration may lead to the performance degradation of the anode. Since the Pt/C catalyst is located nearest to the bulk electrolyte, the catalyst was prone to be soaked with the liquified electrolyte materials. The Pt/C surface covered by the electrolyte could become electrochemically inactive. It may be possible that water dissolved in the viscous electrolyte serves as a reactant instead of steam in the gas phase. However, even if that is the case, the anode performance will be deteriorated severely because molecular diffusion in a liquid phase is several orders of magnitude slower than that in a gas phase. Remember that phosphorus, cerium, and oxygen elements were distributed throughout the carbon paper layer after the stability test at 220°C (Figure 3-9b). This means that the electrolyte migrated beyond the Pt/C catalyst layer and penetrated into the carbon paper. The clogging of the pores in the carbon paper may have prevented the gas diffusion to the reaction sites. This finding is consistent with the result of the impedance analysis, which suggested the suppression of gas diffusion.

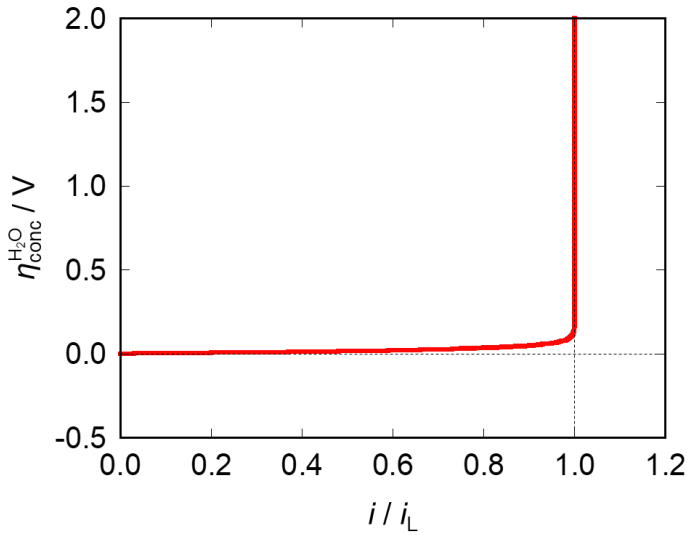

Figure 3-10. The relationship between $\eta_{\mathrm{conc}}^{\mathrm{H_2O}}$ and i/i_{L} calculated by Eq. 3-9.

In the following, the relationship between the electrolyte migration and the increase of overpotentials is discussed in detail. Generally, overpotential of an electrochemical cell can be divided into three parts: ohmic, activation, and concentration overpotentials. The effect of the mass transfer in electrodes on the cell voltage can be understood as concentration overpotential. Sluggish gas diffusion in electrode layers leads to the depletion of reactants and the accumulation of products around the reaction sites, which increases the concentration overpotential. In the SAEC anode, diffusion of steam from the bulk gas phase to the reaction sites (Pt/C catalyst surface) plays an important role. The change in Nernst potential caused by the diffusion of steam in the anode layer, which is a component of the concentration overpotential, can be formulated as follows (for details of the derivation, see Appendix D):

$$\eta_{\mathrm{conc}}^{\mathrm{H_2O}} = \frac{RT}{2F}\ln\left(\frac{1}{1-i/i_{\mathrm{L}}}\right) \tag{3-9}$$

R, T, and i_{L} are the molar gas constant, the temperature, and the limiting current density, respectively. i_{L} sets the upper limit of the current density and is defined as

$$i_{\mathrm{L}} = \frac{2FD_{\mathrm{H_2O}}^{\mathrm{eff}}}{RT}\frac{p_{\mathrm{H_2O}}^{\mathrm{a}}}{\delta_{\mathrm{a}}} \tag{3-10}$$

where $D_{\mathrm{H_2O}}^{\mathrm{eff}}$, $p_{\mathrm{H_2O}}^{\mathrm{a}}$, and δ_{a} are the effective diffusion coefficient of steam, the steam partial pressure in the anode bulk gas, and the thickness of the anode. Note that the electrolyte migration can proceed ununiformly. Actual diffusion coefficients may vary depending on the location in the anode layer. When the anode porous structure is clogged by the migrated electrolyte, the porosity decreases, and the tortuosity increases. Consequently, $D_{\mathrm{H_2O}}^{\mathrm{eff}}$ decreases and i_{L} becomes smaller (Eq. 3-10). At the same time, the flooding of the Pt/C catalyst by the electrolyte decreases the number of electrochemically active sites. Under the constant current load of 10 mA cm^{-2}, local current densities at each remaining active site might increase. The decrease in i_{L} and the increase in local current density, i, both contribute to the increase in $\eta_{\mathrm{conc}}^{\mathrm{H_2O}}$ (Eq. 3-9). As shown in Figure 3-10, $\eta_{\mathrm{conc}}^{\mathrm{H_2O}}$ diverges to infinity when i/i_{L} goes to unity. $i/i_{\mathrm{L}} = 1$ corresponds to a situation where steam is depleted at the reaction sites, and the local current density cannot increase any more. If, even for a very short time, i/i_{L} reaches unity locally, $\eta_{\mathrm{conc}}^{\mathrm{H_2O}}$ will increase steeply. This feature of the concentration overpotential suggests that the electrolyte migration to the anode

is a possible cause of the abrupt decrease in the cell voltage at 220°C and 180°C (Figure 3-5a). Once the cell voltage becomes lower than *ca.* -13 V, the operation will be stopped according to the safety mechanism of the potentio-galvanostat. Such a situation may have happened during the stability tests at 180°C and 220°C. In HT-PEMFCs, the migration of PA is less significant at lower temperatures[191]. Likewise, it is assumed that the electrolyte migration in SAECs at 160°C is moderate compared to those at 180°C or 220°C. The catastrophic decrease of the cell voltage was avoided at 160°C possibly because the mass transfer was sustained not to exceed the criterion for steep increase in the concentration overpotential.

The activation overpotential, which reflects the electrochemical activity of the electrodes, can also be affected by the electrolyte migration. By introducing some suppositions, the activation overpotential of the anode, $\eta_{\mathrm{act}}^{\mathrm{a}}$, can be described as Eq. 3-11 (see Appendix D for details):

$$\eta_{\mathrm{act}}^{\mathrm{a}} = \frac{RT}{2F}\sinh^{-1}\left(\frac{i}{2i_0}\right) \tag{3-11}$$

i_0 is the exchange current density, which indicates the electrochemical activity of the anode per unit area. The loss of electrochemically active sites results in the decrease in i_0 and the increase in $\eta_{\mathrm{act}}^{\mathrm{a}}$. However, the increase in $\eta_{\mathrm{act}}^{\mathrm{a}}$ is not likely to be the cause of the fatal decrease in the cell voltage observed in Figure 3-5a. Based on Eq. 3-11, the relationship between $\eta_{\mathrm{act}}^{\mathrm{a}}$ and i_0 at i = 10 mA cm^{-2} was calculated and shown in Figure 3-11. According to PEM electrolysis studies, proposed i_0 values for the anode range from 10^{-10} to 10^{0} mA cm^{-2}[9,178]. Even if i_0 decreases by more than 10 orders and reaches 10^{-25} mA cm^{-2}, $\eta_{\mathrm{act}}^{\mathrm{a}}$ will increase only to 1.3 V.

The electrolyte migration can affect the ohmic overpotential as well. According to the impedance measurements, the ohmic resistance of the cell was almost doubled during the stability test at 220°C (Figure 3-6). This may be attributed to the electrolyte migration. The conductivity of the electrolyte layer might be decreased due to the loss of the proton-conducting phosphates. In addition, the electric contact between the electrolyte layer and the cathode layer might be weakened by the migration.

Recently, Christensen *et al.* developed SAECs for methane synthesis[147]. They mentioned that the

migration of the electrolyte into the electrodes was a probable cause of the performance deterioration of their SAECs. This implies that the electrolyte migration is a common phenomenon which affects the stability of SAECs. This time, the electrolyte migration was evaluated by the *post mortem* SEM-EDX analysis. Quantification and visualization of the migrated electrolyte during the operation was not achieved. Further investigations with *in operando* techniques are required for the comprehensive understanding of the phenomenon.

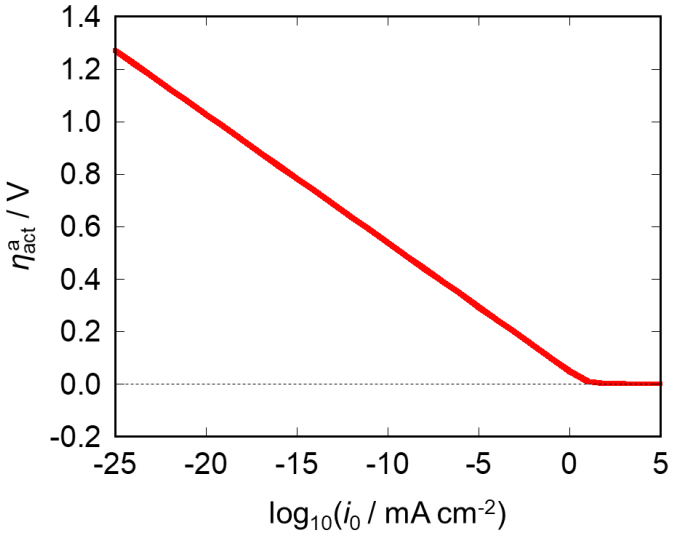

Figure 3-11. The relationship between η^{a}_{act} and i_0 at $i =$ 10 mA cm^{-2} calculated from Eq. 3-11.

3.1.3.2.5. Bidirectional electrolysis tests

To further investigate the performance degradation phenomena, electrolysis tests with bidirectional polarizations were performed at 220°C using the Pt/C|CsH_2PO_4/SiP_2O_7|Pt/C symmetrical cell. Figure 3-12a illustrates the overview of the tests. Runs C1, C2, C3, and C4 were 10 mA cm^{-2} galvanostatic measurements in the standard polarization mode (Figure 3-3a), and runs A1 and A2 were 10 mA cm^{-2} galvanostatic measurements in the inverse polarization mode (Figure 3-3b). Figure 3-12b shows the cell voltage recorded in each galvanostatic measurement. In the run C1, a stable operation continued for about 10 h. However, the cell voltage suddenly decreased, and the operation was disabled at 11.3 h. This replicates the result shown in Figure 3-5a. It is estimated that the CE was damaged as an anode due to the

electrolyte migration, while the WE was not. After an open-circuit period of *ca.* 11 h, the 10 mA cm^{-2} galvanostatic operation was conducted again (run C2). As shown in Figure 3-13, the cell voltage decreased steeply, and the operation was disabled in five seconds. This implies that the migrated electrolyte materials were still present in the CE and its performance as an anode was not recovered at all. Next, the cell was inversely polarized for 30 minutes (run A1). During the measurement, the cell voltage was stable at around 1.4 V. Then the third measurement in the standard operation mode was conducted (run C3). Being similar to the run C2, the cell voltage decreased sharply and reached the limit in 20 seconds (Figure 3-14). This indicates that the 30 minutes of cathodic polarization in the run A1 did not influence the performance of the CE as an anode. After that, the second measurement in the inverse operation mode was performed (run A2). The measurement lasted for more than 9 h and was disabled by a rapid increase in the cell voltage occurred at 9.7 h from the start. It is noteworthy that the time-course of the cell voltage in the runs A1 and A2 were almost symmetrical compared with that in the run C1. Even though the cell was already deteriorated after the standard operation of around 10 h, the same cell could be operated inversely for another 10 h. In the runs A1 and A2, the WE, which had not been deteriorated, was functioned as an anode. The reason why the CE, which had been damaged, was functioned satisfactory as a cathode is expressed as follows. The hydrogen evolution reaction at the cathode (Eq. 3-5) requires only protons and electrons and does not include gas phase reactants. Thus, the reaction can take place on the Pt surface covered by the migrated electrolyte materials, or even at the interface of the migrated electrolyte and fibers of the carbon paper. Furthermore, the product, gaseous hydrogen, is highly diffusible: the interdiffusion coefficient of hydrogen and steam at 220°C, 1 atm is about 3.5 times larger than that of oxygen and steam. The accumulation of hydrogen in the cathode is less likely to happen than the accumulation of oxygen in the anode. Finally, the fourth measurement in the standard operation mode was conducted (run C4) to reexamine the anodic performance of the CE. The operation lasted for about 12 minutes (Figure 3-15), suggesting that the backward migration of the electrolyte materials from the CE during the run A2 was not notable.

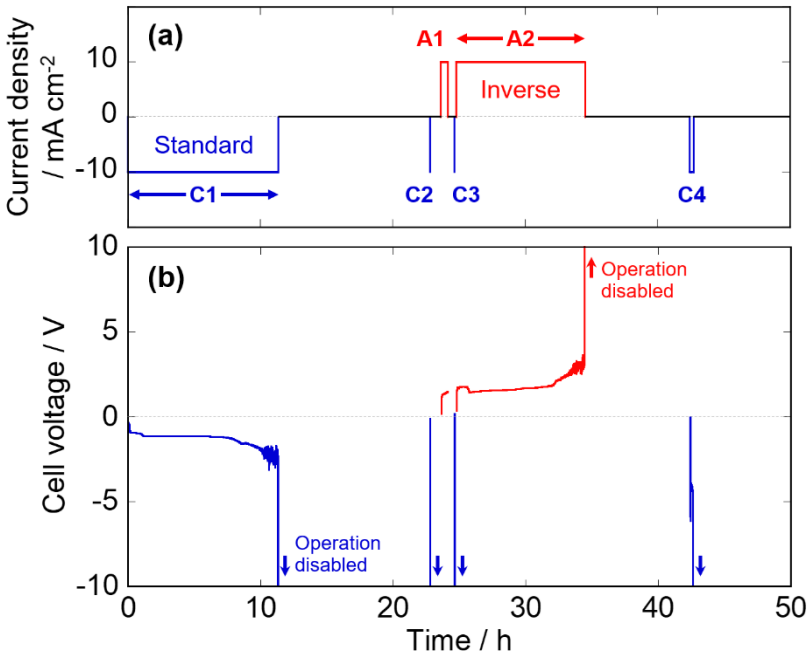

Figure 3-12. Consecutive bidirectional electrolysis tests at 220°C using the Pt/C|CsH_2PO_4/SiP_2O_7|Pt/C cell. (a) The overview of the tests. 10 mA cm^{-2} galvanostatic tests were conducted in the standard operation mode (runs C1, C2, C3, and C4) or in the inverse operation mode (runs A1 and A2). (b) The cell voltage recorded during the tests.

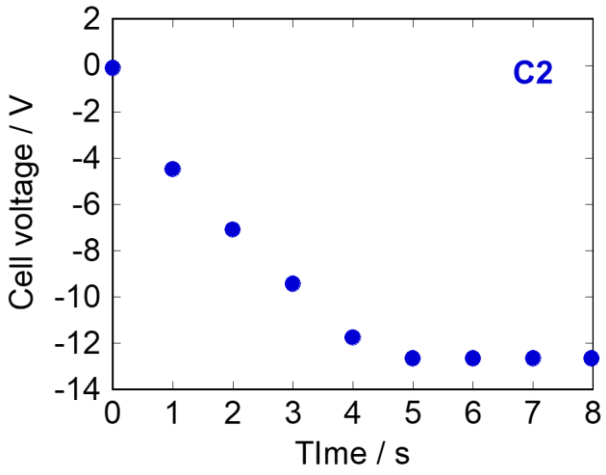

Figure 3-13. Cell voltage during the run C2 in Figure 3-12 (10 mA cm^{-2} galvanostatic measurement at 220°C). From 5 s to 8 s, the voltage was limited to protect the potentio-galvanostat, and the current density was smaller than the set value of 10 mA cm^{-2}.

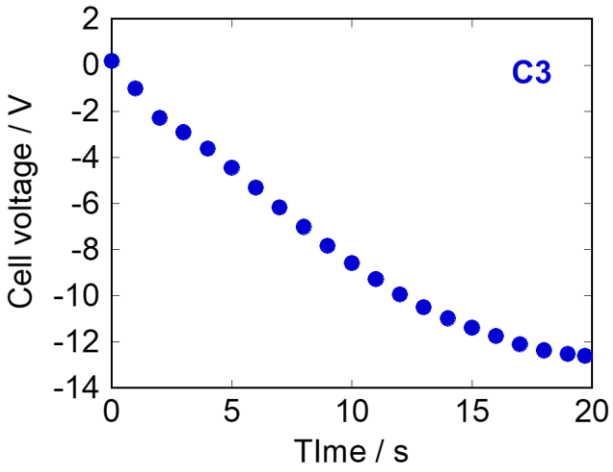

Figure 3-14. Cell voltage during the run C3 in Figure 3-12 (10 mA cm^{-2} galvanostatic measurement at 220°C).

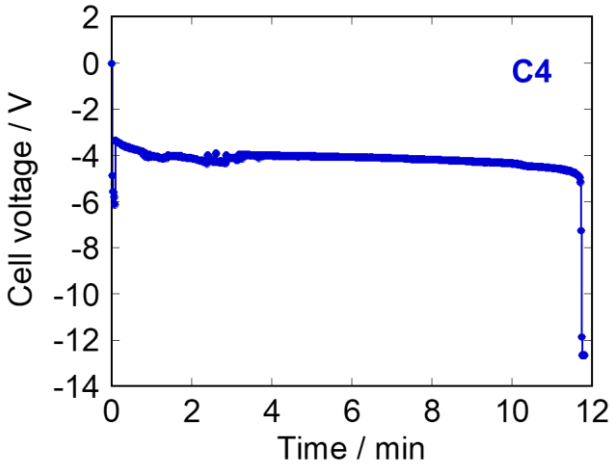

Figure 3-15. Cell voltage during the run C4 in Figure 3-12 (10 mA cm^{-2} galvanostatic measurement at 220°C).

Figure 3-16 shows the results of the gas composition analysis during the consecutive bidirectional electrolysis tests. The outlet gas flow of the working electrode was measured. In the run C1, the working electrode was the cathode. Hydrogen was detected (Figure 3-16a) and no other products were found. The Faraday efficiencies for the hydrogen production were around 80%. This shows again that most of the pumped protons were used for the hydrogen production in the cathode. The gas compositions during the runs C2, C3, and C4 were not available because those measurements were too short. In the runs A1 and A2, the working electrode was the anode, so hydrogen was not observed (Figure 3-16a). Instead, significant amounts of CO_2 were detected (Figure 3-16b). The nominal Faraday efficiencies for the CO_2

formation reached 70-80%. This suggests that most of the oxygen species generated by the steam electrolysis reaction were not combined together to form oxygen molecules but reacted with carbonaceous materials in the anode to form CO_2. Theoretical voltage required for the overall reaction of C(graphite) + $2H_2O \rightarrow CO_2 + 2H_2$ is about 0.09 V at 220°C. As the cell voltage in the runs A1 and A2 was much higher than 0.09 V, and the vicinity of the Pt/C catalyst was in an acidic environment, it is reasonable to consider that electrochemical oxidation of the carbons occurred. Because Pt nanoparticles can catalyze carbon oxidation[186], carbon sources in contact with Pt should have been oxidized preferentially. The carbon support of the Pt/C catalyst and the carbon paper adjacent to the Pt/C layer are considered susceptible to the oxidation. Small amounts of CO were also detected (Figure 3-16c), and corresponding nominal Faraday efficiencies were about 1.0-1.5%. As shown in Figure 3-16d, certain amounts of oxygen were detected even in the run C1, and the amount was almost constant throughout the tests. The oxygen might come from the outside of the reactor. The increase in the oxygen amount in the runs A1 and A2 was not prominent, supporting the consideration that most of the oxygen species formed in the anode was used for the CO_2 formation.

It is possible that the oxidation of carbon weakened the hydrophobicity of the carbon surface[185] and accelerated the migration of the electrolyte materials. Moreover, the oxidation of carbon can decrease the number of reaction sites and deteriorate the electrochemical activity of the anode. Carbon oxidation at the boundaries of Pt nanoparticles and the carbon support of the Pt/C catalyst can lead to a loss of electronic contact between the Pt and the carbons. If a Pt particle is isolated, that particle becomes inactive for the electrochemical reactions.

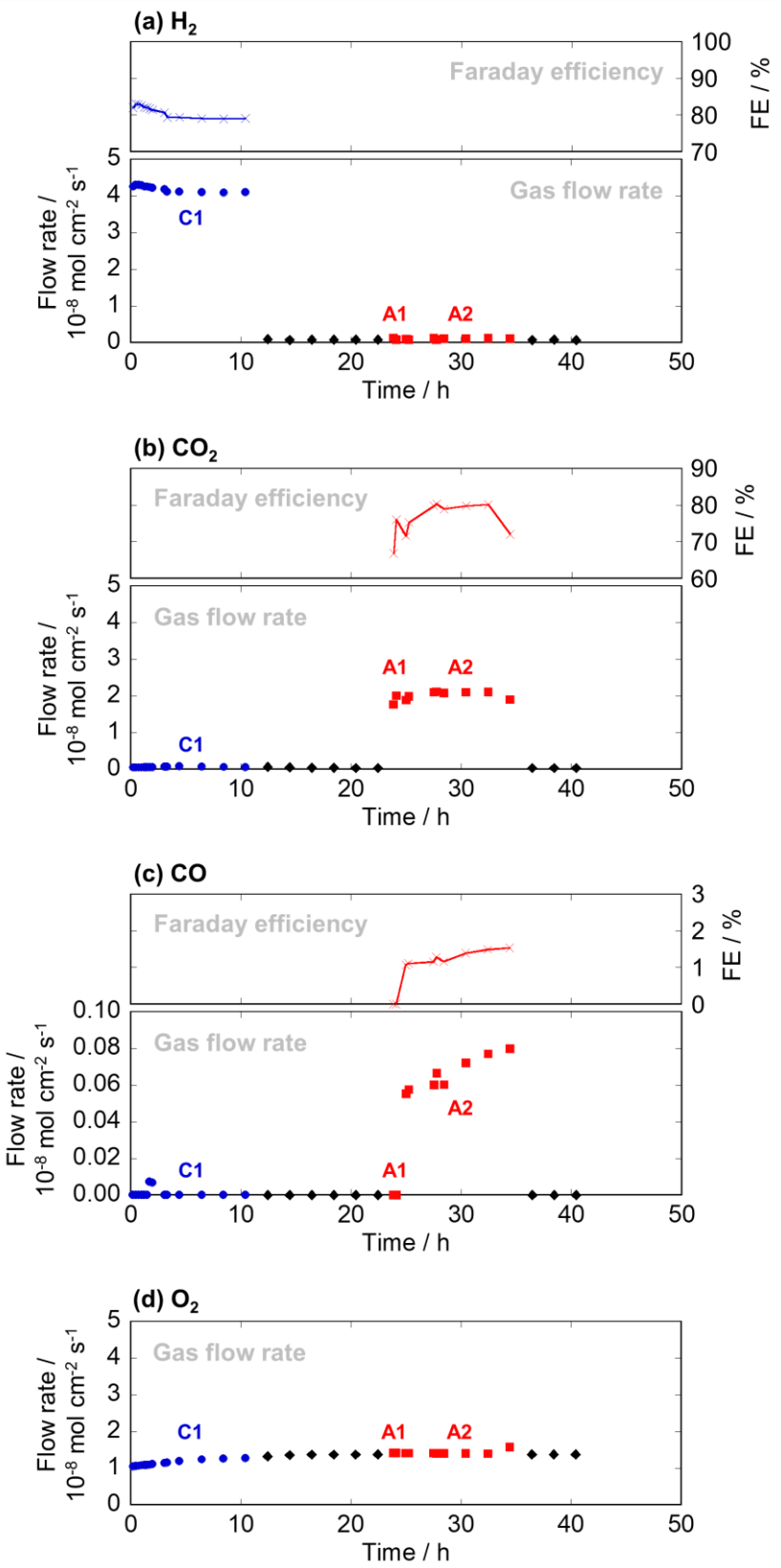

Figure 3-16. Analysis of the outlet gas flow of the working electrode during the bidirectional electrolysis tests at 220°C using the Pt/C|CsH_2PO_4/SiP_2O_7|Pt/C cell. (a)-(c) Molar flow rates of hydrogen, CO_2, and CO, and corresponding (nominal) Faraday efficiencies. (d) Molar flow rates of oxygen.

3.1.3.2.6. Summary of the investigations

Figure 3-17 illustrates the material and structural changes of the Pt/C|CsH_2PO_4/SiP_2O_7|Pt/C cell discussed in the previous sections. Main findings are summarized as follows:

- The CsH_2PO_4/SiP_2O_7 electrolyte reacted to form $CsH_5(PO_4)_2/SiP_2O_7$ composite. Dehydration of the phosphates, which significantly decreases the proton conductivity, was not observed in this study.
- The molten $CsH_5(PO_4)_2$ (and possibly phosphoric acid) with adsorbed water migrated from the electrolyte layer to the porous anode layer under polarization. The electrolyte migration caused the prevention of the gas diffusion and the flooding of the Pt/C catalyst layer. These phenomena are the possible causes of the fatal decrease in the cell voltage.
- The carbonaceous materials in the anode (primarily the carbon support of the Pt/C catalyst) were oxidized to CO_2. This led to the decrease in the number of reaction sites and may have deteriorated the electrochemical activity of the anode.

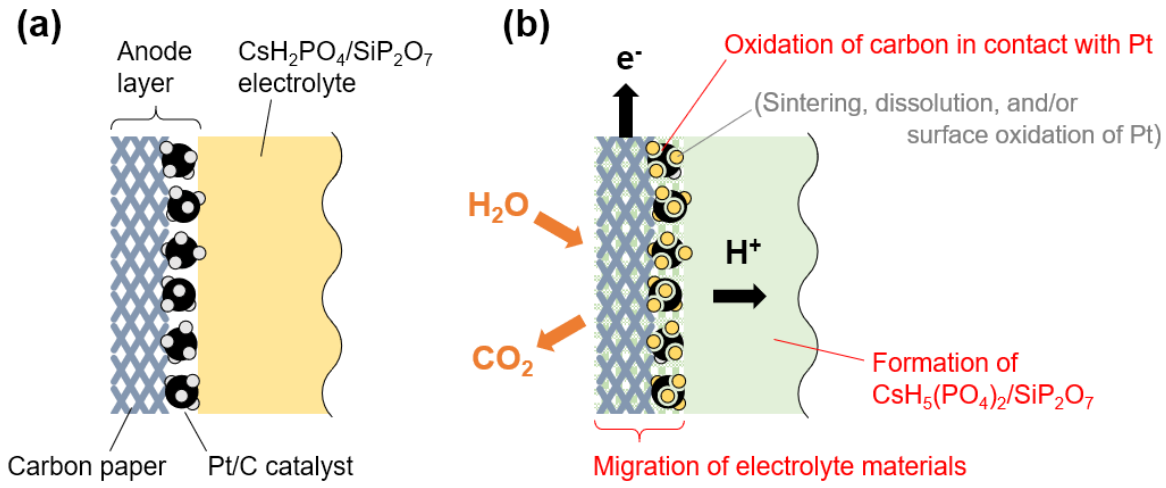

Figure 3-17. Material and structural changes in the electrolyte layer and the anode layer of the Pt/C|CsH_2PO_4/SiP_2O_7|Pt/C cell caused by the steam electrolysis. (a) Schematic image of a cell cross section before the operation. (b) Schematic image of a cell cross section during the operation.

Here, comments are made about other possible phenomena relating to Pt which can affect the cell stability. Sintering and dissolution of Pt in electrodes were reported as the causes of performance degradation of

PEM fuel cells and electrolysis cells[185,194]. Formation of an oxide layer on the anode Pt surface[193,195,196] can also affect the electrochemical activity. These phenomena can occur in SAECs. Further characterization is required for deep understanding of the behavior of Pt in SAEC anodes during the operation.

3.1.3.3. Performance of the SAEC with a Pt mesh anode

According to the investigations of the Pt/C|CsH_2PO_4/SiP_2O_7|Pt/C cell, improvement of the material and structure of the anode is necessary to prevent the severe performance degradation. This time, Pt mesh was employed as an alternative anode. According to the SEM images in Figure 3-9, the thickness of the Pt/C anode (including the carbon paper layer) was about 100 μm. The Pt mesh has a comparable thickness of *ca.* 70 μm. On the other hand, the Pt amount per unit electrode area differs significantly: 1.0 mg_{Pt} cm^{-2} for the Pt/C sheet and 65 mg_{Pt} cm^{-2} for the Pt mesh. Because the mesh itself is made of Pt metal and the current was directly collected through the Pt wire, the oxidation of carbon can be avoided. Furthermore, it was expected that the Pt mesh anode was resistant to the electrolyte migration. In the Pt/C anode, the thin catalyst layer was flooded by the migrated electrolyte and electrochemically active sites became unavailable. On the contrary, in the Pt mesh anode, contact of the gas phase and the Pt metal can be maintained due to the abundance of Pt metal. Therefore, electrochemical activity should be maintained even if the electrolyte migrates severely.

Figure 3-18 compares the results of long-term 10 mA cm^{-2} galvanostatic tests at 220°C with the Pt/C anode and the Pt mesh anode. The data of the Pt/C anode is replicated from Figure 3-5. Initial cell voltage was higher (*i.e.* the overpotential was smaller) in the case of the Pt/C anode despite the much smaller Pt loading (Figure 3-18a). This can be attributed to the difference in the number of electrochemically active sites. In the Pt/C catalyst layer (1.0 mg_{Pt} cm^{-2}), a large number of active sites were available owing to the high dispersion of Pt metal. On the other hand, the Pt utilization efficiency in the Pt mesh anode (65 mg_{Pt} cm^{-2}) was quite low, resulting in the low initial activity. As discussed previously, the operation of the Pt/C|CsH_2PO_4/SiP_2O_7|Pt/C cell was disabled at around 8.8 h with the steep decrease of the cell voltage.

On the contrary, the cell with the Pt mesh anode showed stable performance. The cell voltage was almost constant at around -2.2 V for 48 h (Figure 3-18a). A fatal decrease in the cell voltage was not observed. Faraday efficiency for the hydrogen production was also maintained around 80% for 48 h (Figure 3-18b). The superior stability of the cell with the Pt mesh anode supports the discussion about the performance degradation of the Pt/C|CsH_2PO_4/SiP_2O_7|Pt/C cell: the increase of the overpotential was caused by the electrolyte migration to the anode and the carbon oxidation in the anode. The Pt mesh anode mitigated these problems. It should be noted that the Pt mesh anode is quite expensive and is not suitable for practical use. Therefore, further investigations of the anode materials and structures are required. Utilization of metal oxide catalysts such as IrO_2 or RuO_2 is one of the promising ideas as those oxides are widely studied as anode materials of PEM electrolysis cells[9,197]. The use of oxidation-resistant anode gas diffusion layers is also encouraged. For instance, Prag[68] employed tantalum-coated stainless steel felts. For developing durable SAECs, it is also important to suppress the severe migration of phosphate electrolytes to the anode. The problem may be mitigated by designing matrices for electrolytes. Our previous study revealed that the stability of phosphate-based composite electrolytes depends on the properties of the matrices[189].

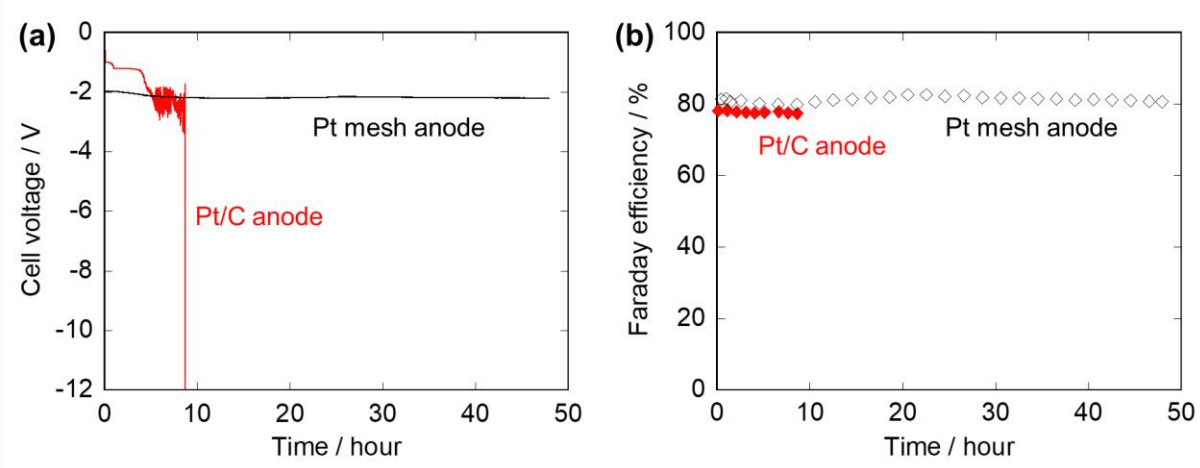

Figure 3-18. Stability tests at 220°C with the Pt/C anode and the Pt mesh anode. The electrolyte and the cathode were fixed to the CsH_2PO_4/SiP_2O_7 composite and the Pt/C sheet, respectively. Current density was kept at 10 mA cm^{-2}. The measurement of with the Pt(mesh)|CsH_2PO_4/SiP_2O_7|Pt/C cell was stopped at 48 h. (a) Cell voltages as functions of time. (b) Corresponding Faraday efficiencies for the hydrogen production.

3.1.4. Summary

In Section 3.1, steam electrolysis was performed at 160-220°C using a solid acid electrolysis cell (SAEC) composed of a CsH_2PO_4/SiP_2O_7 composite electrolyte and Pt/C electrodes. Hydrogen production at different current densities and temperatures was successfully demonstrated with Faraday efficiencies around 80%. However, the cell voltage under a constant current load increased with time. Accordingly, factors affecting the cell stability were investigated in detail. SEM-EDX measurements revealed that a certain part of the electrolyte migrated into the porous anode layer during the operation. The migrated electrolyte filled the anode pores and prevented the gas diffusion. It was suggested that the surface of the Pt/C catalyst in the anode was partially covered by the migrated electrolyte and became electrochemically inactive. It was also found that the carbonaceous materials in the anode, primarily the carbon support of the Pt/C catalyst, was oxidized to CO_2. The oxidation of carbon can decrease the number of electrochemically active sites in the anode. These phenomena are the possible causes of the performance degradation of the SAEC. To mitigate the problems relating to the Pt/C anode, Pt mesh was employed as an alternative anode. With a constant current load of 10 mA cm^{-2}, the cell voltage at 220°C was almost unchanged at around -2 V for 48 h. The superior stability of the Pt mesh anode demonstrated the importance of the anode design. Future investigations for durable and practical SAECs should focus on the control of the electrolyte migration and the development of cost-effective anodes with high oxygen evolution activity. Nevertheless, the Pt mesh anode and the CsH_2PO_4/SiP_2O_7 electrolyte can be applicable for the investigation of SAEC cathodes for CO_2 electrolysis at present.

3.2. Direct CO_2 Conversion

3.2.1. Objective

This section addresses the experimental investigations of SAECs for the direct production of methane and methanol from CO_2.

First, combination of the Pt/C cathode and a CO_2 hydrogenation catalyst layer was examined to demonstrate the stable CO_2 conversion (Figure 3-19a). A (Pt mesh)|CsH_2PO_4/SiP_2O_7|Pt/C cell was fabricated, and the catalyst layer was attached to the Pt/C cathode. This configuration is called **type 1** hereafter. *M*/ZrO_2 (*M* = Ru, Pd, Cu) were prepared as CO_2 hydrogenation catalysts. Ru/ZrO_2 is known as a methanation catalyst[198], while Cu/ZrO_2 and Pd/ZrO_2 are known as catalysts for the methanol synthesis from CO_x and H_2[199,200]. The catalytic methanol synthesis is generally performed at elevated pressures higher than 10 bar[148]. On the contrary, the present electrochemical reactor was operated under atmospheric pressure. Thus, the catalytic activity of *M*/ZrO_2 under atmospheric pressure was also examined.

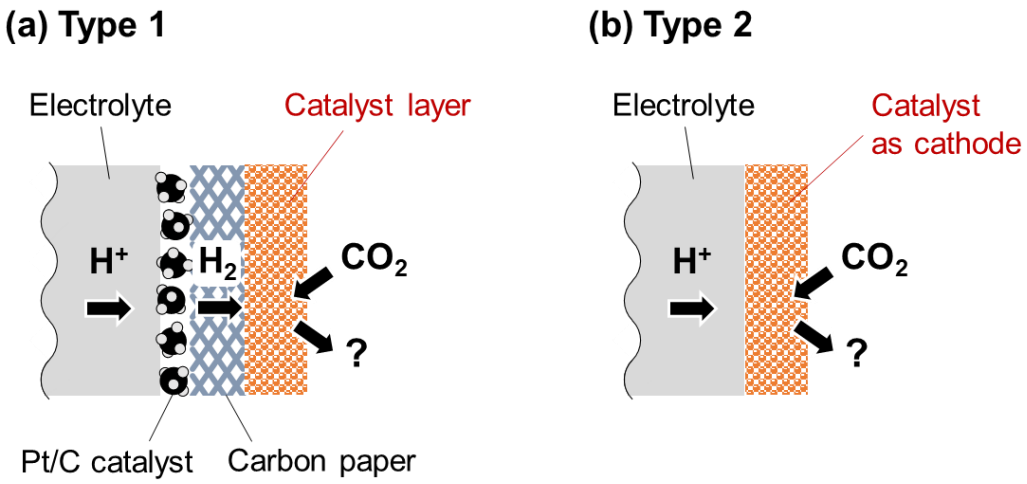

Figure 3-19. Concept of two different cathode types. (a) Type 1. (b) Type 2.

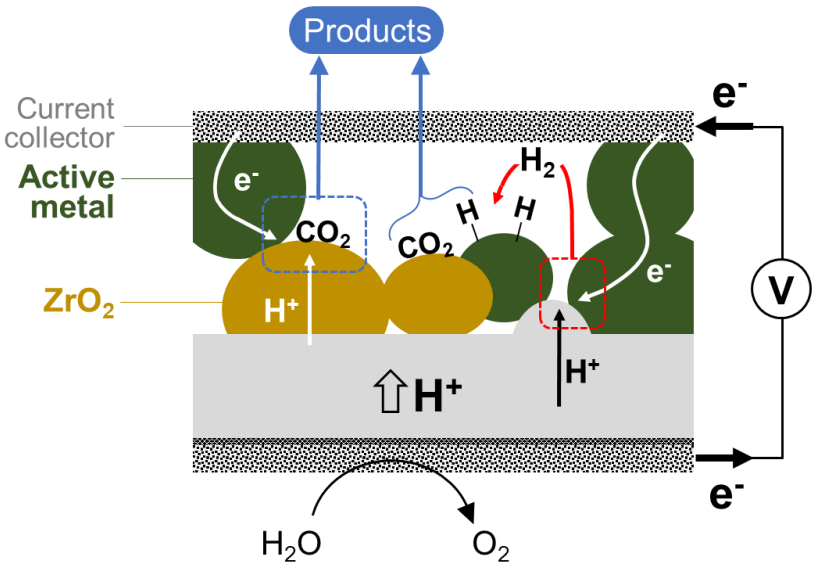

Figure 3-20. Schematic image of the cross section of a SAEC with a type-2 cathode. Anticipated reaction processes are illustrated.

In the type-1 cathodes, protons transported through the electrolyte should be consumed at the Pt/C layer to form hydrogen molecules. Then, the hydrogen will react with CO_2 in the catalyst layer. On the contrary, if the cathode itself has the catalytic activity for CO_2 reduction, protons may react directly with CO_2. It is also possible that a polarization in the cathode alters the catalytic activity (NEMCA effect, Section 1.4). It is worthwhile to investigate these effects because they, if present, may contribute to the highly energy-efficient CO_2 electrolysis. By utilizing unique features of electrochemical reactions, high reaction rates and/or high selectivity to valuable products could be achieved. Here, as the first step of the investigation, physical mixtures of metal powders and oxide powders were applied as catalytic cathodes (Figure 3-19b). This configuration is called **type 2** hereafter. Cu-ZrO_2, (Cu-Ru)-ZrO_2, (Cu-Pd)-ZrO_2 and (Cu-Ru)-SiO_2 composites were synthesized and tested as cathodes. Figure 3-20 shows a schematic image of the cross section of a SAEC with a type-2 cathode. The mixtures of metal powders and oxide powders are expected to possess high electronic conductivity without relying on carbonaceous additives (*e.g.* carbon nanofibers). The choice of Cu and ZrO_2 is based on the composition of a CO_2-to-methanol catalyst, Cu/ZrO_2. ZrO_2 is known to have proton conductivity[201], so it may be possible that protons transported through the electrolyte further travel in the ZrO_2 particles, and react with CO_2 adsorbed on the ZrO_2 surface without

forming hydrogen molecules. Cu-Ru and Cu-Pd were developed to suppress the oxidation of Cu during operation. Ru and Pd are noble metals which are tolerant to oxidation. Hydrogen spillover from Ru or Pd to Cu will prevent the Cu surface from being oxidized. SiO_2 was employed to examine the effect of CO_2 adsorptivity of the oxide phase. The CO_2 adsorptivity of SiO_2 is lower than that of ZrO_2. The thermocatalytic activity of the composites was also examined at ambient pressure.

3.2.2. Experimental

3.2.2.1. Materials preparation

Electrolyte materials, CsH_2PO_4 and SiP_2O_7, were prepared as described in Section 3.1.2.1.

M/ZrO_2 catalysts (*M* = Ru, Pd, Cu, metal loading 10wt%) were prepared as follows. For the synthsis of Ru/ZrO_2 and Pd/ZrO_2, amorphous zirconia (NND, Daiichi Kigenso Kagaku Kogyo) was impregnated with $Ru(NO_3)_3$ nitric acid solution or $Pd(NO_3)_2$ nitric acid solution (Tanaka Kikinzoku Kogyo) at 80°C, and dired at 100°C overnight. The resultant materials were reduced in a qurtz tube by hydrogen at 300°C for 2 h to form Ru/ZrO_2 or Pd/ZrO_2. The reduction temperature was determined by temperature programmed reduction measurements. As obtained powders were used for the cell fabrication. Cu/ZrO_2 was synthesized referring to the literature[199]. Amorphous zirconia (NND, Daiichi Kigenso Kagaku Kogyo) was impregnated with an aqueous solution of $Cu(NO_3)_2{\cdot}3H_2O$ (Wako Pure Chemical Industries) at room temperature. Then the sample was dried at 80°C for 12 h, and calcined at 350°C for 5 h to obtain an amorphous Cu-Zr mixed oxide $Cu_aZr_{1-a}O_b$. The resultant $Cu_aZr_{1-a}O_b$ powder was used for the cell fabrication and was reduced to Cu/ZrO_2 by hydrogen just before the cell operation.

Cu powder was prepared by reducing CuO powder (Wako Pure Chemical Industries) at 350°C for 1 h. For the synthesis of Cu-Ru and Cu-Pd powders, CuO (Wako Pure Chemical Industries) and $Ru(NO_3)_3$ nitric acid solution or $Pd(NO_3)_2$ nitric acid solution (Tanaka Kikinzoku Kogyo) were mixed, and then the water content was evaporated at 80°C. The resultant precursor was pelletized and reduced under a hydrogen flow at 330°C for 1 h. The reduction temperatures were determined by temperature programmed reduction measurements. Noble metal contents in the Cu-Ru and Cu-Pd powders were set

to 5wt%. Cu-ZrO_2, (Cu-Ru)-ZrO_2, and (Cu-Pd)-ZrO_2 composites were prepared by mixing metal powders (Cu, Cu-Ru, or Cu-Pd) and amorphous zirconia (NND, Daiichi Kigenso Kagaku Kogyo) in a mortar at a weight ratio of 1:1 or 2:1. (Cu-Ru)-SiO_2 was prepared in a same manner using SiO_2 (Wako Pure Chemical Industries) instead of ZrO_2.

The morphology of the prepared cathode material powders was examined by a scanning electron microscope (SEM, S-4700, Hitachi).

Table 3-1. Feed gas compositions used in catalytic activity tests of the cathode materials.

No.	Gas flow rate / mL min^{-1}					Note
	CO_2	H_2	5%H_2/Ar	N_2	Total	
#1	12	36	-	12	60	$H_2/CO_2 = 3$
#2	3	9	-	48	60	$H_2/CO_2 = 3$
#3	4	12	-	4	20	$H_2/CO_2 = 3$
#4	12	-	12	36	60	$H/CO_2 = 0.1$
#5	4	-	4	12	20	$H/CO_2 = 0.1$

3.2.2.2. Catalytic activity test of cathode materials at ambient pressure

Catalytic activity of *M*/ZrO_2 catalysts (*M* = Ru, Pd, Cu, metal loading 10wt%) at ambient pressure was examined. Ru/ZrO_2, Pd/ZrO_2, or $Cu_aZr_{1-a}O_b$ powder was pelletized into grains of *ca.* 1.5 mm. The pellets of 200 mg were put in a quartz tube (inner diameter ϕ8) and then mounted in a furnace. Temperature was raised from room temperature to 220°C under a nitrogen atmosphere. Before starting the catalytic reactions, the catalyst was reduced by dry hydrogen (H_2/N_2 = 25/25 mL min^{-1}) at 220°C for 30 min. Ru/ZrO_2 and Pd/ZrO_2 had already been reduced before the activity test, so the treatment here was intended to remove the surface oxide layer formed on Ru or Pd metal. According to ref. [199], $Cu_aZr_{1-a}O_b$ can be reduced to Cu/ZrO_2 at 220°C. The CO_2 hydrogenation reaction was performed with a feed gas of $CO_2/H_2/N_2$ = 12/36/12 mL min^{-1} (composition #1 in Table 3-1). In the case of Ru/ZrO_2, the operation temperature could not be controlled under the composition #1 probably due to the large reaction heat of methanation. Thus, the feed gas was diluted ($CO_2/H_2/N_2$ = 3/9/48 mL min^{-1}, composition #2 in Table 3-1).

The total gas flow rate was 60 mL min^{-1}. This corresponds to a (catalyst weight)/(volume flow rate) ratio of W_{cat}/F_{total} = 200 mg_{cat} s mL^{-1}. The gas composition of H_2/CO_2 = 3 was determined from the stoichiometry of the CO_2-to-methanol reaction. Temperature was varied as 220°C → 200°C → 210°C → 230°C → 250°C (measurements at 250°C was performed only with Ru/ZrO_2 and Pd/ZrO_2). At each temperature, the outlet gas composition was examined. First, the gas was analyzed by a gas chromatograph equipped with a flame ionization detector (GC-FID, GC-2014, Shimadzu). Then the gas was further analyzed by a micro gas chromatograph equipped with a thermal conductivity detector (GC-TCD, Varian CP-4900 or Agilent 490) after dehumidified by a cold trap. The GC-FID was used for the quantitation of methanol, ethanol, and acetaldehyde. The GC-TCD monitored the other gases (H_2, N_2, CH_4, CO, C_2H_4, C_2H_6, *etc.*). For Ru/ZrO_2 and Pd/ZrO_2, the gas was swiched to $CO_2/(5\%H_2/Ar)/N_2$ = 12/12/36 mL min^{-1} (composition #4 in Table 3-1) at 250°C. This composition corresponds to the H/CO_2 ratio of 0.1. The low H/CO_2 ratio simulates the electrochemical tests. For example, 5 mL min^{-1} of CO_2 is introduced to a ϕ10 cathode, and the current density is 50 mA cm^{-2}, the H^+/CO_2 ratio will be 0.12.

To test the effects of adjacent cell materials on the catalytic activity of Cu/ZrO_2, the catalyst was mixed with CsH_2PO_4 or carbon nanofibers (CNF). The compositions were set as Cu/ZrO_2:CsH_2PO_4 = 10:1 and Cu/ZrO_2:CNF = 2:1 (weight ratio). In the case of Cu/ZrO_2-CNF mixture, the effect of steam was also tested by humidifying the feed gas. Steam amount was *ca.* 3%.

Catalytic activity of the metal-oxide composites for the type-2 cathode (Cu-ZrO_2, (Cu-Ru)-ZrO_2, (Cu-Pd)-ZrO_2, and (Cu-Ru)-SiO_2) was also examined at ambient pressure. The composites were pelletized into grains of *ca.* 1.5 mm. The pellets (200 mg) were put in a ϕ8 quartz tube. Temperature was raised from room temperature to 220°C under a nitrogen atmosphere. The catalyst was reduced by dry hydrogen (H_2/N_2 = 25/25 mL min^{-1}) at 220°C for 30 min to remove the surface oxide layer formed on metal particles. First, the feed gas composition #1 in Table 3-1 was tested at 220°C. However, the CO_2 conversion was quite low. To increase the gas contact time, the flow rate was reduced to one third ($CO_2/H_2/N_2$ = 4/12/4 mL min^{-1}, composition #3 in Table 3-1). The temperature was changed as 220°C → 230°C → 250°C → 240°C. At each temperature, the outlet gas composition was analyzed. At 250°C, a composition of

CO_2/(5%H_2/Ar)/N_2 = 4/4/12 mL min^{-1} (composition #5 in Table 3-1) was also tested to see the catalytic activity at a low H/CO_2 ratio (0.1).

3.2.2.3. Cell fabrication

3.2.2.3.1. Cells with type-1 cathodes (Pt/C sheet + catalyst layers)

As type-1 cathodes, two configurations of catalyst layer were tested (Figure 3-21a and b). Here, these two are called **type 1a** and **type 1b**, respectively. For both types, Pt mesh (ϕ10, Nilaco, 100 mesh, 70 μm-thick) was adopted as the anode according to the steam electrolysis study. The CsH_2PO_4/SiP_2O_7 electrolyte (0.44 g) and the cathode Pt/C sheet (ϕ10, Miclab, Pt loading 1.0 mg cm^{-2}) were co-pressed at 20 MPa for 10 min in a ϕ20 uniaxial die. The resultant cell was fitted into a PTFE sheet. PTFE tape was used to fill the gaps between the cell and the PTFE sheet.

For the type-1a cathodes, the catalysts (M/ZrO_2) were mixed with carbon nanofibers (CNF) in a mortar at the weight ratio of M/ZrO_2:CNF = 2:1, aiming at adding the electronic conductivity and the porosity. The resultant powders were pressed at 20 MPa for 10 min in a ϕ10 uniaxial die. The prepared catalyst disk was placed next to the cathode Pt/C sheet. The amount of the catalysts was determined so that the metal loading per unit electrode area became 1.5 mg_{metal} cm^{-2}. Current was collected from the catalyst layer through a Pt wire.

The type-1b cathode employs a catalyst layer made of pellets. This was developed aiming at enhancing the CO_2 conversion by increasing the gas contact time. Ru/ZrO_2 and SiO_2 (Wako Pure Chemical Industries) were mixed in a mortar at the weight ratio of Ru/ZrO_2:SiO_2 = 1:2. The resultant powder was pressed at 20 MPa for 10 min in a uniaxial die. The obtained disk was broken into small pellets and then sieved. The pellets with a size of 300-500 μm were collected. The pellets were put in a ϕ10 hole made in a thick PTFE sheet next to the Pt/C cathode. Carbon paper (TGP-H-120, Toray Industries) was applied to put a lid on the catalyst layer. The amount of the Ru/ZrO_2 + SiO_2 pellets was controlled so that the Ru loading per unit electrode area became 1.5 mg cm^{-2}. In this case, current was collected from the Pt/C sheet because the conductivity of the Ru/ZrO_2 + SiO_2 pellets was not sufficient.

3.2.2.3.2. Cells with type-2 cathodes (CO_2-converting catalysts as cathodes)

For cells with type-2 cathodes (Figure 3-21c), cathode composite powders (Cu-ZrO_2, (Cu-Ru)-ZrO_2, (Cu-Pd)-ZrO_2, and (Cu-Ru)-SiO_2) were pressed in a ϕ10 uniaxial die at 20 MPa for 10 min to form a cathode disk. Table 3-2 summarizes the details of the tested cathodes. For the (Cu-Ru)-ZrO_2 composite, metal-oxide ratios of 1:1 and 2:1 were tested. The cathode disk and 0.44 g of electrolyte powder were co-pressed in a ϕ20 uniaxial die at 20 MPa for 10 min to form a cell. The cell was fitted into a PTFE sheet. PTFE tape was employed to fill the gaps between the cell and the PTFE sheet. Carbon paper (ϕ10, TGP-H-120, Toray Industries) was placed adjacent to the cathode disk as a current collector. Pt mesh (ϕ10, Nilaco, 100 mesh, 70 μm-thick) was adopted as the anode.

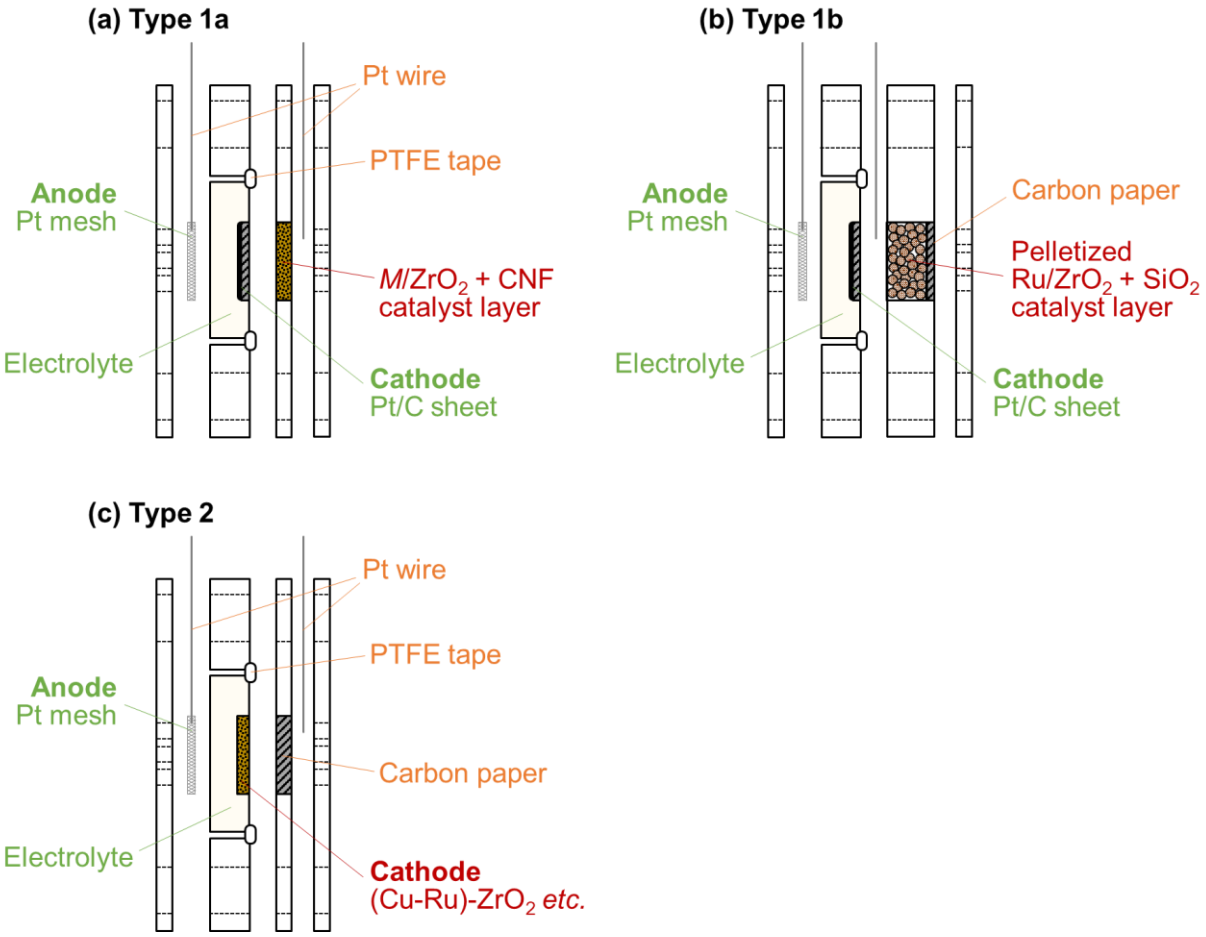

Figure 3-21. Cross-sectional schematic images around the SAECs. (a) Type 1a. (b) Type 1b. (c) Type 2.

Table 3-2. Details of the tested type-2 cathodes.

Cathode notation	Metal-oxide weight ratio	Metal loading / mg cm^{-2}	Total weight / mg
(Cu-Ru)-ZrO_2 [1:1]	1:1	10	15.7
(Cu-Ru)-ZrO_2 [2:1]	2:1	20	23.6
(Cu-Pd)-ZrO_2	1:1	10	15.7
Cu-ZrO_2	1:1	10	15.7
(Cu-Ru)-SiO_2	1:1	10	15.7

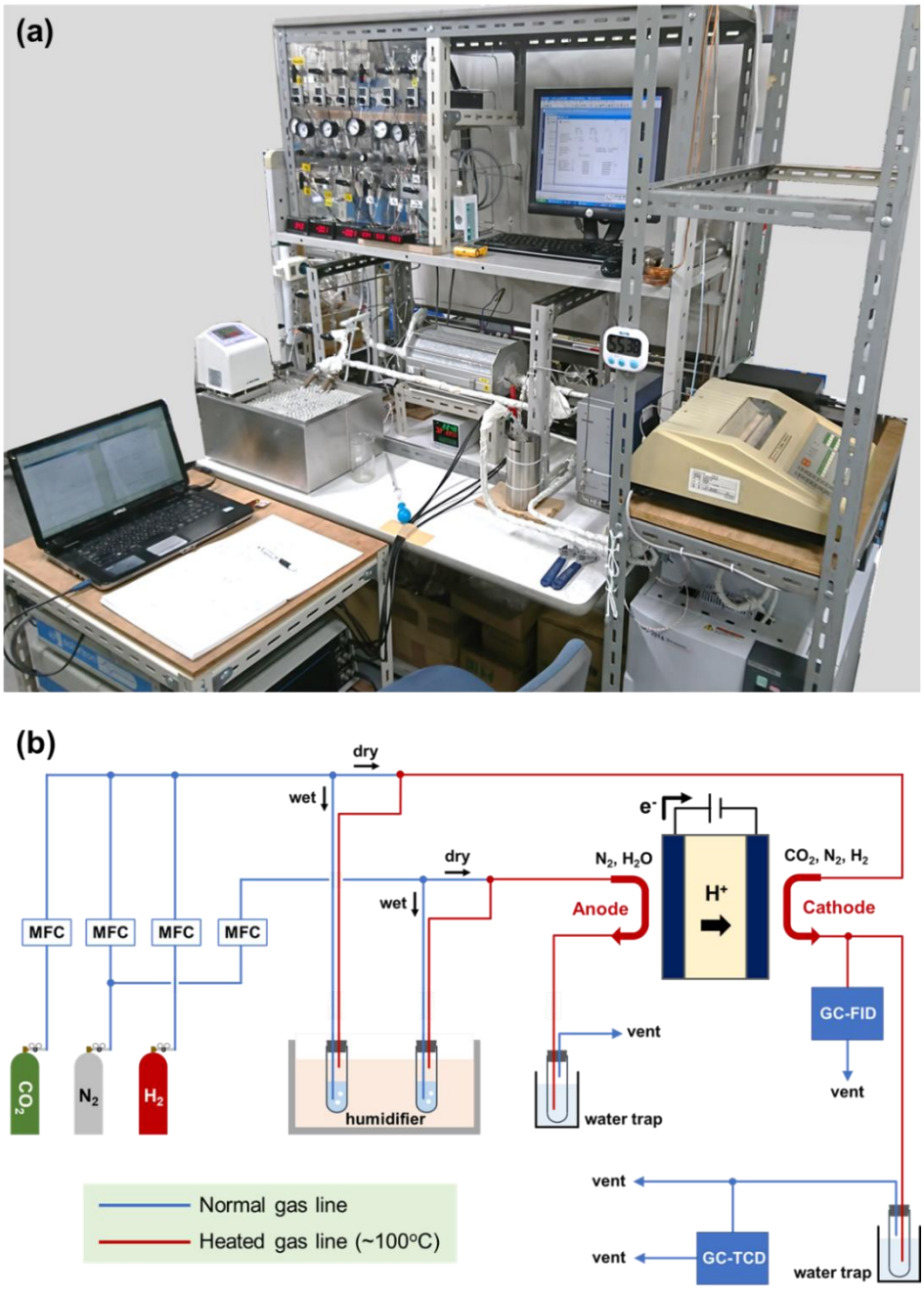

Figure 3-22. Experimental apparatus for the CO_2 electrolysis in SAECs. (a) Photograph of the apparatus. (b) Schematic image of the gas lines, the reactor, and other components.

3.2.2.4. Electrochemical reaction

The parts shown in Figure 3-21 were hot-pressed at 120°C, 6 MPa for 10 min and then set in the stainless-steel reactor like Figure 3-1. Figure 3-22 illustrates the overview of the experimental apparatus. Dry or humidified CO_2, N_2, and H_2 can be introduced to the cathode while dry or humidified N_2 to the anode. Humidification of the inlet gases were done by bubbling the gases in distilled water. The steam partial pressure was controlled by varying the temperature of the bubblers. The cathode outlet gas was analyzed by gas chromatographs: the GC-FID and the GC-TCD were used as explained in Section 3.2.2.2.

3.2.2.4.1. Cells with type-1 cathodes

Figure 3-23 shows the experimental procedure for the cells with type-1 cathodes. After setting the cell in the reactor, nitrogen was introduced to both sides of the cell, and temperature was raised from the room temperature to 250°C at a rate of 200°C h^{-1}. Once the temperature reached 120°C, the gas flows were humidified. Before conducting steam electrolysis at designated temperatures, the cathode was reduced by a humidified hydrogen flow ($H_2/N_2/H_2O$ = 25/20/5 mL min^{-1}) at 250°C for 1 h. 250°C is considered high enough to reduce $Cu_aZr_{1-a}O_b$ to Cu/ZrO_2[199]. Ru/ZrO_2 and Pd/ZrO_2 were already reduced before fabricating the cell, so only surface oxide layers should be reduced. It is considerd that the reduction treatment at 250°C is satisfactory to form metallic Ru and Pd. After purging hydrogen, electrochemical reactions were conducted. First, hydrogen production performance of the cells was evaluated by steam electrolysis. Both the cathode gas and the anode gas were N_2/H_2O = 9/1 mL min^{-1}. After that, CO_2 electrolysis was performed. The cathode gas composition was changed to $CO_2/N_2/H_2O$ = 5/4/1 mL min^{-1} while the anode gas was remained unchanged. In both operation modes, the cathode outlet gas composition was analyzed under a constant current load of 20 mA cm^{-2}. In the case of CO_2 electrolysis with the type-1b cathode, the current density was changed as 20 → 60 → 40 → 100 mA cm^{-2} to examine the effect of H^+/CO_2 ratio.

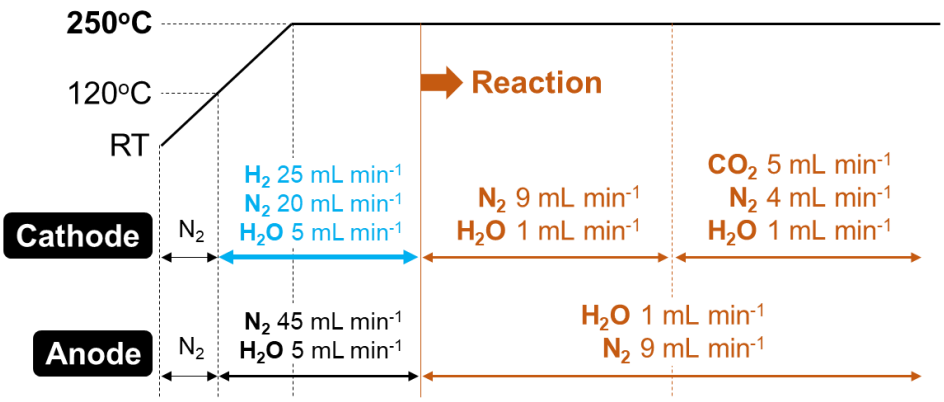

Figure 3-23. Experimental procedure for cells with the type-1 cathodes.

3.2.2.4.2. Cells with type-2 cathodes

Figure 3-24 shows the experimental procedure for the cells with type-2 cathodes. After the temperature was raised to 220°C, reduction treatment was done with a mixed gas flow of $H_2/N_2/H_2O$ = 25/10/15 mL min^{-1}. The cathode was reduced for 1 h. During the electrochemical reactions, the anode gas composition was fixed to H_2O/N_2 = 15/35 mL min^{-1}. The cathode gas was not humidified this time in order to facilitate CO_2 conversion. First, 10 mL min^{-1} of N_2 was supplied to the cathode. Hydrogen production performance of the cells was evaluated under a constant current load of 50 mA cm^{-2}. Then the gas was switched to CO_2/N_2 = 5/5 mL min^{-1} for the CO_2 electrolysis. The cathode outlet gas compositions were analyzed under open circuit conditions and 50 mA cm^{-2} galvanostatic conditions.

Cross sections of the cells before and after the 50 mA cm^{-2} galvanostatic tests were examined by a scanning electron microscope (SEM, S-4700, Hitachi) equipped with an energy dispersive X-ray spectroscopy (EDX) detector (Super Xerophy, Horiba). Distribution of Cu, Cs, and noble metals (Ru or Pd) was visualized. P and Zr were not treated because the signals originating from these elements were overlapped.

To compare the reactivity of protons and hydrogen gas, the following experiment was performed with the (Cu-Ru)-ZrO_2 [1:1] cathode. After the cathode reduction treatment, the cathode inlet gas composition and the current density were changed as Table 3-3, and the cathode outlet gas was analyzed. The same number of H atoms were supplied to the cathode as protons or H_2 molecules (gas).

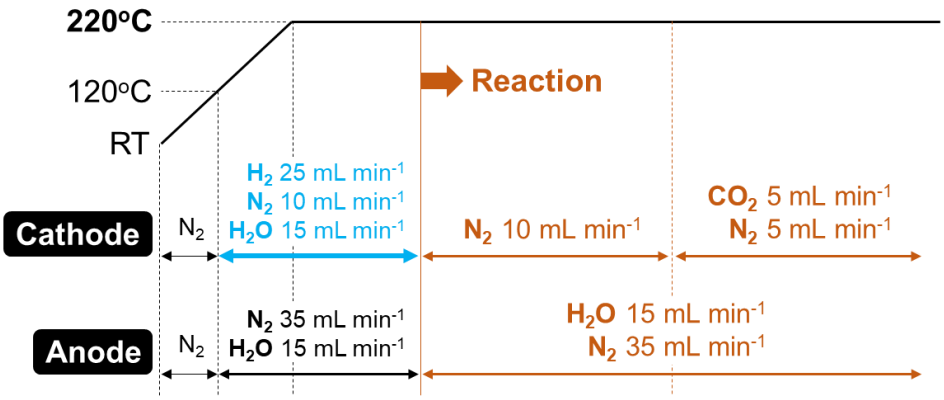

Figure 3-24. Experimental procedure for cells with the type-2 cathodes.

Table 3-3. Experimental conditions for comparing the reactivity of protons and hydrogen gas.

No.	Current density / mA cm^{-2}	Cathode feed gas / mL min^{-1}					Supplied H atom / 10^{-7} mol s^{-1}
		CO_2	5%H_2/Ar		N_2	Inert total (Ar + N_2)	
			H_2	Ar			
#1	-	8	0.3	5.7	6.3	12	4.07
#2	50	8	-	-	12	12	4.07
#3	-	8	0.15	2.85	9.15	12	2.04
#4	25	8	-	-	12	12	2.04

3.2.3. Results and discussion

3.2.3.1. SEM observation of cathode materials

Figure 3-25 shows the SEM images of the as-prepared M/ZrO_2 catalyst powders (M = Cu, Ru, Pd, metal loading 10wt%) for the type-1 cathodes. The grains of $Cu_aZr_{1-a}O_b$ (precursor of Cu/ZrO_2) were *ca.* 50 μm, those of Ru/ZrO_2 were *ca.* 10 μm or smaller, and those of Pd/ZrO_2 were *ca.* 5 μm or smaller. For all the powders, fine structure (< 1 μm) was observed. The amorphous $Cu_aZr_{1-a}O_b$ is considered to be a single phase[199], while the Ru/ZrO_2 and Pd/ZrO_2 catalysts should have two phases (metal and ZrO_2).

Figure 3-26 shows the SEM images of the cathode material powders for the type-2 cathode. The size of secondary particles of Cu, Cu-Ru, and Cu-Pd was *ca.* 5 μm, *ca.* 20 μm, and *ca.* 10 μm, respectively. The secondary particles consisted of primary particles. The size of the primary particles was *ca.* 500 nm for Cu and Cu-Pd, and *ca.* 100 nm for Cu-Ru. ZrO_2 reagent (NND, Daiichi Kigenso Kagaku Kogyo) and SiO_2 reagent (Wako Pure Chemical Industries) were also observed. The size of ZrO_2 particles was relatively large: 10-100 μm. The SiO_2 reagent consisted of small particles (< 50 nm).

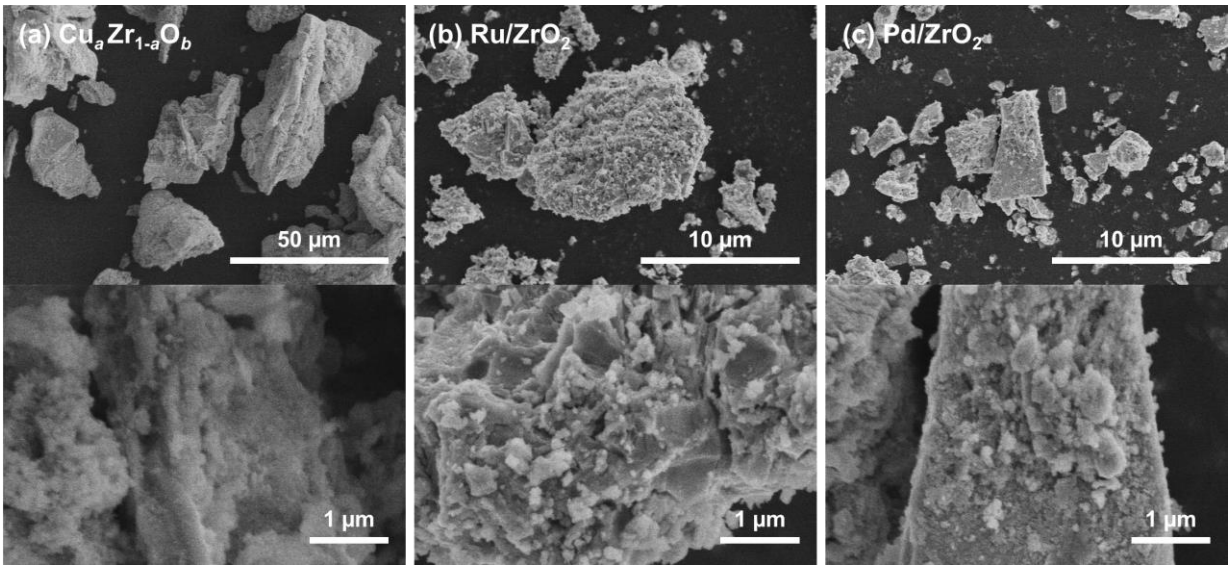

Figure 3-25. SEM images of as-prepared M/ZrO_2 catalyst powders (M = Ru, Pd, Cu, metal loading 10wt%). (a) $Cu_aZr_{1-a}O_b$ (precursor of Cu/ZrO_2). (b) Ru/ZrO_2. (c) Pd/ZrO_2.

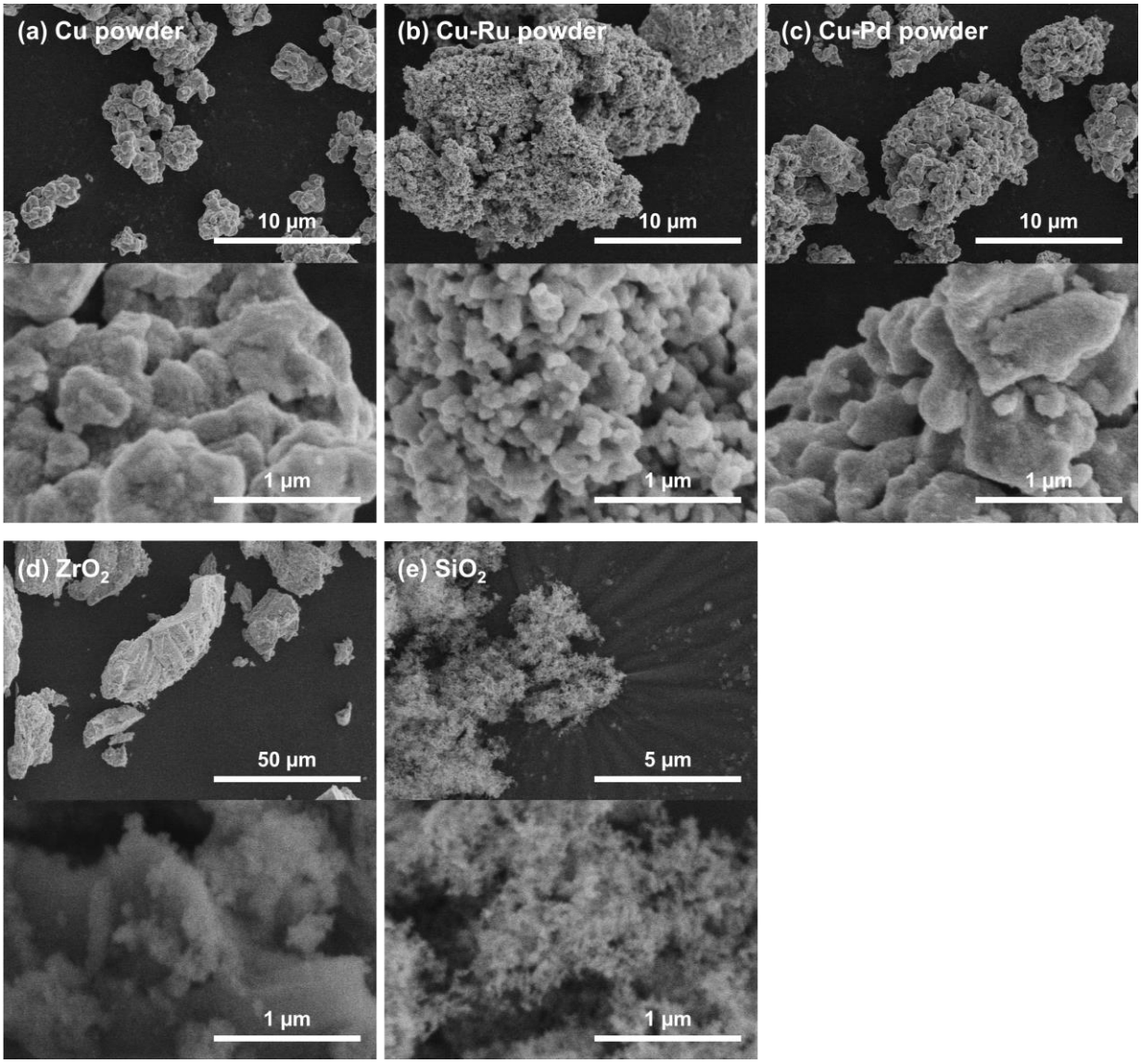

Figure 3-26. SEM images of cathode material powders for the type-2 cathode. (a) Cu powder. (b) Cu-Ru powder. (c) Cu-Pd powder. (d) ZrO_2 reagent. (e) SiO_2 reagent.

3.2.3.2. Catalytic activity of cathode materials at ambient pressure

First, results obtained with pristine Cu/ZrO_2 were presented. The feed gas composition was #1 in Table 3-1. At all the tested temperatures, CO and methanol were detected as products. Figure 3-27a shows the production rates of CO and methanol at different temperatures. Both species were produced at higher rates at higher temperatures. Figure 3-27b is the Arrhenius plot derived from Figure 3-27a. Based on the plot, nominal activation energies of CO formation and methanol formation were calculated to be 100 kJ mol^{-1} and 28 kJ mol^{-1}, respectively. Figure 3-28 shows the CO_2 conversion and methanol selectivity

calculated from gas flow rates by the following equations:

$$(\mathrm{CO_2\ conversion}) = \frac{F_{\mathrm{CO,out}} + F_{\mathrm{CH_3OH,out}}}{F_{\mathrm{CO_2,out}} + F_{\mathrm{CO,out}} + F_{\mathrm{CH_3OH,out}}} \quad (3\text{-}12)$$

$$(\mathrm{CH_3OH\ selectivity}) = \frac{F_{\mathrm{CH_3OH,out}}}{F_{\mathrm{CO,out}} + F_{\mathrm{CH_3OH,out}}} \quad (3\text{-}13)$$

The CO_2 conversion increased with temperature while the methanol selectivity decreased. This follows the general trend of conversion and selectivity in catalytic CO_2-to-methnaol reactions.

The performance of Cu/ZrO_2 catalysts with different Cu loadings at 230°C, 10 bar, and W_{cat}/F_{total} = 430 mg_{cat} s mL^{-1} was reported in ref. [199]: methanol production rate, CO_2 conversion, and methanol selectivity were around 1 mmol h^{-1} g_{cat}^{-1}, 2%, and 70%, respectively. The present study was performed at 1 atm and W_{cat}/F_{total} = 200 mg_{cat} s mL^{-1}. At 230°C, the methanol production rate, CO_2 conversion, and methanol selectivity were 0.29 mmol h^{-1} g_{cat}^{-1}, 1.1%, and 17.6%. All these values are smaller than those in the literature because of the low operation pressure and the low W_{cat}/F_{total} ratio. However, it is notable that methanol was successfully produced with the Cu/ZrO_2 catalyst under atmospheric pressure.

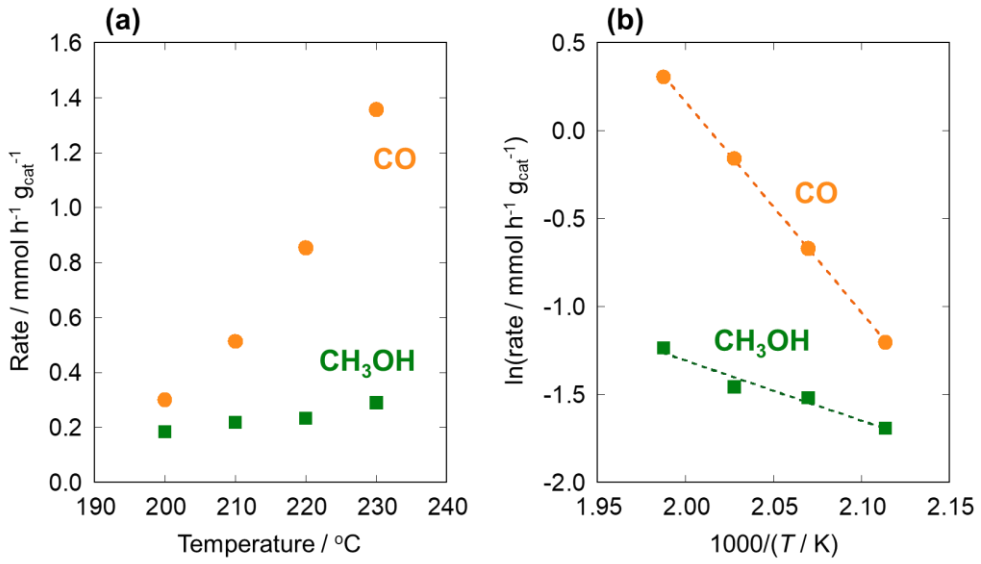

Figure 3-27. Catalytic activity of Cu/ZrO_2 at ambient pressure and different temperatures. (a) Production rates of CO and methanol. (b) Corresponding Arrhenius plots. The feed gas composition was #1 in Table 3-1 (H_2/CO_2 = 3).

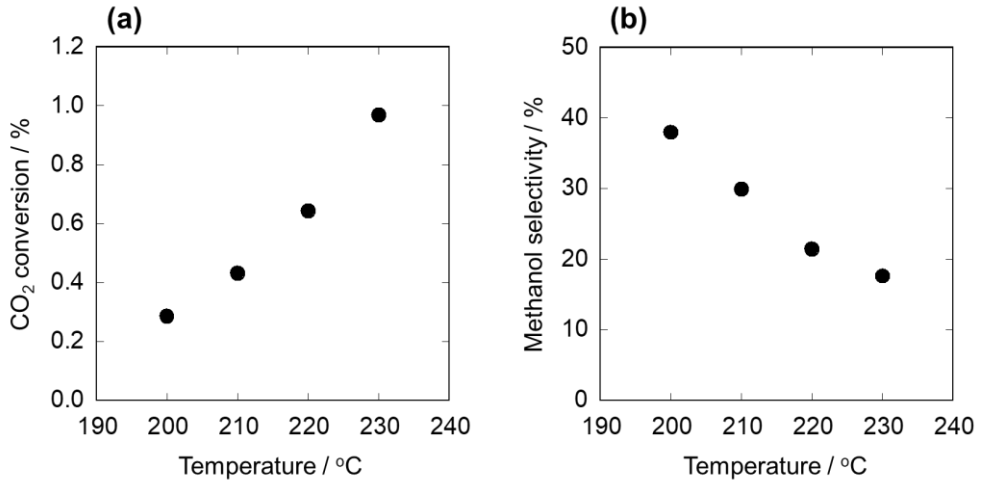

Figure 3-28. Catalytic activity of Cu/ZrO_2 at ambient pressure and different temperatures. (a) CO_2 conversion. (b) Methanol selectivity. The feed gas composition was #1 in Table 3-1 ($H_2/CO_2 = 3$).

Table 3-4 summarizes the results obtained with Cu/ZrO_2 mixed with CsH_2PO_4 and CNF. Entry #1 is the results explained above. When Cu/ZrO_2 was mixed with CsH_2PO_4 (entry #2), the production rate of CO decreased a little while that of methanol decreased significantly. This means that the CO_2 conversion was not affected so much but the selectivity for methanol decreased notably. The activation energy of CO formation was almost unchanged while that of methanol formation nearly doubled. These results may be attributed to changes of the surface properties of Cu/ZrO_2 by CsH_2PO_4. Because CsH_2PO_4 is acidic, the basicity of ZrO_2 surface might be weakened. The electronic property of Cu metal might also be altered. Although detailed mechanisms are unknown, these changes can be related to the change in selectivity. During the operation, some of the active sites of the Cu/ZrO_2 catalyst (boundary of Cu and ZrO_2) may have been covered by CsH_2PO_4. This may explain the decrease in the CO_2 conversion. In the type-1 cathode configurations (Figure 3-21a and b), the catalyst layer and the electrolyte are separated by the Pt/C sheet, which is suitable for maintaining the catalytic activity of Cu/ZrO_2. When Cu/ZrO_2 was mixed with CNF (entry #3), no significant change of catalytic activity was observed. However, when the feed gas was humidified (entry #4), the formation rate of CO and methanol decreased significantly. The trend was consistent with Le Chatelier's principle, as H_2O is the by-product of methanol formation reaction (Eq. 2-66) or reverse water gas shift reaction (Eq. 2-67). In addition, it might be possible that steam

molecules prevented CO_2 molecules from adsorbing on the ZrO_2 surface, and that Cu surface was partially oxidized by the steam.

Table 3-4. Catalytic activity tests of Cu/ZrO_2 at 1atm. The standard feed gas composition was #1 in Table 3-1.

Entry No.	Dry / Wet	Mixed with	Production rate at 220°C / mmol h^{-1} $g_{Cu/ZrO2}^{-1}$		Activation energy (200-230°C) / kJ mol^{-1}	
			CO	CH_3OH	CO	CH_3OH
#1	Dry	-	0.85	0.23	100	28
#2	Dry	CsH_2PO_4 [*2]	0.65	0.01	96	53
#3	Dry	CNF [*3]	0.60	0.20	105	26
#4	Wet [*1]	CNF [*3]	0.30	0.007	-	-

[*1] Steam amount was *ca.* 3%. [*2] Cu/ZrO_2:CsH_2PO_4 = 10:1 (weight). [*3] Cu/ZrO_2:CNF = 2:1 (weight).

Figure 3-29 shows the performance of the Ru/ZrO_2 catalyst at ambient pressure. The feed gas composition was #2 in Table 3-1 (H_2/CO_2 = 3). The main product was methane. CO, ethane, and propane were also produced, but the production rate of those compounds were two or three orders of magnitude lower than that of methane (Figure 3-29a and b). Methanol was not detected. The production of ethane and propane indicated the catalytic activity of Ru for the C-C bond formation. The CO_2 conversion was calculated by Eq. 3-14.

$$(CO_2 \text{ conversion}) = \frac{F_{CO,out}+F_{CH_4,out}+2F_{C_2H_6,out}+3F_{C_3H_8,out}}{F_{CO_2,out}+F_{CO,out}+F_{CH_4,out}+2F_{C_2H_6,out}+3F_{C_3H_8,out}} \quad (3\text{-}14)$$

The resultant values ranged from 10% to 33% (Figure 3-29c), which is significantly higher than the values recorded with the Cu/ZrO_2 catalyst.

Figure 3-30 shows the performance of the Pd/ZrO_2 catalyst with the feed gas #1 (H_2/CO_2 = 3). As described earlier, Pd/ZrO_2 catalysts can promote CO_2-to-methanol reaction at elevated pressures. However, as shown in Figure 3-30a, main products at ambient pressure were CO and methane. Small amounts of methanol and ethane were also produced (Figure 3-30b). The methanol production rate decreased with the temperature. These results reflect the fact that the methanol production is thermodynamically unfavored at low pressure and high temperature. The CO_2 conversion calculated by

Eq. 3-15 ranged from 0.7% to 3.1% (Figure 3-30c). The performance of Pd/ZrO_2 as a methanation catalyst was inferior to that of Ru/ZrO_2.

$$(CO_2 \text{ conversion}) = \frac{F_{CO,out}+F_{CH_3OH,out}+F_{CH_4,out}+2F_{C_2H_6,out}}{F_{CO_2,out}+F_{CO,out}+F_{CH_3OH,out}+F_{CH_4,out}+2F_{C_2H_6,out}} \quad (3\text{-}15)$$

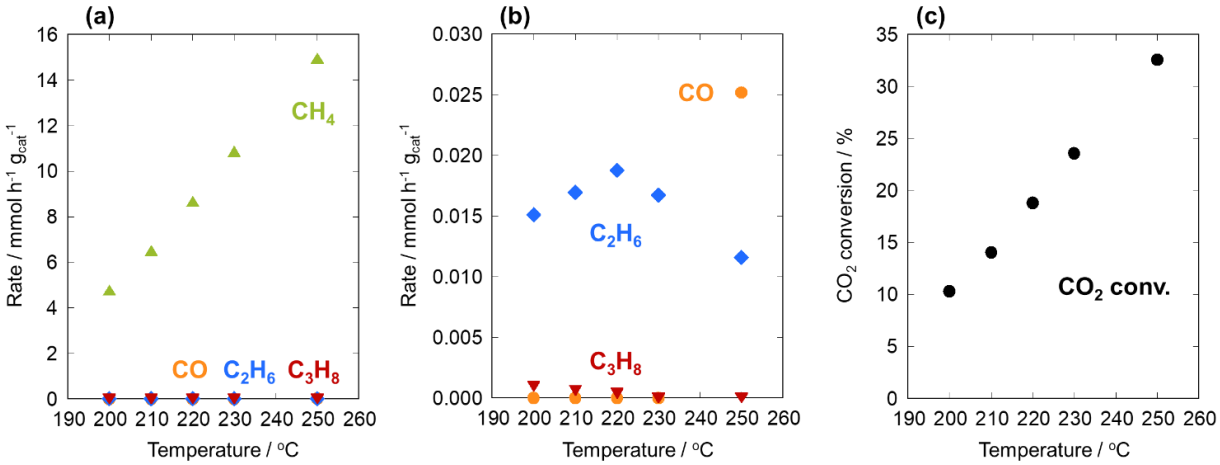

Figure 3-29. Catalytic activity of Ru/ZrO_2 at ambient pressure and different temperatures. (a) Production rates. (b) Magnified plot for CO, ethane, and propane. CO was detectable only at 250°C. Propane was not detected at 230°C and 250°C. (c) CO_2 conversion. The feed gas composition was #2 in Table 3-1 ($H_2/CO_2 = 3$).

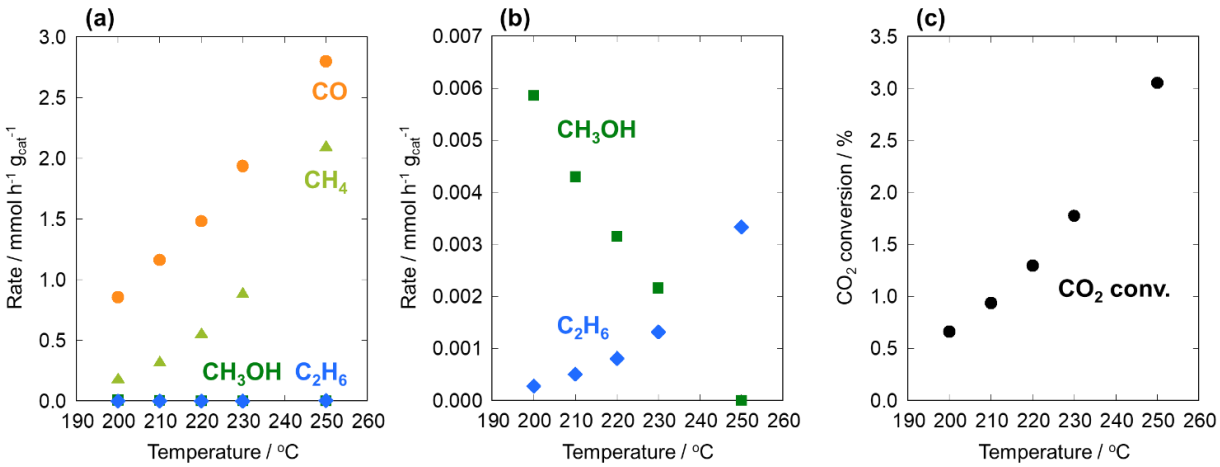

Figure 3-30. Catalytic activity of Pd/ZrO_2 at ambient pressure and different temperatures. (a) Production rates. (b) Magnified plot for methanol and ethane. Methanol was not detected at 250°C. (c) CO_2 conversion. The feed gas composition was #1 in Table 3-1 ($H_2/CO_2 = 3$).

Table 3-5 describes the performance of the Ru/ZrO_2 and Pd/ZrO_2 catalysts at 250°C with the feed gas composition #4 in Table 3-1 ($H/CO_2 = 0.1$). The Ru/ZrO_2 catalyst produced methane selectively with the feed gas #2 ($H_2/CO_2 = 3$, Figure 3-29), but in the present case the main product was CO, and the methane production was suppressed due to the low hydrogen partial pressure. The selectivity for C2 compounds also changed. With the feed gas #2, only alkanes (ethane and propane) were produced. On the other hand, with the feed gas #4, alkenes (ethylene and propylene) were produced along with the alkanes. This phenomenon can also be ascribed to the low hydrogen partial pressure in the feed gas #4. In the case of Pd/ZrO_2, the detected products were CO, methane, and ethane. Methanol was not detected. Compared to the results with the feed gas #1 (Figure 3-30), the methane selectivity decreased significantly.

Table 3-5. Catalytic activity test results at 250°C with the feed gas composition #4 in Table 3-1 ($H/CO_2 = 0.1$).

Catalyst	Production rate / mmol h^{-1} g_{cat}^{-1}						
	CO	CH_3OH	CH_4	C_2H_4	C_2H_6	C_3H_6	C_3H_8
Ru/ZrO_2	0.87	0	0.0096	0.0017	0.0016	0.0010	0
Pd/ZrO_2	1.25	0	0.0127	0	0.0011	0	0

Table 3-6 compares the performance of the Cu/ZrO_2 catalyst and the metal-oxide composites prepared for the type-2 cathode. The temperature was 220°C and the feed gas composition was #1 in Table 3-1 ($H_2/CO_2 = 3$). Although the components of the Cu/ZrO_2 catalyst and the $Cu\text{-}ZrO_2$ composite were the same, the catalytic activity of the former was much higher than that of the latter. No methanol was detected with the $Cu\text{-}ZrO_2$ composite. The Cu/ZrO_2 catalyst possessed Cu nanoparticles (< 5 nm)[199], while the Cu particles in the $Cu\text{-}ZrO_2$ composite was about three orders of magnitude larger (*ca.* 5 μm, Figure 3-26a). The difference of the morphology resulted in the different catalytic activities. The $(Cu\text{-}Ru)\text{-}ZrO_2$ composite produced more CO than the $Cu\text{-}ZrO_2$, while $(Cu\text{-}Pd)\text{-}ZrO_2$ and $(Cu\text{-}Ru)\text{-}SiO_2$ produced nothing under the condition. According to the present results, the catalytic activity tests of the metal-oxide composites were done with the feed gas composition #3 in Table 3-1. Compared to the feed gas #1, the total flow rate was reduced to one third, so higher CO_2 conversion was expected.

Table 3-6. Comparison of performance of the Cu/ZrO_2 catalyst and the metal-oxide composites. The temperature was 220°C and the feed gas composition was #1 in Table 3-1 ($H_2/CO_2 = 3$).

Catalyst	Production rate / mmol h^{-1} g_{cat}^{-1}	
	CO	CH_3OH
Cu/ZrO_2 (Cu 10wt%)	0.85	0.23
$Cu\text{-}ZrO_2$ [1:1]	0.03	0
$(Cu\text{-}Ru)\text{-}ZrO_2$ [1:1]	0.06	0
$(Cu\text{-}Pd)\text{-}ZrO_2$ [1:1]	0	0
$(Cu\text{-}Ru)\text{-}SiO_2$ [1:1]	0	0

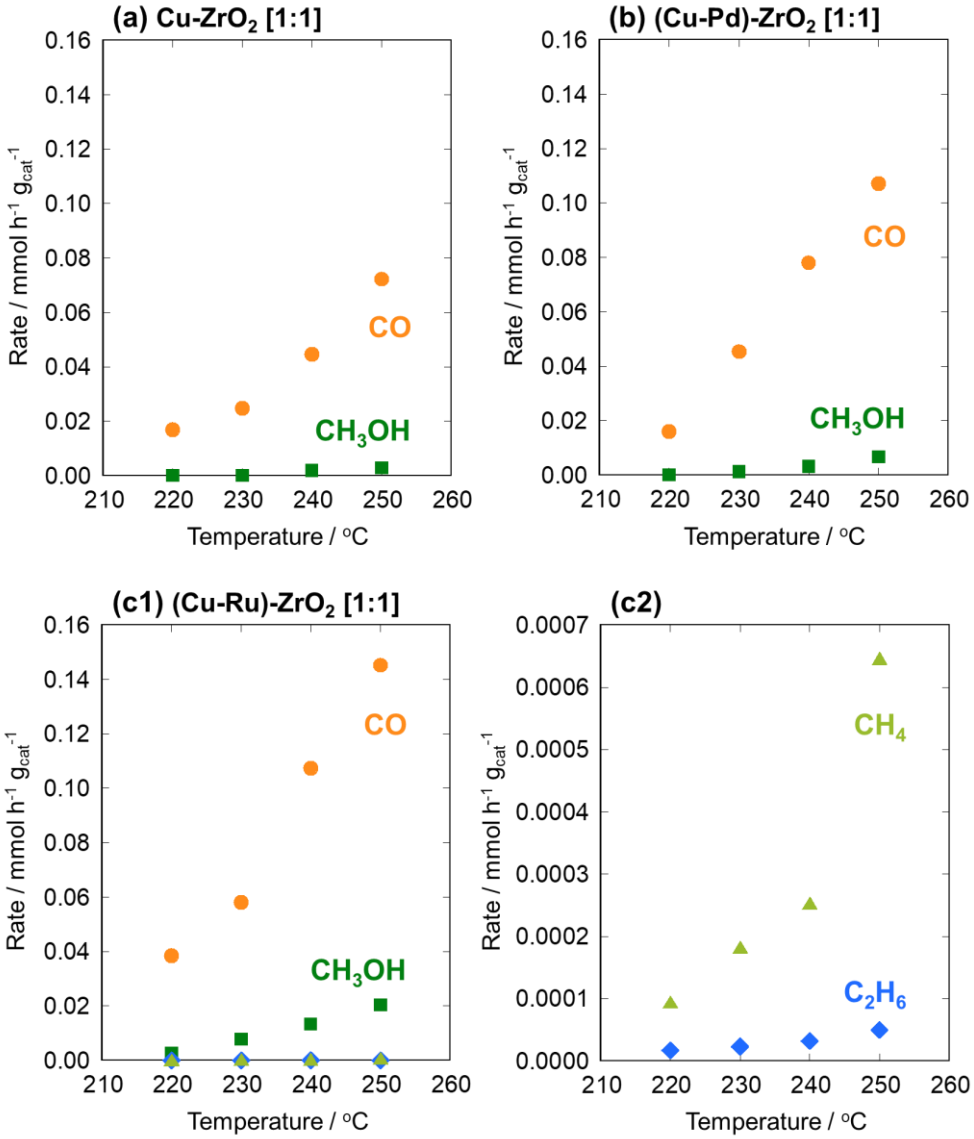

Figure 3-31. Catalytic activity of metal-oxide composites at ambient pressure and different temperatures. The feed gas composition was #3 in Table 3-1 ($H_2/CO_2 = 3$). (a) $Cu\text{-}ZrO_2$ [1:1] composite. (b) $(Cu\text{-}Pd)\text{-}ZrO_2$ [1:1] composite. (c1) $(Cu\text{-}Ru)\text{-}ZrO_2$ [1:1] composite. (c2) Magnified plot of (c1) for methane and ethane.

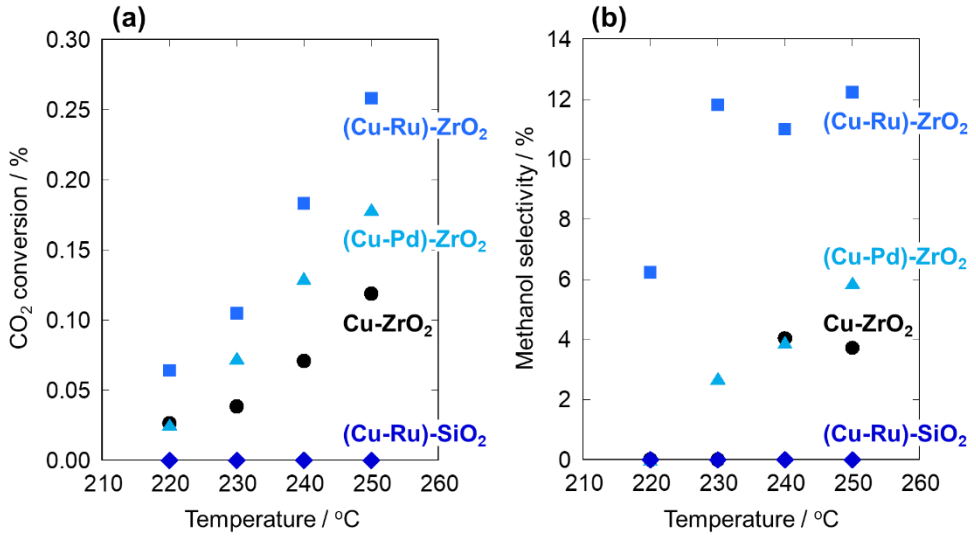

Figure 3-32. Catalytic activity of metal-oxide composites at ambient pressure and different temperatures. The feed gas composition was #3 in Table 3-1 ($H_2/CO_2 = 3$). (a) CO_2 conversion. (b) Methanol selectivity.

Figure 3-31 shows the catalytic activity of metal-oxide composites at ambient pressure and different temperatures. The feed gas composition was #3. Results obtained with the Cu-ZrO_2, (Cu-Pd)-ZrO_2, and (Cu-Ru)-ZrO_2 composites are presented. The (Cu-Ru)-SiO_2 composite was also tested, but no products were detected under examined conditions. The basicity of ZrO_2 was necessary to facilitate the CO_2 activation. CO and methanol were produced with the Cu-ZrO_2, (Cu-Pd)-ZrO_2, and (Cu-Ru)-ZrO_2 composites (Figure 3-31a, b, and c1). The order of the production rates of CO and methanol was (Cu-Ru)-ZrO_2 > (Cu-Pd)-ZrO_2 > Cu-ZrO_2. In the case of (Cu-Ru)-ZrO_2, small amounts of methane and ethane were also detected. The formation of these alkanes is ascribed to the activity of Ru. This means that Ru in the Cu-Ru powder acted as active sites, although its contribution to the overall catalytic activity of the (Cu-Ru)-ZrO_2 composite was not notable. The main reaction site in the tested catalysts is considered to be the boundary of Cu and ZrO_2. Figure 3-32 shows the CO_2 conversion and the methanol selectivity calculated according to Eqs. 3-15 and 3-16, respectively.

$$(\mathrm{CH_3OH\ selectivity}) = \frac{F_{\mathrm{CH_3OH,out}}}{F_{\mathrm{CO,out}}+F_{\mathrm{CH_3OH,out}}+F_{\mathrm{CH_4,out}}+2F_{\mathrm{C_2H_6,out}}} \quad (3\text{-}16)$$

The addition of noble metals (Ru and Pd) to Cu enhanced the CO_2 conversion and the methanol selectivity. The increase of CO_2 conversion may be attributed to hydrogen spillover. It is known that hydrogen

adsorbed on Ru or Pd surface can migrate to adjacent particles. Such an effect can facilitate the hydrogen supply to the main reaction sites (the boundary of Cu and ZrO_2), promoting the conversion of CO_2. According to the literature[199,202], CO_2 hydrogenation with Cu/ZrO_2 catalysts is a successive reaction of the methanol formation from CO_2 and the methanol decomposition to CO. Therefore, suppression of methanol decomposition is required for high methanol selectivity. In the present experiments, the methanol formation was enhanced by the addition of noble metals. On the other hand, it is assumed that the methanol decomposition was not so much promoted as the methanol formation by the noble metals. This is a possible explanation for the increase in the methanol selectivity. The catalytic activity of (Cu-Ru)-ZrO_2 was higher than that of (Cu-Pd)-ZrO_2. The difference may be related to the morphology of the metal particles. As shown in Figure 3-26, primary particles of the Cu-Ru powder were larger than those of the Cu-Pd powder. Thus, it was possible that the number of contacts between the metal particles and the ZrO_2 particles was larger in the case of (Cu-Ru)-ZrO_2. The difference of the significance of the hydrogen spillover effect may also have influenced the results. The noble metals may have altered the electronic state of the adjacent Cu, leading to the different catalytic activities.

Table 3-7 shows the performance of the metal-oxide composites at a low H/CO_2 ratio. The temperature was 250°C and the feed gas composition was #5 in Table 3-1 ($H/CO_2 = 0.1$). It was found that CO and methanol were produced even if the hydrogen partial pressure was low. No other species were detected. The order of catalytic activity was (Cu-Ru)-ZrO_2 > (Cu-Pd)-ZrO_2 > Cu-ZrO_2 > (Cu-Ru)-SiO_2, which was the same as that with the feed gas #3.

Table 3-7. Catalytic performance of the metal-oxide composites at 250°C and ambient pressure with the feed gas composition #5 in Table 3-1 ($H/CO_2 = 0.1$).

Catalyst	Production rate / mmol h^{-1} g_{cat}^{-1}	
	CO	CH_3OH
Cu-ZrO_2 [1:1]	0.022	0.0011
(Cu-Ru)-ZrO_2 [1:1]	0.070	0.0012
(Cu-Pd)-ZrO_2 [1:1]	0.043	0.0011
(Cu-Ru)-SiO_2 [1:1]	0	0

3.2.3.3. SAECs with type-1 cathodes

First, the reaction test results with the type-1a cathodes are discussed. Figure 3-33 shows the cell voltages during 20 mA cm^{-2} galvanostatic operations at 250°C under the H_2 production condition and the CO_2 electrolysis condition. For the hydrogen production (Figure 3-33a), the cell voltage with the Ru/ZrO_2 and Pd/ZrO_2 layers were around -2.4 V, which is consistent with the results in Section 3.1. The cell voltage with the Cu/ZrO_2 layer was much lower (< -3 V). The reason for this behavior is not clear at the present stage. For the CO_2 electrolysis (Figure 3-33b), the cell voltage was first decreased and then increased back, and finally became constant. For all the catalysts, the cell voltage became lower than that in the hydrogen production. This is mainly due to the increase in non-ohmic overpotentials. Unreacted CO_2 and product gases (mainly CO) might approach the Pt/C electrocatalyst layer and adsorb on the Pt/C surface to hinder the kinetics of hydrogen evolution.

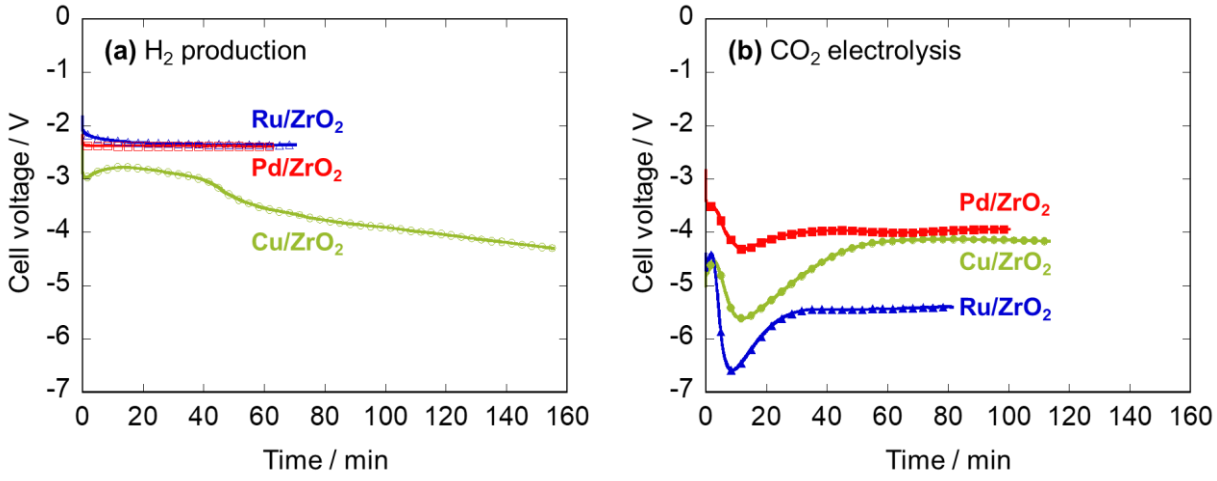

Figure 3-33. Cell voltage during (a) H_2 production (cathode inlet: N_2/H_2O = 9/1 mL min^{-1}) and (b) CO_2 electrolysis (cathode inlet: $CO_2/N_2/H_2O$ = 5/4/1 mL min^{-1}) with different type-1a cathodes. In all measurements, the temperature was 250°C, and the current density was fixed at 20 mA cm^{-2}. In the CO_2 electrolysis mode, the current density of 20 mA cm^{-2} corresponded to H^+/CO_2 = 0.048.

Figure 3-34 shows the nominal Faraday efficiencies calculated from the cathode outlet gas compositions (corresponding to Figure 3-33). The values were taken when the cell voltage and the signals of gas chromatographs became stable. In all cells, the FE for the hydrogen production exceeded 80% (Figure

3-34a). This is consistent with the results in Section 3.1. In the CO_2 electrolysis condition, the current density of 20 mA cm^{-2} corresponded to $H^+/CO_2 = 0.048$. CO was produced with all the catalysts. Methane was detected only in the case of Ru/ZrO_2. It was demonstrated that the reactivity of CO_2 and the selectivity for products vary depending on the active metal species. Methane was not detected with the Pd/ZrO_2 catalyst, and methanol was not detected with the Cu/ZrO_2 catalyst. These results were possibly due to the low reaction rates. The catalytic activity of Pd/ZrO_2 and Cu/ZrO_2 were not high enough to produce detectable amounts of methane or methanol under the examined condition. For Cu/ZrO_2, it was also speculated that the surface of Cu was oxidized and lost the activity for the methanol formation.

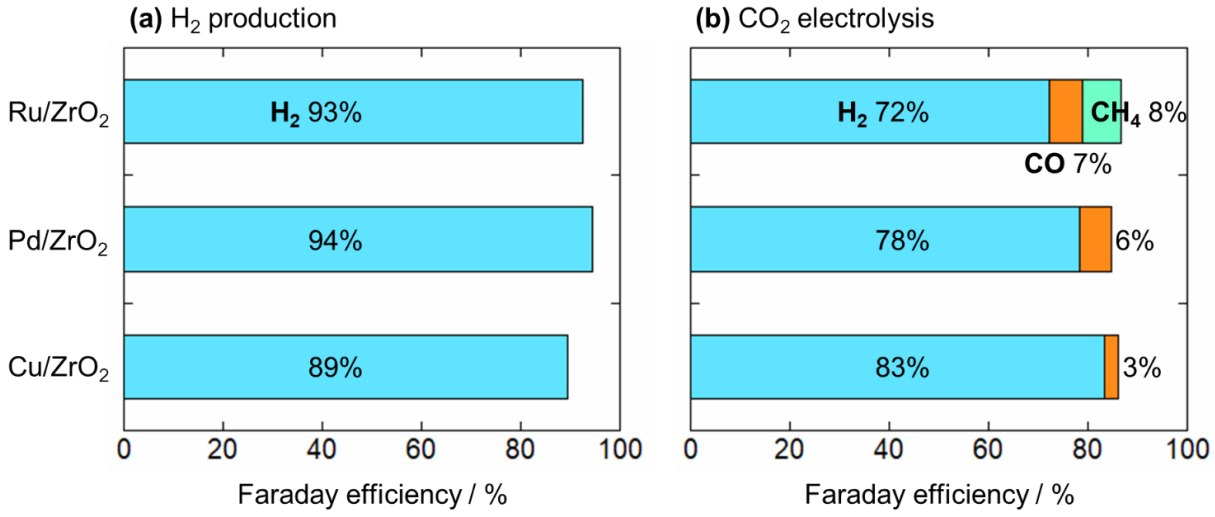

Figure 3-34. Nominal Faraday efficiencies recorded with different type-1a cathodes. (a) H_2 production condition (cathode inlet: N_2/H_2O = 9/1 mL min^{-1}). (b) CO_2 electrolysis condition (cathode inlet: $CO_2/N_2/H_2O$ = 5/4/1 mL min^{-1}). In both cases, the temperature was 250°C, and the current density was fixed at 20 mA cm^{-2}. In the CO_2 electrolysis mode, the current density of 20 mA cm^{-2} corresponded to $H^+/CO_2 = 0.048$.

In the cells with type-1a cathodes, the CO_2 conversion and the selectivity to methane (and methanol) were lower than the maximum values predicted by thermodynamics. One of the possible reasons is that the gas contact time was quite short in the present reactor configuration. Type-1b cathode was developed aiming at increasing the gas contact time. Although the exact thickness of the catalyst layer under operation was not measurable, the thickness can be estimated from the thickness of PTFE sheets where the catalyst was

located. In the type-1a cathodes, the catalyst disk was put in a 0.5 mm-thick PTFE sheet. On the other hand, the catalyst pellets in the type-1b cathode were put in a 3 mm-thick PTFE sheet. Therefore, roughly estimated, the type-1b catalyst layer was about six times thicker than the type-1b catalyst disk. If all the feed gas flows through the catalyst layer, the gas contact time will increase sixfold. Figure 3-35 compares the nominal Faraday efficiencies recorded with type-1a cathode and type-1b cathode based on Ru/ZrO_2. Being against the expectation, the efficiencies with the type-1b cathode were comparable or even inferior to those with the type-1a cathode. As illustrated in Figure 3-1, the reactor has a double-tube structure: the inlet gas is delivered to the electrode through the inner tube, and the outlet gas is discharged from the outer tube. Figure 3-36 shows schematic images of the reactor configurations with type-1a cathodes and the type-1b cathode. There is some space between the inner tube and the electrode surface, so it is possible that a part of the inlet gas is discharged without any contact with the electrodes. This may be the reason why the CO_2 electrolysis performance was not improved by employing the type-1b cathode. By designing gas flow channels properly, the gas contact time will increase. To develop the practical SAEC reactors, the reactor design is important as well as the intrinsic performance of the cell.

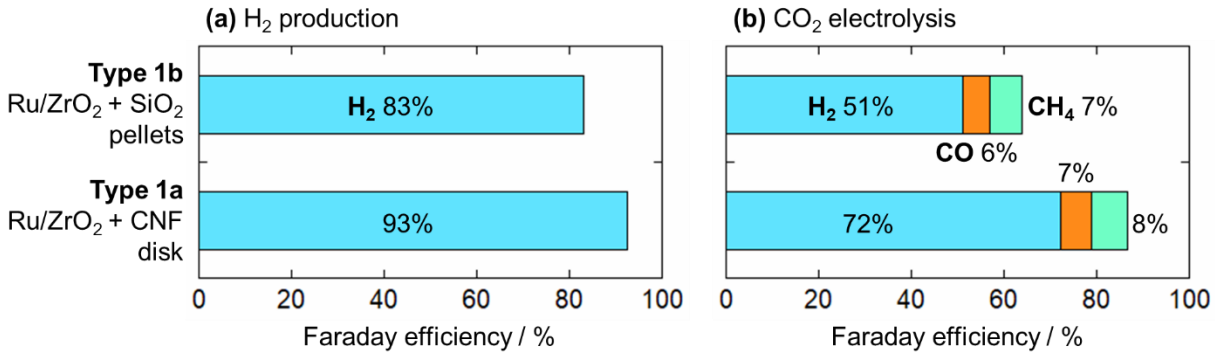

Figure 3-35. Nominal Faraday efficiencies recorded with different cathode configurations. Type-1a cathode and type-1b cathode based on Ru/ZrO_2 are compared. (a) H_2 production condition (cathode inlet: N_2/H_2O = 9/1 mL min^{-1}). (b) CO_2 electrolysis condition (cathode inlet: $CO_2/N_2/H_2O$ = 5/4/1 mL min^{-1}). In all cases, the temperature was 250°C, and the current density was fixed at 20 mA cm^{-2}. In the CO_2 electrolysis mode, the current density of 20 mA cm^{-2} corresponded to H^+/CO_2 = 0.048.

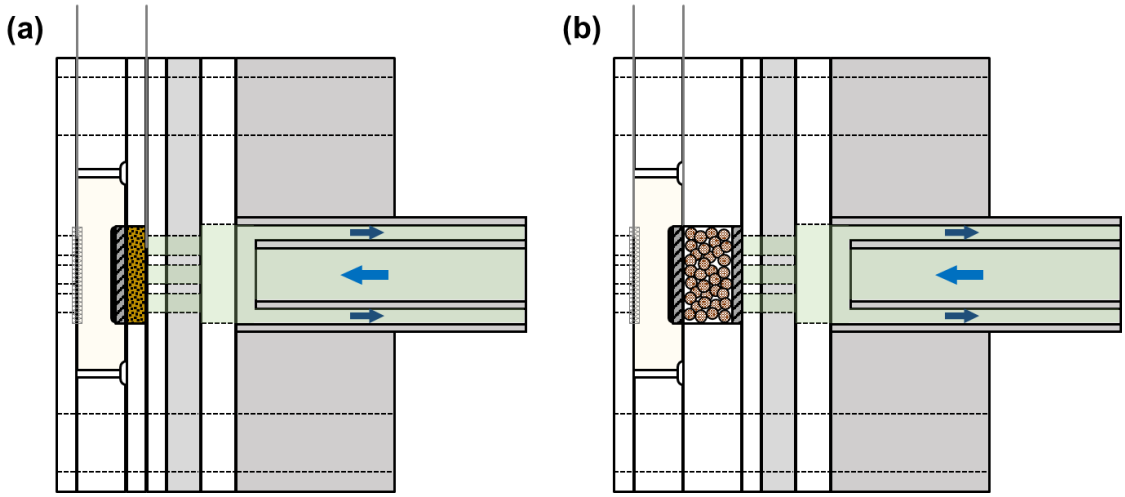

Figure 3-36. Schematic images of the reactor configurations with type-1 cathodes. (a) Type 1a. (b) Type 1b. Pale-green shading indicates the cathode gas flow channel. The anode side is omitted.

Figure 3-37 shows the methane selectivity at different current densities recorded with the type-1b cathode. The selectivity increased with the current density. This can be ascribed to the increase in the hydrogen partial pressure at large current densities. The high hydrogen partial pressure increased the rate of the methanation reaction. Note that the NEMCA effect (Section 1.4) is not expected in the type-1b case because the current was collected from the Pt/C sheet and no potential gradient was applied to the catalyst layer.

Figure 3-38 shows the cell voltage at different current densities (corresponding to Figure 3-37). At 20, 40, and 60 mA cm^{-2}, the cell voltage became nearly constant in 40 min. However, at 100 mA cm^{-2}, the voltage behaved differently from the other cases and reached -10 V or even lower. This suggests that 100 mA cm^{-2} was too large for the present cell to be operated stably.

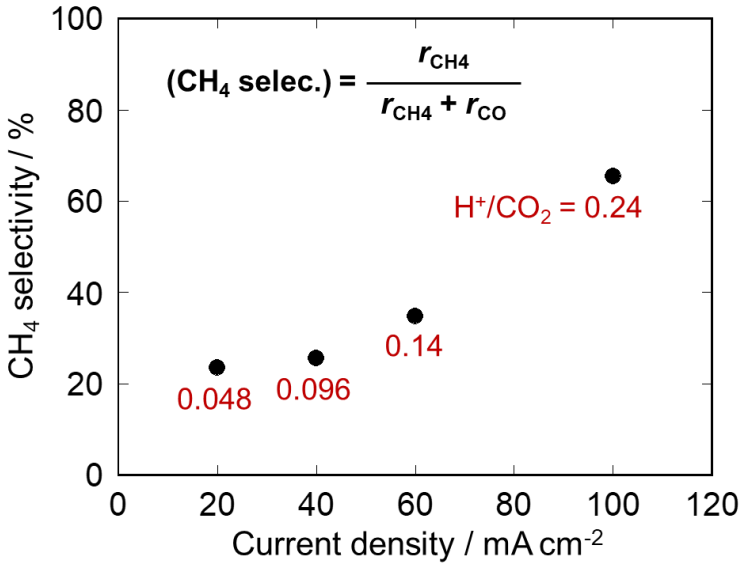

Figure 3-37. Methane selectivity at different current densities recorded with the type-1b cathode (pelletized Ru/ZrO_2 + SiO_2). A cathode inlet gas of $CO_2/N_2/H_2O$ = 5/4/1 mL min^{-1} was used. The cell operation temperature was 250°C. H^+/CO_2 ratios at each current density are also shown.

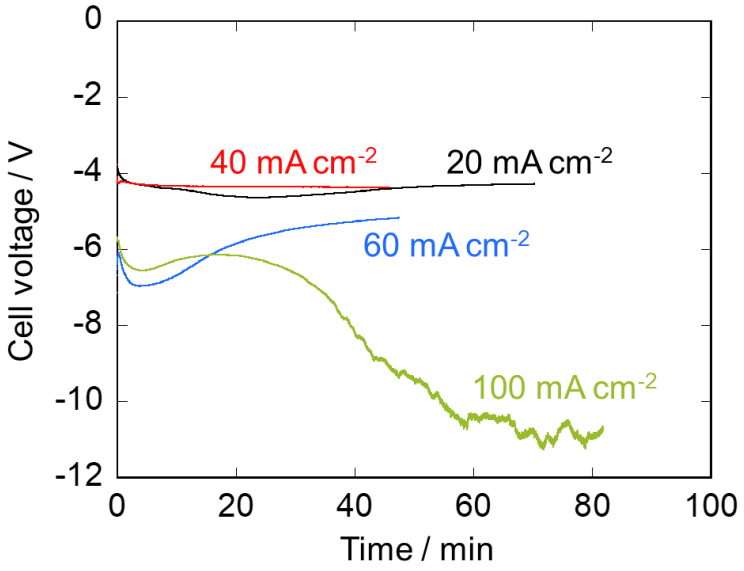

Figure 3-38. Cell voltage during the galvanostatic tests at different current densities with a type-1b cathode (pelletized Ru/ZrO_2 + SiO_2). A cathode inlet gas of $CO_2/N_2/H_2O$ = 5/4/1 mL min^{-1} was used. The cell operation temperature was 250°C.

3.2.3.4. SAECs with type-2 cathodes

Figure 3-39 shows the Faraday efficiencies for hydrogen production recorded with different type-2 cathodes. The cathode feed gas was 10 mL min^{-1} dry N_2. In all cases, the FE exceeded 80%, indicating that the cells were applicable for hydrogen production. It is considered that the boundary of Cu-based metal and the electrolyte worked as the active site for the hydrogen evolution.

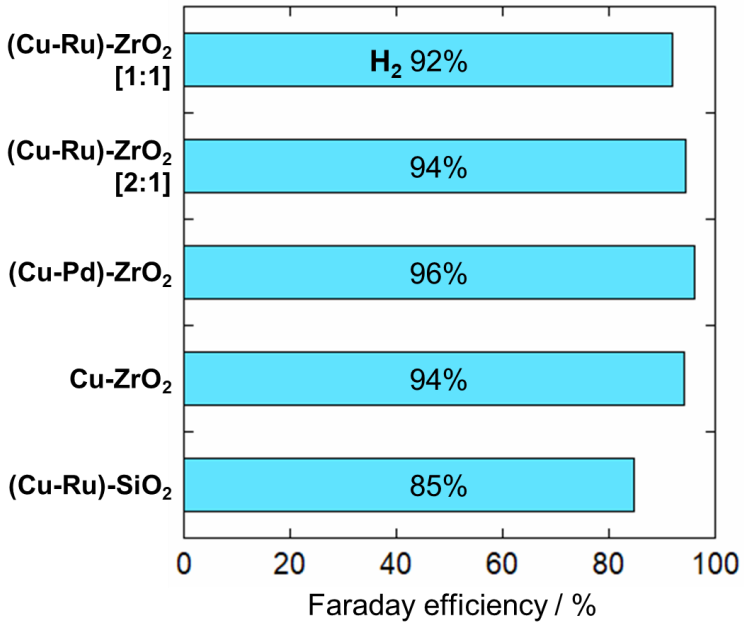

Figure 3-39. Faraday efficiencies for hydrogen production recorded with different type-2 cathodes. 10 mL min^{-1} of N_2 was fed to the cathode. The temperature was 220°C, and the current density was fixed at 50 mA cm^{-2}.

Under the CO_2 electrolysis condition (cathode feed gas: CO_2/N_2 = 5/5 mL min^{-1}), no products were detected under open circuit conditions. By applying a constant current load of 50 mA cm^{-2} (H^+/CO_2 = 0.12), several carbon-containing species were produced besides hydrogen. When only N_2 was introduced to the cathode, no carbon-containing compounds were produced with a current load of 50 mA cm^{-2} (Figure 3-39). Therefore, the carbon-containing species observed under the CO_2 electrolysis condition were synthesized from CO_2 in the feed gas. Figure 3-40 shows nominal Faraday efficiencies of recorded with different type-2 cathodes (metal:oxide = 1:1). The products include hydrogen, CO, methane, methanol,

ethane, ethylene, ethanol, acetaldehyde, and propylene. Acetaldehyde was quantified only in the case of the (Cu-Ru)-ZrO_2 [1:1] cathode. With the other cathodes, the amount of acetaldehyde was less than the detection limit of the GC-FID. To the best of the author's knowledge, this is the first demonstration of the production of methanol, ethane, ethylene, ethanol, acetaldehyde, and propylene in SAECs. In the thermocatalytic activity tests, carbon-containing products were CO, methanol, methane, and ethane (Figure 3-31). The formation of ethylene, ethanol, acetaldehyde, and propylene was unique to the electrochemical CO_2 hydrogenation. Figure 3-40a shows the overview of the FEs. The total Faraday efficiencies were 40-65%, which are much lower than the FEs recorded in the steam electrolysis tests (Figure 3-39). This may be attributed to the partial dehydration of the electrolyte. In the type-2 cathode tests, the cathode feed gas was not humidified to facilitate the CO_2 conversion. Thus, there was the risk of the dehydration. When the electrolyte was partially dehydrated, the gas tightness might become lower, and the gas crossover could be facilitated. If that was the case, produced hydrogen or the other compounds could be re-oxidized to H_2O and CO_2, leading to the lower nominal Faraday efficiencies. Figure 3-40b shows the detailed results of products other than hydrogen and CO (denoted as highly-reduced products hereafter). Comparing the ZrO_2-containg cathodes, the total FE for the highly-reduced products was the largest with the (Cu-Ru)-ZrO_2 cathode, followed by (Cu-Pd)-ZrO_2 and Cu-ZrO_2. Even though the CO_2 conversion was different among the ZrO_2-containg cathodes, the selectivity for the highly-reduced products was almost the same. It is considered that the noble metal additives (Ru and Pd) were not so responsible for the product selectivity but mainly helped Cu function as the active sites. The superiority of the (Cu-Ru)-ZrO_2 and (Cu-Pd)-ZrO_2 cathodes over the Cu-ZrO_2 cathode can be attributed to the existence of hydrogen spillover effect. The hydrogen spillover from the noble metals to Cu may have prevented the oxidation of the Cu surface by steam. Comparing the (Cu-Ru)-ZrO_2 cathode and the (Cu-Ru)-SiO_2 cathode, the Faraday efficiencies were higher with the former cathode. ZrO_2 is a basic oxide and has high CO_2 adsorptivity than SiO_2, so the use of ZrO_2 may facilitate the CO_2 supply to the reaction sites. The impact of the choice of oxide materials on the CO_2 electrolysis performance was moderate. The (Cu-Ru)-SiO_2 composite showed no thermocatalytic activity, but the composite worked successfully as a

cathode in the electrolysis. This suggests that the reaction pathways in the CO_2 electrolysis may be different from those in the thermal CO_2 hydrogenation.

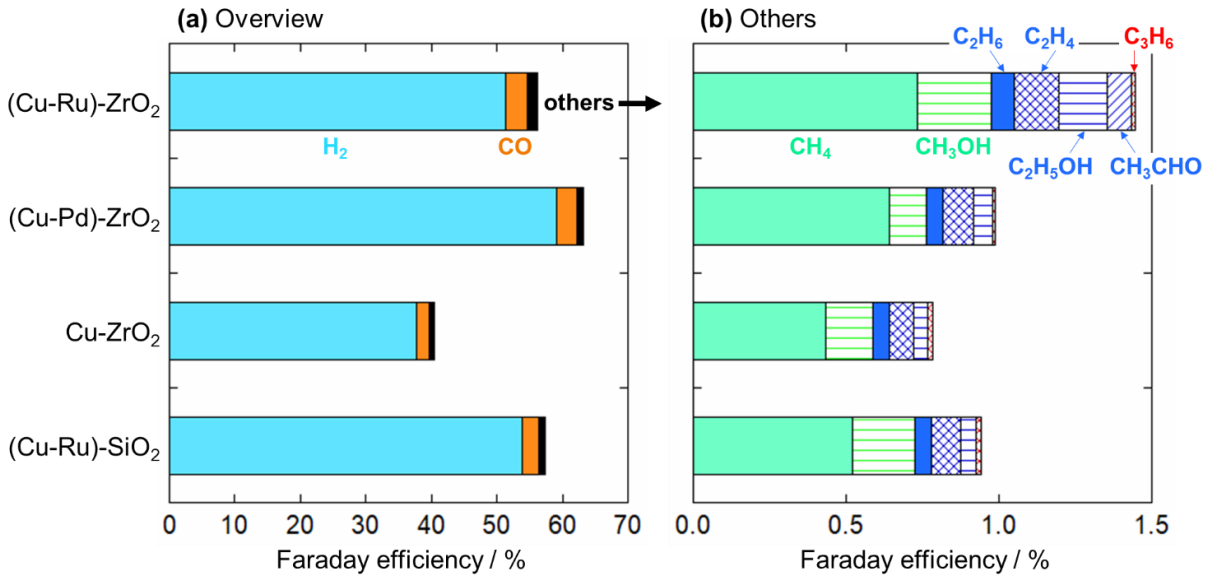

Figure 3-40. Nominal Faraday efficiencies of products recorded with different type-2 cathodes (metal:oxide = 1:1). (a) Overview. (b) Detailed results of products other than hydrogen and CO. For all cathodes, the weight ratio of the metal powder to the oxide powder was 1:1. A cathode inlet gas of CO_2/N_2 = 5/5 mL min^{-1} was used. The temperature was 220°C, and the current density was fixed at 50 mA cm^{-2} (H^+/CO_2 = 0.12).

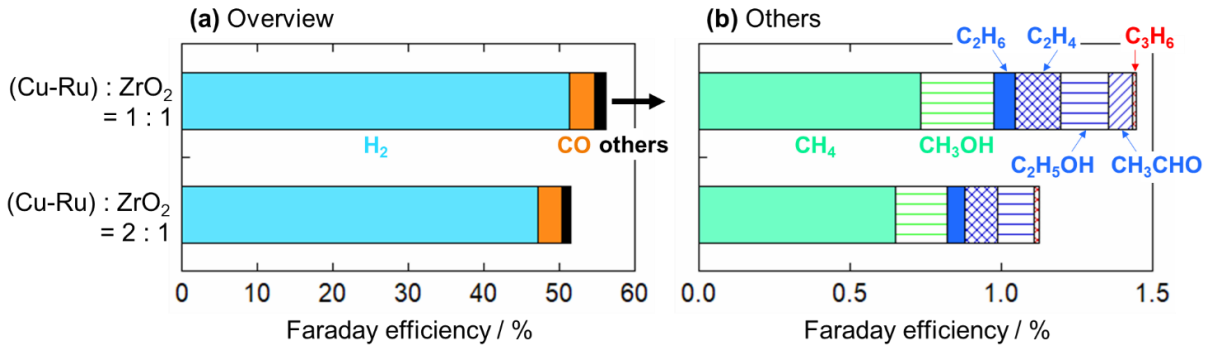

Figure 3-41. Nominal Faraday efficiencies of products recorded with (Cu-Ru)-ZrO_2 [1:1] cathode and (Cu-Ru)-ZrO_2 [2:1] cathode. (a) Overview. (b) Detailed results of products other than hydrogen and CO. A cathode inlet gas of CO_2/N_2 = 5/5 mL min^{-1} was used. The temperature was 220°C, and the current density was fixed at 50 mA cm^{-2} (H^+/CO_2 = 0.12).

Figure 3-41 compares the results obtained with the (Cu-Ru)-ZrO_2 [1:1] cathode and the (Cu-Ru)-ZrO_2 [2:1] cathode. Even though the latter cathode contains twice as much metal as the former, the Faraday efficiencies for the highly-reduced products are lower. This implies that the metal powders in the cathodes are not fully utilized.

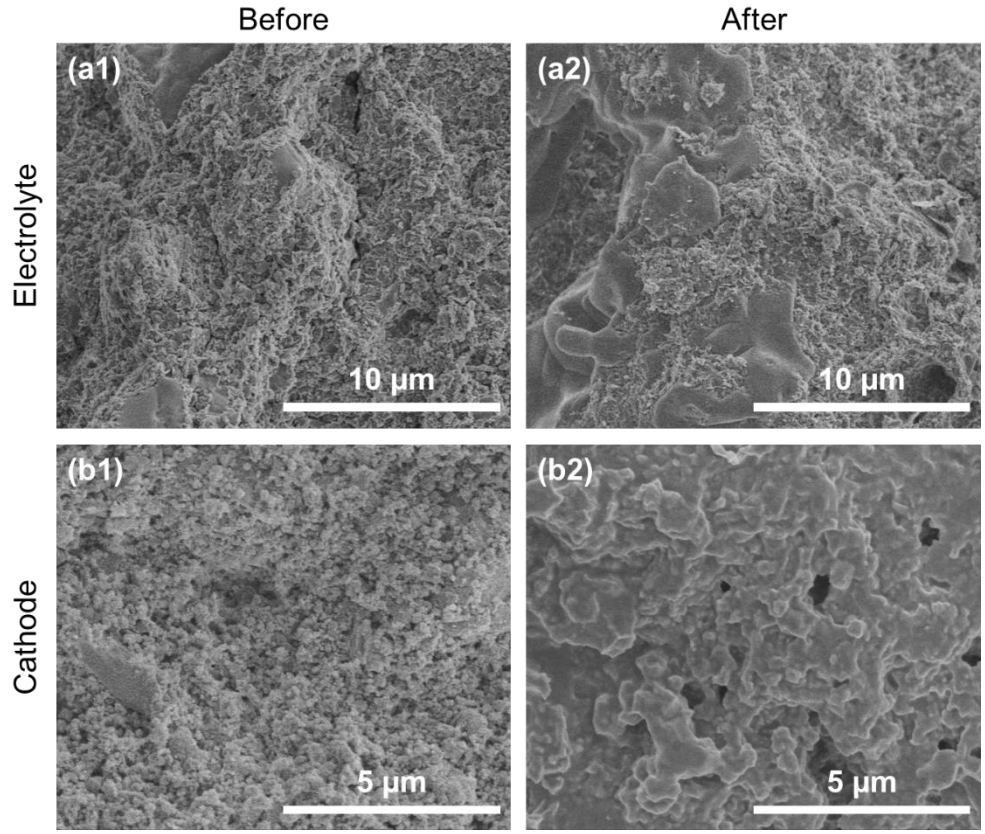

Figure 3-42. SEM images of cross sections of the CsH_2PO_4/SiP_2O_7 electrolyte and the (Cu-Ru)-ZrO_2 [1:1] cathode before and after the 50 mA cm^{-2} galvanostatic CO_2 electrolysis test at 220°C.

Figure 3-42 shows the SEM images of cross sections of the CsH_2PO_4/SiP_2O_7 electrolyte and the (Cu-Ru)-ZrO_2 [1:1] cathode before and after the 50 mA cm^{-2} galvanostatic CO_2 electrolysis test at 220°C. Grains with a size of < 1 μm were observed in the electrolyte before the test (Figure 3-42a1). After the test, smooth structure with a size of ~10 μm was appeared (Figure 3-42a2). This should be the CsH_2PO_4 or $CsH_5(PO_4)_2$, which were in a viscous state during the operation at 220°C. In the cathode before the test (Figure 3-42b1), grains with a size of 100-500 nm were observed. After the test, the morphology was

changed notably. It seems that the grains were covered by a smooth layer (Figure 3-42b2). This can be attributed to the migration of the electrolyte, which was found by the SEM-EDX analysis. Figure 3-43 shows the SEM-EDX analysis results of different type-2 cathodes. The location of the cathodes can be identified by the distribution of Cu and noble metals. Before the test, Cs element was hardly detected from the (Cu-Ru)-ZrO_2 [1:1] cathode (Figure 3-43a). On the contrary, Cs was detected from the cathode layer after the test (Figure 3-43b). The trend was the same in the (Cu-Pd)-ZrO_2 cathode, the Cu-ZrO_2 cathode, the (Cu-Ru)-ZrO_2 [2:1] cathode, and the (Cu-Ru)-SiO_2 cathode (Figure 3-43c, d, e, and f). These results indicate that the electrolyte migrated to the cathode during the operation. As discussed in Section 3.1, electrolyte migration to cathodes was not observed in the Pt/C|CsH_2PO_4/SiP_2O_7|Pt/C cell. The migration to the type-2 cathodes may have been facilitated by the capillary phenomenon and/or the wettability of the oxide phase (ZrO_2 or SiO_2). Because the electrolyte migration decreases the cathode porosity, the gas diffusion inside the cathode layer might be suppressed. This is consistent with the consideration that the metal powders in the cathodes are not fully utilized (Figure 3-41).

Figure 3-44 shows the cell voltage during the 50 mA cm^{-2} galvanostatic tests with different type-2 cathodes. The voltage became stable in *ca.* 30 min, except the turbulence observed with Cu-ZrO_2 and (Cu-Ru)-SiO_2. The turbulence may have been caused by the gas crossover between the anode side and the cathode side. In all cases, the average cell voltage was *ca.* -7 V or lower, which indicated large overpotentials. Improvement of cell components is required to suppress the overpotential. Development of thinner electrolyte will decrease the ohmic overpotential. Optimization of the anode material and structure will result in the decrease in the anodic overpotentials. As mentioned in Section 3.1, the Pt mesh anode has much room for the improvement. Increasing the cathode porosity will also contribute to the superior current-voltage characteristics. Use of reference electrodes is desired to distinguish the components of the cell overpotential. Development of novel experimental setup suitable for the use of reference electrodes is needed.

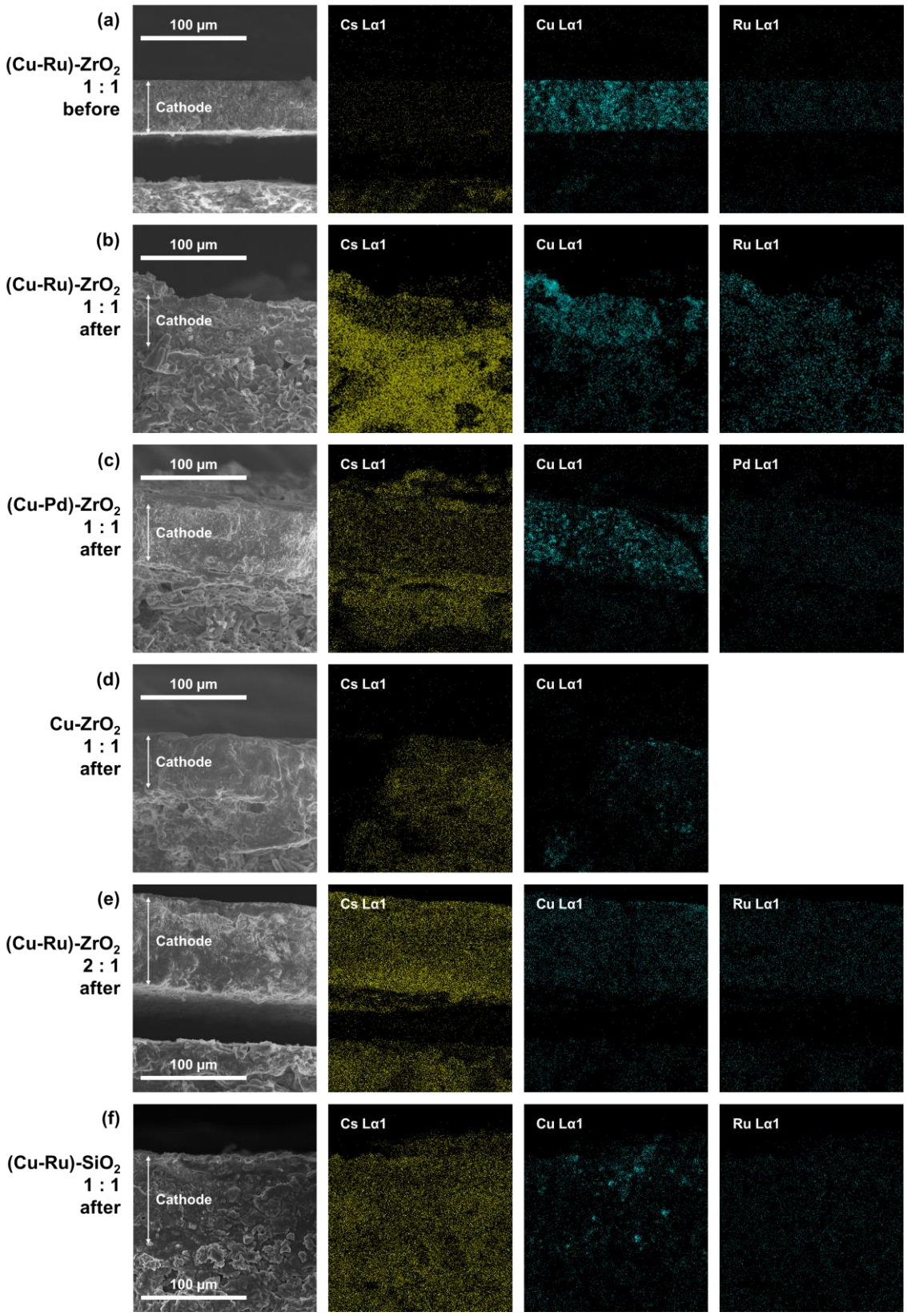

Figure 3-43. SEM-EDX analysis of different type-2cathodes. (a) As prepared (Cu-Ru)-ZrO_2 [1:1] cathode. (b-f) Cathodes after the 50 mA cm^{-2} galvanostatic CO_2 electrolysis tests at 220°C. For each cathode, an SEM image of a cross section and corresponding EDX mappings are shown.

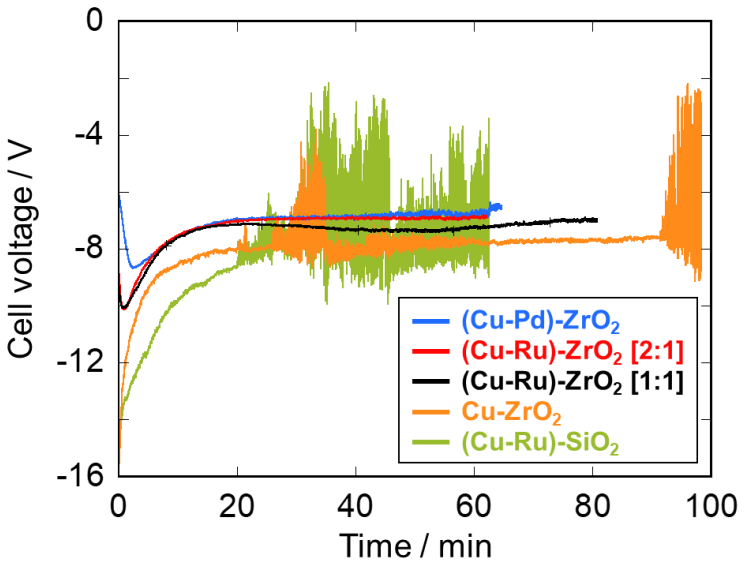

Figure 3-44. Cell voltage during the 50 mA cm^{-2} galvanostatic tests with different type-2 cathodes (H^+/CO_2 = 0.12). A cathode inlet gas of CO_2/N_2 = 5/5 mL min^{-1} was used. The cell operation temperature was 220°C.

The reactivity of protons and hydrogen gas were compared using a cell with the (Cu-Ru)-ZrO_2 [1:1] cathode. The experimental conditions are summarized in Table 3-3. Entries #1 and #3 were performed under open circuit conditions by introducing hydrogen gas to the cathode. The amount of hydrogen gas was controlled so that the number of supplied H atoms corresponded to current densities of 50 mA cm^{-2} and 25 mA cm^{-2} (H^+/CO_2 = 0.037 and 0.075, respectively). However, no carbon-containing products were observed in these cases, *i.e.*, the (Cu-Ru)-ZrO_2 [1:1] cathode exhibited no thermal catalytic activity under the tested conditions. One possible reason is the short gas contact time discussed above. In addition, the existence of the electrolyte material may have decreased the catalytic activity of the (Cu-Ru)-ZrO_2 composite. As found in Section 3.2.3.2, the catalytic activity of Cu/ZrO_2 catalyst was weakened by the existence of CsH_2PO_4. Similar phenomenon may have happened in the present cases. Entries #2 and #4 are CO_2 electrolysis tests. 50 mA cm^{-2} and 25 mA cm^{-2} were applied, respectively. Hydrogen, CO, methane, methanol, ethane, and ethylene were detected from the cathode outlet gas. The amount of produced ethanol, acetaldehyde, and propylene was too small to detect by gas chromatographs. Figure 3-45 shows the comparison of methanol production rates. Data obtained in the thermocatalytic experiments (entries #1 and #3) and the electrochemical experiments (Entries #2 and #4) are compared

with theoretical rates. The theoretical values were calculated by using *Aspen Plus* model developed in Section 2.2. Blue squares indicate the rates calculated by assuming the thermodynamic equilibrium with CO. Hydrogen, methanol, and CO were considered as the possible products. The rates are quite small (8.3×10^{-15} mol s^{-1} cm^{-2} and 7.0×10^{-14} mol s^{-1} cm^{-2} for 25 mA cm^{-2} and 50 mA cm^{-2}, respectively) and indicate that the methanol production is not favored thermodynamically. Green triangles indicate theoretical methanol production rates calculated by assuming the thermodynamic equilibrium without CO. Only hydrogen and methanol were considered as the possible products. This corresponds to the situation where methanol is synthesized from CO_2 without forming CO, and methanol decomposition is perfectly suppressed. Despite the idealization, the calculated rates are smaller than the CO_2 electrolysis results (black circles). These results clearly show that the protons are more reactive than the gaseous hydrogen. The methanol production rates larger than the equilibrium values suggest that the CO_2 reduction proceeded electrochemically. In other words, reaction pathways different from those of thermochemical CO_2 hydrogenation existed, where protons and electrons were directly functioned as reducing agents. The present result indicates the possibility of methanol production under atmospheric pressure by utilizing the electrochemical reaction pathways.

Figure 3-46 shows the time courses of the production rates of CO and highly-reduced products during the 50 mA cm^{-2} CO_2 electrolysis test with the (Cu-Ru)-ZrO_2 [1:1] cathode. A constant current load of 50 mA cm^{-2} corresponded to $H^+/CO_2 = 0.12$. Methanol, ethanol, and acetaldehyde were analyzed by the GC-FID, and three data points are available. Ethanol and acetaldehyde were not detectable in the second and the third measurements. The other products were analyzed by the GC-TCD, and 24 data points are available. For all the products, the rates were not constant during the 50 mA cm^{-2} galvanostatic operation: the rate increased sharply and then decreased. The exact reason of the decrease is unclear, but the phenomenon might be ascribed to the gas crossover between the anode chamber and the cathode chamber.

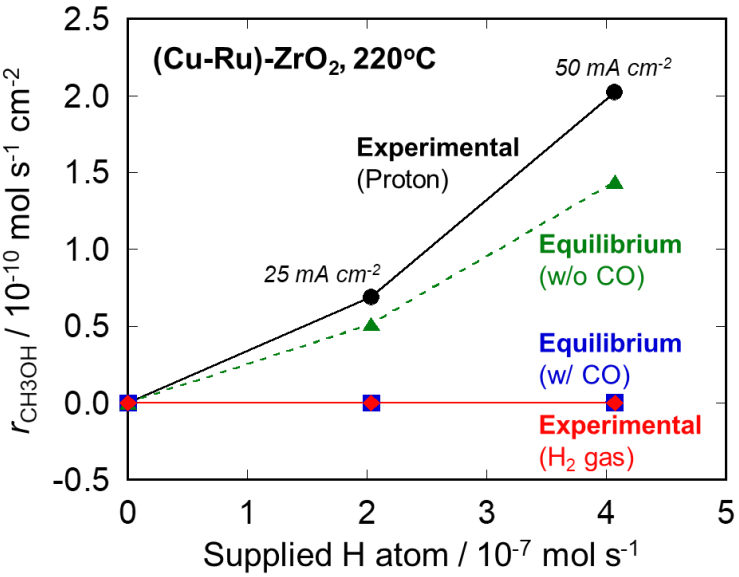

Figure 3-45. Comparison of methanol production rates obtained with the (Cu-Ru)-ZrO_2 [1:1] cathode at 220°C. **(Circle)** Experimental data recorded under constant current densities. The cathode feed gas was CO_2/inert = 8/12 mL min^{-1}. 25 mA cm^{-2} and 50 mA cm^{-2} correspond to H^+/CO_2 = 0.037 and 0.075, respectively. **(Diamond)** Experimental data obtained under open circuit conditions with gaseous hydrogen in the cathode feed. The cathode gas composition was CO_2/inert/H_2 = 8/12/*x* mL min^{-1}. *x* was determined so that the number of supplied H atoms became the same as that of the electrochemical tests. **(Triangle)** Theoretical rates calculated by assuming the thermodynamic equilibrium. Only hydrogen and methanol were considered as the possible products (CO was excluded). **(Square)** Theoretical rates calculated by assuming the thermodynamic equilibrium. Hydrogen, methanol, and CO were considered as the possible products.

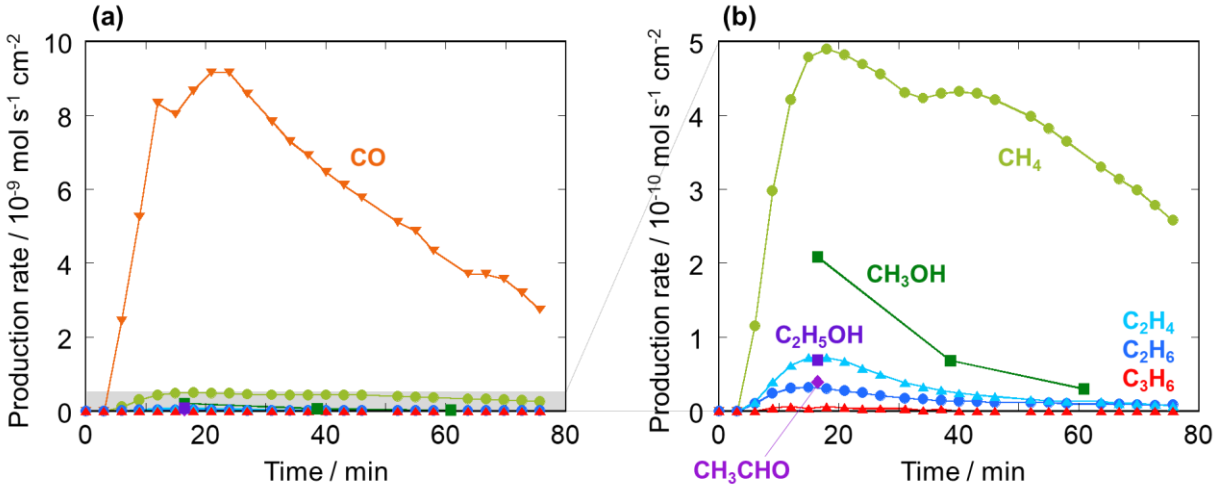

Figure 3-46. Time courses of the production rates of CO, methane, methanol, ethane, ethylene, ethanol, acetaldehyde, and propylene with the (Cu-Ru)-ZrO_2 [1:1] cathode. The cathode inlet gas composition was CO_2/N_2 = 5/5 mL min^{-1}. A constant current load of 50 mA cm^{-2} was applied (H^+/CO_2 = 0.12). The cell operation temperature was 220°C.

To extract information about the reaction pathways, the $(r_{C2H6} + r_{C2H4})/r_{CH4}$ ratio was calculated. r_{C2H6}, r_{C2H4}, and r_{CH4} are the production rates of ethane, ethylene, and methane. This analysis is based on the assumption that the decrease in the total Faraday efficiency (or the production rates) are independent from the product selectivity. Figure 3-47 shows the time courses of the $(r_{C2H6} + r_{C2H4})/r_{CH4}$ ratio with different cathodes. In all cases, the ratio decreases with time, indicating the decline in the selectivity for C2 species. This phenomenon may be related to the surface coverage of the cathode catalyst. Under open circuit conditions, CO_2 molecules are adsorbed on the catalyst surface. Once the current is applied, those molecules may react with protons to form CO or other products. It is assumed that the hydrogen evolution occurs more easily than the CO_2 hydrogenation. Therefore, more and more reaction sites (triple-phase boundary of Cu, oxide, and gas) will be used for the hydrogen evolution with time. If that is the case, the surface coverage of hydrogen species will increase and less sites will be available for CO_2 adsorption. The decrease in the population of CO_2-derived species will prevent them to meet each other, suppressing the formation of C-C bonds. The decrease in the $(r_{C2H6} + r_{C2H4})/r_{CH4}$ ratio was moderate with the Cu-ZrO_2 cathode compared to the other cathodes. This can be explained by the hydrogen spillover effect of noble metals. When Ru or Pd is present, hydrogen is supplied from those noble metals to the reaction sites, increasing the surface coverage of hydrogen species. Because noble metals were absent in the Cu-ZrO_2 cathode, the increase in the population of hydrogen species around the reaction sites was suppressed, and the selectivity for C2 species was maintained. On the contrary, the decrease in the $(r_{C2H6} + r_{C2H4})/r_{CH4}$ ratio was most significant with the (Cu-Ru)-ZrO_2 [2:1] cathode. Because the volumetric ratio of ZrO_2 to the Cu-based metal is small in the (Cu-Ru)-ZrO_2 [2:1] cathode, the concentration of CO_2-derived species might be decreased easily. In the present case, the cathode feed gas was the mixture of CO_2 and N_2. N_2 was introduced as the internal standard for the gas chromatograph analysis. Higher CO_2 partial pressures may be beneficial to maintain the surface coverage of CO_2-derived species. Further examinations are needed to verify the considerations. Direct observation of surface adsorbed species by spectroscopic techniques is desirable.

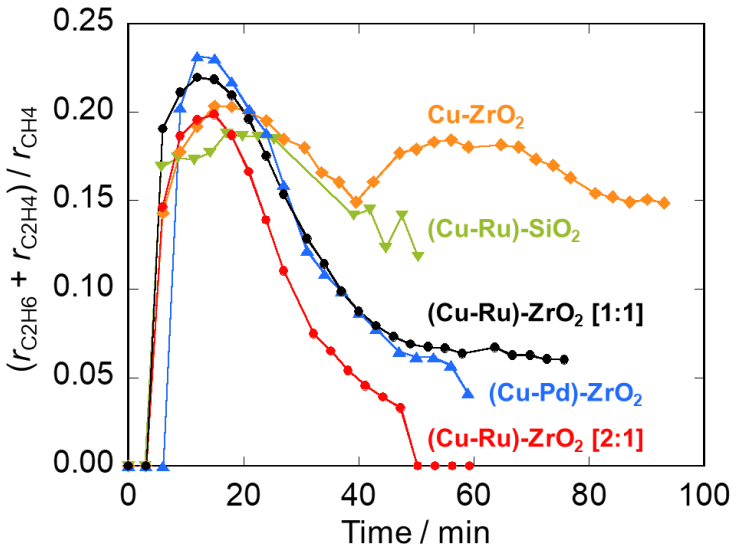

Figure 3-47. Time courses of the $(r_{C2H6} + r_{C2H4})/r_{CH4}$ ratio with different cathodes. The cathode inlet gas composition was CO_2/N_2 = 5/5 mL min^{-1}. A constant current load of 50 mA cm^{-2} was applied (H^+/CO_2 = 0.12). The cell operation temperature was 220°C.

Based on the experimental results, possible reaction pathways are speculated. Reported reaction mechanisms of thermocatalytic CO_2 hydrogenation[203–205] and electrochemical CO_2 reduction in aqueous electrolytes[85,206–208] were referred to. In low-temperature CO_2 electrolysis systems, Cu can produce various hydrocarbons and oxygenates (Section 1.3.1.2). The variety of products in the present system is similar to that in the low-temperature systems, suggesting the occurrence of the direct electrochemical reduction steps with protons. As depicted in Figure 3-20, protons can travel through ZrO_2 and access the reaction sites. However, it was found that the electrolyte migrated into the cathode layer during the operation (Figure 3-43). Therefore, protons might have been directly supplied to the reaction sites in the present study.

Figure 3-48 illustrates the plausible reaction pathways. Steps indicated by light-blue arrows are considered characteristic of electrochemical hydrogenation by protons and electrons. CO_2 adsorbed on the Cu-based metal can form surface carboxyl groups (*COOH). Hereafter, the asterisk (*) is used to indicate the surface species. The carboxyl groups are further reduced to form carbonyl species (*CO). This route is reported in low-temperature CO_2 electrolysis systems[206]. On the other hand, CO_2 adsorbed on the oxide (ZrO_2 or SiO_2) is converted into bicarbonate (*HCO_3) and formate (*HCOO). Formate is

further reduced to form carbonyl or methoxy (*OCH_3). The direct formation of methoxy from formate is reported in thermal CO_2-to-methanol reactions with Cu/ZrO_2 catalysts[199,202]. The formation of carbonyl from formate requires dehydration. The dehydration is attained when a H atom approached an O atom of formate. On the contrary, to convert formate into methoxy, H atoms should approach the C atom of formate. Considering that protons are positively charged and that C-O bonds in formate are polarized as $C^{\delta+}$-$O^{\delta-}$, protons will prefer the O atom to the C atom. Thus, it is considered that the direct conversion of formate into methoxy was minor during the CO_2 electrolysis. Methoxy may be formed by the hydrogenation of carbonyl. Remember that no methane was produced in the catalytic activity test of Cu/ZrO_2 (Section 3.2.3.2). This means that C-O bond cleavage is difficult to occur on Cu catalytically. However, a significant amount of methane was produced in the electrolysis tests. C-O cleavage may be accelerated by protons. C-C bond may be formed from two carbonyl species or CH_2 species. The competing pathways from carbonyl to methanol, methane, and C2 species are consistent with the discussion about the $(r_{C2H6} + r_{C2H4})/r_{CH4}$ ratio above.

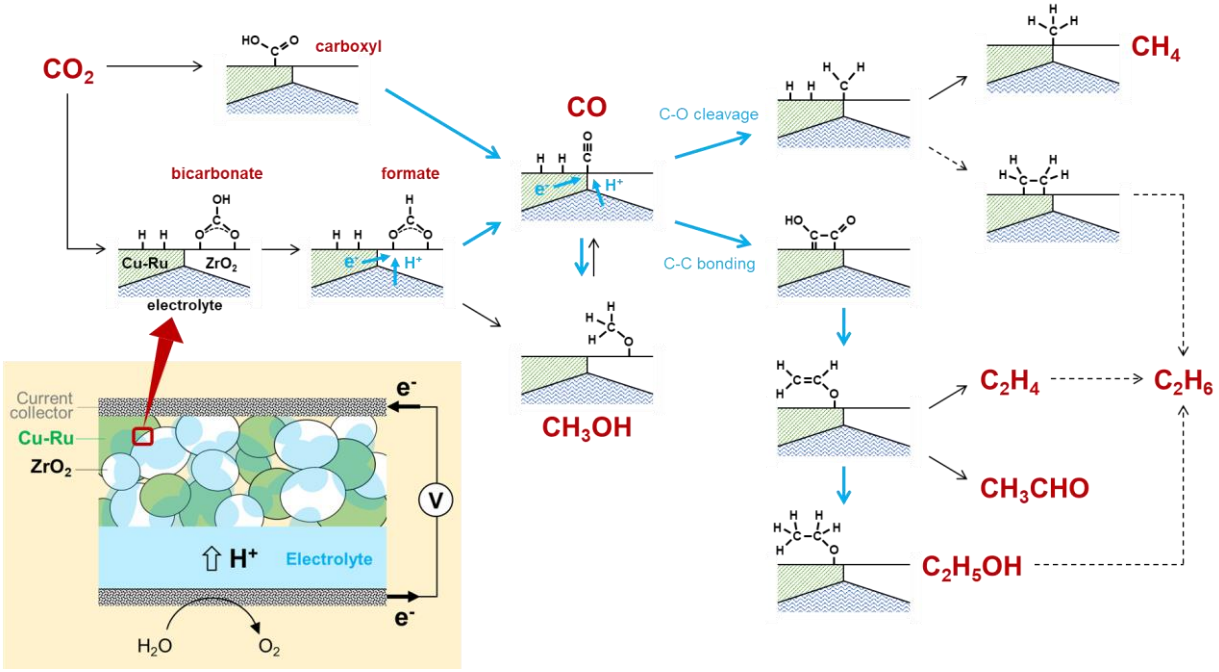

Figure 3-48. Plausible reaction pathways in type-2 cathodes. The (Cu-Ru)-ZrO_2 cathode is selected as an example, but it is considered that the pathways are shared by all the tested type-2 cathodes in this study. Steps indicated by light-blue arrows are considered characteristic of electrochemical hydrogenation by protons and electrons.

Although the plausible reaction pathways are proposed in Figure 3-48, more information is needed to verify the mechanism. *In situ* spectroscopy techniques are powerful tools to investigate the mechanisms of the electrochemical reactions. For example, reaction intermediates can be observed directly by *in situ* DRIFTS (diffuse reflectance infrared Fourier transform spectroscopy). Application of such techniques is desired to fully understand the nature of the electrochemical reduction of CO_2. The understanding of the reaction mechanism will help us improve the SAEC performance by adequately designing the cathode reaction sites.

Table 3-8 compares the methanol production rate in this study with those of thermocatalytic CO_2-to-methanol systems. The methanol production rate normalized by the catalyst weight, r_{CH3OH}, was 0.0012 g g_{cat}^{-1} h^{-1} with the (Cu-Ru)-ZrO_2 [1:1] cathode. This value was two or more orders of magnitude smaller than those in thermal systems. However, attentions should be paid to the experimental conditions. The operation pressure was *ca.* 1 bar (ambient pressure) in the present study, while typical CO_2-to-methanol catalytic reactions are performed at > 10 bar. The H/CO_2 ratio in this work was much smaller than those in thermocatalytic systems, which is disadvantageous to achieve high reaction rates. To increase the reaction rate, large current densities are desired. Larger current densities will result in higher CO_2 conversion and higher production rates. To make the operation at large current densities practical, cell overpotentials must be decreased. As discussed earlier, improvement of the anode and the electrolyte is needed to suppress the overpotential, as well as the development of the cathode. Note that the product selectivity can be affected by changing the H/CO_2 ratio. The effect of the current density (or the H/CO_2 ratio) on the selectivity should be investigated carefully.

Table 3-9 shows the comparison of Faraday efficiencies for major carbon-containing products in different CO_2 electrolysis systems. The FEs in this work are significantly lower than those reported in literature. The variety of the products in the present study (CO, methane, methanol, ethane, ethylene, ethanol, acetaldehyde, and propylene) demonstrates the possibility of direct production of valuable chemicals in SAECs. However, for making the SAEC technology practical, it is necessary to increase the selectivity for a specific product.

Table 3-8. Comparison of methanol production rates in this work and in thermocatalytic systems.

Type	Catalyst	Temp. / °C	Pressure / bar	Space velocity		H/CO_2 ratio	r_{CH3OH} / g g_{cat}^{-1} h^{-1}	Ref.
Thermal	Cu-ZnO-Al_2O_3	280	442	100,000	h^{-1}	6	15.2	[209]
Thermal	Cu-ZnO-ZrO_2	240	40	4,000	h^{-1}	6	0.293	[210]
Thermal	Cu/ZrO_2	280	30	7,200	mL g^{-1} h^{-1}	6	0.09	[211]
Electro-chemical	(Cu-Ru)-ZrO_2	220	1	130,000 38,000	h^{-1}* mL g^{-1} h^{-1}	0.12	0.0012	This work**

* Calculated as (cathode gas flow rate)/(cathode disk volume).
** (Cu-Ru)-ZrO_2 [1:1] cathode. i = 50 mA cm^{-2}, cathode feed: CO_2/N_2 = 5/5 mL min^{-1}.

Table 3-9. Comparison of Faraday efficiencies in different CO_2 electrolysis systems.

Cathode	Electro-lyte	Temp. / °C	Current density / mA cm^{-2}	Reactor type	Faraday efficiency for C-containing products / %					Ref.	Note
					CO	CH_4	CH_3OH	C_2H_5OH	CH_3CHO		
Ni	CsH_2PO_4/SiC/PBI/PA	300	14	SAEC	-	~98	-	-	-	[147]	*a
PD-Ag	$KHCO_3$ aq.	RT	3	Batch cell	~97	-	-	-	-	[212]	*b
n-Cu/C	$NaHCO_3$ aq.	RT	9	Flow cell	< 10	~80	-	-	-	[81]	*c
Cu_2O	$KHCO_3$ aq.	RT	10	Flow cell with GDE	-	-	42	10	-	[83]	*d
20%Cu-AC	PEM	90	1.6	PEMEC	-	-	10	-	32	[213]	*e
(Cu-Ru)-ZrO_2	CsH_2PO_4/SiP_2O_7	220	50	SAEC	3.4	0.73	0.24	0.16	0.08	This work	*f

a PBI: polybenzimidazole, PA: phosphoric acid. Operated at ~8 bar.
b PD-Ag: phosphate silver-derived silver.
c n-Cu/C: copper nanoparticles supported on glassy carbon. Current density was normalized by copper surface area. Ethylene was also produced.
d GDE: gas diffusion electrode. n-propanol was also produced.
e AC: activated carbon, PEM: proton exchange membrane (Sterion). Methyl formate, Acetone, and n-propanol were also produced.
f Cathode feed: CO_2/N_2 = 5/5 mL min^{-1}. Ethane, ethylene, and propylene were also produced.

In the following part, possible approaches to high methanol selectivity are discussed. The high FEs for hydrogen production indicates that most of the protons were converted in to H_2 gas and not used for the CO_2 reduction. Possible reasons include the insufficient adsorption of CO_2 on the cathode surface and/or high activation barrier for the reduction of adsorbed species. Quantitative analysis of surface adsorbed species is required to figure out the problems. It should also be noted that the electrolyte migrated through the cathode layer may have reached the carbon paper, which was used as a current collector. The interface between the electrolyte material and the carbon paper may have functioned as hydrogen evolution sites. To avoid such a situation, the control of the electrolyte morphology is required.

Figure 3-49 shows the detailed pathways starting from carbonyl species[206,214,215]. The formation of methanol, methane, and C2 species are competing. To obtain high methanol selectively, C-C bond formation should be suppressed. According to the studies of low-temperature CO_2 electrolysis, C2 species are favored on Cu(100) surface while C1 species are favored on Cu(111) surface[216–218]. C-C coupling is facilitated when low-coordinated binding sites exist in close proximity to each other[85,216]. Thus, the control of the crystallinity of Cu will be beneficial. It is also known in the low-temperature systems that C1 products are favored at lower pH whereas C2 products become dominant at more elevated pH[215,218]. This suggests that the H^+/CO_2 ratio affects the C1/C2 selectivity. The high H^+/CO_2 ratio at low pH may lead to the formation of C1 species. In SAECs, the H^+/CO_2 ratio can be controlled by the current density, the cathode feed gas composition, and the gas flow rate. Effects of such parameters should be investigated.

To facilitate the hydrogenation of carbonyl, the hydrogenated species, *CHO or *COH, should be stabilized on the cathode surface[219]. Alloying is one of the promising methods to control the free energy of the adsorbed *CHO and *COH[214,219]. The main difference between the pathways for the methanol production and the methane production is whether C-O bond is broken or not. Generally, the C-O bond cleavage is accelerated under the cathodic polarization because electrons are fed to the cathode. This is one of the reasons why significant amount of methane was produced in the CO_2 electrolysis tests while almost no methane was produced in the catalytic activity tests. Recently, it is reported that Cu_2O is a promising electrocatalyst for the methanol synthesis[83,220,221]. Cu_2O contains oxidized copper atoms (Cu^+)

and may have low thermocatalytic activity for CO_2 hydrogenation. However, under the cathodic polarization, the electron-attracting feature of Cu^+ may be weakened, and the strength of the C-O bond of adsorbed carbonyl will become suitable for the formation of methanol. Thus, the utilization of Cu-containing oxides in SAEC cathodes is a possible method to increase the selectivity for methanol. Challenges include the relatively low electronic conductivity of such oxides and the instability caused by the reduction of the oxides to metallic Cu.

To summarize the discussion about the competing pathways starting from carbonyl, the possible approaches to high methanol selectivity are the following:

- To control the crystallinity and the morphology of Cu
- To control the H^+/CO_2 ratio
- To alloy Cu with other metals
- To utilize Cu-containing oxides

Future development of Cu-based SAEC cathodes for the methanol synthesis should be based on these considerations.

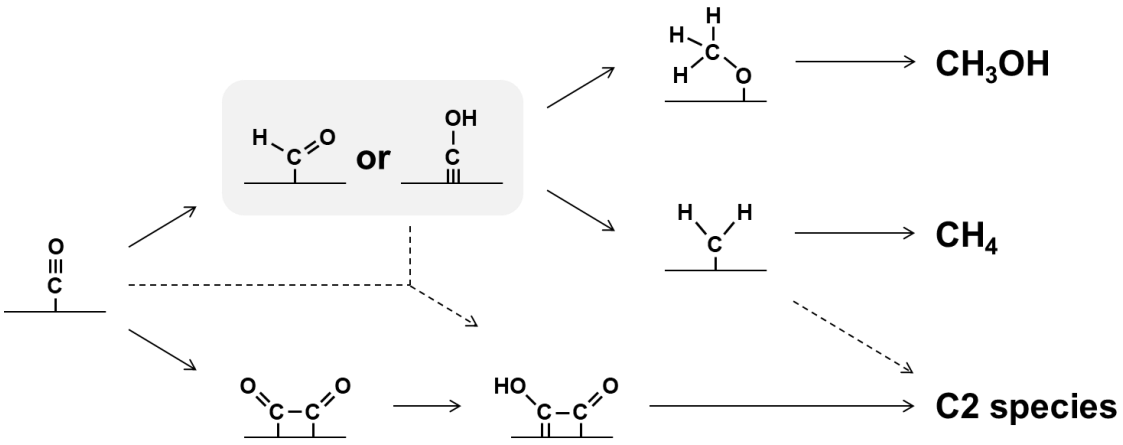

Figure 3-49. Detailed plausible reaction pathways from carbonyl (*CO) to methanol, methane, and C2 species.

3.2.4. Summary

In Section 3.2, CO_2 electrolysis was performed using SAECs with different cathode materials and structures.

By combining the Pt/C cathode and the Ru/ZrO_2 catalyst, methane formation was demonstrated. The Cu/ZrO_2 catalyst, whose activity for the methanol production under ambient pressure was confirmed, was also applied to a SAEC. However, methanol formation was not observed under the tested conditions. This can partially be attributed to the design of the reactor. Increase in the gas contact time in the cathode is necessary to obtain high CO_2 conversion and high product selectivity.

Composites of $Cu\text{-}ZrO_2$, $(Cu\text{-}Ru)\text{-}ZrO_2$, $(Cu\text{-}Pd)\text{-}ZrO_2$, and $(Cu\text{-}Ru)\text{-}SiO_2$ were examined as SAEC cathodes. Products detected from the cathode outlet gas include CO, methane, methanol, ethane, ethylene, ethanol, acetaldehyde, and propylene. It was found that both the active metal species and the oxide materials affected the performance of the cells. The methanol production rates were larger than the values calculated by assuming the thermodynamic equilibrium. By comparing the reactivity of protons and hydrogen molecules, the existence of reaction pathways unique to the electrochemical CO_2 hydrogenation was suggested. Even though the direct electrochemical CO_2 reduction by protons was demonstrated, the present results are of low CO_2 conversion and low product selectivity. Possible approaches to high methanol selectivity were discussed based on the plausible reaction pathways. Future development of SAEC cathodes for the CO_2 electrolysis should focus on the investigation of the reaction mechanism and the design of the active sites.

Chapter 4

Conclusions

4.1. Summary

This dissertation is devoted to the investigations of electrolysis technologies which can contribute to the establishment of the sustainable society. In particular, direct synthesis of methane and methanol from CO_2 and water in intermediate-temperature electrolysis cells was focused on.

Chapter 1 introduces the background of my research with detailed reviews of the electrolysis technologies. The CO_2 electrolysis at intermediate temperatures is considered promising because high reaction rates and high selectivity to the desired products may be achieved simultaneously.

Chapter 2 describes the modeling studies to reveal the characteristics of intermediate-temperature CO_2 electrolysis processes. The simulations were performed to select the target electrolysis system. This approach was useful for determining the direction of the research and is applicable to the other electrochemical reaction systems (hydrocarbon conversion, ammonia synthesis, *etc.*).

In **Section 2.1**, a power-to-methane (PtM) process featuring the direct internal methanation in solid oxide electrolysis cell (SOEC) cathodes was modeled by using *Aspen Plus*. The performance of the direct PtM process was compared to that of the two-step process, which consists of a serial combination of the high-temperature SOEC unit and the methanation unit. Energy conversion efficiencies of the direct process were lower than that of the two-step process, mainly due to the large overpotentials at low temperatures and the thermodynamic limitation of the methane formation. To make the direct process feasible, drastic performance improvement at around 400°C is required.

In **Section 2.2**, solid acid electrolysis cells (SAECs) working at around 200°C were focused on. Simulations were performed to quantitate the characteristics of SAECs for the production of methane and

methanol. It was confirmed that the methane formation is highly favored from the thermodynamic viewpoint. The direct methane synthesis in SAECs is a promising candidate for the energy-efficient PtM. The methanol synthesis was not so thermodynamically advantageous as the methane production. Low temperatures and high pressures are required to obtain a significant production rate.

Chapter 3 describes the experimental investigations to develop SAECs for the CO_2 conversion.

Section 3.1 addresses the development of SAECs for steam electrolysis. To establish the basic experimental setup for stable measurements, the factors affecting the cell stability were examined in detail. By using a Pt/C|CsH_2PO_4/SiP_2O_7|Pt/C cell, it was found that the electrolyte migration to the anode and the carbon oxidation in the anode were the main causes of the cell degradation. These issues were mitigated by applying a Pt mesh anode.

In **Section 3.2**, CO_2 electrolysis in SAECs was investigated. Different cathode materials and structures were tested. Using the Pt/C cathode and the adjacent Ru/ZrO_2 catalyst layer, the formation of methane and CO were demonstrated. Composites of Cu-based metal powder and oxide powder (ZrO_2 or SiO_2) were tested as SAEC cathodes. Under a constant current load of 50 mA cm^{-2}, CO, methane, methanol, ethane, ethylene, ethanol, acetaldehyde, and propylene were produced. Notably, the production of methanol, ethane, ethylene, ethanol, acetaldehyde, and propylene by CO_2 electrolysis in SAECs was demonstrated for the first time. The methanol production rates were larger than the values calculated by assuming the thermodynamic equilibrium. The variety of the products showed the potential of SAECs for the direct production of valuable chemicals from CO_2 and steam. Plausible reaction pathways were discussed, and possible methods to improve the methanol selectivity were suggested.

4.2. Future Perspective

This dissertation covered a wide range of aspects regarding the development of intermediate-temperature electrolysis cells. However, there are still a large number of issues to be solved in future.

For the development of practical SAECs, improvement of the cell components is essential. Robust electrolyte membranes and cost-effective anodes with high activity are required. The key component for the CO_2 electrolysis is the cathode. Not only the material but also the structure of cathodes affects the CO_2 conversion and the selectivity. Attention should be paid to controlling the morphology of the materials.

SAECs for the direct synthesis of valuable chemicals from CO_2 and water is expected to possess the following advantages:

- **Compact apparatus**

  By combining multiple reaction processes, the apparatus will become more compact than that of traditional processes. Initial investments may become smaller. High product selectivity is desired because the separation process can be omitted. Intermediate- or small-scale plants will be suitable for the utilization of distributed energy sources, although the running costs may become larger than that of large-scale plants.

- **High energy conversion efficiencies** (methane production)

  As discussed in Section 2.2, a CH_4-producing SAEC can be more energy-efficient than the combination of a H_2-producing SAEC and a catalytic methanator.

- **Operation at low pressures** (methanol production)

  As demonstrated in Section 3.2, methanol production rates higher than the thermodynamic equilibrium values can be achieved by the electrochemical CO_2 reduction with protons. This offers the possibility of methanol production at ambient or relatively low pressures. Typically, thermocatalytic methanol production from CO_2 is conducted at pressures higher than 10 bar, so the start-up and the shut-down of the system cannot be done quickly. Practical low-pressure methanol

production by SAECs will have high operation flexibility, which is suitable for the use of intermittent renewable power.

Figure 4-1 shows the schematic image of the future application of CO_2-converting SAECs. Because the infrastructure for the transportation of CO_2 is not widely available in society, the SAECs should be located near the CO_2 sources. For example, steelworks and thermal power plants are promising. CO_2 will be collected from the flue gas and reduced in the SAECs. The products such as methane and methanol will be stored, transported, and/or used as a fuel or a raw material of other chemicals.

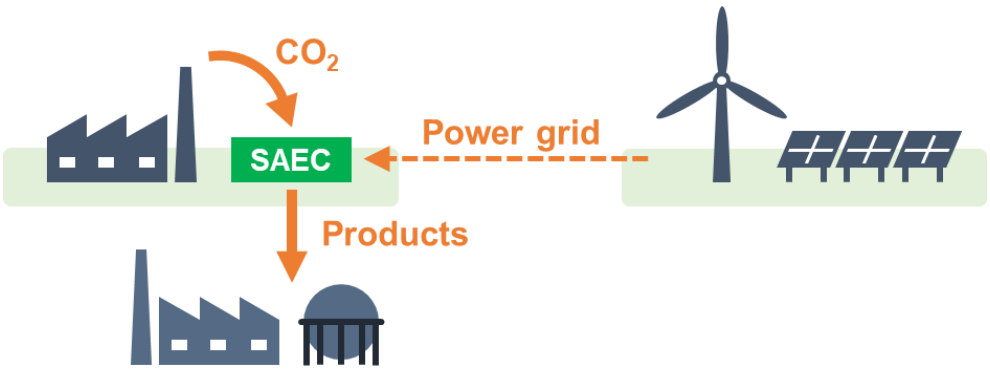

Figure 4-1. Schematic image of the future energy system featuring an SAEC for the direct synthesis of methane or methanol from CO_2 and steam.

Appendices

Appendix A.

Temperature dependence of standard enthalpy of formation and standard entropy

The standard enthalpy of formation of species *i*, $\Delta_f H_i^0$, at 298.15 K (= T_0) is liseted in Table A-1[165]. $\Delta_f H_{H_2O}^0$ at temperatures other than T_0 was calculated as follows:

$$\Delta_f H_{H_2O}^0(T) = \left[\Delta_f H_{H_2O}^0(T_0) + \int_{T_0}^{T} C_{p,H_2O} dT\right] - \int_{T_0}^{T} C_{p,H_2} dT - 0.5 \int_{T_0}^{T} C_{p,O_2} dT \quad \text{(A-1)}$$

Here, $C_{p,i}$ is the molar heat capacity of species *i* at constant pressure. $C_{p,i}$ can be expressed as

$$C_{p,i} = a + bT + cT^2 \quad \text{(A-2)}$$

where *a*, *b*, and *c* are constants. Table A-2 lists the values of *a*, *b*, and *c* for each species[165]. $\Delta_f H_{H_2}^0$, $\Delta_f H_{O_2}^0$, and $\Delta_f H_{N_2}^0$ are defined as zero regardless of the temperature.

The standard entropy of species *i*, S_i^0, at 298.15 K (= T_0) is also listed in Table A-1[165]. S_i^0 at temperatures other than T_0 was calculated as follows:

$$S_i^0(T) = S_i^0(T_0) + \int_{T_0}^{T} \frac{C_{p,i}}{T} dT \quad \text{(A-3)}$$

The standard Gibbs energy of formation, $\Delta_f G_i^0$, can be calculated from $\Delta_f H_i^0$ and S_i^0. For example, $\Delta_f G_{H_2O}^0$ was obtained as

$$\Delta_f G_{H_2O}^0(T) = \Delta_f H_{H_2O}^0(T) - T[S_{H_2O}^0(T) - S_{H_2}^0(T) - 0.5 S_{O_2}^0(T)] \quad \text{(A-4)}$$

Table A-1. Standard enthalpy of formation and standard entropy at 298.15 K[165].

Gas species	$\Delta_f H_i^0$ / kJ mol^{-1}	S_i^0 / J mol^{-1} K^{-1}
H_2O(g)	-241.82	188.72
H_2	0	130.57
O_2	0	205.03
N_2	0	191.5
CO_2	-393.51	213.6
CO	-110.57	197.56
CH_4	-74.5	186.0
CH_3OH(g)	-201.6	239.6

Table A-2. Coefficients used for calculating the molar heat capacity[165].

Gas species	a	$b\times10^3$	$c\times10^6$	Applicable temp. range / K
H_2O(g)	30.204	9.933	1.117	298-1500
H_2	29.062	-0.820	1.9903	300-1500
O_2	25.594	13.251	-4.205	273-1500
N_2	27.016	5.812	-0.289	300-1500
CO_2	26.748	42.258	-14.247	300-1500
CO	26.5366	7.6831	-1.1719	300-1500
CH_4	14.146	75.496	-17.991	298-1500
CH_3OH(g)	14.859	104.822	-30.054	298-1000

Appendix B. Pressure dependence of exchange current densities in SOECs

Partial pressure dependence of exchange current densities has been examined in the field of SOFC (solid oxide fuel cell). It is reasonable to apply the values obtained in the SOFC studies to SOEC simulations because exchange current densities represent the rate of reversible reaction at open circuit conditions. In most cases, the partial pressure dependences are examined in a range of 0-1 atm, and expressed by the following formulae:

$$i_{0,\mathrm{H_2}} = \gamma_{\mathrm{H_2}} \left(\frac{p_{\mathrm{H_2}}}{p_{\mathrm{std}}}\right)^{\mathrm{A}} \left(\frac{p_{\mathrm{H_2O}}}{p_{\mathrm{std}}}\right)^{\mathrm{B}} \exp\left(-\frac{E_{\mathrm{a,H_2}}}{RT}\right) \quad \text{(B-1)}$$

$$i_{0,\mathrm{CO}} = \gamma_{\mathrm{CO}} \left(\frac{p_{\mathrm{CO}}}{p_{\mathrm{std}}}\right)^{\mathrm{C}} \left(\frac{p_{\mathrm{CO_2}}}{p_{\mathrm{std}}}\right)^{\mathrm{D}} \exp\left(-\frac{E_{\mathrm{a,CO}}}{RT}\right) \quad \text{(B-2)}$$

Here we focus on the exponents A-D. Table B-1 summarizes the values reported in the literature. The results differ significantly, possibly due to the cell geometries and test conditions. The value of A+B obtained from Table B-1 ranges from 0.23 to 3.

Table B-1. Reported pressure dependence of exchange current densities (0-1 atm).

Reference	Year	Electrode	A	B	C	D	Note
[222]	1993	Ni-YSZ	1	1			Low p_{H2}
			2	1			High p_{H2}
[223]	1994	Ni pattern	0	1			$p_{H2O} >> p_{H2}$
			0.5	0			$p_{H2O} << p_{H2}$
[224]	1999	Ni-YSZ	0.1	0.5			
[168]	2009	Ni-YSZ	-0.10	0.33			
[225]	2011	Ni-YSZ			-0.058	0.25	
[226]	2011	Ni-ScSZ	0.41	0.40			

It is noted again that most of the previous studies explored the pressure dependence in the range of 0-1 atm. Only a few experimental data are available for the pressure dependence at operating pressures higher than 1 atm. Matsui *et al.*[227] performed an impedance analysis in a total pressure range of 100-300 kPa, and suggested that the results were consistent with the partial pressure dependence reported by Mizusaki

et al.[223] even at elevated pressures. Kikuchi *et al.*[228] reported impedance spectra measured at different H_2 or H_2O partial pressures in a range of 0-10 atm. According to the spectra, it is qualitatively assumed that the exponent A is around zero while the exponent B is positive. However, further quantitative analysis is still needed to determine the dependences at high pressures. Kazempoor and Braun[229,230] performed simulations of pressurized solid oxide cells by applying the equations developed for near atmospheric pressure conditions. They pointed out that more activities are necessary to check the validity of those equations for pressurized operation[230].

Appendix C. Chapman-Enskog theory

The interdiffusion coefficient in a binary system containing two gas species *i* and *j*, D_{ij}^{M}, can be calculated as follows according to Chapman-Enskog theory[171].

$$D_{ij}^{\mathrm{M}}\ [\mathrm{m^2 s^{-1}}] = 1.8587 \times 10^{-7} \frac{\sqrt{T^3 \frac{M_i + M_j}{M_i M_j}}}{P \sigma_{ij}^2 \Omega_D} f_D \quad \text{(C-1)}$$

P is the pressure of the gas mixture (unit: atm), and *T* is the temperature. M_i and M_j are the molecular weight of *i* and *j*. σ is one of intermolecular force constants in Lennard-Jones(12-6) potential (Eq. C-2), and differs depending on the species.

$$U(r) = 4\varepsilon \left[\left(\frac{\sigma}{r}\right)^{12} - \left(\frac{\sigma}{r}\right)^{6} \right] \quad \text{(C-2)}$$

σ_{ij} in a binary system is obtained from σ_i and σ_j:

$$\sigma_{ij} = (\sigma_i + \sigma_j)/2 \quad \text{(C-3)}$$

The unit of σ_{ij} is Å. The reduced collision integral, Ω_D, and a numerical factor, f_D, are functions of the normalized temperature, T_N. T_N is defined as

$$T_N = \frac{T}{\varepsilon/k} \quad \text{(C-4)}$$

ε is another intermolecular force constant in the Lennard-Jones(12-6) potential (Eq. C-2). k is the Boltzmann constant. ε_{ij} in a binary system is obtained from ε_i and ε_j:

$$\varepsilon_{ij} = \sqrt{\varepsilon_i \varepsilon_j} \quad \text{(C-5)}$$

For the calculation, the values of σ and ε were taken from the literature[171,231]. The dependence of Ω_D and f_D on T_N was also taken from the literature[171,232].

Appendix D. Derivation of equations describing overpotentials in SAECs

D.1. Activation overpotential

Activation overpotential originates from the electrochemical reaction kinetics. The relationship between the current density and the activation overpotential at an electrode is described by a Butler-Volmer type equation[178]:

$$i = i_0 \left[\exp\left(\frac{\alpha_1 F \eta_{\text{act}}}{RT}\right) - \exp\left(\frac{-\alpha_2 F \eta_{\text{act}}}{RT}\right)\right] \quad \text{(D-1)}$$

where i_0 is the exchange current density and η_{act} is the activation overpotential of the electrode. α_1 and α_2 are parameters. Assuming that $\alpha_1 = \alpha_2 = \alpha$, Eq. D-1 can be rearranged as

$$\eta_{\text{act}} = \frac{RT}{\alpha F} \sinh^{-1}\left(\frac{i}{2i_0}\right) \quad \text{(D-2)}$$

For PEM electrolysis cells, $\alpha = 2$ and $\alpha = 0.5$ are typically used for the anode and the cathode, respectively[9]. Providing that the same values can be applied to SAECs, the anodic and cathodic activation overpotentials become

$$\eta_{\text{act}}^{\text{a}} = \frac{RT}{2F} \sinh^{-1}\left(\frac{i}{2i_0}\right) \quad \text{(D-3)}$$

$$\eta_{\text{act}}^{\text{c}} = \frac{2RT}{F} \sinh^{-1}\left(\frac{i}{2i_0}\right) \quad \text{(D-4)}$$

D.2. Concentration overpotential

Concentration overpotential originates from the partial pressure changes at reaction sites during the cell operation. The partial pressure changes affects the Nernst potential and the electrochemical reaction rates[170]. Here, the former contribution is discussed. According to Nernst equation, Nernst potential (or reversible potential) of a water electrolysis SAEC can be written as

$$E_{\text{Nernst}} = E^0(T) + \frac{RT}{2F} \ln \frac{\left(p_{\text{H}_2}^{\text{c}}\right)\left(p_{\text{O}_2}^{\text{a}}\right)^{0.5}}{p_{\text{H}_2\text{O}}^{\text{a}}} \quad \text{(D-5)}$$

where E^0, R, T, and F are the standard reversible potential, the molar gas constant, the temperature, and the Faraday constant, respectively. $p_{\text{H}_2}^{\text{c}}$, $p_{\text{O}_2}^{\text{a}}$, and $p_{\text{H}_2\text{O}}^{\text{a}}$ are the partial pressures. Superscripts a and

c indicate anode and cathode. Thus, the concentration overpotential ascribed to the change of Nernst potential can be expressed as

$$\eta_{\text{conc}} = E^{*}_{\text{Nernst}} - E_{\text{Nernst}} = \left[E^{0} + \frac{RT}{2F}\ln\frac{\left(p^{\text{c}*}_{\text{H}_2}\right)\left(p^{\text{a}*}_{\text{O}_2}\right)^{0.5}}{p^{\text{a}*}_{\text{H}_2\text{O}}}\right] - \left[E^{0} + \frac{RT}{2F}\ln\frac{\left(p^{\text{c}}_{\text{H}_2}\right)\left(p^{\text{a}}_{\text{O}_2}\right)^{0.5}}{p^{\text{a}}_{\text{H}_2\text{O}}}\right]$$

$$= \frac{RT}{2F}\ln\left(\frac{p^{\text{a}}_{\text{H}_2\text{O}}}{p^{\text{a}*}_{\text{H}_2\text{O}}}\right) + \frac{RT}{2F}\ln\left(\frac{p^{\text{c}*}_{\text{H}_2}}{p^{\text{c}}_{\text{H}_2}}\right) + \frac{RT}{4F}\ln\left(\frac{p^{\text{a}*}_{\text{O}_2}}{p^{\text{a}}_{\text{O}_2}}\right) = \eta^{\text{H}_2\text{O}}_{\text{conc}} + \eta^{\text{H}_2}_{\text{conc}} + \eta^{\text{O}_2}_{\text{conc}} \quad \text{(D-6)}$$

In Eq. D-6, $p^{\text{a}*}_{\text{H}_2\text{O}}$, $p^{\text{c}*}_{\text{H}_2}$, and $p^{\text{a}*}_{\text{O}_2}$ indicate the partial pressures at the reaction sites during the operation while $p^{\text{a}}_{\text{H}_2\text{O}}$, $p^{\text{c}}_{\text{H}_2}$, and $p^{\text{a}}_{\text{O}_2}$ indicate the bulk gas partial pressures. $\eta^{\text{H}_2\text{O}}_{\text{conc}}$ and $\eta^{\text{O}_2}_{\text{conc}}$ are related to the anode and $\eta^{\text{H}_2}_{\text{conc}}$ is related to the cathode.

Hereafter, relation between $\eta^{\text{H}_2\text{O}}_{\text{conc}}$ and the gas diffusion property in the anode is discussed. Considering the mass balance, the diffusion flux of steam in the anode layer should be equal to the electrochemical consumption rate of steam, that is

$$\frac{D^{\text{eff}}_{\text{H}_2\text{O}}}{RT}\frac{\left(p^{\text{a}}_{\text{H}_2\text{O}} - p^{\text{a}*}_{\text{H}_2\text{O}}\right)}{\delta_{\text{a}}} = \frac{i}{2F} \Leftrightarrow i = \frac{2FD^{\text{eff}}_{\text{H}_2\text{O}}}{RT}\frac{\left(p^{\text{a}}_{\text{H}_2\text{O}} - p^{\text{a}*}_{\text{H}_2\text{O}}\right)}{\delta_{\text{a}}} \quad \text{(D-7)}$$

$D^{\text{eff}}_{\text{H}_2\text{O}}$, δ_{a}, and i are the effective diffusion coefficient of steam, the thickness of the anode, and the current density, respectively. A linear steam partial pressure profile across the anode is assumed. From Eq. D-7, one can find that the current density reaches an upper limit when the steam is depleted at the reaction sites. The value, called limiting current density, is obtained by setting $p^{\text{a}*}_{\text{H}_2\text{O}} = 0$ in Eq. D-7:

$$i_{\text{L}} = \frac{2FD^{\text{eff}}_{\text{H}_2\text{O}}}{RT}\frac{p^{\text{a}}_{\text{H}_2\text{O}}}{\delta_{\text{a}}} \quad \text{(D-8)}$$

From Eqs. D-7 and D-8, it holds that

$$\frac{i}{i_{\text{L}}} = \frac{p^{\text{a}}_{\text{H}_2\text{O}} - p^{\text{a}*}_{\text{H}_2\text{O}}}{p^{\text{a}}_{\text{H}_2\text{O}}} \Leftrightarrow \frac{p^{\text{a}}_{\text{H}_2\text{O}}}{p^{\text{a}*}_{\text{H}_2\text{O}}} = \frac{1}{1 - i/i_{\text{L}}} \quad \text{(D-9)}$$

Therefore, referring to Eq. D-6,

$$\eta^{\text{H}_2\text{O}}_{\text{conc}} = \frac{RT}{2F}\ln\left(\frac{p^{\text{a}}_{\text{H}_2\text{O}}}{p^{\text{a}*}_{\text{H}_2\text{O}}}\right) = \frac{RT}{2F}\ln\left(\frac{1}{1 - i/i_{\text{L}}}\right) \quad \text{(D-10)}$$

Appendix E. Experimental study of CO_2 methanation in SOEC cathodes

E.1. Objective

This section addresses the experimental study of CO_2 methanation in SOEC cathodes. The experiments were performed to examine the effect of polarization on the catalytic activity of the cathode. When CO_2 and steam are introduced to the cathode, the following reactions will take place:

$$H_2O + 2e^- \rightarrow H_2 + O^{2-} \quad \text{(E-1)}$$

$$CO_2 + 2e^- \rightarrow CO + O^{2-} \quad \text{(E-2)}$$

$$H_2 + CO_2 \rightarrow H_2O + CO \quad \text{(E-3)}$$

$$CO + 3H_2 \rightarrow CH_4 + H_2O \quad \text{(E-4)}$$

Eqs. E-1 and E-2 are the steam electrolysis and the CO_2 electrolysis, respectively. Eqs. E-3 and E-4 are the reverse water gas shift reaction and the CO methanation reaction, respectively. According to these reactions, H_2, CO, and methane are produced under cathodic polarization. The question here is whether the methane formation (Eq. E-4) is accelerated by the polarization or not. It is known that catalytic activity can be altered by applying voltage (NEMCA effect, Section 1.4). In SOEC cathodes, the evaluation of the effects of the cell potential on the catalytic activity is difficult because parameters are dependent on each other: when the cell potential is changed, current will flow, and the formation of H_2 and CO will proceed (Eqs. E-1 and E-2). To evaluate the contribution of the change in the catalytic activity, changes in the gas partial pressures should be taken into consideration. Atsumi *et al.*[233] performed electrochemical reaction tests with an SOEC (Ni-YSZ|YSZ|LSM) by feeding a gas mixture of CO_2/H_2 = 5/20 mL min^{-1} to the cathode. They calculated the Faraday efficiency by the following equation:

$$\varepsilon = \frac{(2r_{CH_4} + r_{CO}) - (2r_{CH_4,OCV} + r_{CO,OCV})}{F_{O^{2-}}} \quad \text{(E-5)}$$

r_{CH_4} and r_{CO} are the production rates of methane and CO under polarization, $r_{CH_4,OCV}$ and $r_{CO,OCV}$ are the production rates at open circuit voltage (OCV), and $F_{O^{2-}}$ is the rate of the oxide ion transfer corresponding to the current density. The coefficient of 2 in "$2r_{CH_4}$" and "$2r_{CH_4,OCV}$" came from the

assumption that electrochemical methane formation (Eq. E-6) took place. Note that hydrogen gas was supplied to the cathode, so the electrons used for the steam electrolysis was not taken into consideration.

$$CO_2 + 2H_2 + 4e^- \rightarrow CH_4 + 2O^{2-} \quad \text{(E-6)}$$

They found that the FE exceeded unity at 500°C and 400°C. In particular, the value was larger than 10000 at 400°C, indicating that the reverse water gas shift reaction (Eq. E-3) and the CO methanation reaction (Eq. E-4) were promoted under the polarization. However, ε calculated by Eq. E-5 is not perfect as a descriptor of the NEMCA effect because Eq. E-5 does not include the effects of the change in gas partial pressures. In addition, the occurrence of steam electrolysis is neglected in Eq. E-5. Even though no steam was fed to the cathode, steam was synthesized by the catalytic reactions (Eqs. E-3 and E-4).

Here, a different approach using kinetic equations is proposed to evaluate the NEMCA effect. The approach is based on the consideration that all the detected methane was formed *via* the CO methanation reaction (Eq. E-4). First, the catalytic CO methanation activity of the SOEC cathode was examined at 600°C under the open circuit condition, and the dependence of the activity on the CO partial pressure was figured out. The dependence on the hydrogen partial pressure was disregarded because a certain amount of hydrogen gas was supplied to the cathode and the hydrogen partial pressure change caused by the electrolysis was considered negligible. Then, electrochemical tests were performed at 600°C, and the cathode outlet gas compositions were measured under the open circuit condition and the polarized conditions. The methane production rates under polarized conditions were compared to that at OCV by considering the change in the CO partial pressure.

E.2. Experimental

E.2.1. Preparation of materials

Gadolinium-doped ceria (GDC, $Ce_{0.9}Gd_{0.1}O_{1.95}$) was prepared by co-precipitation method. Stoichiometric amounts of $Ce(NO_3)_3 \cdot 6H_2O$ and $Gd(NO_3)_3 \cdot 6H_2O$ (Wako Pure Chemical Industries) were dissolved in distilled water [solution A]. Total concentration was set to 0.2 M. Separately, a 0.2 M aqueous solution of $(COOH)_2 \cdot 2H_2O$ (Wako Pure Chemical Industries) was mixed with ammonia water (28%, Wako Pure

Chemical Industries), and the pH was adjusted to 7 [solution B]. The solution A was added to the solution B, and the resultant solution was stirred overnight at room temperature. Then the precipitate was filtered under reduced pressure. The obtained white matter was dried at 100°C overnight and crushed in a mortar. Finally, the powder was calcined at 500°C for 2 h and further calcined at 1000°C for 2 h to obtain GDC. NiO-GDC cermet was prepared as follows. First, the GDC powder was sintered at 1500°C for 5 h to increase the particle size. GDC with large particle sizes will facilitate the segregation of Ni in the Ni-GDC cermet, leading to the formation of electron conducting pathways[234]. Large crystallites will decrease the grain boundary resistance of GDC. The sintered GDC powder was ball-milled with NiO (Wako Pure Chemical Industries) for 24 h and sintered at 1300°C for 5 h to obtain NiO-GDC. The amount of NiO was determined so that the Ni amount in reduced Ni-GDC became 60wt%.

$La_{0.6}Sr_{0.4}Co_{0.2}Fe_{0.8}O_{3-\delta}$ (LSCF) was synthesized by polymerized complex method[235]. A buffer solution was prepared from ammonia water and ethylenediaminetetraacetic acid (EDTA, Sigma-Aldrich). Nitrate precursors ($La(NO_3)_3 \cdot 6H_2O$, $Sr(NO_3)_2$, $Co(NO_3)_2 \cdot 6H_2O$, and $Fe(NO_3)_3 \cdot 9H_2O$, Wako Pure Chemical Industries) and citric acid (Sigma-Aldrich) were added to the buffer solution, and the pH was adjusted to 8 with ammonia water. The resultant solution was stirred at 100°C for 48 h and further dried at 100°C for 24 h. The gelled sample was heated at 200°C for 6 h and calcined at 900°C for 5 h to obtain LSCF powder. LSCF-GDC (LSCF 50wt%) was prepared by physical mixing. LSCF powder and GDC powder (sintered at 1500°C for 5 h) were ball-milled for 24 h.

E.2.2. Cell fabrication

The cell was prepared by using a Hionic electrolyte disk (Nexceris), which is based on scandia-stabilized zirconia. The size of the Hionic disk is 20 mm in diameter and *ca.* 150 μm in thickness. First, a GDC interlayer was prepared by using spin coating technique[236]. This interlayer was placed between the electrolyte and LSCF-GDC anode to prevent them from reacting each other. GDC powder, ethyl cellulose (Nacalai Tesque), α-terpineol (Wako Pure Chemical Industries) were mixed in a mortar at a weight ratio of 30:2:68 to form a slurry. The slurry was cast on the Hionic disk in a ϕ15 circular shape using a spin

coater (ACT-220DII, Active). The setting was 6000 rpm, 120 s. The sample was sintered at 1300°C for 5 h. Next, NiO-GDC cathode was fabricated on the reverse side of the Hionic disk. 0.4 g of NiO-GDC and a proper amount (50-100 μL) of polyethylene glycol (average molecular weight 560-640, Wako Pure Chemical Industries) were mixed in a mortar to form a slurry. The resultant slurry was screen-printed on the Hionic disk and sintered at 1300°C for 5 h. The size of the NiO-GDC cathode was ϕ12. Finally, LSCF-GDC anode (ϕ12) was fabricated on the GDC interlayer. LSCF-GDC powder was mixed with polyethylene glycol, and the obtained slurry was screen-printed. The sample was sintered at 1100°C for 5 h.

E.2.3. Electrochemical measurements

Reaction tests were performed by using an all-ceramic cell holder (Chino). Figure E-1 shows the schematic image of the experimental apparatus. The NiO-GDC|Hionic|GDC|LSCF-GDC call was sandwiched between two ceramic parts. Porous Ag foam was used as current collectors at both the anode side and the cathode side. The cathode gas sealant was Thermiculite (a vermiculite-based material provided by Flexitallic) and the anode gas sealant was alumina felt. Electrochemical measurements were conducted with a potentio-galvanostat (SP-300, Bio-Logic).

Before starting the reactions, the NiO-GDC cathode was reduced with hydrogen at 800°C. During the reduction treatment, open circuit voltage was monitored. The treatment was stopped when the cell voltage became constant. After purging hydrogen, the temperature was decreased to 600°C, and the reaction tests were performed. The cathode gas composition was set to CO_2:H_2O:H_2:N_2 = 15:30:30:25. The total flow rate was 2.0 L min^{-1} $g_{Ni\text{-}GDC}^{-1}$. (The weight of the Ni-GDC cathode was *ca.* 15mg, so the flow rate was *ca.* 30 mL min^{-1}.) Air was supplied at 30 mL min^{-1} to the anode. The current density was changed as 0 → 25 → 100 → 200 mA cm^{-2}. The cathode outlet gas composition was analyzed by an on-line gas chromatograph (Agilent 490).

The dependence of the catalytic CO methanation performance of the Ni-GDC cathode on the CO partial pressure was measured at 600°C. CO and hydrogen were introduced to the cathode, and the outlet gas

was analyzed under open circuit conditions. The detailed cathode inlet gas compositions are summarized in Table E-1. The CO partial pressure was changed as 0.012 → 0.006 → 0.003 atm while the hydrogen partial pressure was kept constant at 0.2 atm. Total cathode gas flow rate was 2.0 L min^{-1} $g_{Ni\text{-}GDC}^{-1}$.

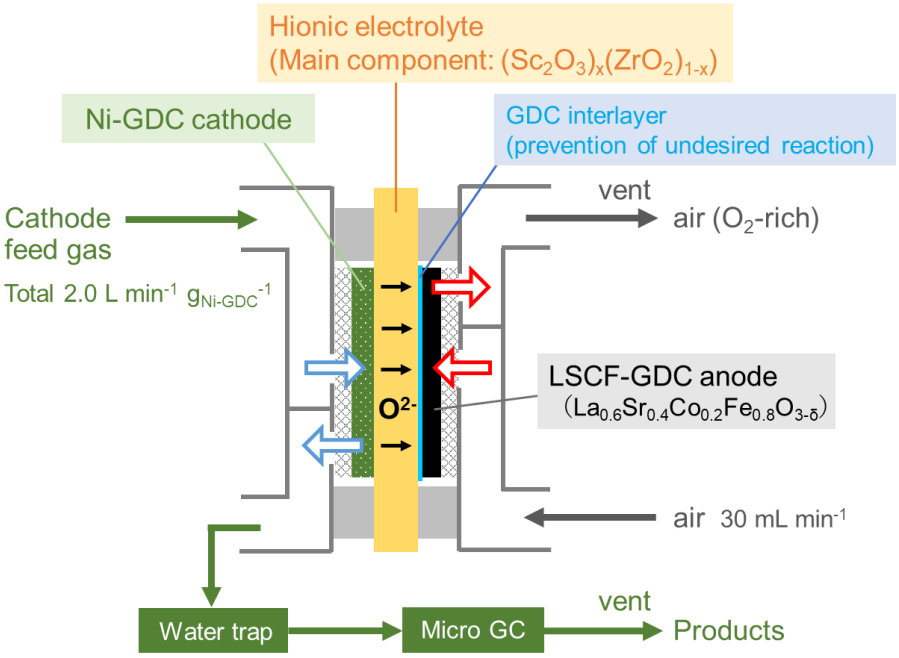

Figure E-1. Schematic image of the apparatus for SOEC experiments.

Table E-1. Cathode inlet gas compositions for the catalytic CO methanation tests.

No.	p_{H_2} / atm	p_{CO} / atm	Gas flow rate / L min^{-1} $g_{Ni\text{-}GDC}^{-1}$			
			H_2	CO/He (CO 10.36%)	N_2	total
#1	0.2	0.012	0.4	0.23	1.37	2.0
#2	0.2	0.006	0.4	0.12	1.48	2.0
#3	0.2	0.003	0.4	0.06	1.54	2.0

E.3. Results and discussion

Figure E-2 shows the results of the catalytic CO methanation test with the Ni-GDC cathode at 600°C under open circuit conditions. Figure E-2a exhibits the methane production rates at different CO partial pressures. The methane production rate can be expressed as a function of partial pressures of CO and hydrogen[237,238].

$$r_{CH_4} = k(p_{CO})^{\alpha}(p_{H_2})^{\beta} \quad \text{(E-7)}$$

If the hydrogen partial pressure is constant, the rate becomes

$$r_{CH_4} = k'(p_{CO})^{\alpha} \quad \text{(E-8)}$$

Therefore,

$$\log_{10}(r_{CH_4}) = \alpha \log_{10}(p_{CO}) + \log_{10} k' \quad \text{(E-9)}$$

Figure E-2b shows the relationship between $\log_{10}(r_{CH_4})$ and $\log_{10}(p_{CO})$. From the slope of the regression line, α, was determined to be 1.16.

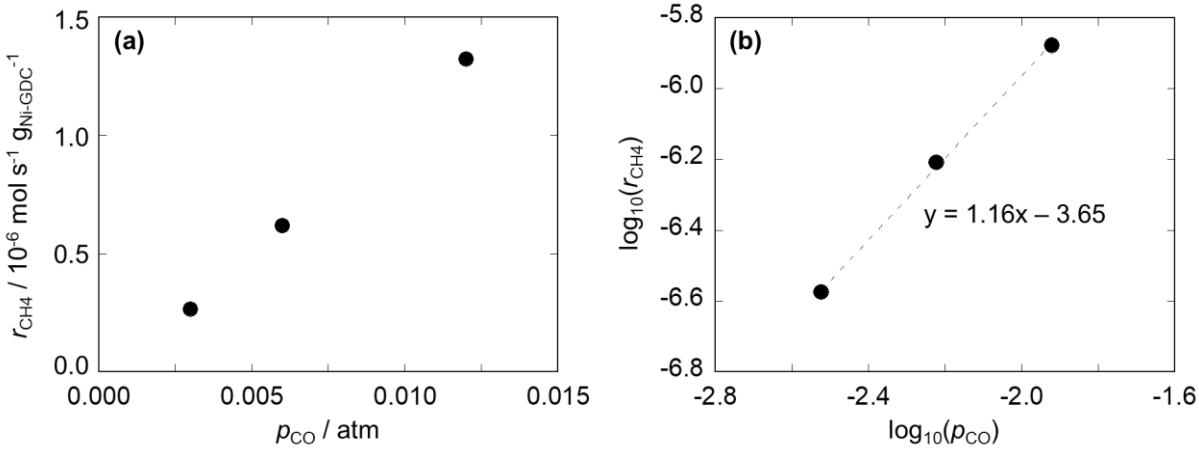

Figure E-2. The dependence of the catalytic CO methanation performance of the Ni-GDC cathode on the CO partial pressure at 600°C. The measurements were performed at OCV. The cathode inlet gas compositions are shown in Table E-1. (a) Methane production rates at different CO partial pressures. The hydrogen partial pressure was kept at 0.2 atm. (b) relationship between $\log_{10}(r_{CH_4})$ and $\log_{10}(p_{CO})$.

Figure E-3 shows the cell voltage during the electrochemical reaction tests at different current densities. Although some spikes were observed, the cell voltage was almost constant at all the tested current densities, indicating that the cell was operated stably.

Figure E-4 shows the results of the cathode outlet gas analysis. The products were CO and methane. Figure E-4a shows the production rates of CO (r_{CO}) normalized by the weight of the Ni-GDC cathode. The rates increased with the current density according to Eqs. E-1, E-2, and E-3. The corresponding CO partial pressure was 0.003-0.005 atm, which is in the range where the catalytic performance test was

conducted (0.003-0.012 atm, Table E-1). The black circles in Figure E-4b indicate the methane production rates (r_{CH_4}) measured at different current densities. The rate increased monotonically with the current density. The rate at OCV is denoted as $r_{CH_4,OCV}$ hereafter. According to Eq. E-8, $r_{CH_4,OCV}$ can be expressed as

$$r_{CH_4,OCV} = k''\left(p_{CO,OCV}\right)^{1.16} \quad \text{(E-10)}$$

If the CO methanation activity of the Ni-GDC cathode was not affected by the polarization, r_{CH_4} at a polarized condition will become

$$r^*_{CH_4,pol} = k''\left(p_{CO,pol}\right)^{1.16} \quad \text{(E-11)}$$

The asterisk indicates that the value is not measured but estimated. From Eqs. E-10 and E-11,

$$r^*_{CH_4,pol} = r_{CH_4,OCV}\left(\frac{p_{CO,pol}}{p_{CO,OCV}}\right)^{1.16} \quad \text{(E-12)}$$

The ratio of CO partial pressures was approximated by the ratio of CO production rates:

$$r^*_{CH_4,pol} = r_{CH_4,OCV}\left(\frac{r_{CO,pol}}{r_{CO,OCV}}\right)^{1.16} \quad \text{(E-13)}$$

The red diamonds in Figure E-4b indicate the $r^*_{CH_4,pol}$ values obtained by Eq. E-13. The values were significantly smaller than the measured values, r_{CH_4}. The ratio of $r_{CH_4}/r^*_{CH_4,pol}$ were 2.7, 5.4, and 8.8 at 25 mA cm^{-2}, 100 mA cm^{-2}, and 200 mA cm^{-2}, respectively. The discrepancy became larger with the current density. These results suggest that the CO methanation was promoted by the cathodic polarization. Because electrons were supplied to the cathode under the polarization, the cathode surface may have become electron-rich, and the cleavage of the C-O bond of surface-adsorbed carbonyl species may have been accelerated. It was also possible that O atom of the carbonyl was extracted and became an oxide ion (O^{2-}), although the O^{2-} extraction from H_2O or CO_2 should be preferred.

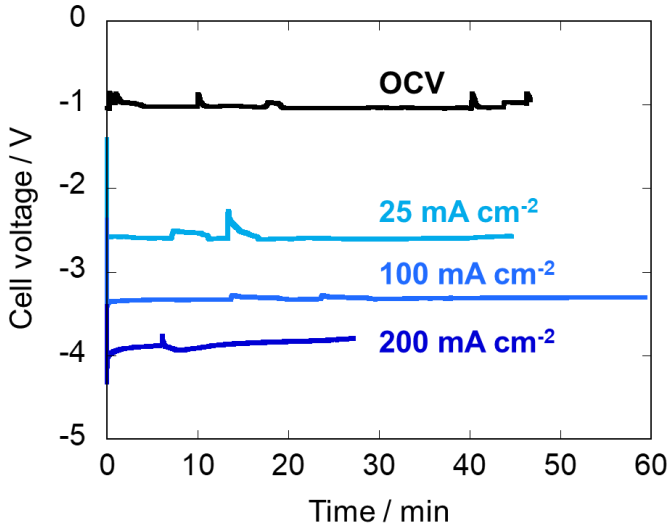

Figure E-3. Cell voltage during the electrochemical reaction tests at different current densities.

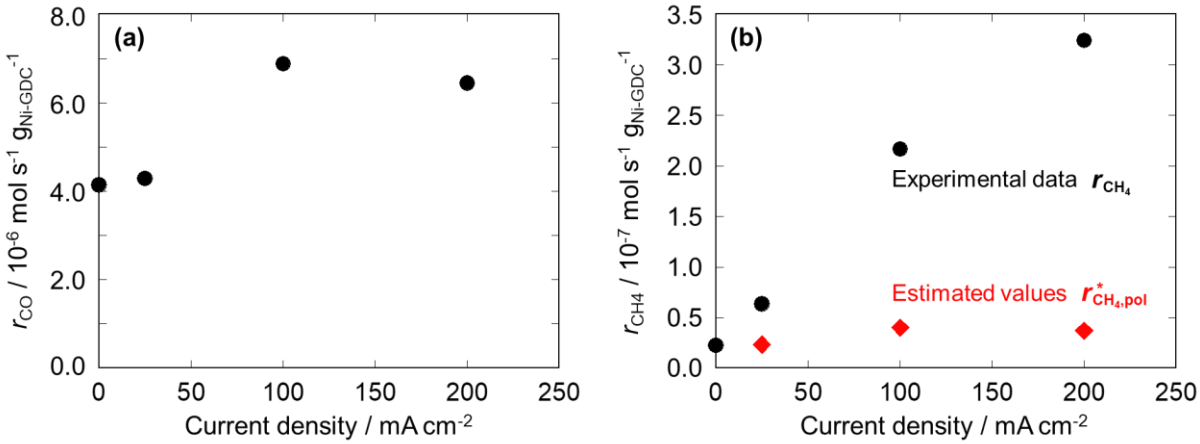

Figure E-4. Results of the electrochemical reactions at 600°C. The cathode inlet gas compositon was CO_2:H_2O:H_2:N_2 = 15:30:30:25. (a) Production rates of CO at different current densities. (b) Comparison of measured methane production rates (r_{CH_4}) and estimated methane production rates ($r^*_{CH_4,pol}$) at different current densities.

E.1. Summary

SOEC experiments were performed to examine the effect of polarization on the catalytic methanation activity of the cathode. A Ni-GDC|Hionic|GDC|LSCF-GDC cell was fabricated, and a gas mixture with a composition of CO_2:H_2O:H_2:N_2 = 15:30:30:25 was introduced to the cathode. CO and methane were produced, and the production rates increased with the current density. Separately, catalytic CO

methanation tests were conducted to investigate the effect of CO partial pressure on the activity. A gas mixture consisting of CO_2 and hydrogen was fed to the SOEC cathode, and the cathode outlet gas was measured. By assuming a power-law type kinetic equation, the dependence of the catalytic activity on the CO partial pressure was described. Using the power-law equation, the results of the electrochemical reaction tests were analyzed. The methane production rates measured under polarized conditions were much larger than the values calculated by assuming the power-law equation. This result indicates that the CO methanation activity was enhanced under the cathodic polarization.

The present section proposes a new approach to the investigation of the NEMCA effect, which utilizes a kinetic equation. By introducing the equation, the gas partial pressure changes accompanied by the current was successfully taken into consideration. The proposed method will be applicable to the analysis of the NEMCA effect in other complicated electrocatalytic systems.

Nomenclature

Symbols

a	activity
B_g	oxygen permeability [Section 2.1]
D^{eff}	effective diffusion coefficient
D^K	Knudsen diffusion coefficient
D^M	molecular diffusion coefficient
d_p	pore diameter
E	cell voltage
E_{TN}	thermoneutral voltage
E_{Nernst}	Nernst potential
E_a	activation energy
F	Faraday constant
F	molar flow rate [Section 2.2]
F_{total}	total volume flow rate in catalytic activity tests [Section 3.2]
G	Gibbs free energy
H	enthalpy
i	current density
i_L	limiting current density
i_0	exchange current density
I	current
k_B	Boltzmann constant
M	molecular weight
$\dot{n}$	molar flow rate
p	partial pressure
P	power
Q	heat duty
r	production rate
R	molar gas constant
S	entropy
T	temperature
U	feedstock conversion [Section 2.1]
W_{cat}	catalyst weight [Section 3.2]
x_I	parameter for current contributions in co-electrolysis [Section 2.1]
x_{CH_4}	ratio of η_{CH_4} to η_{total} [Section 2.1]
y	molar fraction

Z	impedance
Z'	real part of impedance
α	symmetry factor in Butler-Volmer equations
δ	thickness
ε	porosity
η_{act}	activation overpotential
η_{conc}	concentration overpotential
η_{ohm}	ohmic overpotential
$\eta_{\mathrm{CH_4}}$	energy conversion efficiency to methane [Section 2.1]
η_{total}	energy conversion efficiency to all products [Section 2.1]
μ	kinetic viscosity [Section 2.1]
ξ	tortuosity
σ	conductivity
ω	angular frequency

Abbreviations

AC	alternate current
AEM	anion exchange membrane
ASR	area specific resistance
CE	counter electrode
CEM	cation exchange membrane
CNF	carbon nanofiber
DRIFTS	diffuse reflectance infrared Fourier transform spectroscopy
EDX	energy dispersive X-ray spectroscopy
EPOC	electrochemical promotion of catalysis
FE	Faraday efficiency
FID	flame ionization detector
GC	gas chromatograph
GDC	gadolinium-doped ceria; $Ce_{1-x}Gd_xO_{2-x/2}$
GDE	gas diffusion electrode
HT-PEMFC	high-temperature proton exchange membrane fuel cell
LHV	lower heating value
LSCF	lanthanum strontium cobalt ferrite; $La_{1-x}Sr_xCo_{1-y}Fe_yO_{3-\delta}$
LSGM	strontium- and magnesium-doped lanthanum gallate; $La_{1-x}Sr_xGa_{1-y}Mg_yO_{3-\delta}$
LSM	lanthanum strontium manganate; $La_{1-x}Sr_xMnO_{3-\delta}$
MU	methanation unit
NEMCA	non-Faradaic electrochemical modification of catalytic activity

OCV	open circuit voltage
PA	phosphoric acid
PAFC	phosphoric acid fuel cell
PBI	polybenzimidazole
PEM	proton exchange membrane
PTFE	polytetrafluoroethylene
PtM	power-to-methane
RE	reference electrode
ReSOC	reversible solid oxide cell
SAEC	solid acid electrolysis cell
SEM	scanning electron microscope
ScSZ	scandia-stabilized zirconia; $(Sc_2O_3)_x(ZrO_2)_{1-x}$
SDC	samarium-doped ceria; $Ce_{1-x}Sm_xO_{2-x/2}$
SOEC	solid oxide electrolysis cell
TCD	thermal conductivity detector
WE	working electrode
XRD	X-ray diffraction
YSZ	yttria-stabilized zirconia; $(Y_2O_3)_x(ZrO_2)_{1-x}$

References

[1] International Energy Agency, “World Energy Outlook 2020,” can be found under https://www.iea.org/reports/world-energy-outlook-2020, **2020**.

[2] 独立行政法人新エネルギー・産業技術総合開発機構, “NEDO再生可能エネルギー技術白書 第2版,” can be found under https://www.nedo.go.jp/library/ne_hakusyo_index.html, **2014**.

[3] G. A. Olah, G. K. S. Prakash, A. Goeppert, *J. Am. Chem. Soc.* **2011**, *133*, 12881–12898.

[4] J. C. Koj, C. Wulf, P. Zapp, *Renew. Sustain. Energy Rev.* **2019**, *112*, 865–879.

[5] M. David, C. Ocampo-Martínez, R. Sánchez-Peña, *J. Energy Storage* **2019**, *23*, 392–403.

[6] S. Trasatti, *J. Electroanal. Chem.* **1999**, *476*, 90–91.

[7] R. de Levie, *J. Electroanal. Chem.* **1999**, *476*, 92–93.

[8] A. Buttler, H. Spliethoff, *Renew. Sustain. Energy Rev.* **2018**, *82*, 2440–2454.

[9] M. Carmo, D. L. Fritz, J. Mergel, D. Stolten, *Int. J. Hydrogen Energy* **2013**, *38*, 4901–4934.

[10] S. D. Ebbesen, S. H. Jensen, A. Hauch, M. B. Mogensen, *Chem. Rev.* **2014**, *114*, 10697–10734.

[11] J. S. Wainright, J. -T. Wang, D. Weng, R. F. Savinell, M. Litt, *J. Electrochem. Soc.* **1995**, *142*, L121–L123.

[12] S. S. Araya, F. Zhou, V. Liso, S. L. Sahlin, J. R. Vang, S. Thomas, X. Gao, C. Jeppesen, S. K. Kær, *Int. J. Hydrogen Energy* **2016**, *41*, 21310–21344.

[13] R. E. Rosli, A. B. Sulong, W. R. W. Daud, M. A. Zulkifley, T. Husaini, M. I. Rosli, E. H. Majlan, M. A. Haque, *Int. J. Hydrogen Energy* **2017**, *42*, 9293–9314.

[14] D. Aili, M. K. Hansen, C. Pan, Q. Li, E. Christensen, J. O. Jensen, N. J. Bjerrum, *Int. J. Hydrogen Energy* **2011**, *36*, 6985–6993.

[15] M. K. Hansen, D. Aili, E. Christensen, C. Pan, S. Eriksen, J. O. Jensen, J. H. Von Barner, Q. Li, N. J. Bjerrum, *Int. J. Hydrogen Energy* **2012**, *37*, 10992–11000.

[16] I. Vincent, D. Bessarabov, *Renew. Sustain. Energy Rev.* **2018**, *81*, 1690–1704.

[17] H. Ito, N. Kawaguchi, S. Someya, T. Munakata, N. Miyazaki, M. Ishida, A. Nakano, *Int. J. Hydrogen Energy* **2018**, *43*, 17030–17039.

[18] L. Barelli, G. Bidini, G. Cinti, J. Milewski, *Int. J. Hydrogen Energy* **2020**, DOI 10.1016/j.ijhydene.2020.07.220.

[19] S. Frangini, A. Masi, *Int. J. Hydrogen Energy* **2016**, *41*, 18739–18746.

[20] N. Q. Minh, *J. Am. Ceram. Soc.* **1993**, *76*, 563–588.

[21] V. V. Kharton, F. M. B. Marques, A. Atkinson, *Solid State Ionics* **2004**, *174*, 135–149.

[22] J. W. Fergus, *J. Power Sources* **2006**, *162*, 30–40.

[23] T. Ishihara, H. Matsuda, Y. Takita, *J. Am. Chem. Soc.* **1994**, *116*, 3801–3803.

[24] S.-L. Zhang, T. Liu, C.-J. Li, S.-W. Yao, C.-X. Li, G.-J. Yang, M. Liu, *J. Mater. Chem. A* **2015**, *3*, 7535–7553.

[25] S. P. Jiang, *J. Power Sources* **2003**, *124*, 390–402.

[26] B. Fan, J. Yan, X. Yan, *Solid State Sci.* **2011**, *13*, 1835–1839.

[27] T. Ishihara, M. Honda, T. Shibayama, H. Minami, H. Nishiguchi, Y. Takita, *J. Electrochem. Soc.* **1998**, *145*, 3177–3183.

[28] J. Laurencin, M. Hubert, K. Couturier, T. Le Bihan, P. Cloetens, F. Lefebvre-Joud, E. Siebert, *Electrochim. Acta* **2015**, *174*, 1299–1316.

[29] W. Jiang, B. Wei, Z. Lü, Z. H. Wang, X. B. Zhu, L. Zhu, *Fuel Cells* **2014**, *14*, 966–972.

[30] J. Kim, S. Sengodan, S. Kim, O. Kwon, Y. Bu, G. Kim, *Renew. Sustain. Energy Rev.* **2019**, *109*, 606–618.

[31] A. Goñi-Urtiaga, D. Presvytes, K. Scott, *Int. J. Hydrogen Energy* **2012**, *37*, 3358–3372.

[32] A. I. Baranov, V. P. Khiznichenko, V. A. Sandur, L. A. Shuvalov, *Ferroelectrics* **1988**, *81*, 183–186.

[33] J. Otomo, N. Minagawa, C. J. Wen, K. Eguchi, H. Takahashi, *Solid State Ionics* **2003**, *156*, 357–369.

[34] G. Kim, F. Blanc, Y. Y. Hu, C. P. Grey, *J. Phys. Chem. C* **2013**, *117*, 6504–6515.

[35] G. Kim, J. M. Griffin, F. Blanc, S. M. Haile, C. P. Grey, *J. Am. Chem. Soc.* **2015**, *137*, 3867–3876.

[36] G. Y. Foran, D. H. Brouwer, G. R. Goward, *J. Phys. Chem. C* **2017**, *121*, 25641–25650.

[37] D. A. Boysen, T. Uda, C. R. I. Chisholm, S. M. Haile, *Science* **2004**, *303*, 68–70.

[38] Y. Taninouchi, T. Uda, Y. Awakura, *Solid State Ionics* **2008**, *178*, 1648–1653.

[39] Y. Taninouchi, N. Hatada, T. Uda, Y. Awakura, *J. Electrochem. Soc.* **2009**, *156*, B572–B579.

[40] H. Muroyama, T. Matsui, R. Kikuchi, K. Eguchi, *J. Phys. Chem. C* **2008**, *112*, 15532–15536.

[41] G. Qing, R. Kikuchi, *Solid State Ionics* **2016**, *289*, 133–142.

[42] K. S. Lee, *J. Phys. Chem. Solids* **1996**, *57*, 333–342.

[43] H. Muroyama, K. Kudo, T. Matsui, R. Kikuchi, K. Eguchi, *Solid State Ionics* **2007**, *178*, 1512–1516.

[44] M. Nagao, T. Kamiya, P. Heo, A. Tomita, T. Hibino, M. Sano, *J. Electrochem. Soc.* **2006**, *153*, 1604–1609.

[45] Y. Shen, K. Kojima, M. Nishida, P. Heo, K. H. Choi, H. Chang, T. Hibino, *J. Mater. Chem.* **2012**, *22*, 14907–14915.

[46] G. Qing, K. Sukegawa, R. Kikuchi, A. Takagaki, S. T. Oyama, *J. Appl. Electrochem.* **2017**, *47*, 803–814.

[47] G. Qing, R. Kikuchi, A. Takagaki, T. Sugawara, S. T. Oyama, *J. Power Sources* **2014**, *272*, 1018–1029.

[48] P. Bocchetta, R. Ferraro, F. Di Quarto, *J. Power Sources* **2009**, *187*, 49–56.

[49] P. Bocchetta, G. Chiavarotti, R. Masi, C. Sunseri, F. Di Quarto, *Electrochem. Commun.* **2004**, *6*, 923–928.

[50] K. Lee, S. Maurya, Y. S. Kim, C. R. Kreller, M. S. Wilson, D. Larsen, S. E. Elangovan, R. Mukundan, *Energy Environ. Sci.* **2018**, *11*, 979–987.

[51] G. Qing, R. Kikuchi, A. Takagaki, T. Sugawara, S. T. Oyama, *Electrochim. Acta* **2015**, *169*, 219–226.

[52] G. Qing, R. Kikuchi, A. Takagaki, T. Sugawara, S. T. Oyama, *J. Electrochem. Soc.* **2014**, *161*, F451–F457.

[53] D. Dang, B. Zhao, D. Chen, S. Yoo, S. Y. Lai, B. Doyle, S. Dai, Y. Chen, C. Qu, L. Zhang, S. Liao, M. Liu, *J. Power Sources* **2017**, *359*, 1–6.

[54] M. Wagner, C. Dreßler, F. P. Lohmann-Richters, K. Hanus, D. Sebastiani, A. Varga, B. Abel, *J. Mater. Chem. A* **2019**, *7*, 27367–27376.

[55] Y. C. Jin, M. Nishida, W. Kanematsu, T. Hibino, *J. Power Sources* **2011**, *196*, 6042–6047.

[56] X. Chen, Y. Zhang, P. Ribeiorinha, H. Li, X. Kong, M. Boaventura, *RSC Adv.* **2018**, *8*, 5225–5232.

[57] Y. Jin, K. Fujiwara, T. Hibino, *Electrochem. Solid-State Lett.* **2010**, *13*, 93–96.

[58] R. Kikuchi, A. Ogawa, T. Matsuoka, A. Takagaki, T. Sugawara, S. T. Oyama, *Solid State Ionics* **2016**, *285*, 160–164.

[59] S. M. Haile, C. R. I. Chisholm, K. Sasaki, D. A. Boysen, T. Uda, *Faraday Discuss.* **2007**, *134*, 17–39.

[60] M. Nagao, A. Takeuchi, P. Heo, T. Hibino, M. Sano, A. Tomita, *Electrochem. Solid-State Lett.* **2006**, *9*, A105–A109.

[61] T. Uda, S. M. Haile, *Electrochem. Solid-State Lett.* **2005**, *8*, 245–246.

[62] D. Lim, J. Liu, S. A. Pandey, H. Paik, C. R. I. Chisholm, J. T. Hupp, S. M. Haile, *Electrochim. Acta* **2018**, *288*, 12–19.

[63] O. Naumov, S. Naumov, R. Flyunt, B. Abel, A. Varga, *ChemSusChem* **2016**, *9*, 3298–3306.

[64] W. D. Tennyson, M. Tian, A. B. Papandrew, C. M. Rouleau, A. A. Puretzky, B. T. Sneed, K. L. More, G. M. Veith, G. Duscher, T. A. Zawodzinski, D. B. Geohegan, *Carbon* **2017**, *123*, 605–615.

[65] M. Wagner, O. Lorenz, F. P. Lohmann-Richters, A. Varga, B. Abel, *Sustain. Energy Fuels* **2020**, *4*, 5284–5293.

[66] C. Forman, I. K. Muritala, R. Pardemann, B. Meyer, *Renew. Sustain. Energy Rev.* **2016**, *57*,

1568–1579.

[67] A. Firth, B. Zhang, A. Yang, *Appl. Energy* **2019**, *235*, 1314–1334.

[68] C. B. Prag, Intermediate Temperature Steam Electrolysis with Phosphate-Based Electrolytes, PhD thesis, Technical University of Denmark, **2014**.

[69] L. Navarrete, A. Andrio, S. Escolástico, S. Moya, V. Compañ, J. M. Serra, *Membranes* **2019**, *9*, 49.

[70] R. W. Berg, A. V. Nikiforov, I. M. Petrushina, N. J. Bjerrum, *Appl. Energy* **2016**, *180*, 269–275.

[71] A. V Nikiforov, R. W. Berg, N. J. Bjerrum, *Ionics* **2018**, *24*, 2761–2782.

[72] B. Kumar, J. P. Brian, V. Atla, S. Kumari, K. A. Bertram, R. T. White, J. M. Spurgeon, *Catal. Today* **2016**, *270*, 19–38.

[73] M. E. Royer, *C. R. Hebd. Seances Acad. Sci.* **1870**, *70*, 731–732.

[74] A. Coehn, S. Jahn, *Berichte der Dtsch. Chem. Gesellschaft* **1904**, *37*, 2836–2842.

[75] R. Ehrenfeld, *Berichte der Dtsch. Chem. Gesellschaft* **1905**, *38*, 4138–4143.

[76] F. Fischer, O. Prziza, *Berichte der Dtsch. Chem. Gesellschaft* **1914**, *47*, 256–260.

[77] Y. Hori, K. Kikuchi, S. Suzuki, *Chem. Lett.* **1985**, *14*, 1695–1698.

[78] I. Merino-Garcia, E. Alvarez-Guerra, J. Albo, A. Irabien, *Chem. Eng. J.* **2016**, *305*, 104–120.

[79] Q. Lu, F. Jiao, *Nano Energy* **2016**, *29*, 439–456.

[80] Y. Wang, Z. Chen, P. Han, Y. Du, Z. Gu, X. Xu, G. Zheng, *ACS Catal.* **2018**, *8*, 7113–7119.

[81] K. Manthiram, B. J. Beberwyck, A. P. Alivisatos, *J. Am. Chem. Soc.* **2014**, *136*, 13319–13325.

[82] I. Merino-Garcia, J. Albo, A. Irabien, *Energy Technol.* **2017**, *5*, 922–928.

[83] J. Albo, A. Irabien, *J. Catal.* **2016**, *343*, 232–239.

[84] S. Ma, M. Sadakiyo, R. Luo, M. Heima, M. Yamauchi, P. J. A. Kenis, *J. Power Sources* **2016**, *301*, 219–228.

[85] M. Rahaman, A. Dutta, A. Zanetti, P. Broekmann, *ACS Catal.* **2017**, *7*, 7946–7956.

[86] C.-T. Dinh, T. Burdyny, M. G. Kibria, A. Seifitokaldani, C. M. Gabardo, F. P. G. de Arquer, A. Kiani, J. P. Edwards, P. De Luna, O. S. Bushuyev, C. Zou, R. Quintero-bermudez, Y. Pang, D.

Sinton, E. H. Sargent, *Science* **2018**, *360*, 783–787.

[87] J.-J. Lv, M. Jouny, W. Luc, W. Zhu, J.-J. Zhu, F. Jiao, *Adv. Mater.* **2018**, 1803111.

[88] I. Merino-Garcia, J. Albo, A. Irabien, *Nanotechnology* **2018**, *29*, 014001.

[89] C. Hahn, T. Hatsukade, Y. Kim, A. Vailionis, J. H. Baricuatro, D. C. Higgins, S. A. Nitopi, M. P. Soriaga, T. F. Jaramillo, *Proc. Natl. Acad. Sci.* **2017**, *114*, 5918–5923.

[90] C. S. Le Duff, M. J. Lawrence, P. Rodriguez, *Angew. Chemie Int. Ed.* **2017**, *56*, 12919–12924.

[91] R. Reske, H. Mistry, F. Behafarid, B. Roldan Cuenya, P. Strasser, *J. Am. Chem. Soc.* **2014**, *136*, 6978–6986.

[92] J. Resasco, L. D. Chen, E. Clark, C. Tsai, C. Hahn, T. F. Jaramillo, K. Chan, A. T. Bell, *J. Am. Chem. Soc.* **2017**, *139*, 11277–11287.

[93] S. Ringe, E. L. Clark, J. Resasco, A. Walton, B. Seger, A. T. Bell, K. Chan, *Energy Environ. Sci.* **2019**, *12*, 3001–3014.

[94] J. He, N. J. J. Johnson, A. Huang, C. P. Berlinguette, *ChemSusChem* **2018**, *11*, 48–57.

[95] T. T. H. Hoang, S. Verma, S. Ma, T. T. Fister, J. Timoshenko, A. I. Frenkel, P. J. A. Kenis, A. A. Gewirth, *J. Am. Chem. Soc.* **2018**, *140*, 5791–5797.

[96] G. Wen, D. U. Lee, B. Ren, F. M. Hassan, G. Jiang, Z. P. Cano, J. Gostick, E. Croiset, Z. Bai, L. Yang, Z. Chen, *Adv. Energy Mater.* **2018**, *8*, 1802427.

[97] S. Chatterjee, C. Griego, J. L. Hart, Y. Li, M. L. Taheri, J. Keith, J. D. Snyder, *ACS Catal.* **2019**, *9*, 5290–5301.

[98] W. Li, N. Fechler, T. J. Bandosz, *Appl. Catal. B Environ.* **2018**, *234*, 1–9.

[99] M. Tomisaki, S. Kasahara, K. Natsui, N. Ikemiya, Y. Einaga, *J. Am. Chem. Soc.* **2019**, *141*, 7414–7420.

[100] X. Sun, X. Kang, Q. Zhu, J. Ma, G. Yang, Z. Liu, B. Han, *Chem. Sci.* **2016**, *7*, 2883–2887.

[101] X. Sun, Q. Zhu, X. Kang, H. Liu, Q. Qian, Z. Zhang, B. Han, *Angew. Chemie Int. Ed.* **2016**, *55*, 6771–6775.

[102] J. Yuan, W.-Y. Zhi, L. Liu, M.-P. Yang, H. Wang, J.-X. Lu, *Electrochim. Acta* **2018**, *282*, 694–

701.

[103] C. Delacourt, P. L. Ridgway, J. B. Kerr, J. Newman, *J. Electrochem. Soc.* **2008**, *155*, B42-B49.

[104] Y. C. Li, D. Zhou, Z. Yan, R. H. Gonçalves, D. A. Salvatore, C. P. Berlinguette, T. E. Mallouk, *ACS Energy Lett.* **2016**, *1*, 1149–1153.

[105] Y. C. Li, Z. Yan, J. Hitt, R. Wycisk, P. N. Pintauro, T. E. Mallouk, *Adv. Sustain. Syst.* **2018**, *2*, 1700187.

[106] J. Durst, A. Rudnev, A. Dutta, Y. Fu, J. Herranz, V. Kaliginedi, A. Kuzume, A. A. Permyakova, Y. Paratcha, P. Broekmann, T. J. Schmidt, *Chim. Int. J. Chem.* **2015**, *69*, 769–776.

[107] D. M. Weekes, D. A. Salvatore, A. Reyes, A. Huang, C. P. Berlinguette, *Acc. Chem. Res.* **2018**, *51*, 910–918.

[108] D. Higgins, C. Hahn, C. Xiang, T. F. Jaramillo, A. Z. Weber, *ACS Energy Lett.* **2019**, *4*, 317–324.

[109] S. M. A. Kriescher, K. Kugler, S. S. Hosseiny, Y. Gendel, M. Wessling, *Electrochem. Commun.* **2015**, *50*, 64–68.

[110] D. Gao, F. Cai, Q. Xu, G. Wang, X. Pan, X. Bao, *J. Energy Chem.* **2014**, *23*, 694–700.

[111] N. Gutiérrez-Guerra, J. L. Valverde, A. Romero, J. C. Serrano-Ruiz, A. de Lucas-Consuegra, *Electrochem. Commun.* **2017**, *81*, 128–131.

[112] H. Meskine, E. Gürbüz, V. Albin, A. Meléndez-Ceballos, M. Cassir, A. Ringuedé, V. Lair, *Int. J. Hydrogen Energy* **2020**, DOI 10.1016/j.ijhydene.2020.08.028.

[113] J. Ren, M. Johnson, R. Singhal, J. Licht, *J. CO2 Util.* **2017**, *18*, 335–344.

[114] X. Wang, X. Liu, G. Licht, S. Licht, *Sci. Rep.* **2020**, *10*, 15146.

[115] M. Götz, J. Lefebvre, F. Mörs, A. McDaniel Koch, F. Graf, S. Bajohr, R. Reimert, T. Kolb, *Renew. Energy* **2016**, *85*, 1371–1390.

[116] S. Rönsch, J. Schneider, S. Matthischke, M. Schlüter, M. Götz, J. Lefebvre, P. Prabhakaran, S. Bajohr, *Fuel* **2016**, *166*, 276–296.

[117] S. Tada, T. Shimizu, H. Kameyama, T. Haneda, R. Kikuchi, *Int. J. Hydrogen Energy* **2012**, *37*,

5527–5531.

[118] G. Gahleitner, *Int. J. Hydrogen Energy* **2012**, *38*, 2039–2061.

[119] L. Chen, F. Chen, C. Xia, *Energy Environ. Sci.* **2014**, *7*, 4018–4022.

[120] D. M. Bierschenk, J. R. Wilson, S. A. Barnett, *Energy Environ. Sci.* **2011**, *4*, 944–951.

[121] Y. Luo, W. Li, Y. Shi, T. Cao, X. Ye, S. Wang, N. Cai, *J. Electrochem. Soc.* **2015**, *162*, F1129–F1134.

[122] Y. Luo, Y. Shi, W. Li, N. Cai, *Energy Convers. Manag.* **2018**, *165*, 127–136.

[123] L. Lei, T. Liu, S. Fang, J. P. Lemmon, F. Chen, *J. Mater. Chem. A* **2017**, *5*, 2904–2910.

[124] S. H. Jensen, C. Graves, M. Mogensen, C. Wendel, R. Braun, G. Hughes, Z. Gao, S. A. Barnett, *Energy Environ. Sci.* **2015**, *8*, 2471–2479.

[125] Y. Luo, X. Wu, Y. Shi, A. F. Ghoniem, N. Cai, *Appl. Energy* **2018**, *215*, 371–383.

[126] L. Barelli, G. Bidini, A. Ottaviano, *Energy* **2015**, *90*, 1180–1191.

[127] C. H. Wendel, P. Kazempoor, R. J. Braun, *J. Power Sources* **2015**, *276*, 133–144.

[128] C. H. Wendel, Z. Gao, S. A. Barnett, R. J. Braun, *J. Power Sources* **2015**, *283*, 329–342.

[129] C. H. Wendel, P. Kazempoor, R. J. Braun, *J. Power Sources* **2016**, *301*, 93–104.

[130] Y. Luo, Y. Shi, Y. Zheng, N. Cai, *J. Power Sources* **2017**, *340*, 60–70.

[131] E. Reznicek, R. J. Braun, *ECS Trans.* **2017**, *78*, 2913–2923.

[132] C. Graves, S. D. Ebbesen, M. Mogensen, K. S. Lackner, *Renew. Sustain. Energy Rev.* **2011**, *15*, 1–23.

[133] W. Li, H. Wang, Y. Shi, N. Cai, *Int. J. Hydrogen Energy* **2013**, *38*, 11104–11109.

[134] T. Yamaguchi, H. Shimada, U. Honda, H. Kishimoto, T. Ishiyama, Y. Fujishiro, *ECS Trans.* **2015**, *68*, 3459–3463.

[135] N. Fujiwara, R. Kikuchi, A. Takagaki, T. Sugawara, S. T. Oyama, *ECS Trans.* **2017**, 78, 3247–3256.

[136] A. G. Jolley, R. Jayathilake, E. D. Wachsman, *Ionics* **2019**, *25*, 3531–3536.

[137] A. S. Painter, Y.-L. Huang, E. D. Wachsman, *J. Power Sources* **2017**, *360*, 391–398.

[138] A. Mineshige, H. Hayakawa, T. Nishimoto, A. Heguri, T. Yazawa, Y. Takayama, Y. Kagoshima, H. Takano, S. Takeda, J. Matsui, *Solid State Ionics* **2018**, *319*, 223–227.

[139] A. Mineshige, M. Momai, A. Matsumaru, S. Yagi, T. Yazawa, *ECS Trans.* **2019**, *91*, 1129–1138.

[140] E. D. Wachsman, K. T. Lee, *Science* **2011**, *334*, 935–939.

[141] C. Zhao, Y. Li, W. Zhang, Y. Zheng, X. Lou, B. Yu, J. Chen, Y. Chen, M. Liu, J. Wang, *Energy Environ. Sci.* **2020**, *13*, 53–85.

[142] L. Bi, S. Boulfrad, E. Traversa, *Chem. Soc. Rev.* **2014**, *43*, 8255–8270.

[143] K. Xie, Y. Zhang, G. Meng, J. T. S. Irvine, *J. Mater. Chem.* **2011**, *21*, 195–198.

[144] T. Pu, W. Tan, H. Shi, Y. Na, J. Lu, B. Zhu, *Electrochim. Acta* **2016**, *190*, 193–198.

[145] N. Bausá, S. Escolástico, J. M. Serra, *J. CO2 Util.* **2019**, *34*, 231–238.

[146] R. Sažinas, C. Bernuy-López, M.-A. Einarsrud, T. Grande, *J. Am. Ceram. Soc.* **2016**, *99*, 3685–3695.

[147] E. Christensen, I. M. Petrushina, A. V. Nikiforov, R. W. Berg, N. J. Bjerrum, *J. Electrochem. Soc.* **2020**, *167*, 044511.

[148] I. U. Din, M. S. Shaharun, M. A. Alotaibi, A. I. Alharthi, A. Naeem, *J. CO2 Util.* **2019**, *34*, 20–33.

[149] M. Stoukides, C. G. Vayenas, *J. Catal.* **1981**, *70*, 137–146.

[150] C. G. Vayenas, *J. Solid State Electrochem.* **2011**, *15*, 1425–1435.

[151] C. G. Vayenas, *Catal. Lett.* **2013**, *143*, 1085–1097.

[152] P. Vernoux, L. Lizarraga, M. N. Tsampas, F. M. Sapountzi, A. De Lucas-Consuegra, J. L. Valverde, S. Souentie, C. G. Vayenas, D. Tsiplakides, S. Balomenou, E. A. Baranova, *Chem. Rev.* **2013**, *113*, 8192–8260.

[153] V. Jiménez, C. Jiménez-Borja, P. Sánchez, A. Romero, E. I. Papaioannou, D. Theleritis, S. Souentie, S. Brosda, J. L. Valverde, *Appl. Catal. B Environ.* **2011**, *107*, 210–220.

[154] I. Kalaitzidou, M. Makri, D. Theleritis, A. Katsaounis, C. G. Vayenas, *Surf. Sci.* **2016**, *646*, 194–

203.

[155] M. Makri, A. Katsaounis, C. G. Vayenas, *Electrochim. Acta* **2015**, *179*, 556–564.

[156] D. Theleritis, S. Souentie, A. Siokou, A. Katsaounis, C. G. Vayenas, *ACS Catal.* **2012**, *2*, 770–780.

[157] D. Theleritis, M. Makri, S. Souentie, A. Caravaca, A. Katsaounis, C. G. Vayenas, *ChemElectroChem* **2014**, *1*, 254–262.

[158] Y. Zheng, J. Wang, B. Yu, W. Zhang, J. Chen, J. Qiao, J. Zhang, *Chem. Soc. Rev.* **2017**, *46*, 1427–1463.

[159] E. Giglio, A. Lanzini, M. Santarelli, P. Leone, *J. Energy Storage* **2015**, *1*, 22–37.

[160] J.-C. Njodzefon, D. Klotz, A. Kromp, A. Weber, E. Ivers-Tiffée, *J. Electrochem. Soc.* **2013**, *160*, F313–F323.

[161] L. Kleiminger, T. Li, K. Li, G. H. Kelsall, *Electrochim. Acta* **2015**, *179*, 565–577.

[162] J. Ashok, S. Pati, P. Hongmanorom, T. Zhang, J. Chen, S. Kawi, *Catal. Today* **2020**, *356*, 471–489.

[163] J. P. Stempien, O. L. Ding, Q. Sun, S. H. Chan, *Int. J. Hydrogen Energy* **2012**, *37*, 14518–14527.

[164] J. P. Stempien, Q. Sun, S. H. Chan, *Energy* **2013**, *55*, 647–657.

[165] 社団法人化学工学協会, 改訂五版 化学工学便覧, 丸善, **1988**.

[166] J.-H. Park, R. N. Blumenthal, *J. Electrochem. Soc.* **1989**, *136*, 2867–2876.

[167] M. Ni, *J. Power Sources* **2012**, *202*, 209–216.

[168] A. Leonide, Y. Apel, E. Ivers-Tiffée, *ECS Trans.* **2009**, *19*, 81–109.

[169] M. Ni, *Energy Convers. Manag.* **2013**, *70*, 116–129.

[170] R. O'Hayre, S.-W. Cha, W. Colella, F. B. Prinz, *Fuel Cell Fundamentals*, Wiley, New Jersey, **2016**.

[171] 蒔田董, 粘度と熱伝導率 データの検索と計算法, 培風館, **1975**.

[172] M. Ni, M. K. H. Leung, D. Y. C. Leung, *J. Power Sources* **2006**, *163*, 460–466.

[173] B. Todd, J. B. Young, *J. Power Sources* **2002**, *110*, 186–200.

[174] H. Zhu, R. J. Kee, V. M. Janardhanan, O. Deutschmann, D. G. Goodwin, *J. Electrochem. Soc.* **2005**, *152*, A2427–A2440.

[175] O. Yamamoto, Y. Arati, Y. Takeda, N. Imanishi, Y. Mizutani, M. Kawai, Y. Nakamura, *Solid State Ionics* **1995**, *79*, 137–142.

[176] A. Goeppert, M. Czaun, J. P. Jones, G. K. Surya Prakash, G. A. Olah, *Chem. Soc. Rev.* **2014**, *43*, 7995–8048.

[177] T. Matsui, T. Kukino, R. Kikuchi, K. Eguchi, *Electrochem. Solid-State Lett.* **2005**, *8*, A256–A258.

[178] F. Marangio, M. Santarelli, M. Calì, *Int. J. Hydrogen Energy* **2009**, *34*, 1143–1158.

[179] Z. Wang, M. Mori, T. Araki, *Int. J. Hydrogen Energy* **2010**, *35*, 4451–4458.

[180] M. Gruber, P. Weinbrecht, L. Biffar, S. Harth, D. Trimis, J. Brabandt, O. Posdziech, R. Blumentritt, *Fuel Process. Technol.* **2018**, *181*, 61–74.

[181] T. Matsui, T. Kukino, R. Kikuchi, K. Eguchi, *J. Electrochem. Soc.* **2006**, *153*, A339–A342.

[182] T. Matsui, T. Noto, H. Muroyama, M. Iijima, K. Eguchi, *J. Power Sources* **2011**, *196*, 9445–9450.

[183] S. Kishira, G. Qing, S. Suzu, R. Kikuchi, A. Takagaki, S. T. Oyama, *Int. J. Hydrogen Energy* **2017**, *42*, 26843–26854.

[184] K. Imamura, J. Kubota, *Sustain. Energy Fuels* **2018**, *2*, 1278–1286.

[185] T. Ioroi, Z. Siroma, S. Yamazaki, K. Yasuda, *Adv. Energy Mater.* **2019**, *9*, 1–20.

[186] K. G. Gallagher, R. M. Darling, T. F. Fuller, in *Handbook of Fuel Cells – Fundamentals, Technology and Applications* (Eds.: W. Vielstich, H.A. Gasteiger, A. Lamm, H. Yokokawa), John Wiley & Sons, Ltd., **2010**, pp. 1–10.

[187] S. H. Jensen, A. Hauch, P. V. Hendriksen, M. Mogensen, N. Bonanos, T. Jacobsen, *J. Electrochem. Soc.* **2007**, *154*, B1325–B1330.

[188] S. Tada, S. Tajima, N. Fujiwara, R. Kikuchi, *Int. J. Hydrogen Energy* **2019**, *44*, 26545–26553.

[189] G. Qing, R. Kikuchi, A. Takagaki, T. Sugawara, S. T. Oyama, *J. Power Sources* **2016**, *306*, 578–586.

[190] H. R. Kunz, *ECS Trans.* **2007**, *11*, 1447–1460.

[191] S. H. Eberhardt, M. Toulec, F. Marone, M. Stampanoni, F. N. Buchi, T. J. Schmidt, *J. Electrochem. Soc.* **2015**, *162*, F310–F316.

[192] S. Dheenadayalan, R.-H. Song, D.-R. Shin, *J. Power Sources* **2002**, *107*, 98–102.

[193] S. Yoshimi, T. Matsui, R. Kikuchi, K. Eguchi, *J. Power Sources* **2008**, *179*, 497–503.

[194] S. A. Grigoriev, K. A. Dzhus, D. G. Bessarabov, P. Millet, *Int. J. Hydrogen Energy* **2014**, *39*, 20440–20446.

[195] H. A. Laitinen, C. G. Enke, *J. Electrochem. Soc.* **1960**, *107*, 773–781.

[196] S. D. James, *J. Electrochem. Soc.* **1969**, *116*, 1681–1688.

[197] C. Wang, F. Lan, Z. He, X. Xie, Y. Zhao, H. Hou, L. Guo, V. Murugadoss, H. Liu, Q. Shao, Q. Gao, T. Ding, R. Wei, Z. Guo, *ChemSusChem* **2019**, *12*, 1576–1590.

[198] H. Nagase, R. Naito, S. Tada, R. Kikuchi, K. Fujiwara, M. Nishijima, T. Honma, *Catal. Sci. Technol.* **2020**, *10*, 4522–4531.

[199] S. Tada, S. Kayamori, T. Honma, H. Kamei, A. Nariyuki, K. Kon, T. Toyao, K. Shimizu, S. Satokawa, *ACS Catal.* **2018**, *8*, 7809–7819.

[200] T. Fujitani, I. Nakamura, *Bull. Chem. Soc. Jpn.* **2002**, *75*, 1393–1398.

[201] S. Hara, S. Takano, M. Miyayama, *J. Phys. Chem. B* **2004**, *108*, 5634–5639.

[202] S. Tada, A. Katagiri, K. Kiyota, T. Honma, H. Kamei, A. Nariyuki, S. Uchida, S. Satokawa, *J. Phys. Chem. C* **2018**, *122*, 5430–5442.

[203] I. A. Fisher, A. T. Bell, *J. Catal.* **1997**, *172*, 222–237.

[204] A. Álvarez, A. Bansode, A. Urakawa, A. V. Bavykina, T. A. Wezendonk, M. Makkee, J. Gascon, F. Kapteijn, *Chem. Rev.* **2017**, *117*, 9804–9838.

[205] S. Tada, R. Kikuchi, *Catal. Sci. Technol.* **2015**, *5*, 3061–3070.

[206] R. Kortlever, J. Shen, K. J. P. Schouten, F. Calle-Vallejo, M. T. M. Koper, *J. Phys. Chem. Lett.*

2015, *6*, 4073–4082.

[207] K. P. Kuhl, E. R. Cave, D. N. Abram, T. F. Jaramillo, *Energy Environ. Sci.* **2012**, *5*, 7050–7059.

[208] J. Albo, M. Alvarez-Guerra, P. Castaño, A. Irabien, *Green Chem.* **2015**, *17*, 2304–2324.

[209] R. Gaikwad, A. Bansode, A. Urakawa, *J. Catal.* **2016**, *343*, 127–132.

[210] E. Frei, A. Schaadt, T. Ludwig, H. Hillebrecht, I. Krossing, *ChemCatChem* **2014**, *6*, 1721–1730.

[211] T. Witoon, J. Chalorngtham, P. Dumrongbunditkul, M. Chareonpanich, J. Limtrakul, *Chem. Eng. J.* **2016**, *293*, 327–336.

[212] J. Gao, C. Zhu, M. Zhu, Y. Fu, H. Huang, Y. Liu, Z. Kang, *ACS Sustain. Chem. Eng.* **2019**, *7*, 3536–3543.

[213] A. de Lucas-Consuegra, J. Serrano-Ruiz, N. Gutiérrez-Guerra, J. Valverde, *Catalysts* **2018**, *8*, 340.

[214] P. Hirunsit, W. Soodsawang, J. Limtrakul, *J. Phys. Chem. C* **2015**, *119*, 8238–8249.

[215] H. Xiao, T. Cheng, W. A. Goddard, R. Sundararaman, *J. Am. Chem. Soc.* **2016**, *138*, 483–486.

[216] Y. Hori, I. Takahashi, O. Koga, N. Hoshi, *J. Mol. Catal. A Chem.* **2003**, *199*, 39–47.

[217] J. H. Montoya, C. Shi, K. Chan, J. K. Nørskov, *J. Phys. Chem. Lett.* **2015**, *6*, 2032–2037.

[218] K. J. P. Schouten, E. Pérez Gallent, M. T. M. Koper, *J. Electroanal. Chem.* **2014**, *716*, 53–57.

[219] A. A. Peterson, J. K. Nørskov, *J. Phys. Chem. Lett.* **2012**, *3*, 251–258.

[220] J. Albo, A. Sáez, J. Solla-Gullón, V. Montiel, A. Irabien, *Appl. Catal. B Environ.* **2015**, *176–177*, 709–717.

[221] J. Hazarika, M. S. Manna, *Electrochim. Acta* **2019**, *328*, 135053.

[222] M. Mogensen, T. Lindegaard, *Proc. Electrochem. Soc.* **1993**, *PV 1993-04*, 484–493.

[223] J. Mizusaki, H. Tagawa, T. Saito, T. Yamamura, K. Kamitani, K. Hirano, S. Ehara, T. Takagi, T. Hikita, M. Ippommatsu, S. Nakagawa, K. Hashimoto, *Solid State Ionics* **1994**, *70/71*, 52–58.

[224] S. P. Jiang, Y. Ramprakash, *Solid State Ionics* **1999**, *116*, 145–156.

[225] A. Leonide, S. Hansmann, A. Weber, E. Ivers-tiffée, *J. Power Sources* **2011**, *196*, 7343–7346.

[226] T. Yonekura, Y. Tachikawa, T. Yoshizumi, Y. Shiratori, K. Ito, K. Sasaki, *ECS Trans.* **2011**, *35*,

1007–1014.

[227] T. Matsui, M. Futamura, R. Kikuchi, K. Eguchi, *ECS Trans.* **2007**, *7*, 851–858.

[228] R. Kikuchi, T. Yano, T. Takeguchi, K. Eguchi, *Solid State Ionics* **2004**, *174*, 111–117.

[229] P. Kazempoor, R. J. Braun, *Int. J. Hydrogen Energy* **2014**, *39*, 2669–2684.

[230] P. Kazempoor, R. J. Braun, *Int. J. Hydrogen Energy* **2014**, *39*, 5955–5971.

[231] R. A. Svehla, *NASA Tech. Rep.* **1962**, R-132.

[232] J. O. Hirschfelder, R. B. Bird, E. L. Spotz, *J. Chem. Phys.* **1948**, *16*, 968–981.

[233] R. Atsumi, T. Ishiyama, H. Kishimoto, K. Develos-Bagarinao, K. Yamaji, T. Yamaguchi, Y. Fujishiro, *J. Fuel Cell Technol.* **2016**, *16*, 76–80.

[234] N. Fujiwara, T. Minami, R. Kikuchi, A. Takagaki, T. Sugawara, S. Tada, S. T. Oyama, *J. Electrochem. Soc.* **2019**, *166*, F716–F723.

[235] J. Il Jung, M. Risch, S. Park, M. G. Kim, G. Nam, H. Y. Jeong, Y. Shao-Horn, J. Cho, *Energy Environ. Sci.* **2016**, *9*, 176–183.

[236] J. Wang, Z. Lü, K. Chen, X. Huang, N. Ai, J. Hu, Y. Zhang, W. Su, *J. Power Sources* **2007**, *164*, 17–23.

[237] J. Klose, M. Baerns, *J. Catal.* **1984**, *85*, 105–116.

[238] I. Alstrup, *J. Catal.* **1995**, *151*, 216–225.

List of Publications, Presentations, and Awards

A-1. Publications related to this dissertation

(1) Naoya Fujiwara, Shohei Tada, Ryuji Kikuchi*
"Power-to-gas Systems Utilizing Methanation Reaction in Solid Oxide Electrolysis Cell Cathodes: A Model-based Study"
Sustainable Energy & Fuels, 2020, **4**(6), 2691-2706. **[Front cover]**
→ **Section 2.1.**

(2) Naoya Fujiwara, Hironori Nagase, Shohei Tada, Ryuji Kikuchi*
"Hydrogen Production by Steam Electrolysis in Solid Acid Electrolysis Cells"
ChemSusChem, 2021, **14**(1), 417-427.
→ **Section 3.1.**

A-2. Other publications

(3) Naoya Fujiwara, Tatsushi Minami, Ryuji Kikuchi*, Atsushi Takagaki, Takahsi Sugawara, Shohei Tada, Shigeo Ted Oyama
"Low Ni-Containing Cermet Anodes of Solid Oxide Fuel Cells with Size-Controlled Samarium-Doped Ceria Particles"
Journal of The Electrochemical Society, 2019, **166**(12), F716-F723.

(4) Shohei Tada, Seiya Tajima, Naoya Fujiwara, Ryuji Kikuchi*
"High-performance Anode for Solid Acid Fuel Cells Prepared by Mixing of Carbon Substance with Anode Catalysts"
International Journal of Hydrogen Energy, 2019, **44**(48), 26545-26553.

(5) Yusuke Honda, Naoya Fujiwara, Shohei Tada, Yasukazu Kobayashi, Shigeo Ted Oyama, Ryuji Kikuchi*
"Direct Electrochemical Synthesis of Oxygenates from Ethane using Phosphate-based Electrolysis Cells"
Chemical Communications, 2020, **56**(76), 11199-11202. **[Inside back cover]**

(6) Tomohiro Mishina=, Naoya Fujiwara=, Shohei Tada, Atsushi Takagaki, Ryuji Kikuchi*, Shigeo Ted Oyama
"Calcium-Modified Ni-SDC Anodes in Solid Oxide Fuel Cells for Direct Dry Reforming of Methane"
Journal of The Electrochemical Society, 2020, **167**(13), 134512.

(7) Naoya Fujiwara, Ryuji Kikuchi*, Atsushi Takagaki, Takashi Sugawara, Shigeo Ted Oyama
"Investigation of Solid Oxide Electrolysis Cell Electrodes for Methane Synthesis"
ECS Transactions, 2017, **78**(1), 3247-3256.

(8) Naoya Fujiwara, Taro Kayamori, Tomohiro Mishina, Shohei Tada, Yasukazu Kobayashi, Ryuji Kikuchi*
"Hydrogen Oxidation Activity of SOFC Anodes with Metal Oxide Addition"
ECS Transactions, 2019, **91**(1), 1837-1844.

(9) Shu Kodama, Ryuji Kikuchi*, Naoya Fujiwara, Shohei Tada, Yasukazu Kobayashi, Shigeo Ted Oyama
"Oxidative Coupling of Methane in Solid Oxide Electrolysis Cell"
ECS Transactions, 2019, **91**(1), 2697-2705.

(10) 齋藤杏実*, 保田侑亮, 藤原直也
"3D プリンターによる分子間相互作用を導入した新規分子模型の作製"
化学と教育, 2019, **67**(10), 492-495.

B-1. Presentations at international conferences

(1) [Poster] Naoya Fujiwara, Ryuji Kikuchi*, Atsushi Takagaki, Shigeo Ted Oyama
"Conceptual Design of Methane Synthesis Using Solid Oxide Electrolysis Cells"
14th Symposium on Fuel Cell and Battery Modeling and Experimental Validation (ModVal 14), March 2017, Karlsruhe, Germany.

(2) [Poster] Naoya Fujiwara, Ryuji Kikuchi*, Atsushi Takagaki, Takashi Sugawara, Shigeo Ted Oyama
"Investigation of Solid Oxide Electrolysis Cell Electrodes for Methane Synthesis"
15th International Symposium on Solid Oxide Fuel Cells (SOFC-XV), July 2017, Hollywood, Florida, USA.

(3) [Oral] Naoya Fujiwara, Ryuji Kikuchi*, Atsushi Takagaki, Shigeo Ted Oyama
"Development of Solid Oxide Electrolysis Cell Cathodes for Direct Methanation in CO_2/H_2O Co-electrolysis"
Grand Renewable Energy 2018 International Conference and Exhibition (GRE2018), June 2018, Yokohama, Japan.

(4) [Oral] Naoya Fujiwara, Ryuji Kikuchi*, Atsushi Takagaki, Shigeo Ted Oyama
"Study of Solid Oxide Electrolysis Cell Cathodes for Direct Methane Synthesis"
UTokyo-Tsinghua Joint Symposium 2018, July 2018, Tokyo, Japan.

(5) [Poster] Naoya Fujiwara, Ryuji Kikuchi*, Atsushi Takagaki, Shigeo Ted Oyama
"Cathode Catalysts of Solid Oxide Electrolysis Cells for Direct Methane Synthesis"
8th Tokyo Conference on Advanced Catalytic Science and Technology (TOCAT8), August 2018, Yokohama, Japan.

(6) [Poster] Naoya Fujiwara, Shohei Tada, Yasukazu Kobayashi, Ryuji Kikuchi*, Shigeo Ted Oyama
"Development of intermediate-temperature electrolysis reactors using a phosphate-based composite electrolyte"
8th World Hydrogen Technologies Convention (WHTC 2019), June 2019, Tokyo, Japan.

(7) [Oral] Naoya Fujiwara, Taro Kayamori, Tomohiro Mishina, Shohei Tada, Yasukazu Kobayashi, Ryuji Kikuchi*, Shigeo Ted Oyama
"Hydrogen Oxidation Activity of SOFC Anodes with Metal Oxide Addition"
16th International Symposium on Solid Oxide Fuel Cells (SOFC-XVI), September 2019, Kyoto, Japan.

(8) [Oral] Naoya Fujiwara, Tatsushi Minami, Shohei Tada, Ryuji Kikuchi*
"Development of Low Ni-containing SOFC Anodes Based on Percolation Theory"
18th Asian Pacific Confederation of Chemical Engineering Congress (APCChE 2019), September 2019, Sapporo, Japan.

B-2. Presentations at domestic conferences

(9) [口頭] 藤原直也，菊地隆司*，高垣敦，大山茂生
"固体酸化物形電解セルによるメタン合成―カソード材料の検討"
第 46 回石油・石油化学討論会，2016 年 11 月，京都リサーチパーク

(10) [口頭] 藤原直也，菊地隆司*，高垣敦，大山茂生
“二酸化炭素からのメタン合成に向けた固体酸化物形電解セル電極材料の検討”
化学工学会 東京大会，2017 年 8 月，早稲田大学理工キャンパス
※学生特別賞受賞

(11) [ポスター] 藤原直也，菊地隆司*，高垣敦，大山茂生
“SOEC カソードでのメタン化反応を利用したエネルギーキャリア合成―プロセスモデルによる検討”
電気化学会 第 85 回大会，2018 年 3 月，東京理科大学葛飾キャンパス
※燃料電池研究会ポスター賞受賞

(12) [ポスター] 藤原直也，菊地隆司*，高垣敦，大山茂生
“固体酸化物形電解セルでのメタン直接合成に向けたカソード触媒の研究”
化学工学会 第 83 年会，2018 年 3 月，関西大学千里山キャンパス
※優秀学生賞受賞

(13) [口頭] 藤原直也*，多田昌平
“固体酸化物形電解セルを用いたメタン直接合成の展望”
第 6 回 次世代天然ガス利用を考える若手勉強会，2019 年 3 月，成蹊大学

(14) [ポスター] 藤原直也，多田昌平，小林靖和，高垣敦，菊地隆司*，大山茂生
“固体酸化物形電解セルでのメタン直接合成を利用した Power to Gas システムの検討”
化学工学会 第 84 年会，2019 年 3 月，芝浦工業大学豊洲キャンパス

(15) [ポスター] 藤原直也，菊地隆司*，多田昌平，小林靖和，高垣敦，大山茂生
“SOEC カソードでのメタン化反応に着目した新規 Power to Gas システムの検討”
第 26 回燃料電池シンポジウム，2019 年 5 月，タワーホール船堀

(16) [口頭] 藤原直也，多田昌平，小林靖和，大山茂生，菊地隆司*
“中温作動型電解セルを用いた CO_2 還元反応”
第 49 回石油・石油化学討論会，2019 年 10 月，山形テルサ

(17) [口頭] 藤原直也，永瀬寛典，多田昌平，菊地隆司*
“固体リン酸塩電解質を用いた中温作動型電解セルの開発”
化学工学会 第 85 年会，2020 年 3 月，関西大学千里山キャンパス
※開催中止につき要旨のみの発表

(18) [口頭] 藤原直也*

“固体リン酸塩電解質を利用した中温作動型電解セルの開発”

材料化学システム工学討論会 2020，2020 年 10 月，オンライン

C. Received awards

(1) 東京大学工学部 工学部長賞，2016 年 3 月

(2) 化学工学会 東京大会 学生特別賞，2017 年 8 月

(3) 電気化学会 第 85 回大会 燃料電池研究会 ポスター賞，2018 年 3 月

(4) 化学工学会 第 83 年会 優秀学生賞，2018 年 3 月

(5) 東京大学大学院工学系研究科 化学システム工学専攻
修士論文ベストプレゼンテーション賞，2018 年 3 月

Acknowledgements

The work presented in this dissertation was conducted from 2015 to 2020 at Department of Chemical System Engineering, School of Engineering, The University of Tokyo.

I greatly acknowledge my supervisor *Associate Professor Ryuji Kikuchi* for his generous supervising throughout the undergraduate course, the master's course, and the PhD course. He always provided me with opportunities to practice what I wanted to try. The six years in Kikuchi Group has shaped my ability as a chemical engineering researcher. I have learnt a lot from his valuable suggestions about my research.

I also express my gratitude to *Professor Emeritus Shigeo Ted Oyama* for his supervising. His instructions in *danwakai* really helped me obtain the skills for scientific discussions in English. My presentation skills have also been greatly improved by his guidance.

I appreciate the members of my dissertation committee; *Professor Atsuo Yamada* (The University of Tokyo), *Professor Masaru Ogura* (The University of Tokyo), *Professor Jun Kubota* (Fukuoka University), *Professor Junichiro Otomo* (Tokyo Institute of Technology), and *Associate Professor Yasunori Kikuchi* (The University of Tokyo). Their constructive criticism helped me sophisticate this dissertation.

I acknowledge the support from Materials Education Program for the Future Leaders in Research, Industry, and Technology (MERIT) at the University of Tokyo. *Professor Yamada* was my vice-supervisor in MERIT program and gave me valuable advice in regular interviews. I am grateful for the guidance.

Assistant Professor Shohei Tada (Ibaraki University) is greatly acknowledged. He taught me the attitude required for becoming a scientist. I could not accomplish my PhD course without his advice.

I am thankful to *Associate Professor Atsushi Takagaki* (Kyushu University), *Dr. Yasukazu Kobayashi* (National Institute of Advanced Industrial Science and Technology), and *Mr. Takashi Sugawara* (The University of Tokyo) for their instructions in Oyama-Kikuchi Laboratory.

Laboratory secretaries *Ms. Yukie Ichikawa*, *Ms. Noriko Kuwabara*, and *Ms. Yasuko Tanaka* are thanked for the administration.

I acknowledge all the other laboratory members including postdoctoral fellows, students, and visitors from overseas. *Mr. Hironori Nagase* is thanked for his contribution to the experiments regarding Section 3.1. *Dr. Geletu Qing* and *Mr. Shuya Suzu* are thanked for their help in preparing samples.

The research regarding Chapter 3 was supported by Japan Society for the Promotion of Science (JSPS) KAKENHI Grant Number JP20J14232.

A part of XRD measurements was conducted at Advanced Characterization Nanotechnology Platform of the University of Tokyo, supported by "Nanotechnology Platform" of the Ministry of Education, Culture, Sports, Science and Technology (MEXT), Japan.

Finally, I express my cordial gratitude to my mother *Keiko* and my father *Satoshi* for their kind understanding of my studies and their unstinted support.

January 2021

Naoya Fujiwara